AD-A190 169 HIGH DENSITY ION IMPLANTED CONTIGUOUS DISK BUBBLE TECHNOLOGY(U) CARNEGIE-MELLON UNIV PITTSBURGH PA DEPT OF ELECTRICAL AND COM... M H KRYDER ET AL. 31 OCT 87 1/3

UNCLASSIFIED AFOSR-TR-87-2044 AFOSR-84-0341 F/G 9/1 NL

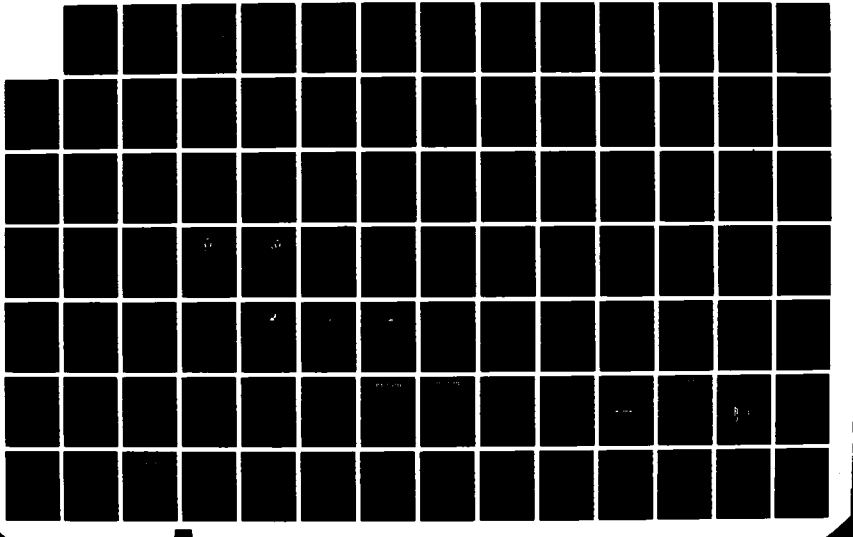

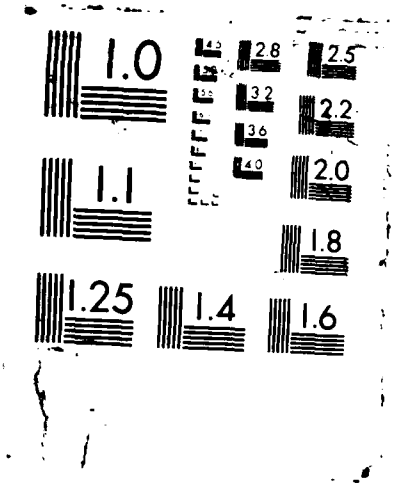
1.0
2.8
2.5
3.2
2.2
3.6
4.0
2.0
1.1
1.8
1.25
1.4
1.6

CARNEGIE-MELLON UNIVERSITY

Department of Electrical and Computer Engineering

HIGH DENSITY ION IMPLANTED CONTIGUOUS DISK BUBBLE TECHNOLOGY
Annual Scientific Report
September 30, 1986 - September 30, 1987

M. H. Kryder, D. W. Greve, A. Guzman, S. C. Jo, M. Ramesh, K. R. Nitzberg, P. H. L. Rasky, M. Alex

Carnegie Mellon University

(2)

AFOSR-TR- 87-2044

HIGH DENSITY ION IMPLANTED CONTIGUOUS DISK BUBBLE TECHNOLOGY

Annual Scientific Report
September 30, 1986 - September 30, 1987

M. H. Kryder, D. W. Greve, A. Guzman, S. C. Jo,
M. Ramesh, K. R. Nitzberg, P. H. L. Rasky,
M. Alex

Carnegie Mellon University

Unclassified
SECURITY CLASSIFICATION OF THIS PAGE

AD-A190 169

REPORT DOCUMENTATION PAGE

1a. REPORT SECURITY CLASSIFICATION: Unclassified	1b. RESTRICTIVE MARKINGS
2a. SECURITY CLASSIFICATION AUTHORITY	3. DISTRIBUTION/AVAILABILITY OF REPORT: Unlimited — Approved for public release; distribution unlimited.
2b. DECLASSIFICATION/DOWNGRADING SCHEDULE	
4. PERFORMING ORGANIZATION REPORT NUMBER(S): 1	5. MONITORING ORGANIZATION REPORT NUMBER(S): AFOSR-TR- 87-2044
6a. NAME OF PERFORMING ORGANIZATION: Carnegie Mellon University; 6b. OFFICE SYMBOL (If applicable)	7a. NAME OF MONITORING ORGANIZATION: Air Force Office of Scientific Research
6c. ADDRESS (City, State and ZIP Code): Pittsburgh, PA 15213-3890	7b. ADDRESS (City, State and ZIP Code): BLDG 410 Bolling Air Force Base Washington, DC 20332
8a. NAME OF FUNDING/SPONSORING ORGANIZATION: AFOSR; 8b. OFFICE SYMBOL (If applicable): NE	9. PROCUREMENT INSTRUMENT IDENTIFICATION NUMBER: AFOSR-84-0341
8c. ADDRESS (City, State and ZIP Code): BLDG 410 Bolling Air Force Base Washington, DC 20332	10. SOURCE OF FUNDING NOS. — PROGRAM ELEMENT NO.: 6102F; PROJECT NO.: 2305; TASK NO.: C1; WORK UNIT NO.:
11. TITLE (Include Security Classification)	

12. PERSONAL AUTHOR(S): M. H. Kryder, M. Alex, S. C. Jo, D. W. Greve, P. H. L. Rasky, A. Guzman, M. Ramesh, K. Nitzberg

13a. TYPE OF REPORT	13b. TIME COVERED	14. DATE OF REPORT (Yr., Mo., Day)	15. PAGE COUNT
Annual Scientific	FROM 9/30/86 TO 9/29/87	October 31, 1987	256

16. SUPPLEMENTARY NOTATION

17. COSATI CODES			18. SUBJECT TERMS (Continue on reverse if necessary and identify by block number)
FIELD	GROUP	SUB GR.	Bubble Memory, Ion Implantation, Garnet, Silicon-on-Insulator, Silicon-on-Garnet

19. ABSTRACT (Continue on reverse if necessary and identify by block number)

HIGH DENSITY ION IMPLANTED CONTIGUOUS DISK
BUBBLE TECHNOLOGY
Annual Scientific Report
September 30, 1986 - September 30, 1987

M. H. Kryder, D. W. Greve, A. Guzman, S. C. Jo, M. Ramesh, K. R. Nitzberg, P. H. L. Rasky, M. Alex

Carnegie Mellon University

ABSTRACT

During the past year we have advanced the state-of-the-art in several areas of magnetic bubble technology. The main thrust of our research has been to advance ion implanted contiguous disk devices because these devices offer order of magnitude higher bit density

20. DISTRIBUTION/AVAILABILITY OF ABSTRACT	21. ABSTRACT SECURITY CLASSIFICATION	
UNCLASSIFIED/UNLIMITED ☒ SAME AS RPT. ☐ DTIC USERS ☐	Unclassified	
22a. NAME OF RESPONSIBLE INDIVIDUAL: DR GERALD WITT	22b. TELEPHONE NUMBER (Include Area Code): (202) 767-4932	22c. OFFICE SYMBOL: NE

DD FORM 1473, 83 APR — EDITION OF 1 JAN 73 IS OBSOLETE.

Unclassified
SECURITY CLASSIFICATION OF THIS PAGE

Continuation of Block 19:

than presently manufactured bubble devices. We succeeded in several regards. Noteworthy accomplishments include demonstration of bubble propagation in devices having 4 μm^2 bit cells and exhibiting operating margins equal to those of today's manufactured devices. These devices were demonstrated to operate from 0°C to 120°C, the limits of our present testing capabilities. A major factor in this success was our development of new epitaxial garnet materials which exhibited isotropic magnetostrictive properties -- a feature previously not obtained.

In addition to the work on bubble propagation we made significant progress on demonstrating a fully operational contiguous disk chip, complete with bubble generators, transfer gates and stretcher/detectors. All components have now been demonstrated to operate with good overlapping margins and a complete chip has been designed and fabricated. We are in the process of testing it.

We have also developed a model which can be used to simulate the operation of contiguous disk devices. To our knowledge, this is the first such model and initial comparisons to experimental results indicate this model will be useful in the design of future devices. Industrial firms have indicated an interest in using this model.

We have also continued our research on depositing silicon-on-garnet for forming silicon detectors and signal processing circuitry for the bubble devices. We believe the reduced size of these detectors will make it possible to significantly enhance the speed of bubble technology. Furthermore, as we look to the future, we hope to develop a new class of hybrid devices combining magnetic, semiconductor and optical devices on a single substrate. Our work in this area thus is an initial step in this direction.

Individual reports describing each of the above areas are attached.

Magnetic Bubble Garnets

M. Ramesh and M. H. Kryder
Department of Electrical and Computer Engineering

ABSTRACT

This article summarizes the design, development and growth of various bubble garnet films in our facility, to be used in the fabrication of high density bubble storage devices. In particular, bubble garnet films which support 0.5 μm diameter bubbles, with large, negative and nearly isotropic magnetostriction, which were used in 2.5μm period ion-implanted contiguous disk devices are discussed. In these films, similar margins for the "good" and "bad" propagation directions (parallel and perpendicular to $[11\bar{2}]$) were measured and were found to overlap significantly. Several materials and growth aspects of these films are discussed. Mention is also made of isotropic 1μm bubble films to be used in current-access devices and garnet films to be used in silicon on garnet technology.

I. Introduction

Materials development has been an important aspect of our study on Ion Implanted Contiguous Disk (IICD) devices fabricated on magnetic bubble garnet films. The need for high-density devices supporting smaller sized bubbles, with a high-quality performance has resulted in the design and development of significantly improved materials. In this article of the report, the activity in the area of materials development during the past year is described.

The design of magnetic bubble garnets to be used in IICD devices has been complicated by the stringent conditions placed on the various materials parameters due to device considerations. Besides having to support smaller bubbles, there are other requirements, the most important of which is the isotropic propagation of the bubbles along tracks oriented in different directions of the film. The propagation margins of bubble domains in IICD devices fabricated on [111] oriented garnets were observed by Lin[1] and Wolfe[2] to exhibit three-fold symmetry. Lin[1] noted that the propagation margins of bubble domains propagating on both sides of tracks parallel to the $[11\bar{2}]$ direction were approximately equal and acceptably large. He referred to these as "good" tracks. On the other hand, he observed that for tracks oriented perpendicular to the $[11\bar{2}]$ directions, margins were anomalously large on one side (the "super" track) and anomalously small on the other side (the "bad" track). These three-fold margins have considerably complicated the design of ion-implanted devices. Initially, it was believed that magnetocrystalline anisotropy alone caused this anisotropic behavior[1], but later it was realized that anisotropic magnetostriction was also a major cause[3,4]. Kryder and Saunders[4] and independently Hubert[3] proposed that the anisotropic effects could be greatly diminished by growing materials with isotropic magnetostriction coefficients, $\lambda_{111} = \lambda_{100}$. Garnet materials with negative magnetostriction coefficients have been reported by Makino et al[5]. and double films supporting 2 μm bubbles by Fratello et al[6]. Additionally, it was desired that these magnetic films have a reasonably large magneto-optical Kerr effect, so that visual observation of the device performance using a polarized microscope can be accomplished while testing devices.

Following the work of several researchers[7], it has been found that bismuth doped magnetic bubble garnets are the ideal candidates for high-density, isotropic storage devices and our efforts are essentially concentrated in developing such films. These films have a general composition $(BiSmLuYDy)_3(FeGa)_5O_{12}$. The presence of bismuth is responsible for the large magneto-optical Kerr rotation. Besides, bismuth is also an important source of uniaxial anisotropy and the ratio

of bismuth ion to the other dodecahedral ions such as samarium, control the value of the anisotropy constant, K_u and can be varied in a controlled fashion to achieve the desired values of quality factor, Q, ($Q = K_u/2\pi M^2$, where $4\pi M$ is the magnetization) for optimal device performance. The element dysprosium is added to obtain isotropic bubble propagation, as will be explained later. Although several other elements were considered, it has been found that this particular choice of elements is ideal, besides being simpler to devolope the appropriate melt systems. It has also been determined that this set of elements is so versatile that by simply varying the composition, a wide range of physical properties can be obtained. For example, the following different melts were developed using the same elements in different proportions:

(1) AK ($Bi_{0.4}Dy_{0.7}Sm_{0.2}Lu_{1.5}Y_{0.2}Fe_{4.9}Ga_{0.1}O_{12}$); series; for isotropic IICD devices supporting 0.5 μm bubbles and the AM series for overcompensated ($\lambda_{100} < \lambda_{111}$) supporting 0.5 μm bubbles.

(2) AH ($Bi_{0.4}Dy_{0.7}Sm_{0.2}Lu_{1.2}Y_{0.5}Fe_{4.45}Ga_{0.55}O_{12}$); and AG series; for isotropic, 1 μm bubbles to be used in current accessed IICD devices.

(3) AP series ($Bi_{0.3}Dy_{1.00}Sm_{0.2}Lu_{1.0}Y_{0.5}Fe_{4.36}Ga_{0.64}O_{12}$); to be used in the fabrication of silicon-on-garnet devices supporting nearly isotropic 2 μm bubbles.

The initial stages of work on some of these melts were reported in the previous annual report and will not be repeated here. Of these different melt systems, series AK will be discussed in great detail to highlight the process of materials development in our facility. This will also complement the research done by S. C. Jo on the performance of the devices fabricated using these films[8].

Section II of this article deals with the design considerations that went into the development of the AK series melt and the next section covers the growth and characterization of these films. Section IV discusses the experimental observations, followed by a section on the other melt system. Section VI concludes this part of the report.

II Film development

The most crucial parameters that need to be optimized are the magnetostriction constants, λ_{111} and λ_{100}. They are not only required to be equal, but also to be large and negative for use in ion-implanted devices.

The exact determination of the magnetostriction coefficients is based on the theory of magnetostriction for substituted garnet films[9]. It is assumed that (1) the contribution to the magnetostriction coefficients due to the Fe^{+3} ions is negligibly small and (2) the contribution arising from the rare-earth ions is diluted by the Ga substitution due to the reduction in the eschange field at the dodecahedral sites. Nearly isotropic magnetostriction in the AK series films is achieved by incorporating bismuth and dysprosium ions. Dysprosium iron garnet is unusual[10] in that it has $\lambda_{100} < \lambda_{111}$ and both being negative, while most other rare-earths have $\lambda_{111} < \lambda_{100}$. Bismuth also affects the magnetostriction marginally, since for bismuth, $\lambda_{100} < \lambda_{111}$, although they are both positive. The magnetostriction coefficients of the bismuth iron garnet were estimated by Makino et al. and Hansen et al. By careful selection of film constituents it is possible to obtain films in which λ_{100} nearly equals λ_{111}.

To aid in the film development, a computer program which can be used to estimate the magnetic parameters of substituted garnet films of various compositions was used. The program is based on the assumption that properties of films containing several constituents can be calculated from the known properties of single constituent rare-earth iron garnets. The final film properties are determined by weighting the particular pure iron garnet values of each element by the amount in the mixed composition and summing all the weighted values. This value is then adjusted for Ga substitution taking into account the tetrahedral-octahedral site preference. Computer analysis provided several acceptable compositions from the $\{BiSmLuYDy\}_3[FeGa]_5(O)_{12}$ film system that would have isotropic magnetostriction, for a given bubble diameter and an acceptable quality factor, Q. A more detailed account of the computer software was included in the previous report and the details of the algorithm are omitted here.

The required magnetization to support 0.5 μm diameter bubbles is provided by the Fe-Ga stoichiometry. Bismuth provides the essential anisotropy by pairing with the other rare-earth ions such as Sm, Lu and Dy and with Y. The Bi-Sm pair provides the largest anisotropy, followed in order by Bi-Y and Bi-Lu pairs. The exact mechanism of anisotropy for bismuth-rare-earth ion pairs is not yet understood completely, although an empirical model is used in the computer design program to estimate the resulting uniaxial anisotropy. The balance of Y and Lu also need to be determined critically in order that the lattice parameter of the magnetic films be reasonably close to that of the GGG substrate, to allow for stable and defect-free films. The dysprosium ions however have one disadvantage - they have a large damping constant and thus

the mobility of the bubbles is reduced. In fact, in melts supporting larger sized bubbles, such as the AP series, relatively large amounts of dysprosium need to be added to make them isotropic and thus increasing the damping constant correspondingly. This is an important design consideration in larger sized bubble films.

III Growth and characterization

After identifying attractive film compositions by computer analysis, the magnetic garnet films were grown by liquid phase epitaxy (LPE) from a Bi_2O_3-PbO flux system. Films were grown with a 60°C to 70°C supercooling at 860°C to 900°C with a rotation of 40 to 100 rpm. The exact growth temperature would depend upon the melt composition and the desired film properties. Two kinds of GGG substrates were used to grow the bubble films; [111] oriented films were used for devices and [100] oriented films were used for measurements of λ_{100}. The process of LPE film growth and the furnace system are described in the previous report.

The film thickness was measured by interferometry, while magnetization and the characteristic length parameter, l, were determined from bubble collapse and domain stripwidth measurements. Ferromagnetic resonance was used to determine the uniaxial anisotropy constant, K_u and hence the Q value of the films. A previously described ferromagnetic resonance apparatus was used to measure the magnetostriction constants[11]. Using films with [111] and [100] orientations, the appropriate magnetostriction coefficients are determined. X-ray double crystal diffraction technique is used to measure the lattice mismatch. The various characterization techniques are described in detail in the previous report. The film composition was also determined by Energy Dispersive Spectroscopy using a scanning electron microscope. The accuracy of this technique was somewhat limited in determining small atomic ratios, although it is an important tool in identifying the compositional change after each alteration of the melt. This technique is also useful in computing the segregation coefficients of the various ions, defined broadly as the molar percentage of a particular ion in the melt that diffuses to the surface epitaxially to form the film.

IV Experimental observations

Garnet films supporting magnetic bubbles whose diameters range from 0.45 μm to 0.65 μm were grown with nearly isotropic magnetostriction. Typical 0.65 μm diameter films had a characteristic length of 0.072 μm, a magnetization of 830G, and an anisotropy field of 2160 G providing a Q of 2.6. The damping of these films was large, but not unusable; α was measured

from the linewidths of the ferromagnetic resonance signals and found to be 0.11. Almost anisotropic magnetostriction was obtained for these films with $\lambda_{111} = -3.9 \times 10^{-6}$ and $\lambda_{100} = -3.5 \times 10^{-6}$. The effect that the growth temperature has on the magnetostriction for nearly isotropic films is shown in Fig. 1. All properties of films were observed to be strongly dependent on the growth temperature. In particular, the magnetostriction coefficients can be varied by about 15% by adjusting the growth temperature. This variation can be attributed to changes in the amount of bismuth and dysprosium incorporated into the films. Compared to the Lu and Y ions, Bi and Dy have large ionic radii, with Bi having the largest radius of the four. Thus at higher growth temperature, the atomic fraction of Dy and Bi ions in the film is small. As the growth temperature is lowered, at first the Dy concentration increases and thus λ coefficients become larger and more negative. At still lower temperatures, the Bi concentration goes up, the λs become less negative, resulting in the behavior shown in Fig. 1. Such information was used in the modification of the melt and in determining the optimum growth temperature. It can be seen from this figure that isotropy is achieved by Dy substitution for Bi and thus at the expense of some uniaxial anisotropy.

One indirect way of measuring the Dy content in the films is through the FMR linewidth. Dy has a very high damping coefficient and hence contributes significantly to the FMR linewidth. If the Dy content is increased, the FMR linewidth, which is essentially due to Dy, is observed to increase almost linearly, as seen in Fig. 2. The variation of the two magnetostriction coefficients, λ_{111} and λ_{100} with the Dy content in the melt was also measured and is shown in Fig. 3

Ion implanted contiguous diamond propagation patterns with 2.5μm period were fabricated on a film which was grown by the above method[9]. The margins for tracks oriented in the conventionally defined "good" and "bad" directions are shown in Fig. 4. Both margins were made for propagation completely around the loops at 1 Hz; thus, the "bad" track margin is actually the intersection of the "super" and "bad" track margins. The propagation margins are seen to be about 12% for both the "good" and the "bad" orientations. The results are similar to the previously reported[12] bias margins obtained from films with nearly isotropic magnetostriction ($\lambda_{111} = -3.1 \times 10^{-6}$ and $\lambda_{100} = -2.1 \times 10^{-6}$) although the margin width decreased and the minimum drive field increased somewhat due to the bigger bubbles used. This shows that the improvement of the degree of isotropy did not change the bias margins

noticeably. This suggests that it may be better using somewhat less isotropic material since it decreases the damping.

V Other melt systems

The AH series melt is the source of 1.00 μm diameter bubble films to be used in the current accessed IICD devices. The requirements on these films were similar to those of the 0.5 μm bubble films. These films were also designed to be iostropic and as can be seen from the propagation margins[8], they are indeed reasonably isotropic.

The AP series films are to be used in silicon-on-garnet devices, supporting 2.00 μm diameter bubbles. It has been observed that the magnetic properties of these films undergo a lot of change through each processing step in the fabrication of these devices. A systematic study of these changes was conducted and the initial film properties were correlated to the properties at the end of the device fabrication. This information is then used to interpolate the set of desired initial properties and the appropriate film composition is then chosen. For example, a typical raw AP film supports a 1.3 μm bubble, whereas after processing, there is a 66% increase in the bubble diameter and the final device supports a 2.00 μm bubble. These films were not completely isotropic, since that would necessitate a large inclusion of dysprosium, which would result in a large damping constant.

The film and the melt compositions of the various series of magnetic garnets are tabulated in Table 1. In Table 2 the nominal values of the various magnetic parameters of these films are given.

VI Conclusion

By developing several bismuth based melt systems, covering a wide range of bubble diameters and other magnetic parameters, a much better understanding of the design process in general and the bismuth based garnet systems in particular has been obtained. In a short time of development, several problems associated with the bismuth based melt system and the growth process have been solved, although some problems such as the surface non-uniformity and flux adhesion still persist to some degree. Our successful incorporation of dysprosium in these films, and thus achieving nearly isotropic bubble propagation, is a significant step toward solving a major problem associated with the design of bubble memory storage devices. Compared with the traditional, non-bismuth rare-earth substituted bubble garnets, the new bismuth-dysprosium based films are demonstrably superior in the development of high-density devices and are likely to be the materials of future magnetic bubbles research.

	PbO	Bi_2O_3	Fe_2O_3	Ga_2O_3	Dy_2O_3	Sm_2O_3	Lu_2O_3	Y_2O_3
AK	453.11	169.23	30.50	1.1544	2.1163	0.5887	2.2523	0.684
AH	324.52	90.00	23.932	1.5412	0.43	0.1598	1.0941	0.4879
AP	468.45	110.48	22.465	2.4028	0.982	0.7989	1.6408	0.5594

Table 1: Weight ratios of various constituent elements in different melts

	AK	AH	AP
$4\pi M_s$ (G)	830	660	420
H_k (Oe)	2160	2300	2300
Q	2.60	3.48	5.5
bubble diameter (μm)	0.65	0.98	1.33
collapse field (Oe)	550	400	278
λ_{111} (X 10^{-6})	- 3.9	-3.7	
λ_{100} (X 10^{-6})	- 3.5	-2.5	
thickness (μm)	0.8	1.4	2.8
growth temp. (^{o}C)	860	880	820

Table 2: Properties of typical films grown from some melts

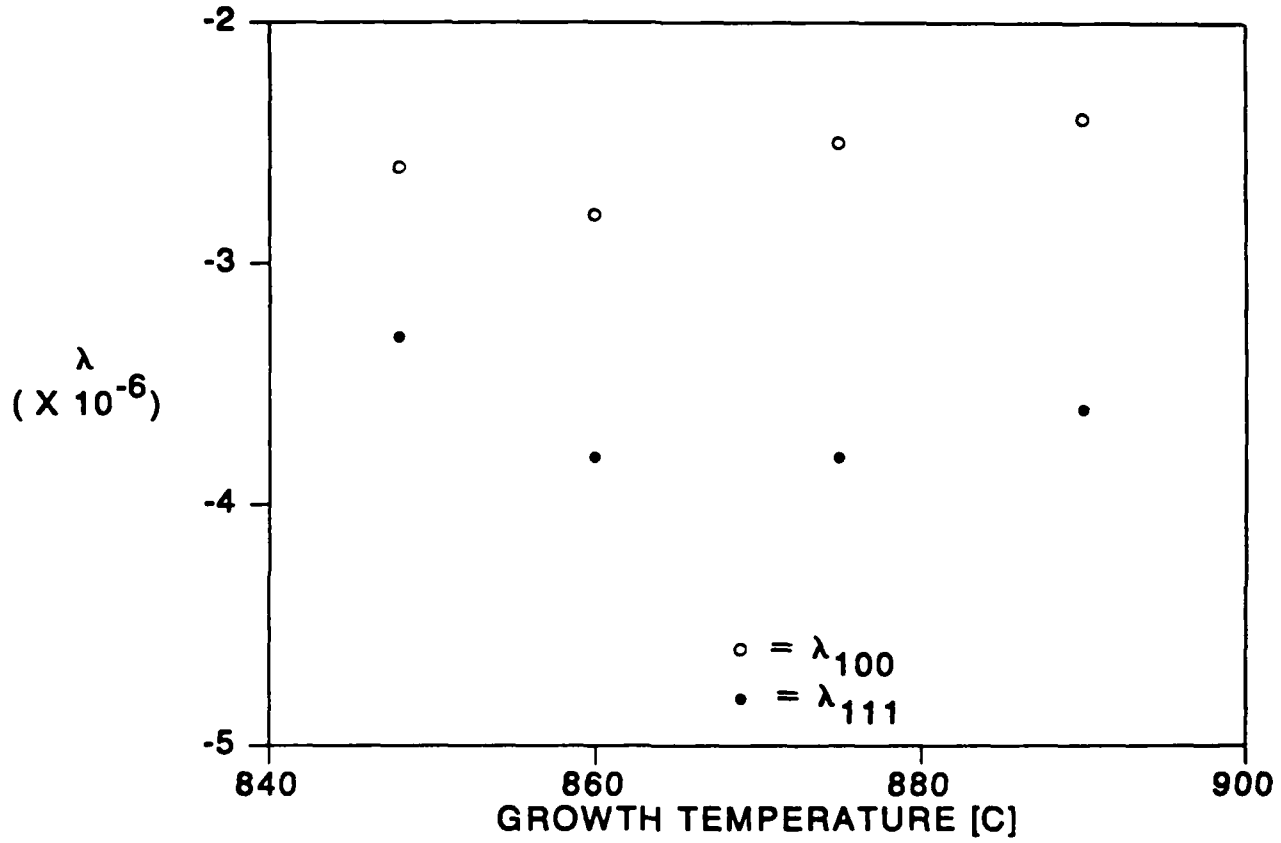

Figure 1: Magnetostriction Dependence on Growth Temperature

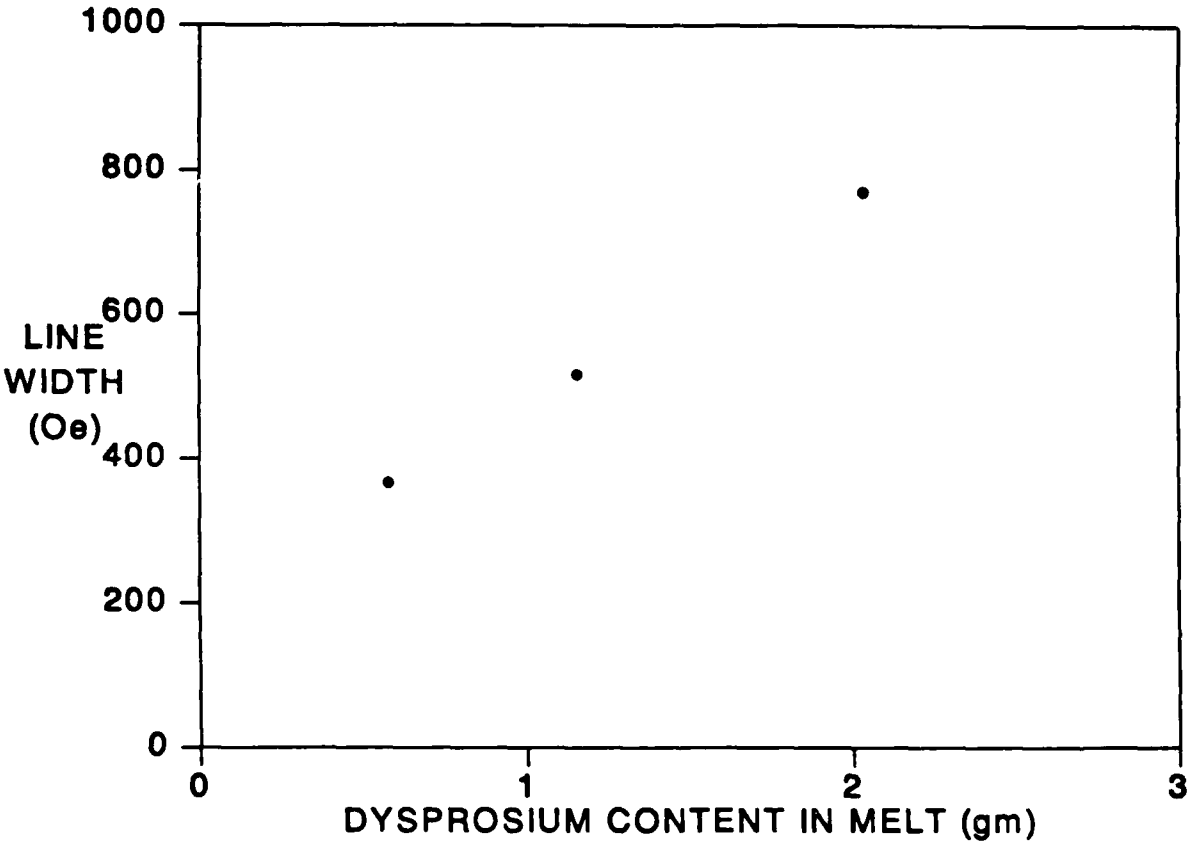

Figure 2: Dependence of FMR linewidth on Dysprosium content in the melt

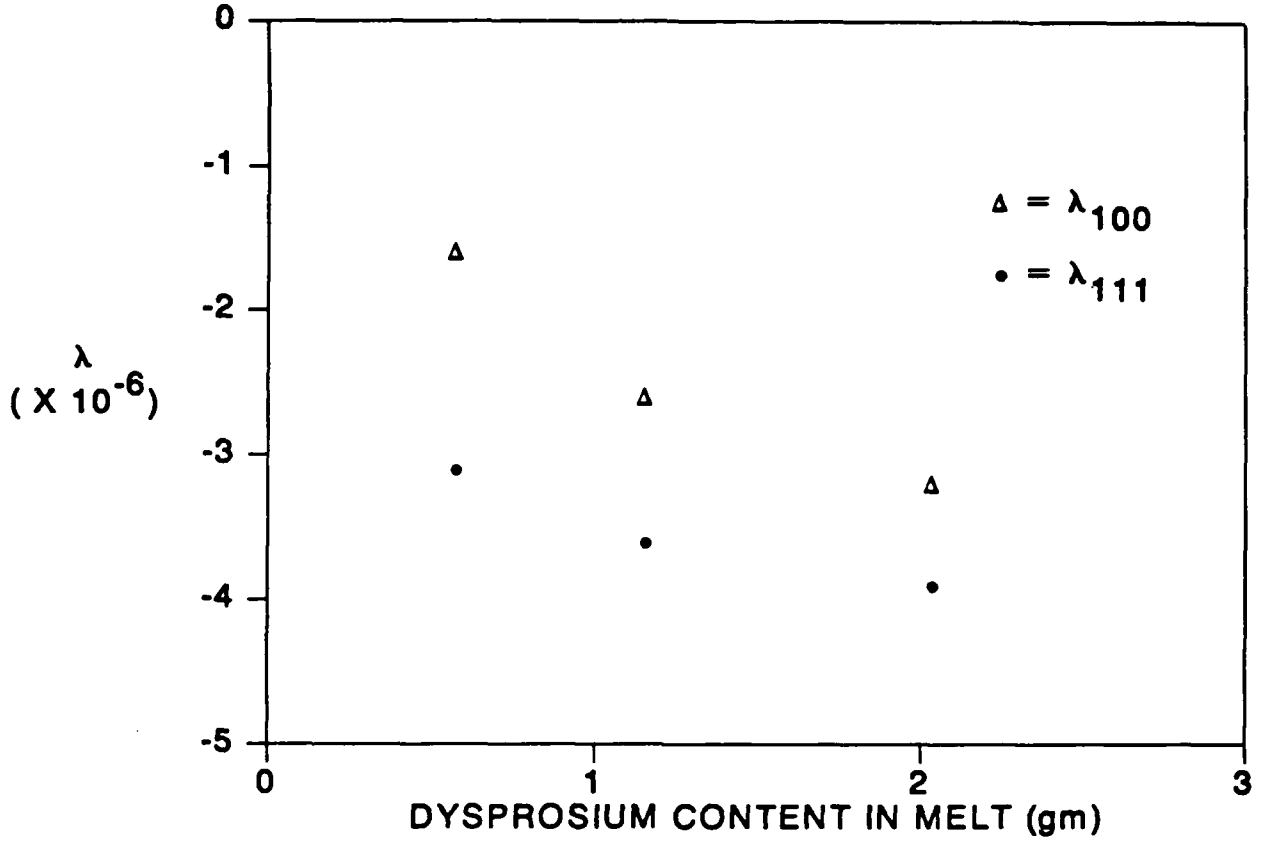

Figure 3: Dependence of magnetostriction coefficients on Dyprosium content in the melt

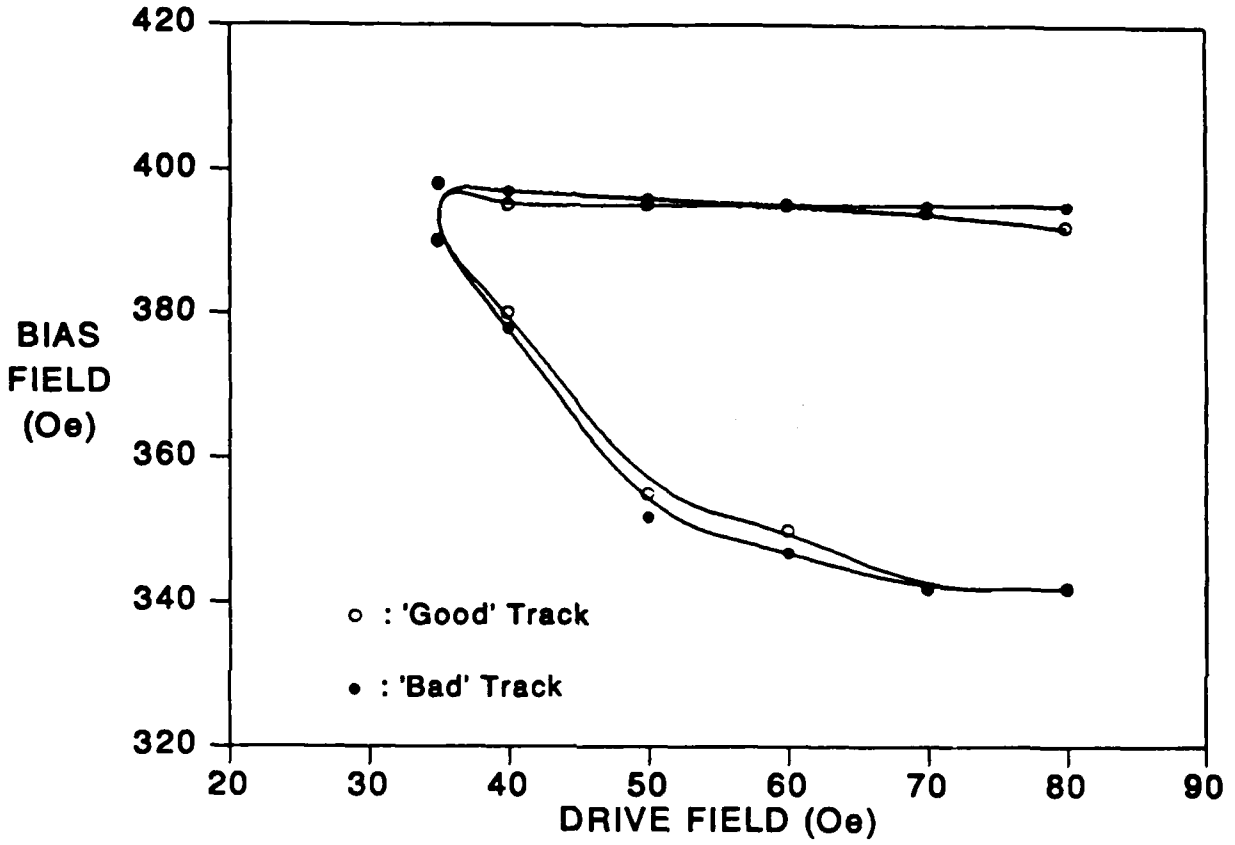

Figure 4: Margins of 2.5μm period IICD pattern

REFERENCES

[1] Y.S. Lin, G.S. Almasi, D.B. Dove, G.E. Keefe, and C.C. Shir, "Orientation dependence of propagation margin of 1-μm bubble contiguous-disk devices -- Clues and Cures", *J. of Appl. Phys.*, 50, 2258, (1979).

[2] R. Wolfe, T.J. Nelson, "Crystal Symmetry Effects in Ion-Implanted Propagation Patterns for Magnetic bubbles: 'Roof-Top' Designs", *I.E.E.E. Trans. Magnet.*, MAG-15, 1323, (1979).

[3] A. Hubert, "Domain Wall Phenomenon in Bubble Propagation Layers", *J. of Magnetism and Magnetic Materials*, 35, 249, (1983).

[4] M.H. Kryder, D.A. Saunders, "The Effects of Stress Relaxation and Anisotropic Magnetostriction On Charged Walls in Ion-Implanted Garnets", *I.E.E.E. Trans. Magnet.*, MAG-19, 1817, (1983).

[5] H. Makino, O. Okada, and Y. Hidaka, "Dysprosium Containing Bubble Garnet Composition for Ion-Implanted Contiguous Disk Devices", *J. Appl. Phys.*, 55, 2551, (1984).

[6] V. J. Fratello, R. D. Pierce and C. D. Brandle, "Variation of the Temperature Coefficient of Collapse Field in Bismuth-Based Bubble Garnets", *Jour. of Appl. Physics*, 57, 4043, (1985).

[7] P. Hansen, K. Witter, and W. Tolksdorf, "Magnetic and Magneto-optic Properties of Lead- and Bismuth-Substituted Yttrium Iron Garnet", *Phys. Rev.*, B27, 6608, (1983).

[8] S. C. Jo "*Propagation in Submicron Ion Implanted Magnetic Bubble Computer Memory Devices*" dissertation, Carnegie-Mellon University, Pittsburgh. (1987) ***included in this report.***

[9] R. L. White, *I.E.E.E Trans. Magnet.*, MAG-9, 606, (1973).

[10] A. H. Eschenfelder, "*Magnetic Bubble Technology*", Springer-Verlag. New York. (1981)

[11] X. Wang, C.S. Krafft, M.H. Kryder, "Measurement of Magnetocrystalline Anisotropy Field and Magnetostriction Coefficient in Garnet Films", *I.E.E.E. Trans. Magnet.*, MAG-18, 1295, (1982).

[12] S. Jo and M. H. Kryder, "Nearly Isotropic Propagation of 0.5 Micrometer Bubbles in Contiguous Disk Devices", *IEEE Trans. MAG-22*, 5, 1278 (1986).

List of Figures

Figure 1: Magnetostriction Dependence on Growth Temperature 9

Figure 2: Dependence of FMR linewidth on Dysprosium content in the melt 10

Figure 3: Dependence of magnetostriction coefficients on Dyprosium content in the melt 11

Figure 4: Margins of 2.5μm period IICD pattern 12

List of Tables

Table 1: Weight ratios of various constituent elements in different melts 7
Table 2: Properties of typical films grown from some melts 8

Computer Simulation of Contiguous Disk Devices

Michael Alex and Mark H. Kryder

Abstract

A computer program which allows the simulation of contiguous disc bubble devices is introduced. Bubble motion on ion-implanted propagation structures, bidirectional bubble transfer between minor and major loops, and current-activated block replication simulation results are given. Error modes encountered in actual device operation, such as bubble collapse, bubble stripeout, spontaneous bubble nucleation and bubble trapping in the cusps of ion-implanted devices are shown. The simulated results are compared with experimental data.

1. Introduction

Of the three basic types of bubble memory devices, ion-implanted contiguous disc, permalloy, and current-access, computer simulation of bubble propagation has only been reported in permalloy and current-access devices.[1, 2, 3] Due to the relative ease in which bubble drive fields may be calculated in current-access devices, bubble propagation as well as logic functions in these types of devices have been extensively simulated.[1, 2, 3] As far as ion-implanted devices are concerned, there have recently been reports on calculating the magnetization distribution in ion-implanted bubble films,[4, 5] but none on simulating bubble behavior in these types of devices. Here we present a magnetic bubble device simulator which is used to simulate bubble propagation as well as current activated functions such as transfer and replication in ion-implanted contiguous-disc devices. Failure modes such as bubble collapse, stripeout, spontaneous nucleation as well as errors occuring during bubble replication and transfer can be identified. In addition, bubble motion can be studied and used as an aid in improving device designs. The computer simulation results are compared with experimental data.

2. Computer Model

In any type of bubble motion simulator, there are at least two calculations that must be performed: (1) computing the forces that act upon the domain and, (2) calculating the effects of these forces on domain wall motion. Depending on the type of device being studied, the forces in (1) may arise from externally applied fields, permalloy propagation elements, current carrying conductors or charged walls. In the simulator described here, the forces taken into consideration that act upon the bubble are due to 1) the applied bias field, 2) the charged wall, 3) the edge-affinity due to the implanted/unimplanted boundary and, 4) conductors used to activate necessary device functions such as block replication or bubble transfer. Once all the forces have been computed, bubble motion as a function of time may be studied.

A device simulator must have certain specific characteristics that enhance its utility. First and foremost is the ability of the simulator to predict failure modes in the devices being studied. In bubble propagation structures, the most common failure modes are bubble collapse and bubble stripeout. In current activated functions, in addition to stripe-out and collapse, bubble nucleation and bubble propagation errors due to stray conductor fields may occur. The simulator described herein has been designed to predict all of these possible error modes in ion-

implanted bubble devices. Also, since bubble wall position can be computed in 1 nsec intervals, the actual motion of the bubble as a function of time can be studied. This can be an invaluable aid in the prediction and rectification of errors caused by inadequate device design.

Through the use of simulation, one should be able to design devices in an intelligent fashion instead of by trial and error, which is time consuming and costly. This is certainly true in the design of field-access bubble devices, whose design rules are based almost entirely on empirical results and the designer's experience. The next-generation bubble devices (known as hybrid devices) utilize ion-implanted minor loops and permalloy major loops, which adds immensely to the fabrication complexity of the device.[6, 7] This is due to the fact that a block-replicator with sufficient operating margin has yet to be implemented in an all ion-implanted chip.[8, 9, 10, 11] In addition, the margins of current controlled hybrid bubble device functions need to be improved. The use of a simulator will make this task easier.

2.1 Bubble Domain Wall Motion Modeling

As mentioned above, in the simulator model under discussion here, all the possible fields that can act upon the bubble domain in a typical device are computed and then the effects these fields have upon the wall are calculated. In this section, the model used to describe and compute domain wall motion is presented.

There have been a number of methods in the past that have been used to model bubble domain motion.[1, 2, 3, 12] The simplest models assume a bubble shape that always remains circular. The perpendicular field difference across the bubble diameter is then responsible for the driving force on the bubble. The bubble moves in the direction of the steepest field gradient. While this model is simple and requires relatively little computing time, it is not accurate because a) bubbles do not always remain circular and, b) certain bubble device functions such as replication require that the bubble stripe out, which this method is not capable of simulating. The method of Hayashi[1, 2, 12] can model bubble domain deformation while only requiring a modest amount of computing time; in addition, bubble stripe out and collapse, the two most common failure mechanisms in bubble devices can be modelled by this method. It was this method that was used to model the devices described in this report. In this model, the bubble domain wall consists of N wall sections that are evenly spaced. N typically varies from 18 to 72 depending on the bubble or stripe circumference. The total effective field acting on the center of each wall section is computed and the section moves in response to the field.

Figure 1 shows a Cartesian coordinate system (X, Y, Z) fixed to the crystal with the Z-axis parallel to the film normal and is used as the laboratory frame. The direction of the magnetization **M** at any point (X, Y, Z) within the crystal is represented by the polar angle θ measured from the Z-axis and the azimuthal angle ϕ_a measured from the X-axis, both of which are assumed not to vary along the Z-axis. The angle θ is assumed to be π within the bubble domain and 0 outside. The locus, c, of points where θ equals to $\pi/2$ is used to represent the wall shape. In order to describe the wall structure and hence the wall shape we also use a local frame (called the R-S frame) with its origin on a wall point P. The R-axis is parallel to the outward normal of the curve c, and the S-axis is normal to the R-axis (tangential to c). Figure 1 also shows the R-S frame and the azimuth of the magnetization vector on the curve c, $\phi_a = \phi_w + \phi_n$, where ϕ_n denotes the angle between the R-axis and the X-axis, and ϕ_w denotes the azimuthal angle of the magnetization vector measured from the R-axis.

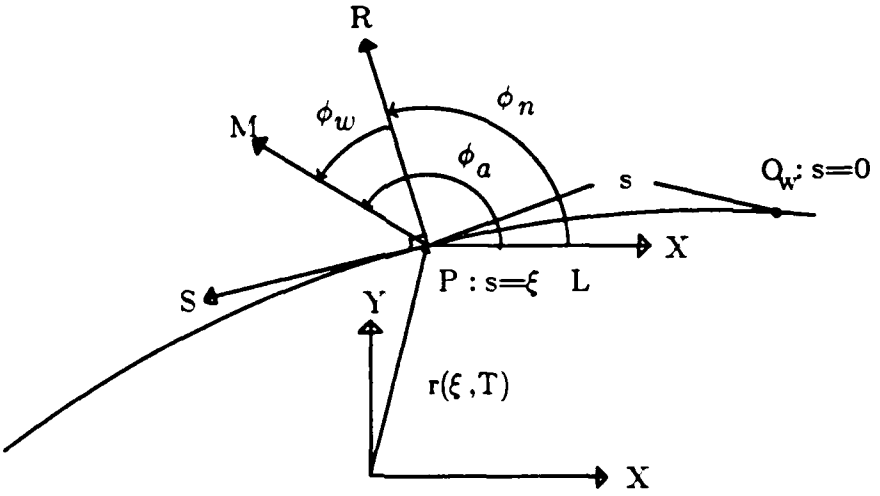

Figure 1: Representation of the bubble domain wall in the laboratory and local frames. The wall point P(ξ) is specified by a parameter ξ which is the wall length O_wP divided by the total wall length L.

The motion of the domain wall is caused by rotation of the magnetization in the domain wall as described by the *Landau-Lifshitz-Gilbert* equation:

$$\dot{\mathbf{M}} = -\gamma \mathbf{M} \times \mathbf{H}_{eff} + \alpha \frac{\mathbf{M} \times \dot{\mathbf{M}}}{|M|}. \qquad (1)$$

In this coordinate system, the following components are obtained:

$$\dot{\theta} = - \frac{|\gamma|}{M_s} \frac{1}{\sin\theta} \frac{\delta\epsilon}{\delta\phi_a} - \alpha \dot{\phi}_a \sin\theta , \tag{2}$$

$$\dot{\phi}_a \sin\theta = \frac{|\gamma|}{M_s} \frac{\delta\epsilon}{\delta\theta} + \alpha \dot{\theta} , \tag{3}$$

where $\delta\epsilon/\delta\phi_a$ and $\delta\epsilon/\delta\theta$ denote the functional derivatives of the magnetic energy density $\epsilon(\theta, \phi_a)$ with respect to ϕ_a and θ, respectively. To solve Eqs. (2) and (3) directly would consume enormous computation time because it is a two-dimensional problem. However, Hayashi derived one-dimensional equations for the wall by assuming that the structure of the moving domain wall can be approximated by that of a stationary wall. With this assumption the angular velocity $\dot{\theta}$ can be converted to the translational velocity in the direction of the wall normal, V_R of the wall as follows:

$$V_R = \dot{\theta} \Big/ \left(\frac{\partial\theta}{\partial R}\right)_S . \tag{4}$$

Equations (2) and (3) are transformed into:

$$\frac{V_R}{4\pi M_s \mu} = f_R + \frac{\ell}{2q\alpha} \frac{\phi_a}{4\pi M_s \mu} , \tag{5}$$

$$\frac{\ell}{2q\alpha} \frac{\phi_a}{4\pi M_s \mu} = - \frac{1}{1+\alpha^2} (f_R - \alpha^2 f_S) , \tag{6}$$

where M_s is the saturation magnetization, $\mu(=|\gamma|\ell/\pi\alpha)$ is the wall mobility, $\ell = \sigma_w/4\pi M_s$ is the characteristic length, q is the quality factor, α is the damping factor, and f_R and f_S are given in the following equations:

$$f_R = - \frac{\ell}{2\rho_0} - \frac{\ell}{4q} \frac{\partial \sin 2\phi_w}{\partial S} + \frac{H_D - H_A}{4\pi M_s} , \tag{7}$$

$$f_S = \frac{1}{2\alpha} (\sin 2\phi_w + \frac{\ell^2}{2\theta} \frac{\partial^2 \phi_a}{\partial S^2}), \tag{8}$$

where ρ_0 denotes the radius of the curve c, H_A and H_D denote the Z components of the applied

field and the demagnetizing field originating from surface pole density averaged over the film thickness, respectively. The effective fields f_R and f_S are evaluated at each wall point ($R = S = 0$).

For a soft bubble with an applied in-plane field large enough to freeze the azimuthal angle of the magnetization in the domain wall, i.e., $\dot{\phi}_a = 0$, the normalized effective field, f_R, is given by :

$$f_R = -\frac{\ell}{2\rho_0} + \frac{H_D}{4\pi M_s} - \frac{H_A}{4\pi M_s}. \tag{9}$$

The first term on the right hand side of Eq.(9) is the equivalent field of wall pressure which tends to decrease the bubble diameter. The second term, the demagnetizing field, tends to increase the bubble diameter and the third term, the applied field, tends to decrease the bubble diameter. The effective force expressed by Eq.(9) must be modified to account for the coercivity and wall saturation velocity. The net effective field, f_R^{**}, is given by:

$$f_R^{*} = \begin{cases} f_R - \dfrac{H_c}{4\pi M_s}\,\mathrm{sign}(f_R), & \text{if } |f_R| > H_c/4\pi M_s \\ 0 & \text{otherwise,} \end{cases} \tag{10}$$

$$f_R^{**} = \begin{cases} \mathrm{sign}(f_R^{*})\,\dfrac{v_s}{4\pi M_s \mu}, & \text{if } |f_R| > v_s/4\pi M_s \mu \\ f_R^{*} & \text{otherwise,} \end{cases} \tag{11}$$

where H_c is the coercivity, v_s is the saturation velocity, μ is the wall mobility, and f_R and f_R^{*} are the effective field before and after subtracting the coercive force, respectively.

Numerical Methods

The bubble domain wall c is represented by a set of N wall points, P(1) to P(N). Each wall point P(I) has its own value of the magnetization azimuth angle ϕ_a(I). Since the azimuth angle ϕ_n(I) of the outward wall normal at P(I) can be obtained from the wall shape, the magnetization azimuth angle ϕ_w(I) can also be obtained if ϕ_a(I) is known. Thus Eqs. (5) and (6) can be solved directly from the current wall shape and wall structure represented by the position of each wall

point P(I) and the value of ϕ_a(I). This style of solution (to be called the *explicit* solution later) has two severe drawbacks: (1) Because each wall point is made to move in the direction of the wall normal alone, iterative calculations may lead to an uneven distribution of the wall points over the bubble wall c. (2) For the calculation to proceed stably, a time step is required with difference ΔT far smaller than required for the accuracy of the calculation. Methods of calculation which overcome these difficulties are presented below.

To keep the displacement uniform, a parametric representation is employed for the wall shape at time T by using a parameter ξ (called normalized distance parameter) equal to the ratio of s to the total wall length L, where s is the wall length between a reference point O_w on c and the wall point P(ξ) to be represented (See Fig.1). Then the velocity $\mathbf{V}(\xi,T)$ of P(ξ) at time T is given by:

$$\mathbf{V}(\xi(T),\,T) = \frac{\mathrm{d}\mathbf{r}(\xi(T),\,T)}{\mathrm{d}T} = \left(\frac{\partial \mathbf{r}(\xi,\,T)}{\partial T}\right)_{\xi} + \left(\frac{\partial \mathbf{r}(\xi,\,T)}{\partial \xi}\right)_{T}\frac{\mathrm{d}\xi}{\mathrm{d}T}, \tag{12}$$

where $\mathbf{r}(\xi,\,T)$ is a vector drawn from the origin of the laboratory frame to P(ξ). Since the derivative $(\partial \mathbf{r}/\partial \xi)_T$ is equal to the unit tangential vector of the curve c at P(ξ) multiplied by L, we have the normal and tangential components of the velocity $\mathbf{V}$ as $V_R(\xi,\,T) = (\partial \mathbf{r}/\partial T)_{\xi} \cdot \boldsymbol{n}$ and $V_s(\xi,\,T) = (\partial \mathbf{r}/\partial T)_{\xi} \cdot \boldsymbol{t} + L\,\mathrm{d}\xi/\mathrm{d}T$, respectively, where $\boldsymbol{n}$ is the unit outward normal vector and $\boldsymbol{t}$ is the unit tangential vector. The wall motion described by Eqs. (5) and (6) is such that $V_R(\xi,\,T)$ is the one obtained from Eq.(5) and that $V_s(\xi,\,T)$ is zero. Therefore we obtain the following equations equivalent to Eqs. (5) and (6):

$$\Delta R(\xi,\,T) = V_R(\xi,\,T)\,\Delta T, \tag{13}$$

$$\begin{aligned}\Delta S(\xi,\,T) &= -\,L\,\mathrm{d}\xi/\mathrm{d}T \\ &= \left\{ L\xi \int_0^1 \frac{V_R(\xi,\,T)}{\rho_0(\xi)}\,\mathrm{d}\xi - L\int_0^{\xi} \frac{V_R(\xi,\,T)}{\rho_0(\xi)}\,\mathrm{d}\xi \right\} \Delta T,\end{aligned} \tag{14}$$

where ΔR and ΔS are the displacements in the R and S directions, respectively, and $\rho_0(\xi)$ is the radius of the curve c at P(ξ). The displacement vector given by the components ΔR and ΔS in Eqs. (13) and (14) equals $(\partial \mathbf{r}/\partial T)_{\xi}\Delta T$, and hence represents wall motion with the normalized distance parameter ξ **unaltered** at each wall point.

In the actual calculation the equations of wall motion, i.e., Eqs. (5) and (6) which are differential equations containing time T and the local coordinate S as independent variables, must be replaced by appropriate difference equations with respect to time difference ΔT and spatial difference δs. Generally ΔT is bounded by an upper limit beyond which the numerical process becomes unstable. We shall show an *implicit* solution that has a much larger upper bound of ΔT than that of the *explicit* solution.

The V_R-equation (Eq.(5)) can be expressed in the following form at a wall point specified by the normalized distance parameter s_0/L :

$$\frac{V_R(s_0)}{4\pi M_s \mu} = p(s_0) - \frac{\ell}{2\rho_0}, \tag{15}$$

where $p(s_0)$ denotes the sum of the effective force terms other than the wall force. In the R-S frame with the origin at the wall point under consideration, the wall shape in the neighborhood of the origin at time T can be expressed as $R(S, T) = - S^2/(2\rho_0)$. Therefore Eq.(15) can be rewritten at the wall point under consideration as:

$$\frac{\partial R(S, T)}{\partial T}\Big|_{S=0} = 2\pi M_s \mu \ell \frac{\partial^2 R(S, T)}{\partial S^2}\Big|_{S=0} + 4\pi M_s \mu p(s_0). \tag{16}$$

The partial derivatives in Eq.(16) can be expressed in the following difference equation form:

$$\frac{\partial R(S, T)}{\partial T}\Big|_{S=0} = \frac{R(0, T+\Delta T)}{\Delta T}, \tag{17}$$

and

$$\frac{\partial^2 R(S, T)}{\partial S^2}\Big|_{S=0} = \frac{R(\delta s, T+\Delta T) - 2\, R(0, T+\Delta T) + R(-\delta s, T+\Delta T)}{\delta s^2}, \tag{18}$$

where wall points P(1) to P(N) are placed at equal distance $\delta s(=L(T)/N)$ on the curve c. Positions $R(0, T+\Delta T)$ and $R(\pm\delta s, T+\Delta T)$ denote the ordinates of the wall points P(I) and P(I$\pm$1), respectively, at time $T+\Delta T$ in the R-S frame placed at P(I) defined at time T and are related with the normal displacements $\Delta R(I, T)$ and $\Delta R(I\pm1, T)$ as follows (see Fig. 2):

$$R(0, T+\Delta T) = \Delta R(I, T),$$

and

$$R(\pm\delta s,\, T+\Delta T) + \frac{\delta s^2}{2\,\rho_0} = \Delta R(I\pm 1,\, T) + O(\delta s^4). \tag{19}$$

From Eqs. (16) to (19) we obtain a set of equations which *implicitly* determine the displacement $\Delta R(I)$ of P(I) when $p(s_0)$ - $\ell/(2\rho_0)$ is given at time T:

$$- \Delta R(I+1,\, T) + (2 + 1/\lambda)\, \Delta R(I,\, T) - \Delta R(I-1,\, T)$$

$$= \frac{2\,\delta s^2\, f(s_0)}{\ell} \qquad (I = 1,\, 2,\, 3,\, \ldots,\, N)\,, \tag{20}$$

where λ equals to $2\pi M_s \mu \ell \Delta T/\delta s^2$ and $f(s_0)$ denotes the right-hand side of Eq.(15). Note that the matrix formed by Eq.(20) is essentially band diagonal so that both the memory requirements and the computation time of solving Eq.(20) are proportional to N not N^2.

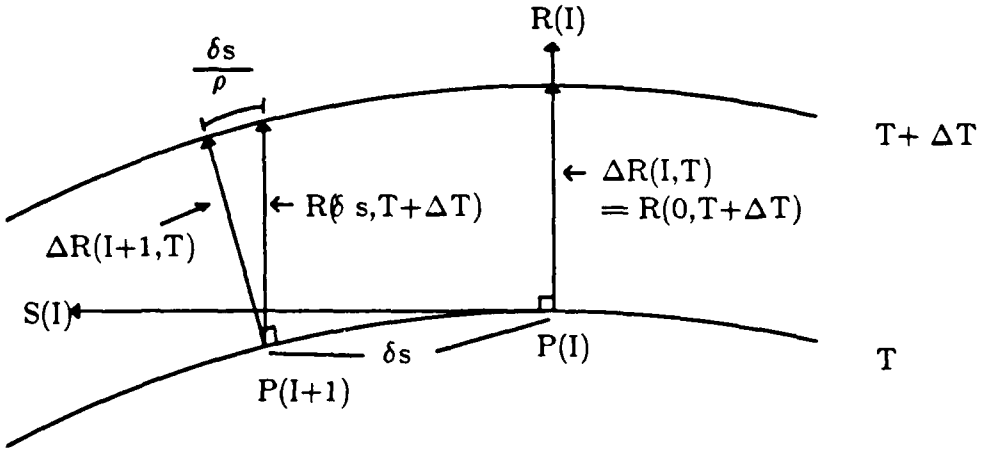

Figure 2: Wall displacement at wall point P(I) in the *R-S* frame.

Most of the computation time is spent in computing the right-hand side of Eq.(7), in particular the demagnetizing field H_D and the applied field H_A. The demagnetizing field is the sum of self and mutual demagnetizing fields, the latter being due to bubble-bubble interaction. The applied field is the sum of the uniform bias field, the field from the charged wall, the field due to the edge affinity of the unimplanted boundary and fields due to stretching and/or chopping conductors. The methods used in computing H_D and H_A are described in this and the following sections, respectively.

The average demagnetizing field on the domain wall P is obtained by summing the field due to all the surface charges and averaging it over the thickness of the film. Actually the magnetic potential at point P is calculated. Assuming the z-axis is normal to the film plane, the average demagnetizing field at point P is :

$$H_d = \frac{1}{h}\int_0^h 2M_s \left[\int_{S^-} \frac{\mathbf{i}_z \cdot \mathbf{i}_p}{p^2}\, dS - \int_{S^+} \frac{\mathbf{i}_z \cdot \mathbf{i}_p}{p^2}\, dS \right] dz, \tag{21}$$

where S^+ is the surface with positive magnetic charge,

S^- is the surface with negative magnetic charge,

$\mathbf{p}$ is the vector pointing from any surface pole to P,

$\mathbf{i}_z$ is the unit vector along the z-axis,

$\mathbf{i}_p$ is the unit vector along the direction of $\mathbf{p}$,

p is the length of the vector $\mathbf{p}$,

h is the thickness of the film, and

$4\pi M_s$ is the saturation magnetization. Since $\int_S \mathbf{i}_z \cdot \mathbf{i}_p\, dS/p^2 = 2\pi$, Eq.(21) becomes:

$$H_d = 4\pi M_s - \frac{4M_s}{h}\int_0^h \int_{S^+} \frac{\mathbf{i}_z \cdot \mathbf{i}_p}{p^2}\, dS\, dz\,, \tag{22}$$

where S^+ is taken to be the surface area of the bubble. Using cylindrical coordinates with z axis normal to the plane, the surface integral in Eq.(22) can be expressed as :

$$H_d = 4\pi M_s - \frac{4M_s}{h}\int_0^h \int_0^{\pi} \int_0^{r} \frac{z}{(\rho^2+z^2)^{3/2}}\, \rho\, d\rho\, d\phi\, dz\,, \tag{23}$$

where $\mathbf{r}$ is the vector pointing from point P to any other point on the bubble domain wall, r is the length of $\mathbf{r}$ and is a function of ϕ, and ϕ is the angle of the vector $\mathbf{r}$ measured from the tangent of the bubble at point P, as shown in Fig.3a. If there is only one bubble, H_d is the self-demagnetizing field which can be reduced to :

$$H_d = 4\pi M_s + \frac{4M_s}{h}\int_0^{\pi} \left[(r^2 + h^2)^{1/2} - (r + h) \right] d\phi. \tag{24}$$

If there is more than one bubble, each additional bubble introduces an additional volume integral term in Eq.(23) due to bubble-bubble interaction. The integral in Eq.(24) must be

carried out numerically. The integration is equivalent to finding the area under the curve shown in Fig.3b. Note that the value of the integrand is always zero at ϕ=0 and ϕ=π, because r=0 at these two points. The shape of the curve is arbitrarily drawn. Because the bubble domain is represented by N wall points, we can only know the value of the integrand at the N ϕ's corresponding to the N wall points. *Simpson's rule* is used to calculate the area of each segment, such as the one between ϕ_{i-1} and ϕ_i, shown in Fig.3b. The value of the mid-point needed in *Simpson's* rule is obtained by finding the value of r corresponding to $1/2(\phi_{i-1}+\phi_i)$. This method is chosen because it requires little computation time and the error is acceptable. The use of other complicated schemes to integrate Eq. (24) is ruled out, because, using *Simpson's* rule with optimized program code, the computation of H_D has accounted for 80% of the CPU time during simulation. Using a more complicated scheme will at least double or triple the computation time but the improvement in accuracy will be small.

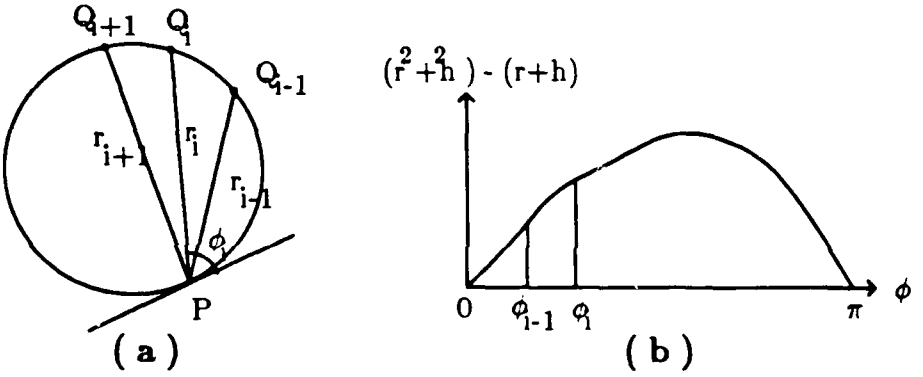

Figure 3: The calculation of the demagnetizing field on a wall point.

2.2 The Edge Affinity Field

It is well known that bubbles couple strongly to an implanted/unimplanted boundary.[13] This is due to the stray field created by the thickness difference between the implanted and unimplanted regions. Bubbles prefer to reside in the thicker unimplanted area, but the field produced at the boundary prevents bubbles from crossing from the thinner implanted area into this region. As a result, bubbles in the implanted region adhere strongly to the unimplanted pattern edge. The demagnetizing field due to the thickness step is modeled by an equivalent current. It can be shown[14] that the stray field of a bubble and a loop current are identical if the bubble is replaced by a loop current with amplitude $I = 2\,M_s h$ where the units are mA, gauss and μm, respectively. Similarly, for a cylindrical hole in a garnet film, the amplitude of the

equivalent loop current is $I = M_s h$. For the case of partially etched holes, i.e., craters, the amplitude is $I = M_s \Delta h$, where Δh is the etched thickness. This concept of equivalent loop current can be extended to the pattern used in contiguous disk devices, since the pattern is generally a continuous chain of circular holes.

By extending the concept of equivalent currents, the calculation of the demagnetizing field is quite straight forward. The contiguous disk pattern is replaced by a current "loop" with the same shape as the unimplanted disk pattern. The z-component of the demagnetizing field, H_z, at point P, is given by:

$$H_z = \int_C \frac{I\, d\mathbf{l} \times \mathbf{r}}{r^3} \cdot \mathbf{i}_z, \tag{25}$$

where I is the equivalent current, $d\mathbf{l}$ is the length vector of a small segment of the current loop, $\mathbf{r}$ is the vector pointing from $d\mathbf{l}$ to point P, r is the length of $\mathbf{r}$, $\mathbf{i}_z$ is the unit vector in the z axis, and C is the path of the current loop. In evaluating Eq.(25), the contour C is broken up into small line segments; the integration is then carried out segment by segment.

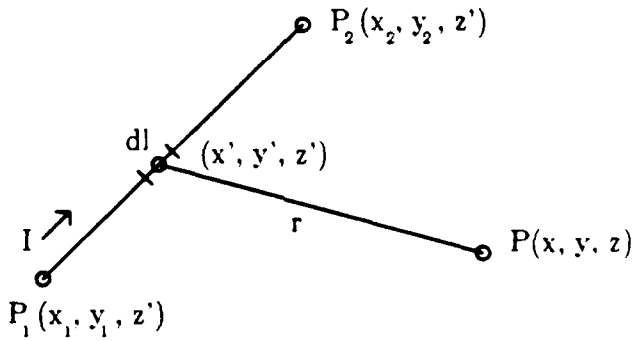

Figure 4: A line segment of a current loop.

Consider a line segment between $P_1(x_1, y_1, z')$ and $P_2(x_2, y_2, z')$ with current flowing from P_1 to P_2, as shown in Fig.4. For a small current element $d\mathbf{l}$ at (x', y', z'), we have

$$d\mathbf{l} = d\ell_x \mathbf{i}_x + d\ell_y \mathbf{i}_y, \qquad \text{and} \qquad \mathbf{r} = (x-x')\mathbf{i}_x + (y-y')\mathbf{i}_y + (z-z')\mathbf{i}_z, \tag{26}$$

where $d\ell_x$ and $d\ell_y$ are the component of $d\mathbf{l}$ in x and y axis, respectively. Inserting Eq.(26) into Eq.(25), the z-field averaged over the film thickness, $H_z(x, y, z)$, at point P due to the current in the line segment is given by:

$$H_z(x, y, z) = \frac{I}{z_2 - z_1} \int_L \int_{z_1}^{z_2} \frac{(y-y')\,d\ell_x - (x-x')\,d\ell_y}{[\,(x-x')^2 + (y-y')^2 + (z-z')^2\,]^{3/2}}\,dz'$$

$$= \frac{I}{z_2 - z_1} \int_L \frac{(y-y')\,d\ell_x - (x-x')\,d\ell_y}{(x-x')^2 + (y-y')^2} \left[\frac{z_2}{[\,(x-x')^2 + (y-y')^2 + z_2^2\,]^{1/2}} \right.$$

$$\left. - \frac{z_1}{[\,(x-x')^2 + (y-y')^2 + z_1^2\,]^{1/2}} \right], \qquad (27)$$

where L is the line segment between P_1 and P_2, and the unimplanted film is between z_1 and z_2 along the z axis. Divide the line segment, L, into N equal small divisions, then $d\ell_x = (x_2 - x_1)/N$, $d\ell_y = (y_2 - y_1)/N$. *Simpson's* rule is used to evaluate Eq.(27) numerically. The total z-field at point P is the summation of the contributions from all the line segments of the current loop.

2.3 Charged Wall Model

In contiguous disc devices, the bubble driving force is produced by charged walls formed at the edge of unimplanted propagation patterns. The charged walls, to which bubbles strongly couple, are rotated by a rotating drive field along the propagation pattern edges, providing a driving force for bubbles in the implanted region.

It is well known that the magnetization distribution in ion-implanted layers is dominated by the stress-induced uniaxial anisotropy, particularly in the vicinity of the implanted/unimplanted boundary.[4, 15, 16, 17, 18, 19] This anisotropy, being parallel to the boundary, is responsible for charged wall formation. Since the form of this anisotropy is known, it may be used to deduce the structure of the charged wall without resorting to a laborious and time consuming calculation that will not enhance the accuracy of the result.[5, 20]

As mentioned above, the dominant stress-induced anisotropy near the implanted/unimplanted boundary is strong and parallel to the boundary. As a result of this uniaxial anisotropy, the magnetization distribution near the boundary is aligned parallel to the boundary. At preferred positions, depending upon the boundary orientation with respect to the crystalline axes and the drive field direction, this magnetization will align itself in one of the two preferred anisotropy directions. By rotating the drive field, the magnetization can be made to

switch or rotate to the other stable direction. Charged walls, formed where this magnetization diverges, rotate and switch their stable positions as the magnetization rotates or switches.

2.3.1 The Charged Wall Field

The charged wall may be modelled as a region of converging or diverging magnetization (depending on its polarity) which occupies a finite volume in the implanted region. The divergence of the magnetization creates a net charge concentration, that is, the charged wall. The stray field from a charged wall is obtained by directly integrating the stray field from the charge in the charged wall. A charged wall has a finite width, length and thickness. Without loss of generality, we can assume that the charged wall length is along the y-axis, extending from 0 to y_2; the width is between x_1 and x_2, and the thickness is between 0 and z_1, as shown in Fig.5. The garnet film is parallel to the xy plane, and located between z_1 and z_2. The z component of the stray field due to the charged wall at point P(x,y), averaged over the thickness of the film is given by:

$$H(x, y) = \frac{\rho}{z_2 - z_1} \int_{x_1}^{x_2} \int_{0}^{y_2} \int_{z_1}^{z_2} \frac{z}{[\,(x-x')^2 + (y-y')^2 + z^2\,]^{3/2}}\, dz\, dy'\, dx', \tag{28}$$

where ρ is the charge density. After carrying out the first two integrations, Eq.(28) becomes:

$$H(x, y) = \frac{\rho}{z_2 - z_1} \int_{x_1}^{x_2} ln \left[\frac{[\,(x-x')^2 + (y-y_2)^2 + z_2^{\,2}\,]^{1/2} + (y-y_2)}{[\,(x-x')^2 + y^2 + z_2^{\,2}\,]^{1/2} + y} \right.$$

$$\left. \frac{[\,(x-x')^2 + y^2 + z_1^{\,2}\,]^{1/2} + y}{[\,(x-x')^2 + (y-y_2)^2 + z_1^{\,2}\,]^{1/2} + (y-y_2)} \right] dx'. \tag{29}$$

Equation (29) is evaluated numerically.

From experimental measurements[21, 22, 23, 5], the charged wall potential well depth at the edge of the unimplanted disk decreases by about 20% when the in-plane field is increased from 20 Oe to 100 Oe. For the same amount of increase in in-plane field, the charged wall length decreases more rapidly; a 100% reduction in length is seen. When the in-plane field is pointing into the cusp of the contiguous disk pattern, a strong charged wall is formed in the cusp whose potential well depth is about 2 times that of the charged wall not in the cusp. The potential

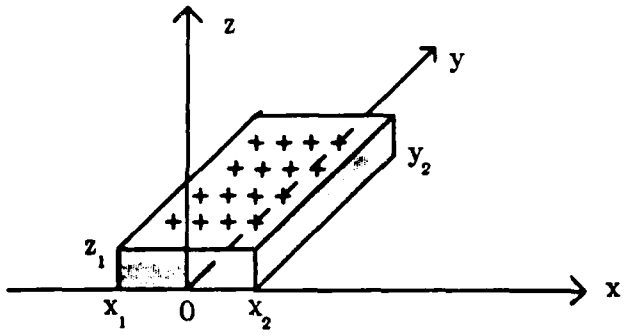

Figure 5: Model for the charged wall.

well depth also varies with the charged wall direction around the disk pattern. Excluding the cusp positions, a 20% variation in well depth is measured around the disk pattern. The charged wall position *vs* rotating in-plane field direction is calculated based on *Calhoun's* model[24].

2.3.2 Charged Wall Motion

In his work, Calhoun simulated the motion of a bubble driven by a charged wall circulating about an unimplanted disc. A schematic of the situation is depicted in Fig. 6.

Several assumptions are used to simplify the analysis. It is assumed that the bubble and charged wall are rigidly coupled and that all the damping of the moving charged wall/bubble system is due to the bubble. Experiments have borne out the latter assumption to be correct.[25]

The damping force of the bubble may be approximated as

$$F_d = \pi d M_s t_s (R/\mu_w) d\theta/dt, \tag{30}$$

where μ_w is the wall mobility of the storage layer, t_s is the storage layer thickness, M_s is the magnetization of the storage layer, R is the radius of the bubble trajectory and d is the bubble diameter.

The bubble/charged wall is driven around the disc by the applied field, H_{xy}. To first order, we may approximate the charged wall as a sheet of length L, height t_d, the thickness of the ion-implanted drive layer, having a uniform charge density $\rho = 2M_d \cos\alpha$, where α is the angle

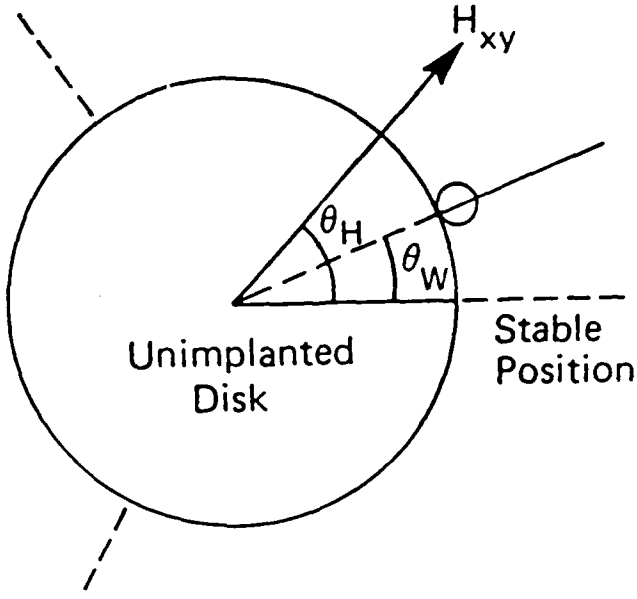

Figure 6: Geometry used to calculate motion of bubble coupled to unimplanted disc.

between the wall normal and M_d, the drive layer magnetization. Then, the force due to H_{xy} driving the wall F_H may be given by:

$$F_H = (2M_d t_d L\cos\alpha)H_{xy}\sin(\theta_H - \theta_w) \tag{31}$$

where θ_H is the angle of the applied field and θ_w is the angular position of the wall and bubble.

In ion-implanted devices of the type described here, crystalline and stress- induced anisotropies play major roles in affecting charged wall behavior. The major component, the stress-induced anisotropy, has the same angular dependence as the crystalline anisotropy and is proportional to $\sin 3\theta_w$. The form of these anisotropies gives rise to the three "easy" and "hard" directions of these devices; the charged wall will prefer to reside at $\theta = 0^\circ$, 120° or 240°. The restoring force is then given as:

$$F_r = (2M_d t_d L\cos\alpha)(H_{eff}/3)\sin 3\theta_w, \tag{32}$$

where H_{eff}, the effective anisotropy field due to crystal symmetry and stress relaxation is:

$$H_{eff} = 9\sqrt{2}[(1/3)K_1+(\lambda_{111}-\lambda_{100})(\sigma_n- \sigma_p)]H_B/(Q_d-1)4\pi M^2 \quad (33)$$

where Q_d is the quality factor of the implanted layer, H_B is the applied bias field, the λ's are the appropriate magnetostriction constants and σ_n and σ_p are the stress components normal and parallel to the implanted edge respectively. Note that for equal magnetostriction constants there is no contribution to the anisotropy field due to magnetostriction.

By equating the driving force with the restoring and damping force, $F_d + F_r = F_H$, we get the following first order non-linear differential equation:

$$v\, d\theta/d\omega t + 1/3\, \sin 3\theta = h\, \sin(\omega t - \theta), \quad (34)$$

where $h = H_{xy}/H_{eff}$, $v = R\omega/\mu_e$, $\theta_H = \omega t$ and $\mu_e = \mu(2M_d t_d L\cos\alpha)/\pi d M_s t_s$.

A computer program was written to solve the equation of motion by the Runge-Kutta method.[26] Two useful results obtained are 1), the position of the charged wall/bubble as a function of the in-plane field position, and 2), the phase lag between the drive field and the charged wall/bubble. In addition, the effects of drive field magnitude, stress and magnetostriction constants, operating frequency and dynamic bubble parameters on bubble circulation may be modelled.

In Fig. 7 is seen the bubble position around an unimplanted disc for two different values of the normalized in-plane field. Note that as the in-plane field is increased, the bubble follows the field more closely. For very high drive field values, the phase lag is virtually eliminated, as is seen in the laboratory.

Of course, in real devices, the propagation structure is more complex than that of an unimplanted disc. However, a contiguous disc propagation pattern can be constructed by piecing together arcs from circles of various radii and matching "boundary conditions" where the arcs intersect.

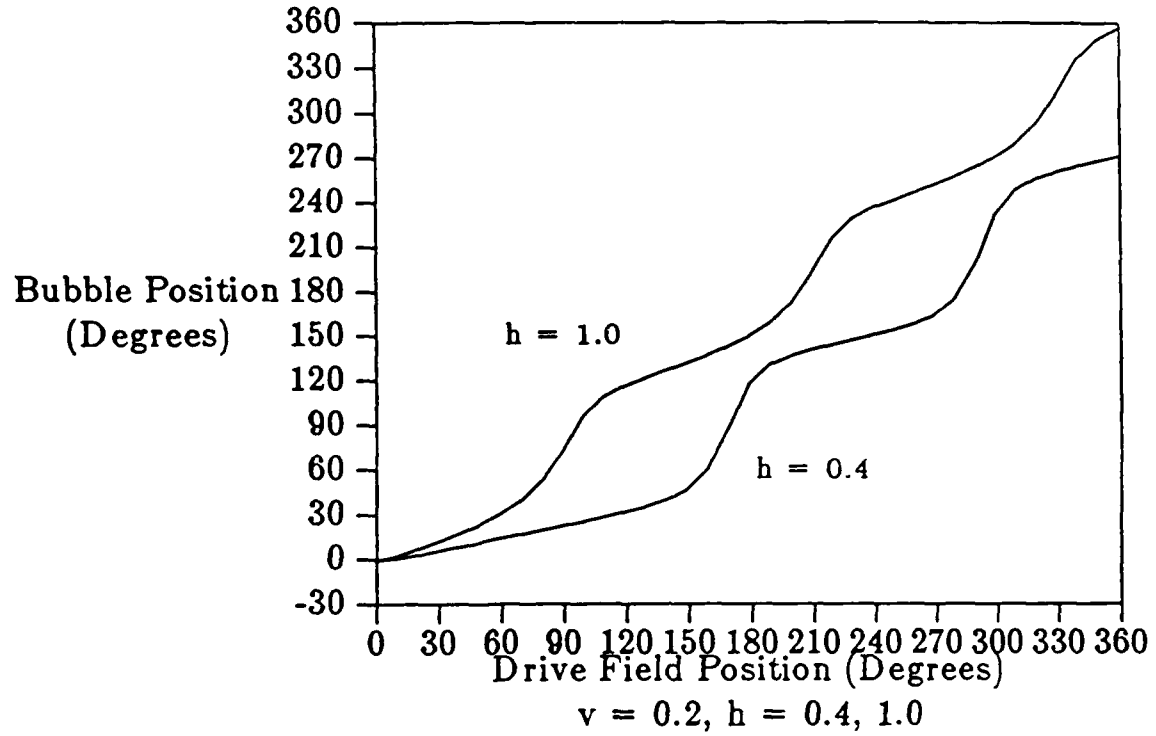

Figure 7: Bubble position as a function of drive field position around an unimplanted disc for two different values of the normalized drive field, h.

2.4 Conductor Field Calculations

Since some bubble device functions such as replication and transfer are performed by current-activated conductors on top of the bubble film, it is necessary to compute the fields from these conductors. In addition, when designing active (current activated) bubble gates and components, a knowledge of the fields produced by the component conductors is certainly the best way to minimize the number of design iterations.

Calculation of the magnetic field due to the current flow in the perforated conductor sheets is done by solving the *Poisson's* equation with the boundary conditions corresponding to the conductor patterns to obtain the electric potential distribution $V(x,y)$. Then the electric potentials are differentiated to give current densities. Finally, the current densities are integrated to give the magnetic fields. The applied field is calculated for each device structure using a unit current density and then stored for use during bubble motion simulation. The simulation program reads the drive field data and scales it to the current density required in the simulation.

In a charge free space, *Poisson's* equation becomes *Laplace's* equation. *Laplace's* equation was solved iteratively using a 9-point finite difference method.

2.5 Spontaneous Bubble Nucleation

One type of failure mode seen in bubbles devices is known as spontaneous nucleation. This failure results in a bubble self-nucleating or forming where a bubble should not exist; this usually occurs at low bias fields. In bubble devices, during the "write" operation, the bias field is locally reduced by a pulsed hairpin conductor, resulting in bubble nucleation. It is easy to see how the use of conductors for other bubble device functions, such as replication or transfer can result in unwanted bubble nucleation, resulting in an error. In the trapping transfer gate studied in this report, and in gates used for block-replication, hairpin conductors are used for bubble stretching, cutting and "trapping". Depending on the field and current parameters used during gate operation, unwanted bubble nucleation may be the dominant failure mode. Thus, the capability of accounting for this type of failure was also put into the simulator.

Since nucleation of a bubble is essentially a magnetization reversal of 180 degrees, it may be modelled by a Stoner-Wohlfarth equation and will occur when the local field exceeds the effective anisotropy field. That is, bubble nucleation will occur when the vector sum of the bias field, the drive field, the conductor fields, the charged wall field and the edge affinity field exceed the critical curve. This is given as:

$$(H_{xd}+H_{cx}+H_{xe})^{2/3} + (H_b+H_{ez}+H_{cz})^{2/3} = (Q\text{-}1)^{2/3}, \tag{35}$$

where H_{xd} is the x component of the drive field, H_{cx} is the x component of the conductor field, H_{xe} is the x component of the edge affinity field, H_b is the bias field, H_{ez} is the z component of the edge affinity field and H_{cz} is the z component of the charged wall field. The critical curve defined by this equation is seen in Fig. 8 where Q is a parameter. The geometry of the situation is depicted in Fig. 9.

3 Simulation Results

In this section, simulation results as performed by the simulator described above are presented and discussed.

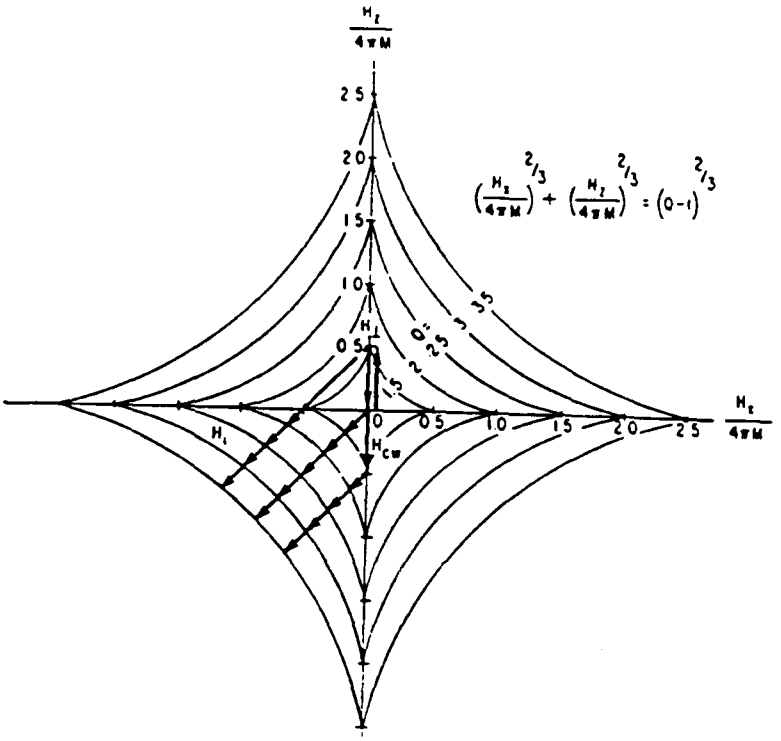

Figure 8: Critical curve for determining bubble nucleation threshold.

3.1 Bubble Propagation

A block-replicate gate that was simulated is depicted in Fig. 10[11]. At the top of the figure are seen two periods of the major line with a cusp between them. The hairpin stretching conductor bridges the gap between the major line and the end of the minor loop at the bottom of the figure, of which two periods are also shown. Finally, the cutting conductor is seen running parallel to the major loop and orthogonal to the stretching conductor.

In this study, before active functions were simulated, bubble propagation margins were first obtained since all gate functions require that the bubble first successfully propagate into the gate before any currents are applied. This simulation of propagation margins is also a good "confidence check" with the experimental data.

In order to simulate propagation margins, a bubble was initially placed at a specific location on the minor loop and the drive field was specified to rotate a designated number of

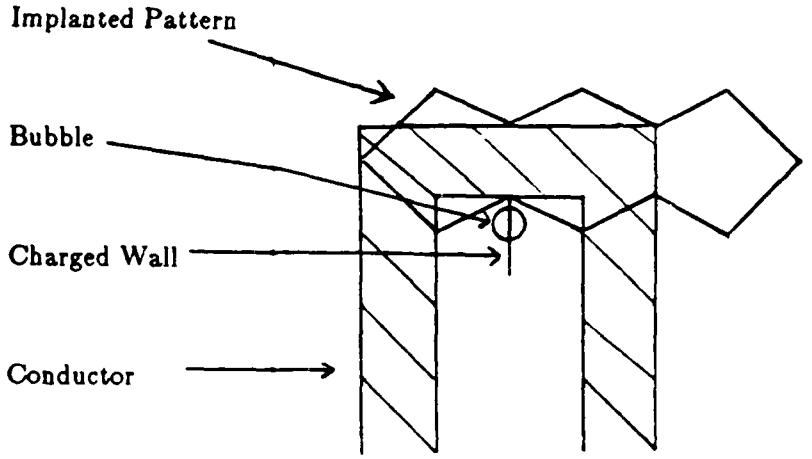

Figure 9: Geometry used to define fields used in computing nucleation threshold.

field cycles; the designated number of field cycles being high enough to propagate the bubble around the minor loop end and into and out of cusps. Simulator results of typical successful propagation are shown in Fig. 11. Also seen in the figure are the three easy bubble stripe-out positions and the sense of the drive field. The initial bubble position was on the right-hand-side of the second disk of the minor loop and its trajectory as it rotated around the minor loop tip counter-clockwise is also depicted. The bubble positions were plotted at 160 nsec intervals, except when the bubble was idling in the cusps; then its position was plotted every 5 μsec. The effect of the three-fold anisotropy is clear as it is seen that the bubble spends more time near the easy stripe-out directions and quickly propagates through the hard directions.

In Fig. 12 depicts the three failure modes predicted by the simulator. In all of these simulations, the initial bubble position was on the right hand side of the second disc and the drive field was rotating in the counter-clockwise direction. The left-most minor loop depicts bubble stripe-out at lower drive fields, the middle shows bubble collapse in the minor loop cusp and on the right hand side the failure mode seen is due to the bubble being "trapped" in the cusp on the left hand side of the loop and being left behind by the rotating drive field.

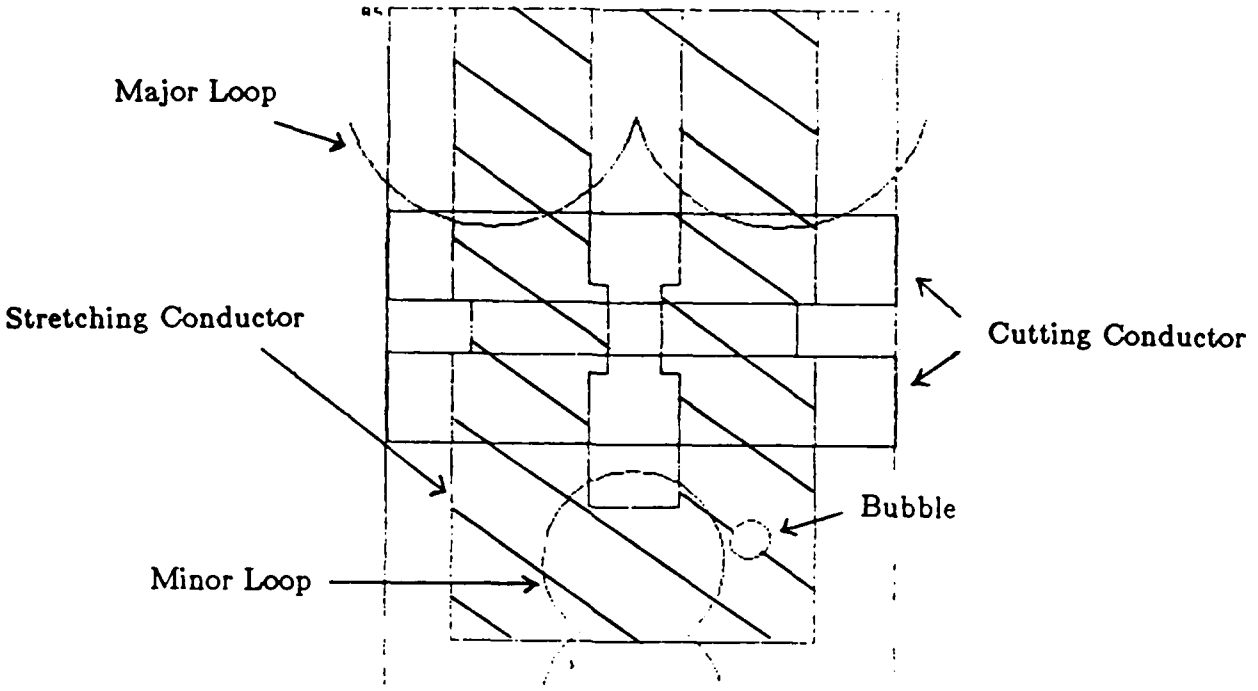

Figure 10: Block-replicate design modelled in this report. The major loop cusp is connected to the minor loop by a hairpin conductor which is used to stretch the bubble. The stripe chopping conductor is seen lying perpendicular to the stretching hairpin.

In Fig. 13 are given the experimental and simulated margins for the minor loop depicted in Fig. 16. The parameters used in the simulation are given in Table 1. The solid line is the experimental data; the diamond, dot and minus sign (-) represent simulated successful propagation, bubble collapse and bubble stripe-out, respectively.

Additionally, the effect of the wall coercivity, H_c, on the bubble propagation margin was studied. In Fig. 14 is seen how the bias margins deteriorate as the wall coercivity value used for the simulations was increased. In the figure, the thin line, thick line and the broken line represent the simulated propagation margins for values of wall coercivity of 1.0, 3.0 and 3.5 Oe respectively. When the coercivity increases from 1.0 Oe to 3.0 Oe, there is a little margin loss from the low bias end only. When the coercivity goes from 3.0 Oe to 3.5 Oe however, the high bias margin degrades dramatically, particularly at high drive.

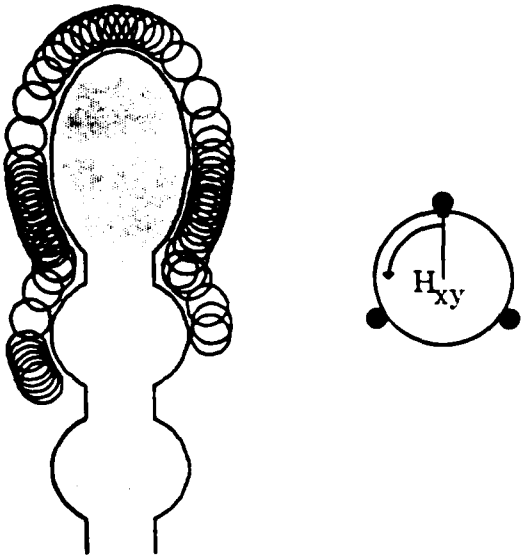

Figure 11: Typical bubble propagation simulation. The three easy stripe-out directions and drive field rotation sense are also shown. Bubble positions plotted every 160 nsec, except in cusps where positions are plotted every 5μsec. Simulation drive field frequency was 125 kHz.

3.2 Block Replication

Before the results of block-replication simulation are presented, a basic description of gate operation is necessary. Ideally, the bubble is propagated underneath the hairpin conductor, which is then activated. The bubble stripes out along the length of the hairpin channel where it sees the cusp of the major loop, which has an attractive charged wall as well as high edge affinity. Thus, one end of the stripe is in or near the cusp of the major loop while the other end is still attached to the minor loop coupled to the charged wall there. Now, the stretch current is turned off and the cutting conductor pulsed. The stripe is cut in two where the two conductors cross each other and due to the externally applied bias field the two stripes shrink into bubbles of stable diameter. Fortuitously, the field gradients of the cutting conductor drive the two bubbles outward, where they are then influenced by attractive charged walls and the edge affinity of the implanted patterns. These processes occur so quickly that the drive field, which of course is applied during the replicate process, has only rotated tens of degrees upon its completion. Thus, the original and replicated bubble positions are in-phase with the charged walls that propagate them out of the gate.

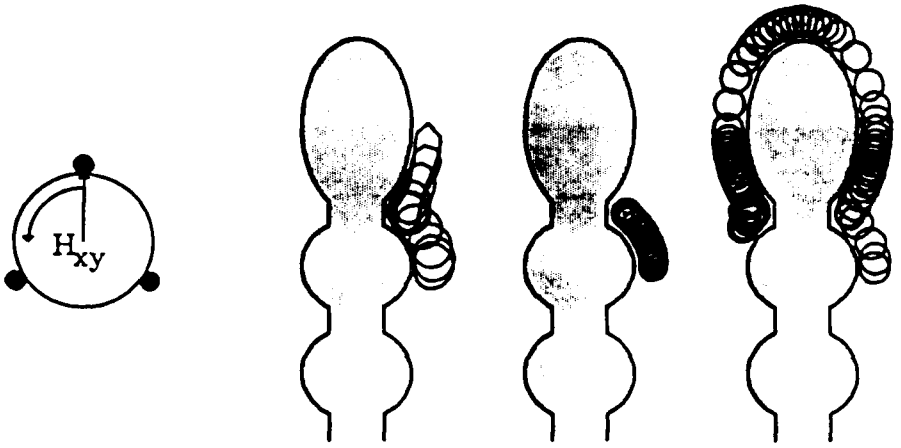

Figure 12: The three types of propagation failure observed during simulation. On the left-hand side is seen bubble stripe-out along the pattern edge. The middle depicts bubble collapse in the cusp, and on the right-hand side is seen bubble lag, explained in detail in the text.

Shown in Fig. 15 are the perpendicular magnetic field contours of the stretch conductor computed by the method described in the previous section, normalized to the fields produced by a current density of 1mA/μm. To get the actual magnetic field values (in Oersteds) of the contours depicted, the contour values are multiplied by the current density through the conductor. Typically, in the simulations reported here, the stretcher current density varied from 30 to 40 mA/μm. Thus, a bubble/stripe in the stretcher channel sees a field reduction of 75 to 100 Oersteds.

In Fig. 16 is seen the replicate gate introduced above with edge affinity field contours produced by an implanted region 0.35μm thick. For the sake of clarity, only 10 and 20 oersted contours are shown. The peak field in the major loop cusp was calculated to be greater that 23 Oe. Comparing the field values of the major and minor loop cusps, which have slightly different geometries (the major loop cusp is "sharper"), shows that cusp geometry can be an important

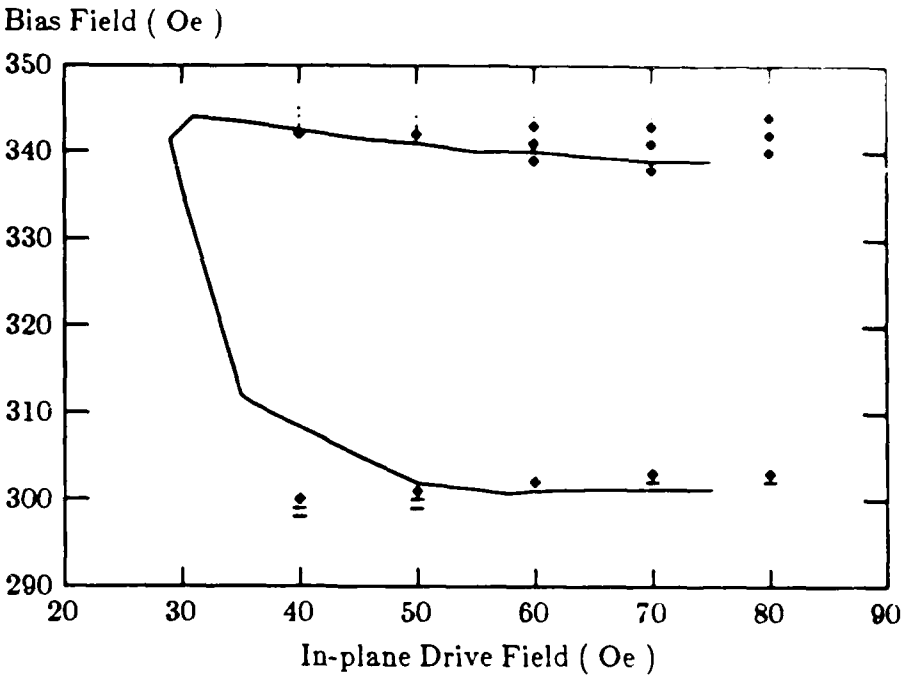

Figure 13: Experimental and simulated propagation margins for the minor loops of the block-replicate gate.

factor in device performance. It is also seen that the replicated bubble has an attractive potential in the major loop cusp, which is, of course, where one wants the bubble to end up following the replicate process.

The following series of figures show the bubble replicate process as performed by the simulator. The parameters used in this simulation are given in Table 1. In Fig. 17a is shown a bubble propagating in counter-clockwise sense around the minor loop just before the stretcher is activated. Seen to the left of the gate is the orientation of the drive field at this point in time. The bubble is being propagated around the loop end by the drive field. When the field reaches approximately 319 degrees, the stretcher is activated. The applied stretch pulse length was 400 nsec and the current density was 40 mA/μm. In Fig. 17b the bubble is shown 100 nsec after the start of the stretch pulse. In Fig. 17c, 200 nsec after the start of the pulse, the bubble has stretched half the length of the hairpin and is strongly attached to the tip of the minor loop along which it is also seen to stripe out. In Fig. 17e, 200 nsec later, the moving stripe head of

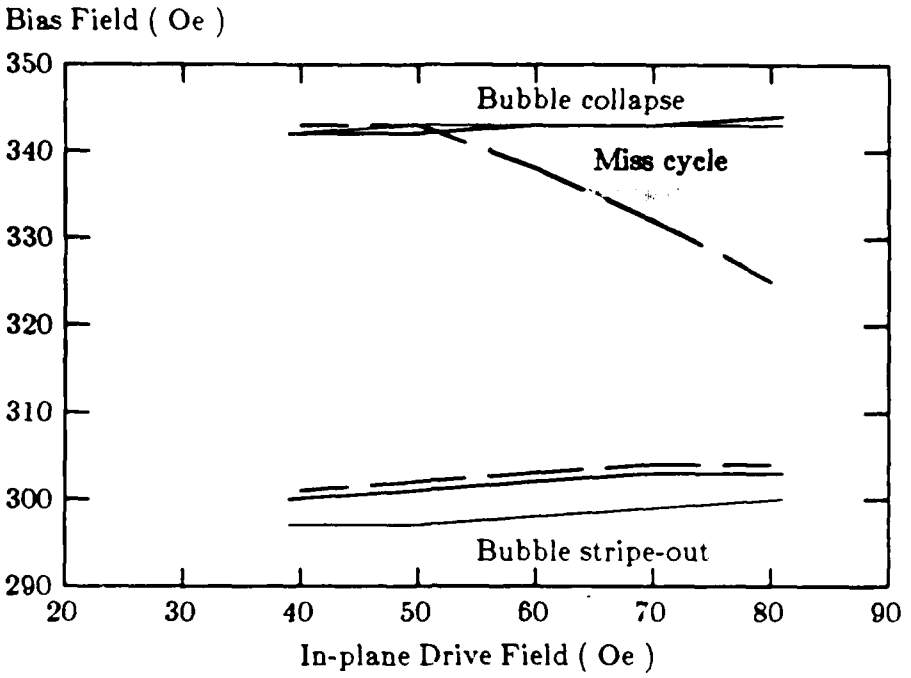

Figure 14: Simulated bias field margins for bubble propagation with the wall coercivity as a parameter. Margins degrade from the low bias end as the coercivity is increased from 1.0 Oe (Light line) to 3.0 Oe (Dark line). When $H_c = 3.5$ Oe, the high bias margins fall drastically. (Dashed line.)

the stretching bubble is seen to be firmly coupled to the cusp of the major loop. At this point, the stretch current has been applied for 400 nsec.

Now, the stretcher is turned off and the cutter is activated. Here, a cutting pulse of 40 nsec duration was applied. The stripe 20 nsec after the start of the cut pulse is seen in Fig. 17f. In Fig. 17g, 20 nsec. later, we see that there are now two "bubbles"; one in the major line cusp and the other still on the minor loop. Note also that the drive field at this point creates favorable charged walls for both the bubbles at their respective locations. Finally, the situation that results 40 nsec after the termination of the cut pulse is seen in Fig. 17h. The bubbles have returned to their stable diameters and will continue propagating along with the drive field.

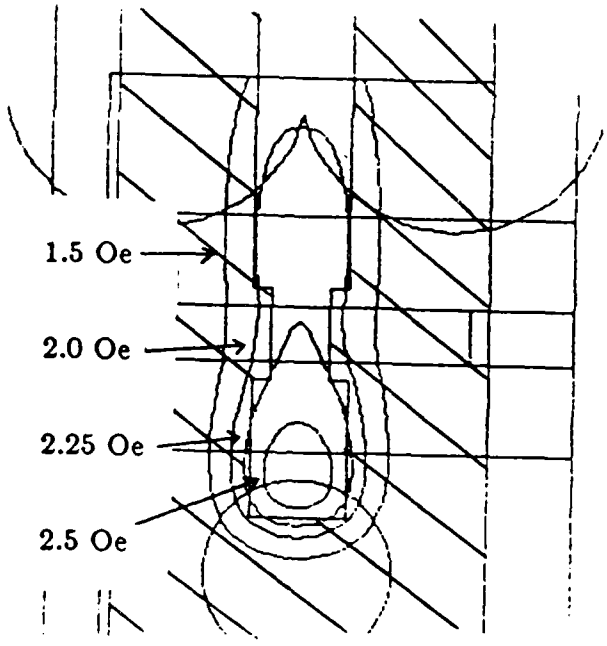

Figure 15: Perpendicular magnetic field contours, in oersteds, of stretching conductor of the block replicate gate due to a current density of 1 mA/μm flowing through it. 1.5, 2.0, 2.25, and 2.50 Oe. contours shown.

In Fig. 18 is seen what happens when an insufficient stretching current is applied. Here, a stretching current density of only 30 mA/μm was applied and even after 400 nsec. of stretching the stripe has not even propagated half the distance towards the major loop.

3.3 Trapping Transfer

The trapping transfer gate as proposed by Bell Laboratories[27] is seen in Fig. 19 It consists simply of a hairpin conductor whose "channel" connects the end of a minor (storage) loop and an enlarged disc on the major (read) path. It is similar to the block-replicate gate of the previous section except that it has only one conductor, and the major loop is translated by one-half the major loop period. In addition, the major loop and minor loop separation is reduced here. The material and device parameters used in the trapping transfer gate simulation are given in Table 2.

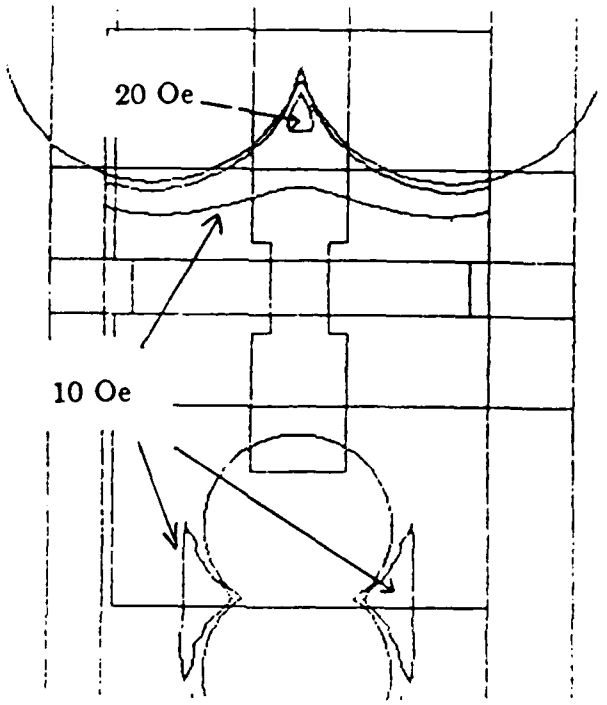

Figure 16: Perpendicular magnetic field contours, in oersteds, due to the edge affinity of the implanted/unimplanted boundaries of the block replicate gate. Only 10 and 20 Oe. contours shown. Reduced thickness due to implantation is 0.35μm here.

Magnetization	$4\pi M_s$	650 G
Characteristic length	l	0.12 μm
Bubble film thickness	t	1.1 μm
Stripe width	w	1.1 μm
Wall Coercivity	H_c	1.0 Oe
Bubble mobility	μ_w	300 cm/sec-Oe
Bubble saturation velocity	v_s	3800 cm/sec
Bias Field	H_B	330 Oe
Operating frequency	f	125 kHz
Stretcher thickness		0.6 μm
Chopper thickness		0.4 μm

Table 1
Parameters used in block replicate gate simulation

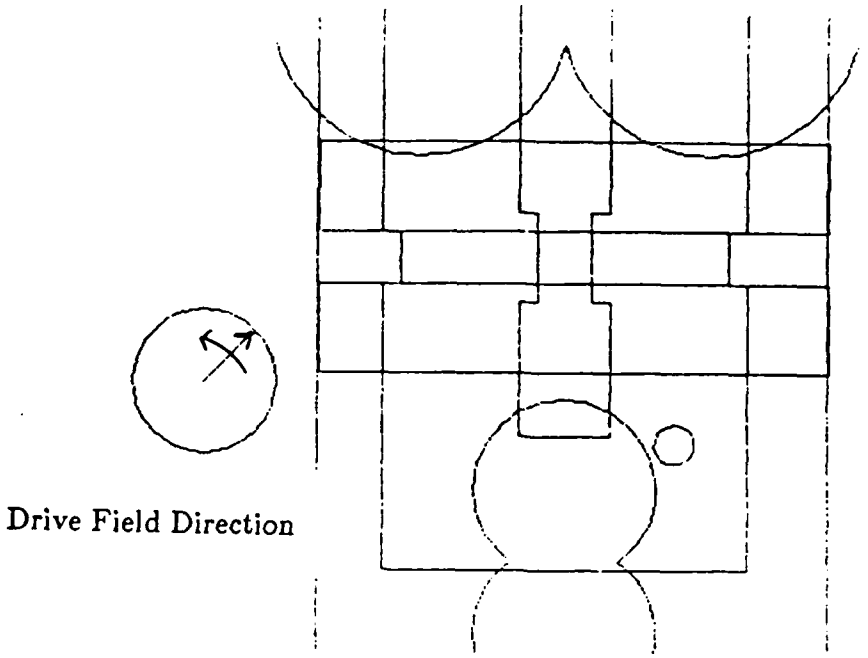

Figure 17: (a) Initial bubble position prior to activating the stretching conductor (t_s = 0) and the position of the drive field, which is rotating counter clockwise. Stretching current density was 40mA/μm.

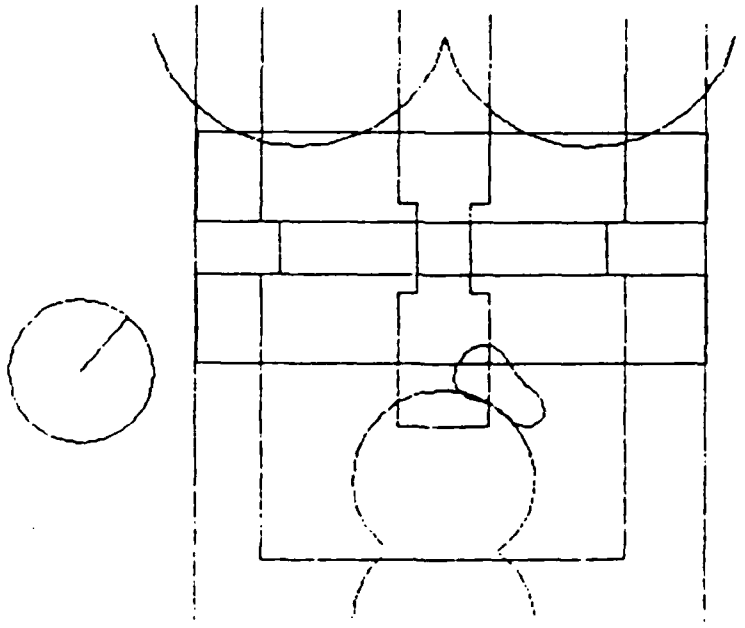

(b) t_s = 100 nsec. The bubble is beginning to stripe out.

As was done for the block-replicate gate of the previous section, the propagation margins of the trapping transfer gate were first simulated before the actual transfer process was. The

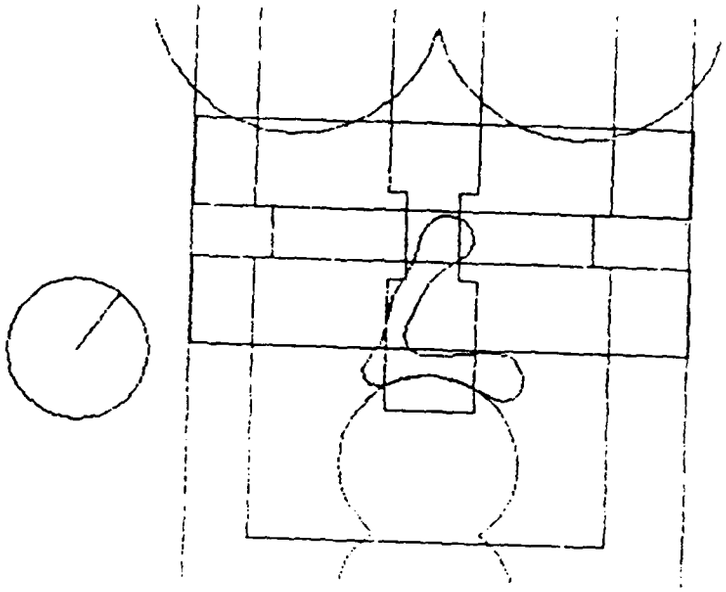

(c) $t_s = 200$ nsec.

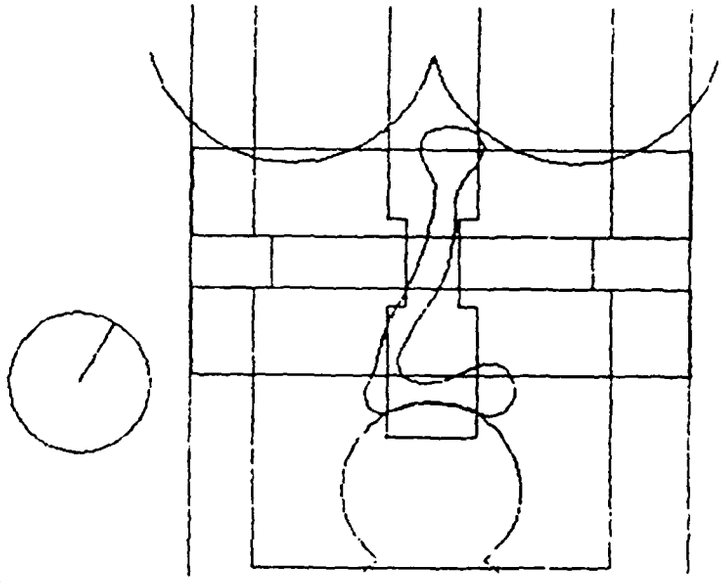

(d) $t_s = 300$ nsec.

experimental and simulated margins are given in Fig. 20. The same failure modes as those described for the minor loops of the block replicate gate were observed here.

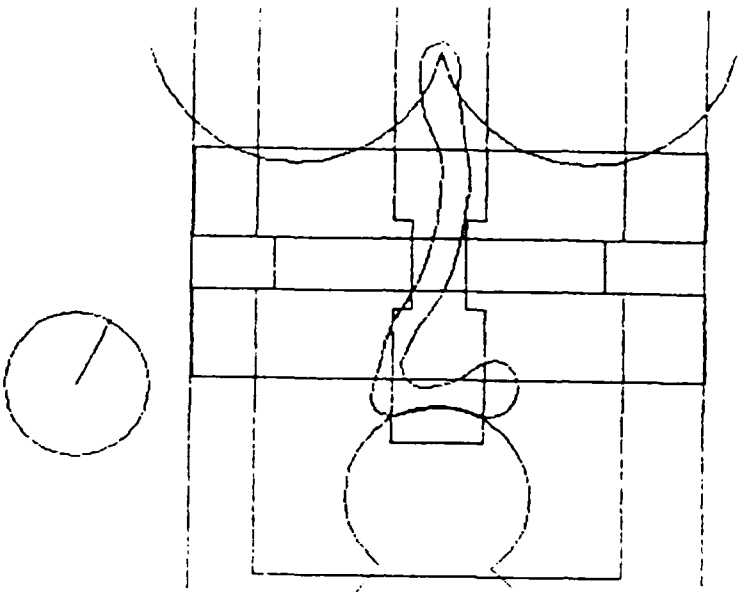

(e) $t_s = 400$ nsec. Stretch current is terminated and cutting current is turned on at this time. ($t_c = 0$ nsec.) Cutting current density is $40 mA/\mu m$.

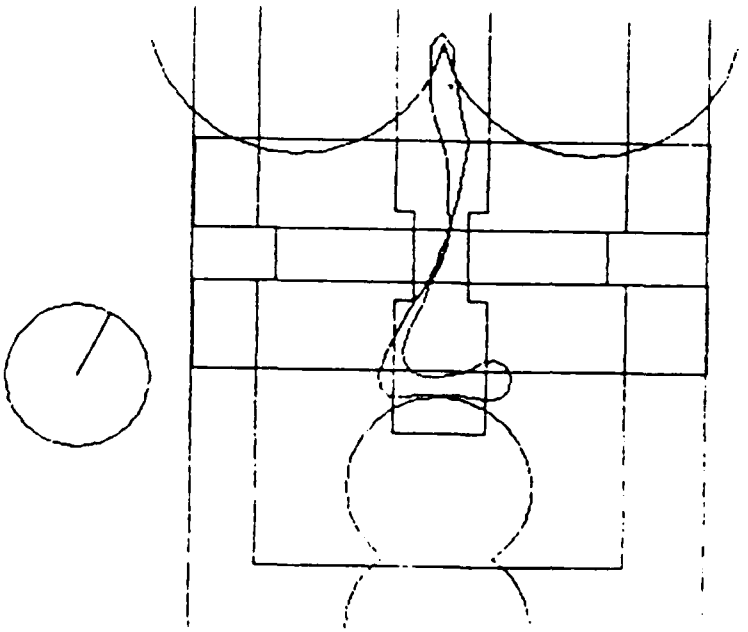

(f) $t_c = 20$ nsec.

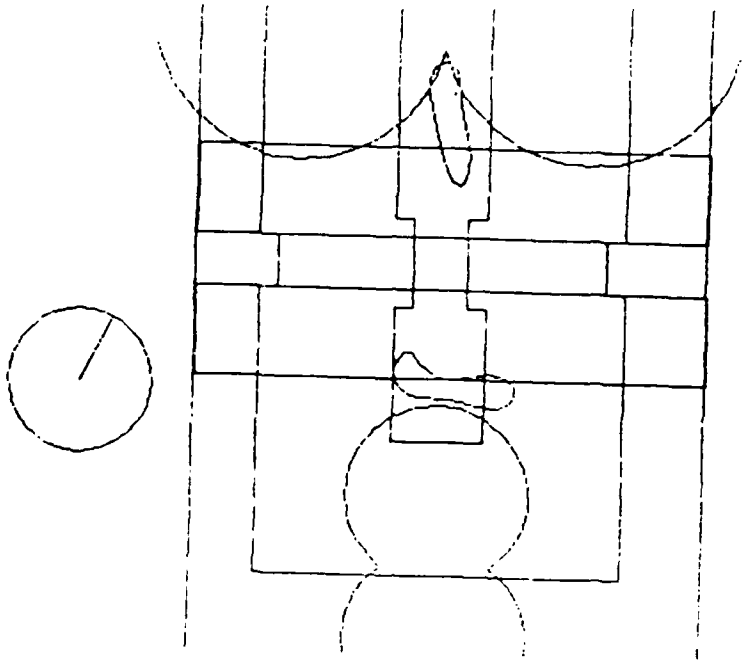

(g) $t_c = 40$ nsec. Cutting current is now turned off.

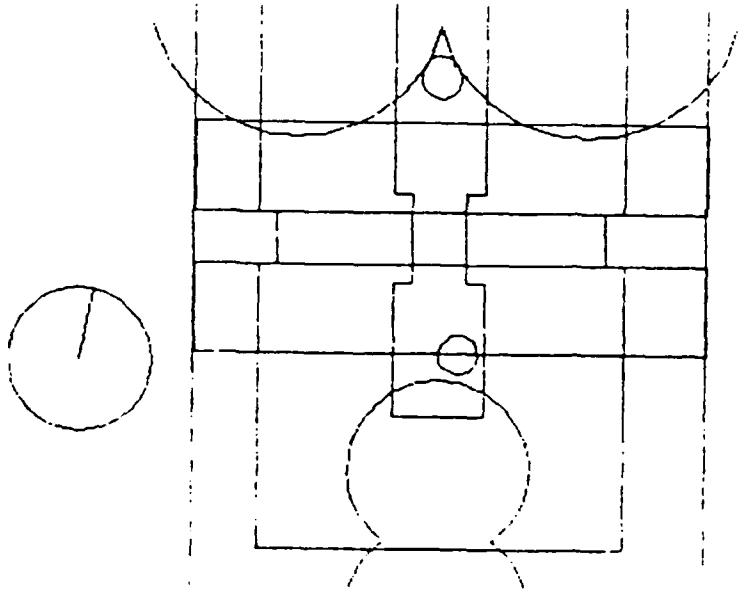

(h) Bubble positions 40 nsec after termination of the cutting pulse.

To enable transfer, the hairpin conductor is pulsed when the rotating field is near 0 degrees. The bubble, rotating along with the drive field, is also near 0 degrees and is attracted towards the potential well produced by the current in the hairpin. Given sufficient current amplitude, the bubble will be trapped by the hairpin field as the drive field and charged wall continue to

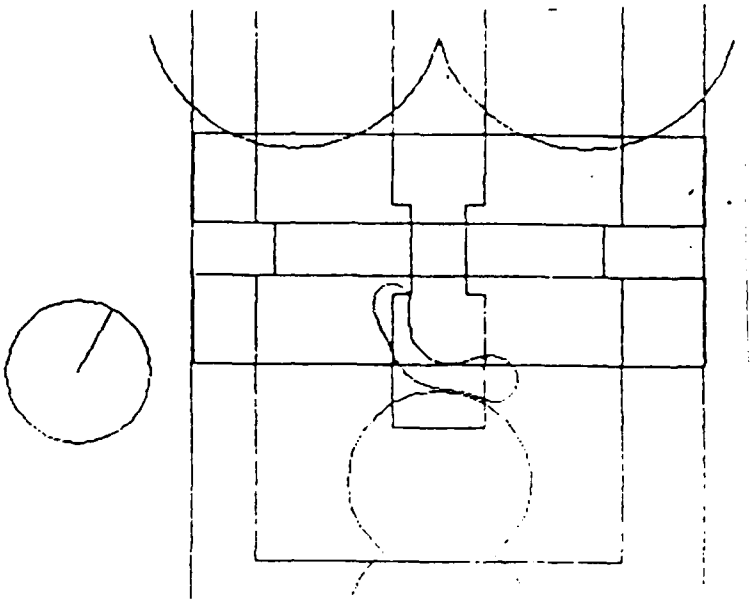

Figure 18: Failure mode due to insufficient stretching current amplitude. Stretching current density was 30mA/μm. All other parameters were the same as those used in Fig. 17.

rotate. As the drive field rotates towards 180 degrees, a charged wall formed on the upper disc and rotating along with the field can "grab" the bubble when the wall reaches 180 degrees. With the current turned off at this point, the bubble is then free to be driven by the charged wall on the major line, completing the transfer process.

The process described in the preceeding paragraph refers to what is commonly called *transfer-out*. To implement *transfer-in*, the process is simply reversed. Of course, the bubble to be transferred in must be propagating on the major line; then, the conductor pulse begins when the drive field phase is approximately 180 degrees and ends at roughly zero degrees. At this point, the nearest attractive charged wall is on the minor loop tip and as the drive field continues rotating it pulls the bubble along with it, onto the storage loop.

In Fig. 21 are seen the edge affinity field contours that were computed for the trapping transfer gate described above. The implanted layer thickness is 0.4 microns here and $4\pi M$ is 851G. It is seen that the field and its gradient can be rather strong, particularly in the cusps. It is quite obvious that these fields, due to their magnitudes, play an important role in affecting

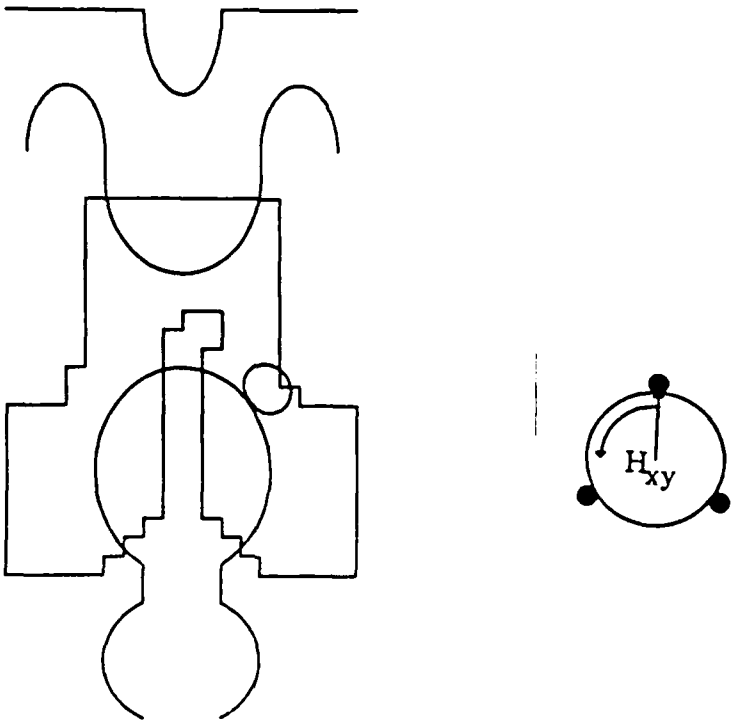

Figure 19: Trapping transfer gate design that was simulated.

bubble behavior. Particularly, in ion-implanted devices of the type being studied here, the collapse field of bubbles propagating along contiguous-disc patterns is usually found to be significantly higher in the cusps than elsewhere on the propagation pattern. This increase in collapse field, most often attributed to the strong charged wall formation in the cusp, is also due to the high edge affinity field in the cusp.

Shown in Fig. 22 are the magnetic z-field contours (in Oe) that result when the trapping transfer gate conductor is carrying a current density of 1mA/μm (4.5 mA).

In Fig. 23 is seen the simulated transfer-out process. The trapping hairpin conductor leading pulse edge was initiated at $\theta = 0$ degrees and was terminated at $\theta = 130$ degrees. The current amplitude used was 25 mA here.

A variety of failure modes were observed in the transfer-out process. At lower transfer current amplitudes, the fields produced would be too weak to trap the bubble; the bubble would

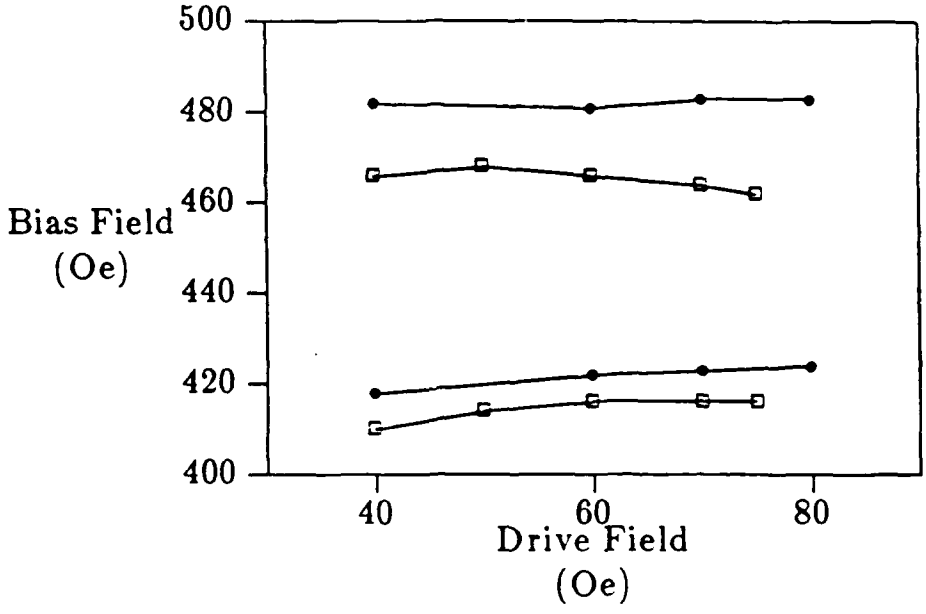

Figure 20: Experimental and simulated propagation margins for the minor loops of the trapping transfer gate. Circles denote simulated margins; boxes are experimentally obtained data points.

Magnetization	$4\pi M_s$	851 G
Anisotropy field	H_k	1.01 kG
Uniaxial Anisotropy	K_u	64.1 kergs/cm^3
Characteristic length	l	0.105 μm
Bubble film thickness	t	1.28 μm
Stripe width	w	1.1 μm
Wall Coercivity	H_c	1.0 Oe
Bubble mobility	μ_w	300 cm/sec-Oe
Bubble saturation velocity	v_s	3800 cm/sec
Operating frequency	f	100 kHz
Stretcher thickness		0.6 μm

Table 2

Parameters used in trapping transfer gate simulation.

simply propagate around the minor loop tip as seen in Fig 24. For the gate under discussion, the minimum transfer current was found experimentally to be 15 mA, very close to the simulated

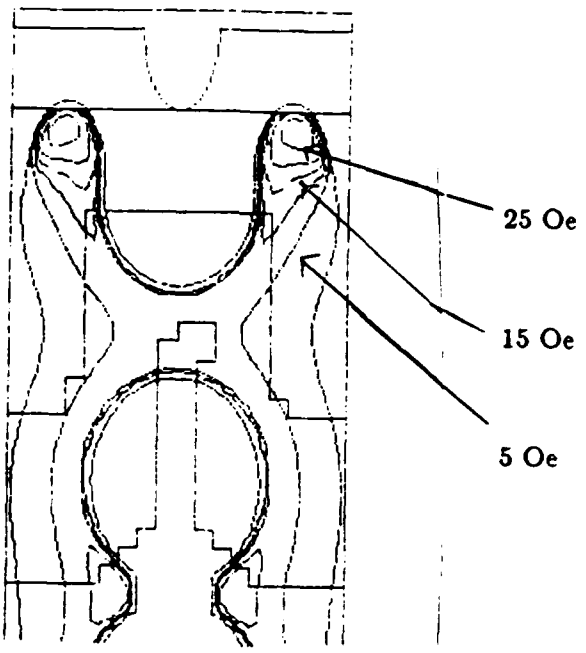

Figure 21: Field contours due to edge affinity in the trapping transfer gate. Shown are 5, 10, 15, 20 and 25 Oe contours.

minimum of 18 mA. At the other extreme, when too high a current was used, the bubble would stripe-out. This problem was particularly exacerbated at lower bias fields, as seen in Fig. 25 where the transfer current value for the simulation shown was 36 mA.

4 Discussion

In general, the simulator results are in very good agreement with the experimental data for the functions discussed in this report. In particular, the failure modes of propagation were more revealing than expected, especially bubble trapping in the cusps. The simulated and experimentally obtained bias margins are found to be almost identical. It should be noted that the only unknown parameter used in the simulations was the wall coercive force, which was estimated to be 1 Oe. To check this assumption, margin variation as a function of coercivity was studied. Our simulations have shown that there appears to be a threshold below which the margins are relatively insensitive to changes in coercivity. However, once this threshold is

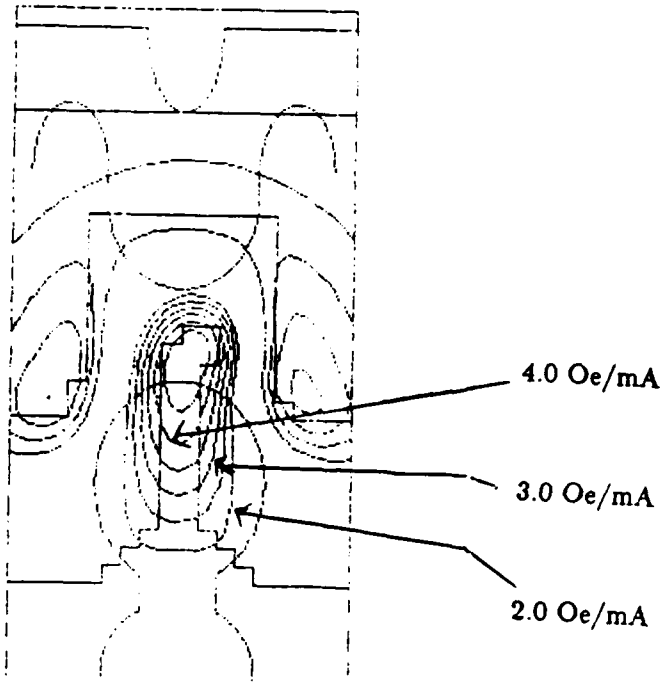

Figure 22: Normalized field contours of the trapping transfer gate conductor. Shown are 2, 2.5, 3, 3.5, 4, and 4.5 Oe/mA contours.

exceeded, margins degrade dramatically, particularly at higher bias and drive fields. The dominant failure mode in the high coercivity regime was failure of the charged wall to pull the bubble out of the cusp, which will be described in detail in the following paragraph.

Three major propagation failure modes were observed: bubble collapse, bubble stripe-out and bubble "lag". Bubble "lag" is defined as the failure that occurs when a bubble gets stuck in a cusp and can not be pulled out of the cusp by the rotating drive field. Bubble collapse usually occured at one of two places on the minor loop at two different drive field phases. It occured in the cusps during the portion of the field cycle that the bubble is held stationary in the cusps and is subject to the influence of a passing negative charged wall, and it occured at the extreme edges or tips of the pattern edge where the edge affinity is low. In the center of Fig. 12 is seen the simulator result obtained for bubble collapse in the cusp. The bubble is seen to propagate successfully into the cusp, but it collapsed due to the negative charged wall there. Both of these collapse failure modes were seen in the devices tested in the laboratory. Stripe-out was observed to occur at low bias fields and the bubble would stripe-out along one of the easy stripe-out directions under the influence of the strong positive charged wall there or along the unimplanted

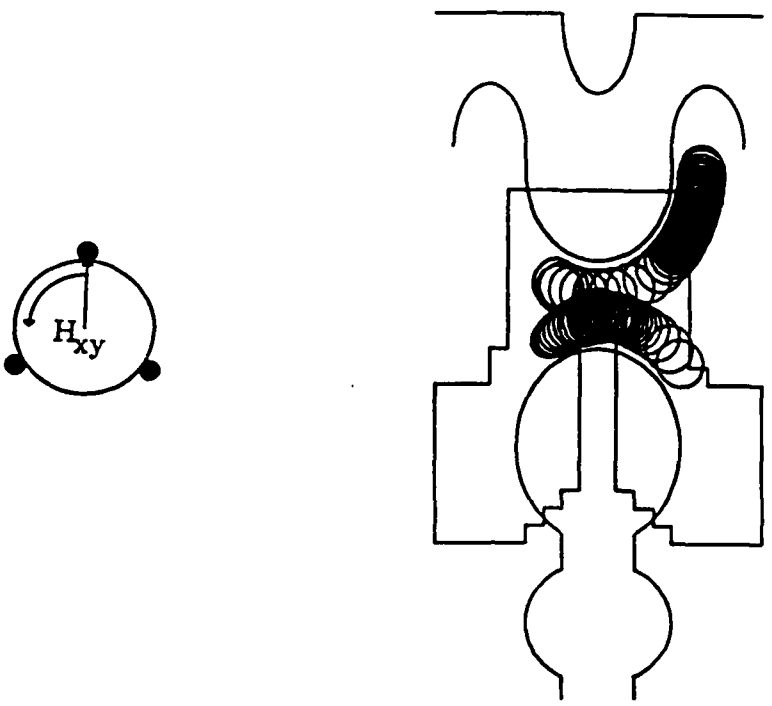

Figure 23: Simulation of the transfer-out process. Transfer pulse of 25 mA amplitude applied for $130<\theta<0$ degrees.

pattern edge where the edge affinity was high. This is depicted on the left-hand side of Fig. 12. Bubble lag would occur in the left-hand side minor loop cusps as seen in the right-hand side of Fig. 12. Note that the bubble, starting on the right side of the minor loop and propagating counter-clockwise, could successfully negotiate the cusp on the right hand side of the pattern, but failed to propagate out of the cusp on the left-hand-side. This is due to the fact that for the right-hand side cusps, the bubble in the cusp couples to the charged wall which *is moving smoothly and relatively slowly due to the proximity of the easy stripe-out direction* as it leaves the cusp. However, on the left-hand-side of the track, the bubble residing in the cusp must couple to a charged wall which is racing through a hard direction towards the nearest stripe-out position, which is essentially in the next cusp, a full pattern period away. If the bubble can not catch up and keep up with the charged wall at this time, it will simply fall back to the cusp, being held there stably by the edge affinity. Observation of this type of failure with the simulator was not anticipated, but has been seen frequently in our experimental devices.

Various aspects of trapping transfer gate operation were simulated. One particular parameter, the minimum current required to implement transfer, was predicted to be 18 mA.

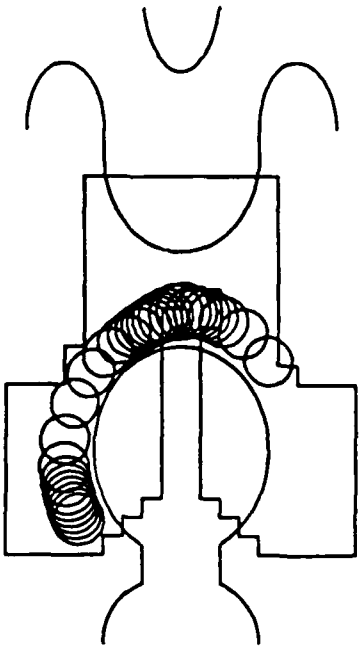

Figure 24: Transfer-out failure due to insufficient current amplitude. The bubble, instead of being trapped by the hairpin, continues to rotate around the end of the minor loop.

This is in good agreement with the experimentally obtained value of 15 mA. Initial phase margin simulations currently being performed and not presented here also show that the simulated phase margins are very close to those measured on actual devices.

5 Present and Future Work

Presently, work is being performed on improving the simulator's speed and flexibility. When first implemented, the bubble wall segment positions were computed at 1 nsec intervals. If the drive field frequency used in the simulation was 100kHz, the drive field period, being 10 μsec, would require 10,000 steps to simulate bubble motion during only one full drive field rotation. As a result, one simulation would take several hours on an HP9836 computer. To decrease computation time two improvements were made. First, the programs used on the simulator were modified to run on a VAX machine. Most important however, were improvements made to the simulator. These are explained below.

When bubble motion is simulated, the fields on each wall segment that comprise the bubble are calculated and the wall segment response to these fields is computed. Of course, for greatest

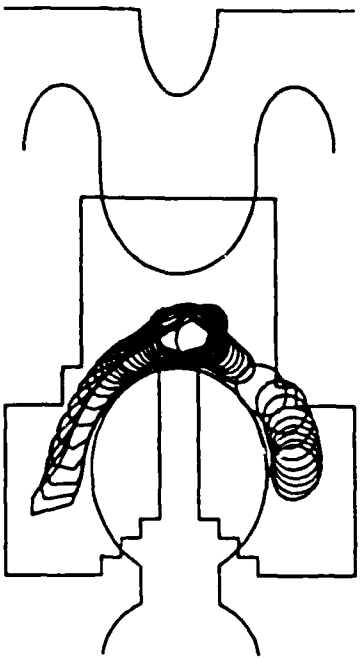

Figure 25: Transfer-out failure at low bias (438 Oe) due to high transfer pulse amplitude (36 mA). The bubble has striped out along the implanted pattern edge.

accuracy, the smaller the time increment between computations the more accurately the bubble position can be calculated. However, in many cases, the wall segment locations will not vary much as a function of time, such as when the bubble is being held by the conductor field of the trapping transfer gate. In this case, the wall positions are essentially constant on both local and global scales; the wall positions are not changing with respect to each other (the bubble is not stretching or shrinking) and the average bubble center as a function of time is constant (the bubble is not translating). Under these conditions there is no reason to calculate the fields and bubble wall segment response using small time increments. Thus, the program was designed to check for local and global invariance of wall shape and increase the time increment up to 32 nsec depending upon the degree of invariance. This greatly reduced simulation time. CPU time for one simulation is on the order of an hour at the time of this writing.

For the gates described and discussed in the previous sections, there is still much work to be done on comparing experimental and simulated results. The degree of anisotropy of the material used in the device and how this impacts gate margins is presently being studied also

References

1. Hayashi, N. and Abe, K., "Computer Simulation of Bubble Motion", *Japan. J. Appl. Phys.*,Vol. 14,No. 11,Nov. 1975, pp. 1705 - 1716.

2. Hayashi, N., Mikami, H. and Abe, K., "Computer Simulation of Bubble Motion", *I.E.E.E. Transactions on Magnetics*,Vol. MAG-13,No. 5,September 1977, pp. 1345 - 1347.

3. D. Shenton, S.H. Charap, H. David and M.H. Kryder, "Computer Simulation Of Dual Conductor Current Access Magnetic Bubble Logic Devices", *I.E.E.E. Transaction on Magnetics*,Vol. MAG-17,No. , 1981, pp. 2677.

4. Douglas A. Saunders, *Stress-induced Magnetic Anisotropies in Ion-implanted, Contiguous-disk, Magnetic Bubble Devices*, PhD dissertation, Carnegie Mellon University, 1987.

5. H. Fukushima And N. Hayashi, "Computer Simulation Of Magnetization Distributions In Contiguous-Disk Bubble Devices", *Presented At The 1987 Intermag Conference*, .

6. Y. Sugita, R. Suzuki, T. Ikeda, T. Takeuchi, N. Kodama, M. Takeshita, R. Imura, T. Satoh, H. Umezaki, and N. Koyama, "Ion-Implanted and Permalloy Hybrid Magnetic Bubble Devices", *I.E.E.E. Transactions on Magnetics*,Vol. MAG-22,No. 3,July 1986, pp. 239 - 246.

7. Kodama, N., Koyama, N., Umezaki, H., Suzuki, R., Takeuchi, T. and Sugita, Y., "Characteristics Of Junctions Between Ion-Implanted And Permalloy Tracks In Hybrid Bubble Devices", *I.E.E.E. Transactions On Magnetics*,Vol. MAG-20,No. 5,September 1984, pp. 1075 - 1077.

8. Mizuno, K., Suga, S. and Urai, H., "Block Replicate Gates for Ion-Implanted Bubble Devices", 9^{th} *Japanese Applied Magnetics Society Meeting Digest*,Vol. 76, 1985, pp. 76, In Japanese

9. Magnin, J., Poirier, M., Fedeli, J.M. and Delaye, M.T., "Two Conductor Levels Block Replicator For 4μm Period Ion-Implanted Devices", *I.E.E.E. Transactions On Magnetics*,Vol. MAG-20,No. 5,September 1984, pp. 1087 - 1089.

10. Komenou, K., Matsuda, K., Miyashita, T., Ohashi, M., Betsui, K., Satoh, Y. and Yamagishi, K., "Design of a Block Replicate Gate for Ion-Implanted Bubble Devices", *I.E.E.E. Transactions on Magnetics*,Vol. MAG-18,No. 6,November 1982, pp. 1352 - 1354.

11. Urai, H., Mizuno, K., Asada, S., Takada, N., Yoshioka, N., Gokan, H. and Yoshimi, K., "4Mb On-Chip-Cache Bubble Memory Chips With 4μm Period Ion-Implanted Propagation Patterns", *I.E.E.E. Transactions On Magnetics*,Vol. MAG-20,No. 5,September 1984, pp. 1072 - 1074.

12. N. Hayashi and K. Abe, "Computer Simulation of Magnetic Bubble Domain Wall Motion", *Japanese Journal of Applied Physics*,Vol. 15,No. , 1976, pp. 1683.

13. P. Pougnet, H. Jouve, P. Gerard and F.B. Humphrey, "Potential Barrier Study of the

Border-line Defined by Ion implantation in Bubble Garnets", *Journal of Applied Physics*,Vol. 53,No. 3,March 1982, pp. 2513 - 2515.

14. A. H. Bobeck, S.L. Blank, A.D. Butherus, F.J. Ciak and W. Strauss, "Current-access magnetic bubble circuits", *Bell System Technical Journal*,Vol. 58,No. , 1979, pp. 1453.

15. Y. Hidaka, "Charged wall formation and propagation analysis in ion-implanted contiguous disk bubble devices", *Journal of Applied Physics*,Vol. 53,No. 8,August 1982, pp. 5815 - 5822.

16. D. A. Saunders And M. H. Kryder, "Stresses And Magnetoelastic Anisotropies At Implantation Edges In Ion Implanted Garnet Films", *J. Appl. Phys.*,Vol. 57, 1985, pp. 4061.

17. S.C.M. Backerra, W.H. De Roode And U. Enz, "The Influence Of Implantation-Induced Stress Gardients In Magnetic Bubble Layers", *Phillips J. Res.*,Vol. 36, 1980, pp. 112.

18. Y. Hidaka and H. Matsutera, "Charged Wall Formation Mechanism In Ion-Implanted Contiguous Disk Bubble Devices", *Appl. Phy. Let.*,Vol. 39, 1982, pp. 116.

19. M.H. Kryder, D. Saunders, "The Effects Of Stress Relaxation And Anisotropic Magnetostriction On Charged Walls In Ion-Implanted Garnets", *IEEE Trans. Magn.*,No. Mag-19, , 1983, pp. 1817.

20. A. Hubert, "Charged Walls In Thin Magnetic Films", *IEEE Trans. Magn.*,Vol. Mag-15, 1979, pp. 1251-1260.

21. J.C. DeLuca and A.P. Malozemoff, "Dynamic Method for Characterizing Potential Wells of Bubbles Under Charged Walls", *I.E.E.E. Transactions on Magnetics*,Vol. MAG-15,No. 6,November 1979, pp. 1651 - 1653.

22. H. Urai, "New Method For Potential Well Measurements Using Bubble Runout In Ion-Implanted Bubble Devices", *IEEE Trans. Magn.*,Vol. Mag-21, 1985, pp. 2676-2679.

23. S. J. Zhang And F. B. Humphrey, "Potential Well Of Charged-Walls", *J. Appl. Phys.*,Vol. , , pp. .

24. Calhoun, B.A., "The Motion Of A Charged Wall Coupled To A Bubble", *I.E.E.E. Transactions On Magnetics*,Vol. MAG-18,No. 6,November 1982.

25. B.E. Argyle, M.H. Kryder, R.E. Mundie and J.C. Slonczewski, "Mobility of a Charged Wall Coupled to a Bubble", *I.E.E.E. Transactions on Magnetics*,Vol. MAG-14,No. 5,September 1978, pp. 593 - 595.

26. Abramowitz, M. and Stegun, I.A., *Handbook of Mathmatical Functions*, Dover Publications, New York, 1965.

27. T.J. Nelson, V.J. Fratello, D.J.Muehlner, B.J. Roman and S.E.G. Slusky, "Four-Micron Period Ion-Implanted Bubble Test Circuits", *I.E.E.E. Transactions on Magnetics*,Vol. MAG-22,No. 2,March 1986, pp. 93 - 100.

List of Figures

Figure 1: Representation of the bubble domain wall in the laboratory and local frames. The wall point P(ξ) is specified by a parameter ξ which is the wall length O_wP divided by the total wall length L. 4

Figure 2: Wall displacement at wall point P(I) in the *R-S* frame. 9

Figure 3: The calculation of the demagnetizing field on a wall point. 11

Figure 4: A line segment of a current loop. 12

Figure 5: Model for the charged wall. 15

Figure 6: Geometry used to calculate motion of bubble coupled to unimplanted disc. 16

Figure 7: Bubble position as a function of drive field position around an unimplanted disc for two different values of the normalized drive field, h. 18

Figure 8: Critical curve for determining bubble nucleation threshold. 20

Figure 9: Geometry used to define fields used in computing nucleation threshold. 21

Figure 10: Block-replicate design modelled in this report. The major loop cusp is connected to the minor loop by a hairpin conductor which is used to stretch the bubble. The stripe chopping conductor is seen lying perpendicular to the stretching hairpin. 22

Figure 11: Typical bubble propagation simulation. The three easy stripe-out directions and drive field rotation sense are also shown. Bubble positions plotted every 160 nsec, except in cusps where positions are plotted every 5μsec. Simulation drive field frequency was 125 kHz. 23

Figure 12: The three types of propagation failure observed during simulation. On the left-hand side is seen bubble stripe-out along the pattern edge. The middle depicts bubble collapse in the cusp, and on the right-hand side is seen bubble lag, explained in detail in the text. 24

Figure 13: Experimental and simulated propagation margins for the minor loops of the block-replicate gate. 25

Figure 14: Simulated bias field margins for bubble propagation with the wall coercivity as a parameter. Margins degrade from the low bias end as the coercivity is increased from 1.0 Oe (Light line) to 3.0 Oe (Dark line). When $H_c = 3.5$ Oe, the high bias margins fall drastically. (Dashed line.) 26

Figure 15: Perpendicular magnetic field contours, in oersteds, of stretching conductor of the block replicate gate due to a current density of 1 mA/μm flowing through it. 1.5, 2.0, 2.25, and 2.50 Oe. contours shown. 27

Figure 16: Perpendicular magnetic field contours, in oersteds, due to the edge affinity of the implanted/unimplanted boundaries of the block replicate gate. Only 10 and 20 Oe. contours shown. Reduced thickness due to implantation is 0.35μm here. 28

Figure 17: (a) Initial bubble position prior to activating the stretching conductor ($t_s = 0$) and the position of the drive field, which is rotating counter clockwise. Stretching current density was 40mA/μm. 29

Figure 18: Failure mode due to insufficient stretching current amplitude. Stretching current density was 30mA/μm. All other parameters were the same as those used in Fig. 17. 33

Figure 19: Trapping transfer gate design that was simulated. 34

Figure 20: Experimental and simulated propagation margins for the minor loops of the trapping transfer gate. Circles denote simulated margins; boxes are experimentally obtained data points. 35

Figure 21: Field contours due to edge affinity in the trapping transfer gate. Shown are 5, 10, 15, 20 and 25 Oe contours. 36

Figure 22: Normalized field contours of the trapping transfer gate conductor. Shown are 2, 2.5, 3, 3.5, 4, and 4.5 Oe/mA contours. 37

Figure 23: Simulation of the transfer-out process. Transfer pulse of 25 mA amplitude applied for $130<\theta<0$ degrees. 38

Figure 24: Transfer-out failure due to insufficient current amplitude. The bubble, instead of being trapped by the hairpin, continues to rotate around the end of the minor loop. 39

Figure 25: Transfer-out failure at low bias (438 Oe) due to high transfer pulse amplitude (36 mA). The bubble has striped out along the implanted pattern edge. 40

The State of Silicon-on-Garnet Devices

P.H.L. Rasky, D.W. Greve, and M.H. Kryder
Department of Electrical and Computer Engineering

ABSTRACT

Silicon MOSFET's with gate leakage currents in the pA range have been fabricated on magnetic bubble substrates coated with SiO_2 and Si_3N_4. Electron mobilities for these devices are in the 100-200 cm^2/V-sec range. We have also fabricated silicon magnetodiodes on silicon and bubble substrates coated with SiO_2 and Si_3N_4. The magnetosensitivity of diodes fabricated on silicon substrates is on the order of 2.5×10^{-4} μA per gauss per μm of diode width. Both MOSFET's and magnetodiodes are fabricated with the same high temperature steps. This processing does alter the magnetic properties of the bubble film. The changes are significant, but they are not catastrophic. For a 1μm bismuth film, the final value of K_u (the uniaxial magnetic anisotropy energy density) drops by 20%; the final value of l (the characteristic length) increases by 49%, and the final value of $4\pi M_s$ (the saturation magnetization) increases by 1%. All increases/decreases are with respect to the as grown values.

INTRODUCTION

Magnetic bubble memories offer high-density non-volatile storage of binary information. Getting information in and out of the memory is somewhat of a problem: data access times are long (compared to semiconductor memories); data transfer rates are low (100 to 400 kbit/sec [1]), and output signals tend to be small (1-40mV [2]). These traits can be traced, in large part, to the bubble detector. A conventional magnetoresistive bubble detector must be large to compensate for its low sensitivity ($\Delta R/R$ is about 5×10^{-3} [3]), and this large size limits the number of detectors that can be placed on a bubble chip. Fujitsu's 4 Mbit bubble memory uses only 4 bubble detectors [1]. Increase the detector count by a factor of 10, and the result would be a memory with a data transfer rate of 4 Mbit/sec. This is possible if small high-sensitivity

detectors can be found. Such detectors exist, and we will next describe one of them. The device in question, a silicon p+(n-)n+ diode, has a sensitivity in the range of 1-30 V/kgauss [4,5].

Diodes with the structure shown in fig. 1(A) have current - voltage characteristics that are dependent on the magnitude and direction of an applied magnetic field **B** (see fig. 1(B)). This field induced current dependence is a consequence of the interfacial properties of the device. If the magnetic field deflects current carriers to the top interface, which is of high quality (low surface recombination velocity s), they will recombine more slowly than if the field deflects them to the bottom interface, which is of low quality (high surface recombination velocity s). A slower rate of recombination in turn means a higher concentration of electrons and holes in the n- base. This increase in carrier concentration causes a higher diode current: the base conductivity has increased [4,6].

If we place the magnetodiode of fig. 1(A) in the circuit of fig. 1(C) with the n+ region tied to ground potential, we have a scheme for the detection of magnetic bubbles. Two identical magnetodiodes (sensors) are required. One sensor serves as the dummy senor; it never sees a domain and operates along the B=0 curve shown in fig. 1(B). Here B indicates the flux added by the presence of a bubble. If a bubble is absent, B=0. The other sensor either sees a bubble or does not: whether it does or does not is dependent on the data stream fed to it. If the sensor does see a bubble it will operate along either the $B>0$ or $B<0$ curve shown in fig. 1(B). The geometry of the circuit and the orientation of the bubble's magnetization will determine which curve is appropriate. Here again, B indicates the flux added by the presence of a bubble. Both branches of the circuit must obey the load line shown in fig. 1(B) and it therefore follows that the presence of a bubble (near the sensor) will produce a non-zero differential output ΔV while the absence of a bubble (near the sensor) will produce a zero differential output in the circuit of fig. 1(C).

Sensitivities of 1-30 V/kgauss are useful, but such sensitivities may still be insufficient for some applications. In such a case, one may further amplify the detector's output with an on-chip silicon-on-garnet MOSFET amplifier. The quality of current silicon-on-garnet MOSFET's is such that they can be considered for use in even more complex circuits. Single-chip computers with truly non-volatile memory are (therefore) one step closer to becoming reality.

FABRICATION PROCESSES

Now we will introduce the silicon-on-garnet process we have used to fabricate our most recent silicon-on-garnet MOSFET's and magnetodiodes. Only the major process steps are listed, and the starting substrates are (111) GGG. Each substrate has a single bubble film on it. The process is as follows:

1. Deposit 0.41μm of LPCVD SiO_2 at 860°C and 0.8-0.9 torr.
2. Deposit 0.24μm or 0.85μm of LPCVD Si_3N_4 at 800°C and 0.7 torr.
3. Deposit 0.55μm of LPCVD polysilicon at 625°C and 0.4 torr
4. Recrystallize the polysilicon with the light from an argon laser (all lines are used). The light beam is focused to a 30-40 μm diameter spot and is scanned in a simple raster like pattern.
5. Define silicon islands using a wet silicon etch (HNO_3:H_2O:HF 50:20:1).
6. Ion implants to define n+ and p+ regions.
7. Wet O_2 (gate) oxidation at 850°C. The resulting SiO_2 layer is $\sim$0.1μm thick.
8. Define metalization contact cuts using a buffered HF etch.
9. Deposit 1μm of Al in a filament evaporator.
10. Pattern and etch the Al to form interconnect and probe pads. A wet Al etch is used.

An older process, used to fabricate the device structure shown in fig. 2(A), is very similar to the one just listed. The major differences are: the oxide+nitride spacer is replaced with a 1μm thick sputtered SiO_2 layer; the polysilicon layer is capped with a 1μm sputtered SiO_2 layer during recrystallization, and the recrystallized silicon layer is doped p-type by a boron implant after the cap oxide is removed. Devices fabricated with the 10 step process have the structure shown in fig. 3(A).

IMPROVED SILICON-ON-GARNET MOSFET's

Our first silicon-on-garnet MOSFET's were fabricated on bubble substrates coated with $\sim$1μm of sputtered SiO_2 (fig. 2(A)). The yield was very low and the devices that did function (fig. 2(B)) had pronounced gate leakage currents. Clearly this is undesirable, and we have recently utilized a new structure that yields silicon-on-garnet MOSFET's of higher quality. The structure is shown in fig. 3(A), and the I-V characteristics for a MOSFET with this structure are

shown in fig. 3(B). The characteristics are well behaved and are typical of most MOSFET's that are fabricated on the SiO_2+Si_3N_4 spacers. Note the absence of negative drain current for small positive drain to source voltages. It has been shown that negative drain current for small positive drain to source voltages, like that seen in fig. 2(B), is characteristic of MOSFET's that have large gate leakage currents [7].

The superiority of the oxide+nitride spacer, over the oxide only spacer, is even more apparent when one views plots of the gate current I_g vs. gate voltage V_g with the source and drain grounded. Figure 4 shows four plots of I_g vs. V_g. The plot shown in fig. 4(A) is for a MOSFET fabricated on a bubble substrate coated with only a silicon dioxide spacer. In fig. 4(B), the plot is for a MOSFET fabricated on a bubble substrate coated with silicon dioxide (first layer on the bubble substrate) and silicon nitride (second layer on the bubble substrate). Increasing the thickness of the Si_3N_4 film from 0.24μm to 0.85μm improves the gate breakdown voltage by nearly 1 volt; compare the plot of fig. 4(B) with the one shown in fig. 4(C). The plot shown in fig. 4(D) is for a MOSFET fabricated on a silicon substrate coated with silicon dioxide (first layer on the silicon substrate) and silicon nitride (second layer on the silicon substrate). This latter substrate served as a control or monitor wafer. Notice how much sharper the characteristics of fig. 4 (B), (C), and (D) are compared to the characteristic of fig. 4(A). Now compare only the characteristics of fig. 4(A) and 4(C). To make the comparison fair, we'll subject the gate oxide of both devices to the same electric field. We selected 25 V/μm for convenience. For the device of fig. 4(A), this corresponds to a gate voltage of 1.25 V as its gate oxide is approximately 0.05μm thick. For the device of fig. 4(C), this corresponds to a gate voltage of 2.5 V as its gate oxide is approximately 0.1μm thick. If we now take note of the gate areas (313 μm^2 for the device of fig. 4(A) and 590 μm^2 for the device of fig. 4(C)), we find: I_g per unit area of gate oxide is nearly 2.5×10^5 times smaller for the MOSFET fabricated on the bubble substrate coated with the oxide+nitride spacer.

Lower gate leakage currents have allowed us to reliably measure the mobility of electrons in the channel of our n channel MOSFET's. We used the method suggested by Muller and Kamins [8]. Briefly stated, one measures the zero-bias channel conductance as a function of gate voltage and calculates the mobility from the slope of the resulting plot (fig. 5(A)). Using this procedure we found, MOSFET's fabricated on bubble substrates coated with the oxide+nitride spacers have top gate electron mobilities on the order of 100-200 cm^2/V-sec. We were also able

to determine from this plot, and ones similar to it, that our MOSFET's had a back gate conductance. The value of the back gate conductance is just the value of I_d/V_{ds} near V_g=0 (the flat part of the curve). One might expect the top gate mobility to be different if the back gate conduction path did not exist. We investigated this possibility by making a set of mobility measurements on silicon substrates coated with oxide+nitride spacer layers. First, we measured the electron mobility for a given device with the back gate on (V_{bg}=0 V). Next, we measured the electron mobility with the back gate turned off (V_{bg}=-40 V). The mobility with the back gate on was 175 cm^2/V-sec, and the mobility with the back gate off was 177 cm^2/V-sec. Within experimental error, these values are the same, and one can, therefore, model a silicon-on-garnet MOSFET with back gate conductance as shown in fig. 5(B). The independence of G_t and G_b is at least true for the mobility measurement.

MAGNETODIODES: RESULTS

Silicon magnetodiodes have been fabricated on silicon and magnetic bubble substrates coated with SiO_2 and Si_3N_4. See fig 6(A) for the structure of our devices. They have well behaved I-V characteristics, and we show one such characteristic in fig 6(B). Magnetic sensitivities on the order of 2.5 x 10^{-4} μA per gauss per μm of diode width are typical. Fig. 7(A) shows a plot of the magnetodiode current as the magnetic field is swept between plus and minus 16kG at a rate of approximately 1.1kG/sec. Current maxima are at +16kG and current minima are at -16kG. The geometry pertinent to this measurement is shown in fig. 7(B). Current is perpendicular to and out of the plane of the paper. The magnetic field is positive when directed to the right, and is negative when directed to the left. The force ($\mathbf{F} = qv \times \mathbf{B}$) on electrons and holes is directed away from the paddle when the magnetic field is positive and is directed toward the paddle when the magnetic field is negative. The magnetodiode's bottom interface is closest to the paddle. So, from the earlier discussion on magnetodiodes, we would expect to see current minima when B is at its minimum value and current maxima when B is at its maximum value. That's exactly what we see in the data of fig. 7(A).

MAGNETIC PROPERTIES: PROCESS INDUCED CHANGES

It is important that silicon-on-garnet devices be fabricated without destroying the magnetic nature of the bubble film. Table 1 lists the room temperature values for $4\pi M_s$, l, and K_u (the saturation magnetization, characteristic length, and uniaxial magnetic anisotropy energy density) after a number of key processing steps. The processing steps are listed in the order in which they were performed. Note that $4\pi M_s$ is essentially the same at the beginning and end of the

silicon-on-garnet process; K_u decreases by 20 %, and l increases by 49 %. After the 850 C oxidation step, we observed some slightly non-ideal domain nucleation (before this step, we saw the typical serpentine domain structure): one stripe would nucleate additional stripe domains as the bias field was lowered below stripe-out. The field was lowered very slowly, on the order of 10-30 oe/sec. Long stripe domains also had a somewhat jagged appearance. Isolated bubble domains were still right-circular cylindrical in structure when the bias field was kept in between stripe-out and collapse.

SUMMARY, CONCLUSIONS, AND PROJECTIONS

The data we have presented firmly establishes that high quality MOSFET's can be fabricated on magnetic bubble substrates. Electron mobilities are typically 100-200 cm^2/V-sec, and most devices have gate breakdown voltages in the 3-4 V range. This 3-4 V value should not, however, be taken as an upper limit since these devices were not processed optimally: thermally induced stresses resulting from the laser recrystallization of large areas of polysilicon (each ~1.8cm x 1.8cm) caused significant cracking of the oxide+nitride spacer, and we speculate that this cracking may have allowed ions from the bubble film to contaminate the islands of recrystallized polysilicon. One can and should minimize the area of polysilicon recrystallized. Smaller recrystallized areas have less tendency to crack than larger ones. We saw no cracking of the spacer in areas that were not recrystallized. It is also important to note that the sputtered oxide spacer is not immune to cracking. This is not surprising as the sputtered oxide was not densified prior to the laser recrystallization step. The back gate channels that characterize our MOSFET's are the result of trapped positive charge present in the oxide+nitride spacer layer (the interface between the silicon and oxide spacer is considered part of the spacer) [9,10]. These channels can be suppressed if one is willing to do a deep implant aimed at the back interface. If the trapped spacer charge is only positive in sign, it would not be a problem for p channel enhancement devices: in the absence of gate bias, the already n-type channel simply becomes more strongly n-type. The device is still off.

The magnetodiode may become the first silicon-on-garnet device structure to detect a magnetic domain once we integrate it with an ion-implanted contiguous-disk propagation pattern. Our preliminary data suggests a nominal sensitivity of at least 2.5 x 10^{-4} μA per gauss per μm of diode width. Improvement is certainly desired, but again we must point out: the device structures fabricated to date were not optimized. We are currently investigating ways to optimize the interfaces of magnetodiodes. Ultimately, one would like to fabricate magnetodiodes with predictably different interfaces.

The silicon-on-garnet fabrication process does alter the magnetic properties of the bubble film. These changes can be non-trivial: the final value of K_u decreases by 20% compared to the as grown value, and the final value of l increases by 49% with respect to its as grown value. For the same 1μm bismuth film, we have found that the final value of $4\pi M_s$ changes very little (1%) with respect to its as grown value. The appearance of non-ideal domain structure and nucleation properties (after the 850°C gate oxidation) is probably linked to an increase in the coercivity of the bubble material. We plan to measure the static and dynamic coercivities of our bubble material in the future. Process induced changes may affect operating margins and yields, but they are not expected to prevent demonstration of silicon-on-garnet magnetodiode bubble sensors.

ACKNOWLEDGMENTS

The recrystallizaton step of our process was carried out at the Westinghouse Research and Development Center (in Pittsburgh) with the assistance of Dr. Paul McMullin and Patricia A. Palaschak. Their willingness to collaborate with us on this project is certainly appreciated. Mahadevan Ramesh and Robert Campbell provided the magnetic bubble substrates used in this work and are hence recognized here. We also recognize Dr. Alberto Guzman and John Tabacchi as they were responsible for most of the ion implants required in our silicon-on-garnet process. Chris Bowman, Robert Harris, Suresh Santhanam, and other members of the clean room staff are acknowledged for the technical assistance they provided.

REFERENCES

[1] H. Inoue, M. Amatsu, T. Yanase, T. Majima, Y. Kaneko, S. Orihara, and S. Iwasa, "Characterization of A 4 Mbit Bubble Memory Device with 'Wide Gap' Permalloy Propagation Tracks," IEEE Transactions on Magnetics, Vol. MAG-21, No. 5, September 1985, pp. 1681-1683.

[2] A. Bobeck, I. Danylchuk, F. C. Rossol, and W. Strauss, "Evolution of Bubble Circuits Processed by a Single Mask Level," IEEE Transactions on Magnetics, Vol. MAG-9, No. 3, September 1973, pp. 474-480.

[3] T. J. Nelson, "Chevron Detector Design Study," IEEE Transactions on Magnetics, Vol. MAG-13, No. 6, November 1977, pp. 1773-1776.

[4] A. Mohaghegh, S. Cristoloveanu and J. De Pontcharra, "Double-Injection Phenomena Under Magnetic Field in SOS Films: A New Generation of Magnetosensitive Microdevices," IEEE

Transactions on Electron Devices, Vol. ED-28, No. 3, March 1981, pp. 237-242.

[5] S. Cristoloveanu, A. Chovet, and G. Kamarinos, "Non-Uniform Recombination in Thin Silicon-on-Sapphire Films," Solid-State Electronics, Vol. 21, pp. 1563-1569.

[6] S. Cristoloveanu, A. Mohaghegh, and J. De Pontcharra, "An integrated magnetic sensor: the silicon on sapphire Schottky magnetodiode," Journal De Physique - Lettres, Vol. 41, No. 9, 1980, L-235 - L237.

[7] P.H.L. Rasky, "Silicon-on-Garnet MOSFET's: The Hybridization of Silicon and Magnetic Bubble Technologies," Masters Project Report, Carnegie-Mellon University, December 1984.

[8] R. S. Muller and T. I. Kamins, "Device Electronics for Integrated Circuits," John Wiley & Sons, 1977, p. 362.

[9] S. M. Sze (editor), "VLSI Technology," McGraw - Hill, 1983, pp. 154-156.

[10] B. G. Streetman, "Solid State Electronic Devices," second edition, Prentice-Hall, 1980, pp. 307-308.

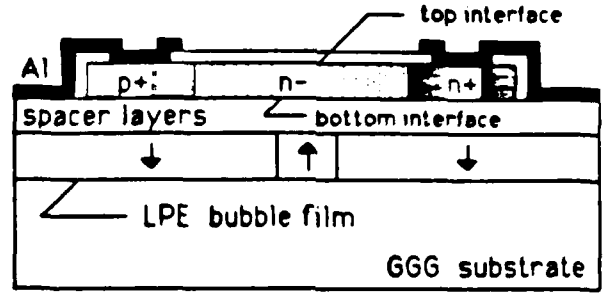

(A)

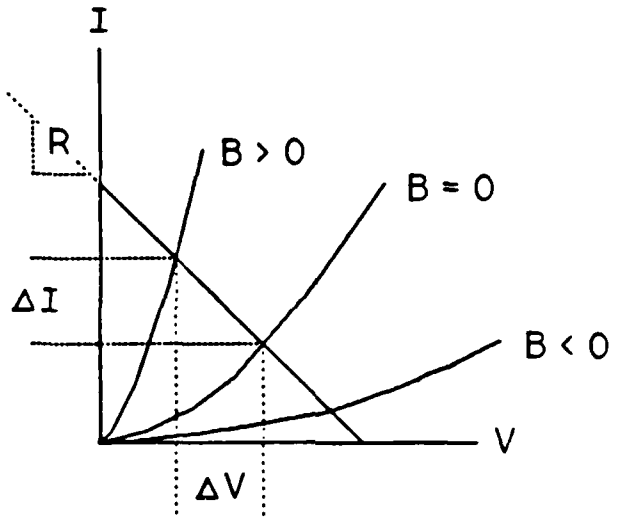

(B)

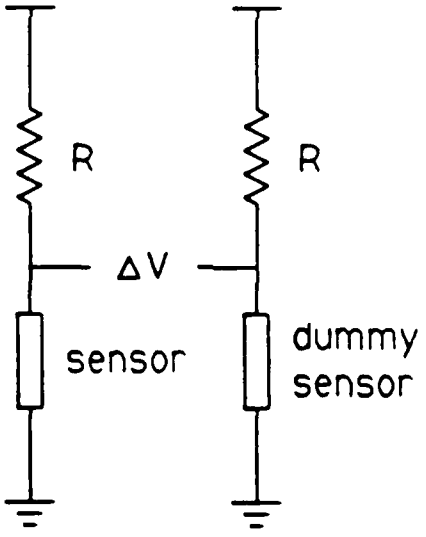

(C)

Figure 1: **(A)** Cross section of a silicon-on-garnet magnetodiode.

(B) Current - voltage characteristics of a magnetodiode. Scales are arbitrary. Load-line for the circuit of fig. 1(C) is also shown.

(C) Differential detection circuit. A change in current ΔI is converted to a change in voltage ΔV.

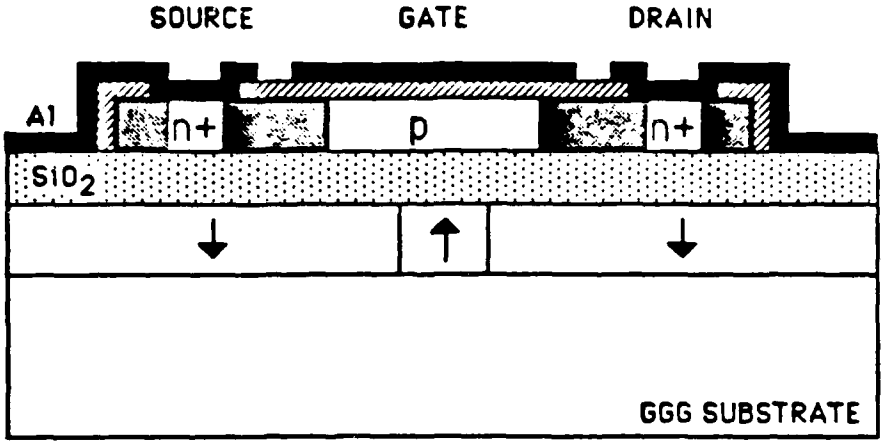

(A)

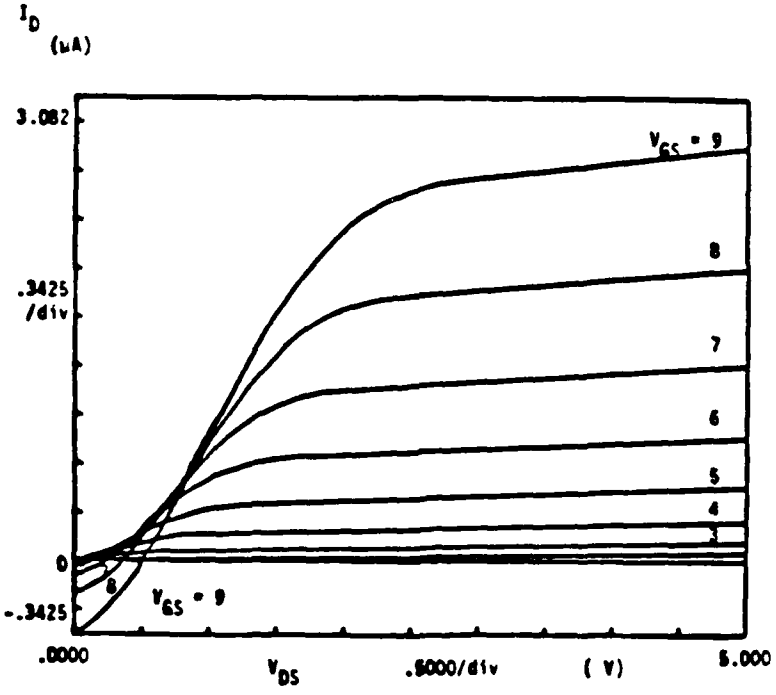

(B)

Figure 2: (A) Cross section of a silicon-on-garnet MOSFET with a sputtered SiO_2 spacer layer. The spacer is $\sim 1\mu m$ thick.

(B) Drain characteristics for a silicon-on-garnet MOSFET with the structure shown in part (A) of this figure. Current is in μA, and voltage is reported in volts. The composition of the bubble film is $(Y_{1.00}Sm_{0.39}Tm_{0.92}Ca_{0.69})\{Ge_{0.70}Fe_{4.30}\}O_{12}$. This MOSFET has a channel length/width ratio of $25\mu m/25\mu m$.

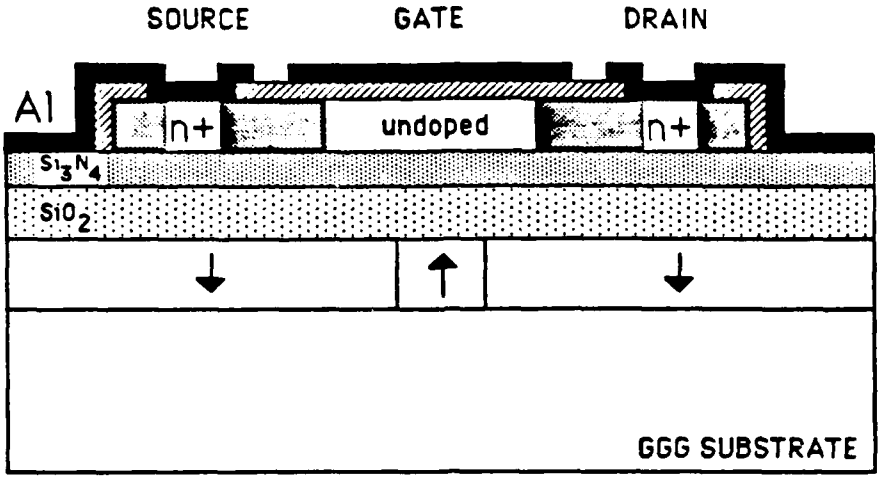

(A)

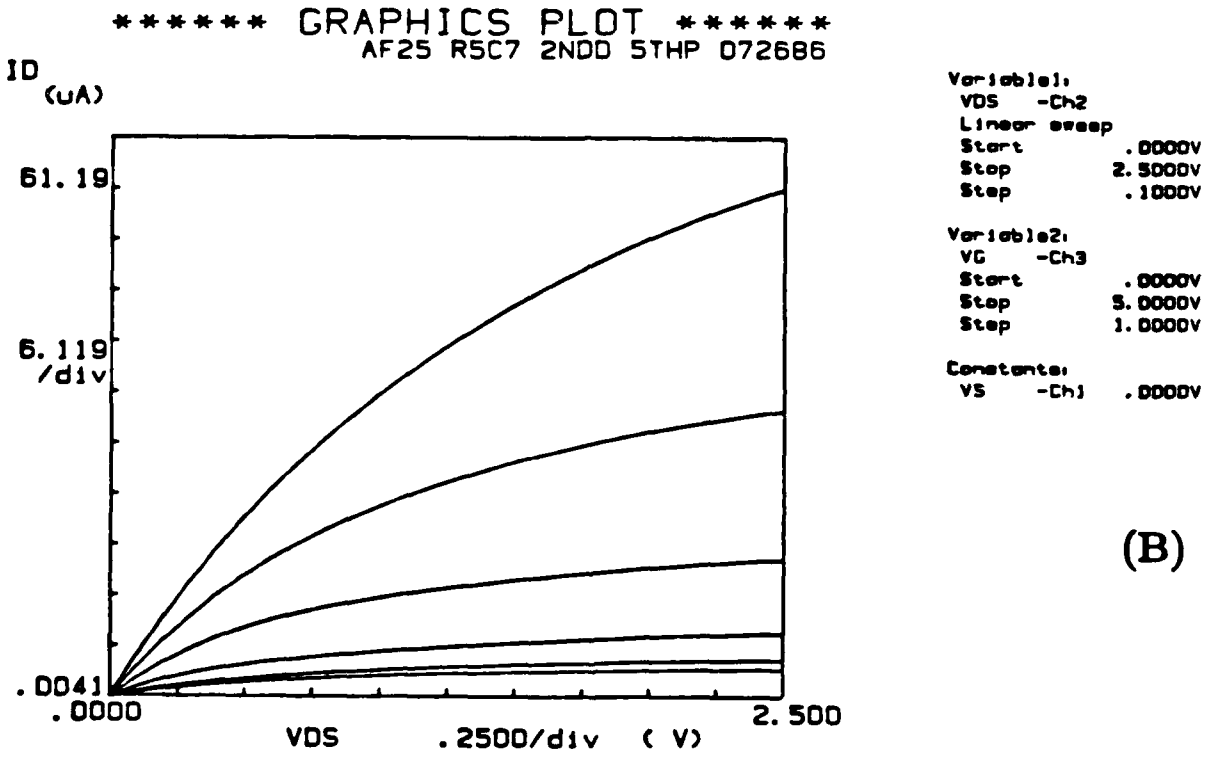

(B)

Figure 3: (A) Cross section of a silicon-on-garnet MOSFET with a double layer spacer.

(B) Drain characteristics for a device with the structure shown in part (A) of this figure; current is in μA, and voltage is in volts. The SiO_2 spacer layer is 0.41 μm thick and the Si_3N_4 film is 0.85 μm thick (devices with 0.24μm of Si_3N_4 have similar drain characteristics). The composition of the magnetic bubble layer is $Sm_xTm_yLu_{3-(x+y)}(Fe_{5-z}Ga_z)O_{12}$. This MOSFET has a channel length/width ratio of 17μm/35μm.

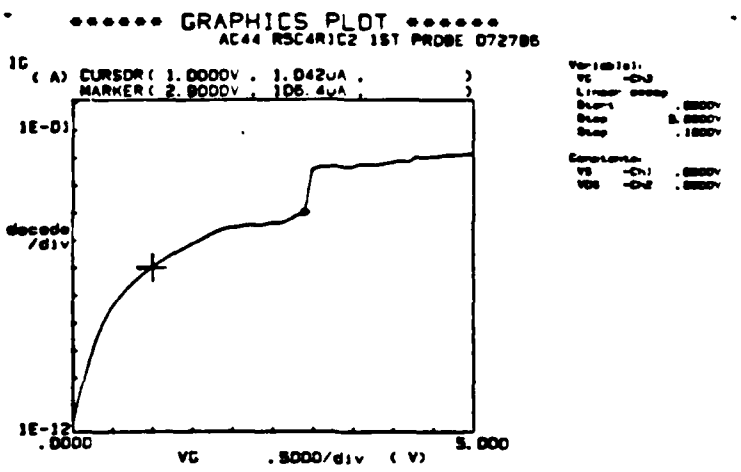

(A)

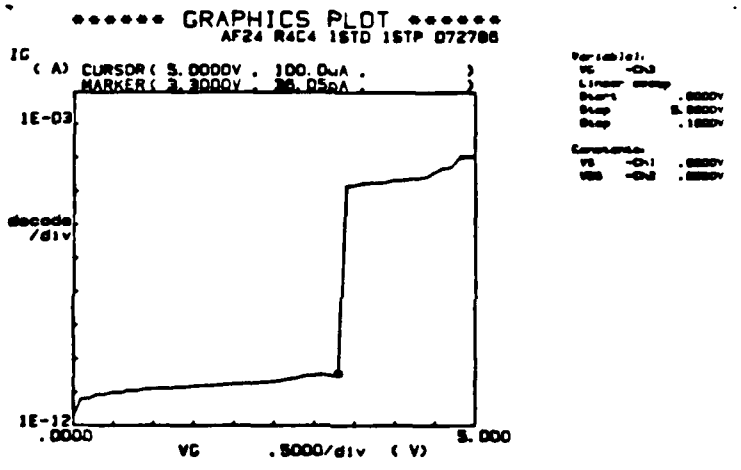

(B)

Figure 4: (A) A plot of the gate leakage current I_G (in amps) vs. the gate voltage V_G (in volts) with the drain and source at ground potential (V_{DS}=0V). The structure of the device is like that of fig. 2(A). In this case, the sputtered SiO_2 layer is ~1μm thick. The composition of the magnetic bubble layer is $(Sm_{1.2}Tm_{0.1}Lu_{1.7})\{Fe_{5-z}Ga_z\}O_{12}$, and the channel length/width ratio of the MOSFET is 12.5μm/25μm.

(B) A plot of the gate leakage current I_G (in amps) vs. the gate voltage V_G (in volts) with the drain and source at ground potential (V_{DS}=0V). The structure of the device is like that of fig. 3(A); the SiO_2 spacer layer is 0.41 μm thick and the Si_3N_4 film is 0.24 μm thick. The composition of the magnetic bubble layer is $Sm_xTm_yLu_{3-(x+y)}(Fe_{5-z}Ga_z)O_{12}$. This MOSFET has a channel length/width ratio of 17μm/35μm.

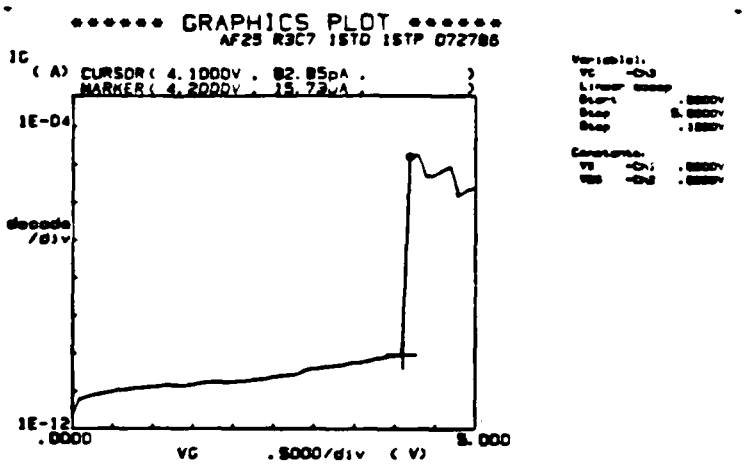

(C)

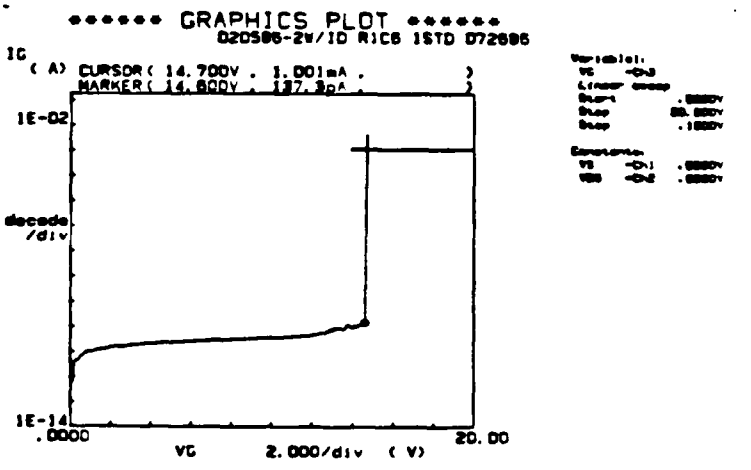

(D)

Figure 4: (C) A plot of the gate leakage current I_G (in amps) vs. the gate voltage V_G (in volts) with the drain and source at ground potential (V_{DS}=0V). Device structure is like that of fig. 3(A). The SiO_2 spacer layer is 0.41 μm thick and the Si_3N_4 film is 0.85 μm thick. The composition of the magnetic bubble layer is $Sm_xTm_yLu_{3-(x+y)}(Fe_{5-z}Ga_z)O_{12}$. This MOSFET has a channel length/width ratio of 17μm/35μm.

(D) A plot of the gate leakage current I_G (in amps) vs. the gate voltage V_G (in volts) with the drain and source at ground potential (V_{DS}=0V). The structure of the device is like that of fig. 3(A) except for the substrate; a silicon substrate was used. The SiO_2 spacer layer is 0.41 μm thick and the Si_3N_4 film is 0.24 μm thick. The channel length/width ratio of the MOSFET is 17μm/35μm.

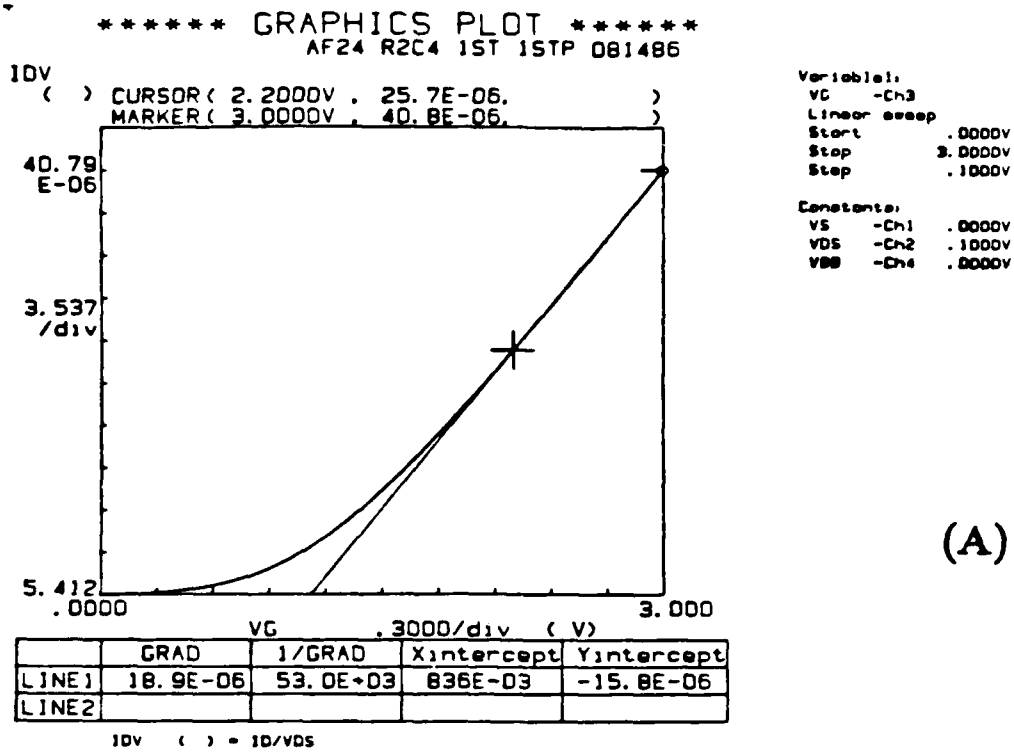

(A)

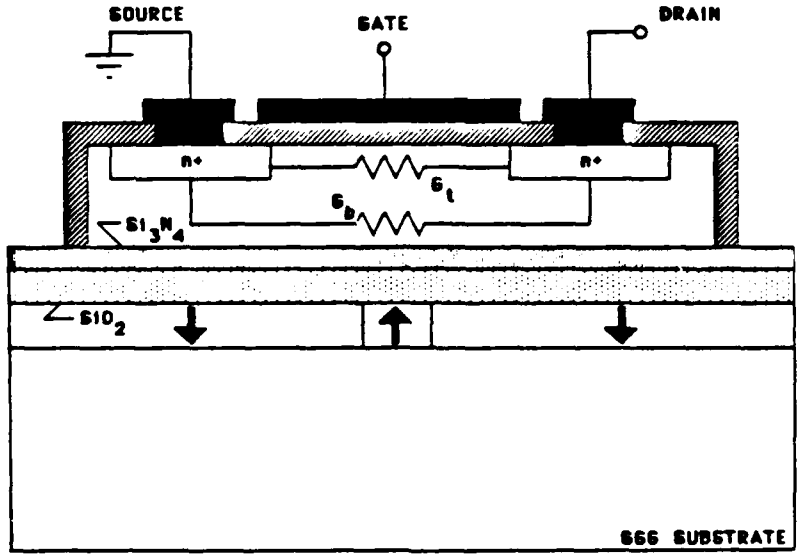

(B)

Figure 5: (A) Zero-bias channel conductance (amps/volt) as a function of gate voltage (volts); a potential of 0.1 V (zero bias for practical purposes) is applied between the source and drain. The SiO_2 spacer layer is 0.41 μm thick and the Si_3N_4 film is 0.24 μm thick. This MOSFET has a length/width ratio of 17μm/35μm. The composition of the magnetic bubble layer is $Sm_xTm_yLu_{3-(x+y)}(Fe_{5-z}Ga_z)O_{12}$. See fig. 3(A) for the relevant cross section.

(B) First order model of a silicon-on-garnet MOSFET with top (intended) and bottom (unintended) conduction channels.

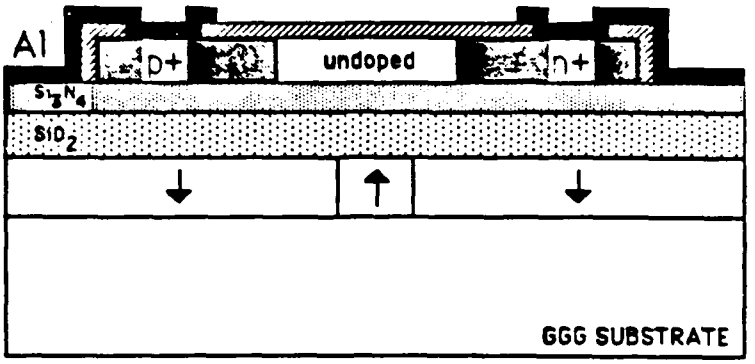

(A)

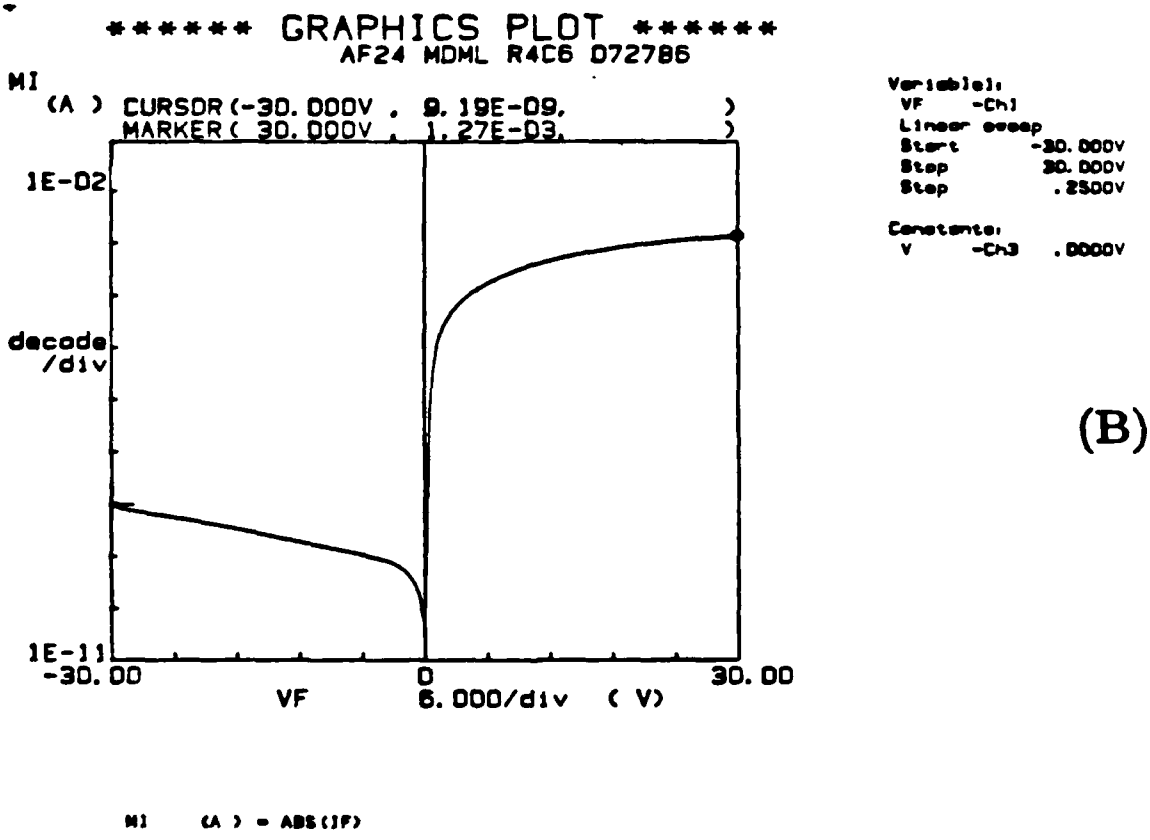

(B)

Figure 6: (A) Silicon-on-garnet magnetodiode cross section.

(B) Current - voltage characteristic for a silicon-on-garnet magnetodiode with the structure shown in part (A) of this figure. Current is in amps, and voltage is reported in volts. The SiO_2 spacer is 0.41μm thick and the Si_3N_4 film is 0.24μm thick. The composition of the magnetic bubble layer is $Sm_xTm_yLu_{3-(x+y)}(Fe_{5-z}Ga_z)O_{12}$. This diode is 22$\mu$m wide.

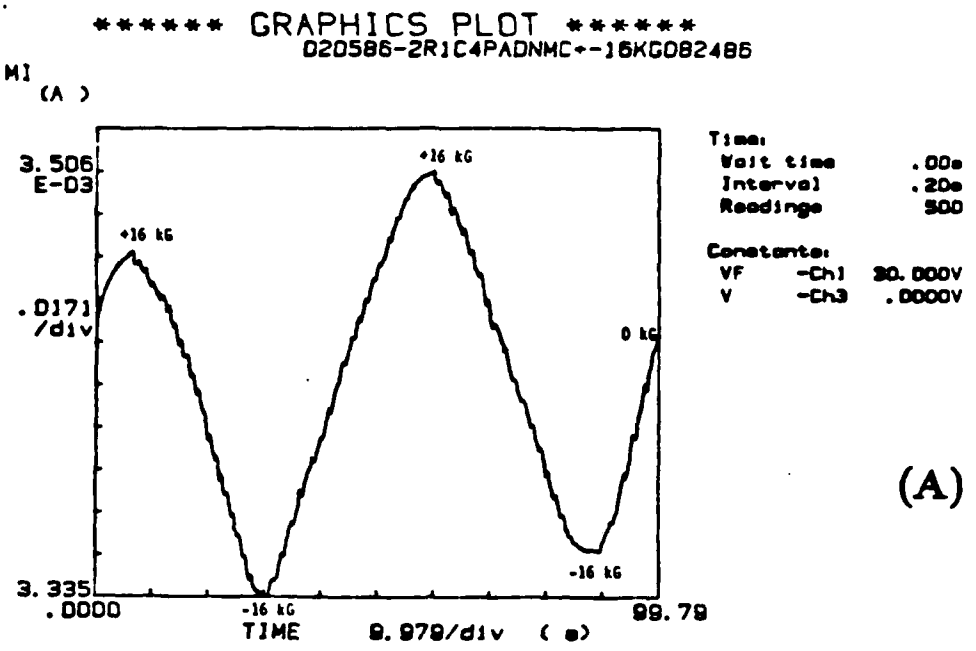

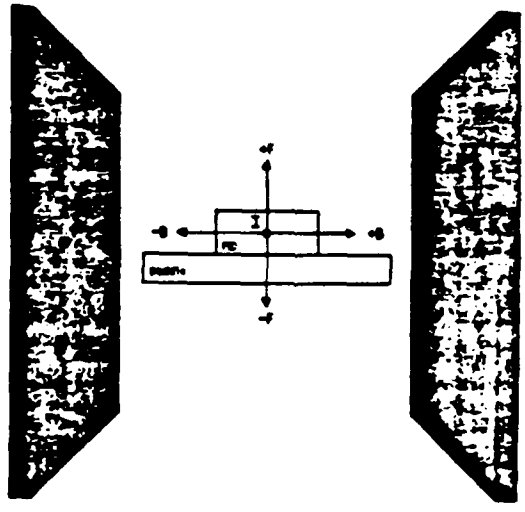

Figure 7: (A) Diode forward current I_D (in amps) with an applied in-plane magnetic field; the field was swept between + and - 16kG. See fig 7(B) for device orientation and sign conventions. The diode is 25 μm wide and was fabricated on a silicon substrate. Otherwise, the structure is identical to that of fig 6(A). The SiO_2 spacer is 0.41μm thick, and the Si_3N_4 spacer is 0.24μm thick.

(B) Orientation of the magnetodiode (MD) during the measurements, the bottom interface is closest to the paddle.

	$4\pi M_s$ (gauss)	l (μm)	K_u (erg/cm^3)	
As Grown	587	0.1209	46,382	23°C
0.41μm LPCVD SiO_2	477	0.1448	——	64 min. 860°C
0.24μm LPCVD Si_3N_4	460	0.1553	——	11 min. 800°C
0.55 μm LPCVD Poly-Si	469	0.1632	41,409	50 min. 625°C
After Laser Anneal	565	0.0871	41,963	350-1412°C
0.1 μm Wet Oxidation	593	0.1796	37,114	50 min. 850°C

Table 1: Room temperature magnetic properties of a 1μm bubble film after key silicon-on-garnet process steps. Processing steps are listed in the order in which they were performed. The composition of the bubble film is $(Sm\ Lu\ Y\ Dy\ Bi)_3(Ga\ Fe)_5O_{12}$.

Design of An Ion-Implanted Bubble Memory Device

K.R. Nitzberg and M.H. Kryder
Department of Electrical and Computer Engineering

ABSTRACT

A four micron period ion-implanted bubble memory device has been designed and fabricated. This device includes new component designs evolved from the results of testing done by John Wullert at the MTC last year[1]. The chip includes a complete major-minor loop propagation path with trapping transfer gates and generator, as well as additional test sites for these functions. The device has been fabricated and preliminary testing of propagation has been completed.

1 Introduction

Improvements in permalloy track bubble memory devices have led to 4-Mbit devices now in production[2]. One limit on the increasing density of permalloy devices is that the bubble diameter must be greater than the minimum linewidth possible with the lithographic process. In contiguous disk devices, a gapless pattern is used as a propagation path and the width of the pattern is approximately five bubble diameters. The principle advantage of contiguous disk devices is the relative coarseness of the lithography required to form them. The features are large compared to the bubble diameter, therefore with the same linewidth much denser devices can be fabricated than with permalloy bar patterns. In addition, ion-implanted circuits operate at a lower drive field than permalloy, so packages can be driven with less power dissipation and decreased temperature rise. Contiguous disks are a natural evolution of the well established permalloy bar devices, retaining such features as the external rotating field access, major-minor loop chip organization, and bubble/no bubble coding scheme, while improving bit densities.

Propagation in ion-implanted devices is achieved by the movement of charged walls around a non-implanted propagation pattern. Charged walls are created when, under the influence of the drive field, the in-plane magnetization of the implanted regions tries to orient around the non-implanted region. The charged walls attract (or repel) bubbles since the bubble provides a flux closure path for the in-plane magnetization above it. As the drive field rotates, the charged walls rotate and carry the bubbles with them. The length of a charged wall depends on the magnetic parameters of the film, the implantation conditions, and the drive field. If the wall is too short, it will not hold the bubble and if it is too long it will interfere with walls from neighboring patterns unless the device density is reduced[3].

Design of ion-implanted propagation patterns is complicated by the cubic crystalline nature of the garnet. Due to variations of the magnetostriction coefficient, certain in-plane directions of the magnetization are more favorable than others. This leads to three preferred bubble positions on an unimplanted disk, as shown in Fig. 1. At low drive fields, the bubble will lead or lag the rotating field in order to stay near these positions.

Four micron period ion-implanted bubble test circuits implemented by Bell Labs[4] were evaluated by John Wullert[1] as part of a masters project in 1986. Wullert's investigation provided insight into failure mechanisms and suggested design improvements. These ideas have been incorporated into a new four micron period device fabricated this year.

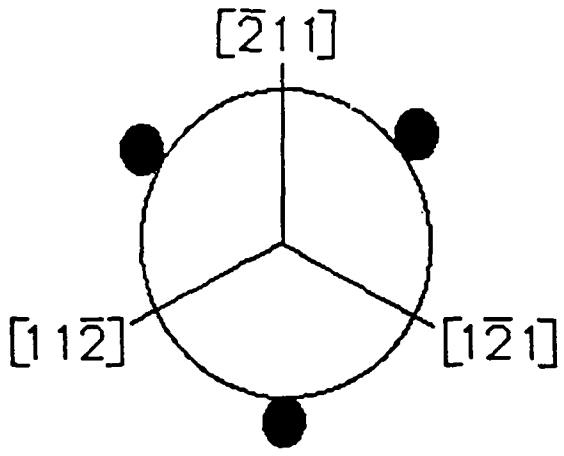

Figure 1: Three Preferred Bubble Positions

2 Experimental Methods

Fabrication

First a thin prespacer of SiO_2 was deposited to protect the bubble film during subsequent processing. Next, the ion implant mask of AZ 4110 resist was deposited and patterned photolithographically. Each wafer was divided into four regions and each region was implanted using different doses (Table 2) to study the effects of ion-implantation conditions on device performance. Double implantation of singly-ionized deuterium molecules (D_2^+) was used. With the implant resist patterns still on the wafers, alignment marks were etched into selected areas by phosphoric acid. The photoresist implantation mask patterns were then removed. Next, an Al layer was deposited to serve as a mirror for the magneto-optical observation of the bubbles. For isolation, a SiO_2 layer was rf sputtered on top of the mirror. Then the conductors were deposited by DC magnetron sputtering. Photoresist was patterned for the conductor layers and baked. The hardbaked photoresist served as a mask as the patterned conductors were etched in a phosphoric acid solution. Additional insulator and conductor layers were deposited for other devices on the wafers. The process is summarized in Table 1.

Test Set-Up

The bubbles are observed with a polarized light microscope. The sample is mounted in a

Processing Parameters

Purpose of Step	Material	Process	Thickness
Bubble Layer Growth			
Spacer	SiO_2	rf Sputter	1000 angstroms
Ion-Implant Mask	AZ 4110 Resist		1 micron
Ion Implantation	Deuterium		
Mirror Layer	AlCu	DC Sputter	250-300 angstroms
Insulator	SiO_2	rf Sputter	1000 angstroms
Conductor Deposition	AlCu	DC Sputter	4500-5000 angstroms
Conductor Patterning	AZ 1470 Resist		

Table 1: Processing Parameters

D^2 Implantation Conditions

Quadrant	Energy	Dose
I	66	1.00×10^{16}
	36	6.70×10^{15}
II	66	1.25×10^{16}
	36	8.30×10^{15}
III	66	1.50×10^{16}
	36	1.00×10^{16}
IV	66	1.75×10^{16}
	36	1.20×10^{16}

Table 2: Implantation Conditions

bias-drive field coil arrangement which is controlled by a computer based test system called Kilotest. Through Kilotest, the magnitude of the drive field as well as the magnitude and phase of the current pulses for the active functions can be controlled. The bias field is adjusted manually. The bias-drive field coil arrangement is placed on the stage of a Leitz polarized-light optical microscope. Light from a mercury arc-lamp is polarized before shining through the objective onto the sample. The sample is viewed in reflection, with another polarizing element in the path set to provide maximum Kerr magneto-optic effect contrast. The resulting image is projected into a camera and fed to a monitor for viewing.

The drive field is referenced as shown in Fig. 2. This definition was chosen so that any time the drive field is not rotating the bubble will stop at a preferred bubble position. This gives the bubbles a much better chance of surviving the lack of the strong charged wall produced by the drive field.

Testing of propagation was done quasi-statically, with a rotating field frequency of one Hertz so that failure modes could be easily observed. Future testing will also be quasi-static, except testing of the transfer gates, which due to heating considerations will be done at twenty five kilohertz.

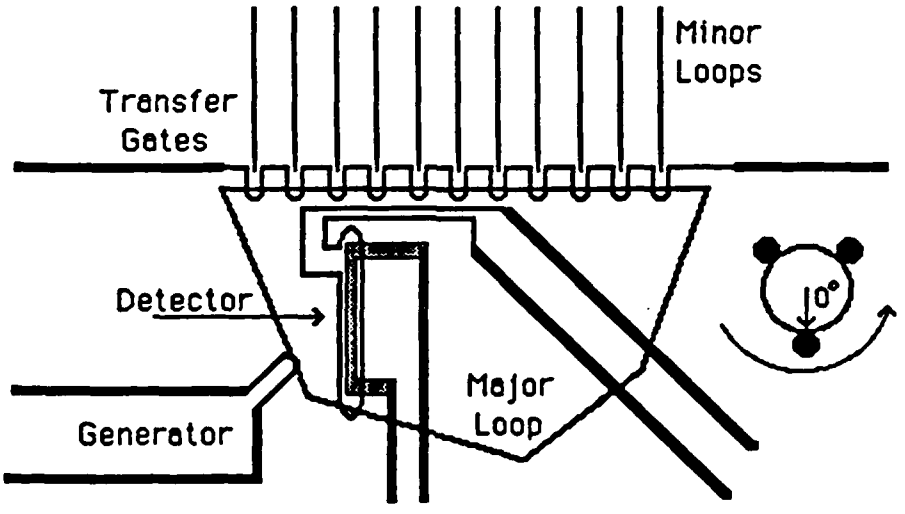

Figure 2: Drive Field Phase Definition[1]

3 Device Design

Propagation Track Design

Early propagation structures[5] consisted of a series of overlapping disks. These gapless patterns allow a 16 fold improvement in bit densities over permalloy asymetric chevron patterns[3]. Many patterns have been investigated, but the name contiguous disk has become generic and continues to be used. A description of different propagation patterns can be found in paper by Nelson et al[6].

The primary minor loop propagation pattern in these circuits is similar to the original contiguous disk patterns, but the peaks are sharper such that the disks resemble diamonds, as shown in Fig. 3. This was done because peak to cusp height was found to be an important parameter[7]. Another critical dimension was determined to be the width of the unimplanted region at the cusp (the narrowest point)[1]. Patterns with varying widths are located around the main chip to determine the relationship between width and bias margin.

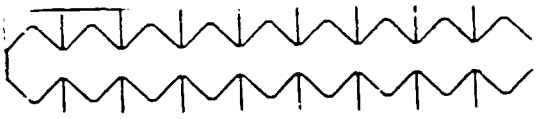

Figure 3: Propagation Patterns

Major Loop Design

The three fold symmetry of the magnetization leads to variations in propagation margins depending on the orientation of the pattern with respect to the crystal[8, 9]. There are three orientations that produce 'super' tracks separated by 120°, three for 'bad' tracks also separated by 120° and six different 'good' track directions separated by 60°. These orientations present some problems when positioning propagation tracks, especially the major loop structure. The major loop can't be a simple rectangular loop, because then at some point the bubbles would be oriented along bad tracks[9]. Given the major-minor loop architecture, if the minor loops are aligned as good tracks, the major loop can then be a combination of good and super tracks

In this design the major loop avoided three problem areas, as described by Wullert. As shown in Fig. 4, the turn away from the horizontal top is a 90 degree turn as bubbles were found to skip cusps in the sharper turns[1]. There are no sides parallel to the minor loops and no backwards turns. By avoiding these designs, the major loop should have wide margins.

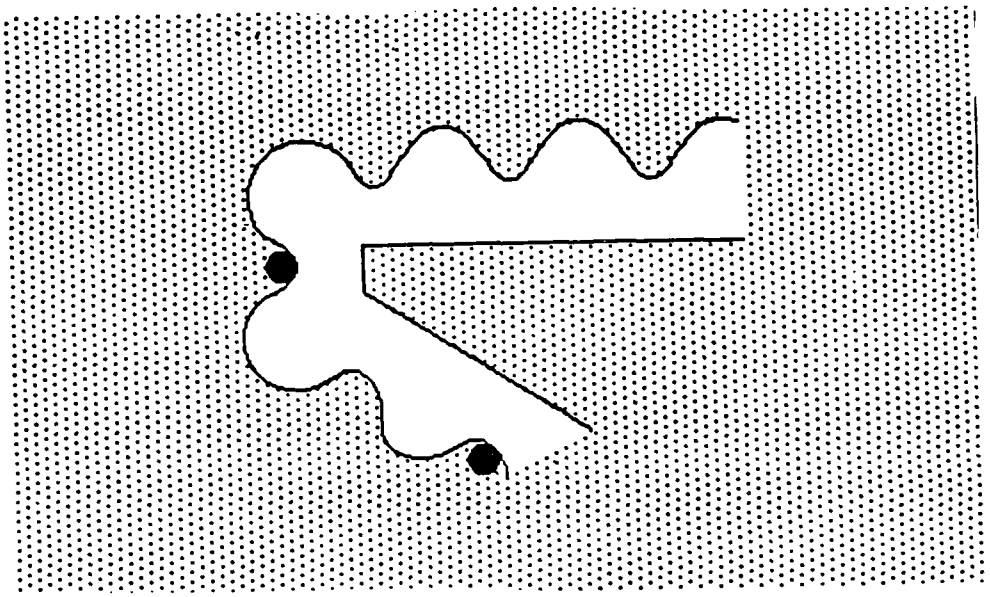

Figure 4: Major Loop Turn[1]

Generator Design

The design of the generator used in ion-implanted devices is not significantly different than those used with permalloy patterns[10]. A bubble is generated when a current pulse is applied through a hairpin turn conductor. The current pulse lowers the local bias field and nucleates a bubble. The generator is usually positioned along a super track since the charged wall there gives the greatest passive assistance to the active current pulse[10]. Three parameters of the conductor design which are varied in these circuits are :

- Distance between the hairpin turn and the cusp the bubble is being generated in
- Position of the first cusp after the generator
- Positions of the conductors away from the turn

Transfer Gates Design

In this design a bidirectional gate using bubble trapping to implement transfer was used. This is the same type of gate tested by Wullert and is shown in Fig. 5. In trapping transfer a current pulse is used to hold the bubble in a conductor turn while the charged wall switches from major loop to minor loop or visa versa, taking the bubble along with it. The distance between the conductor slot and the major loop peaks is varied to determine the optimum position.

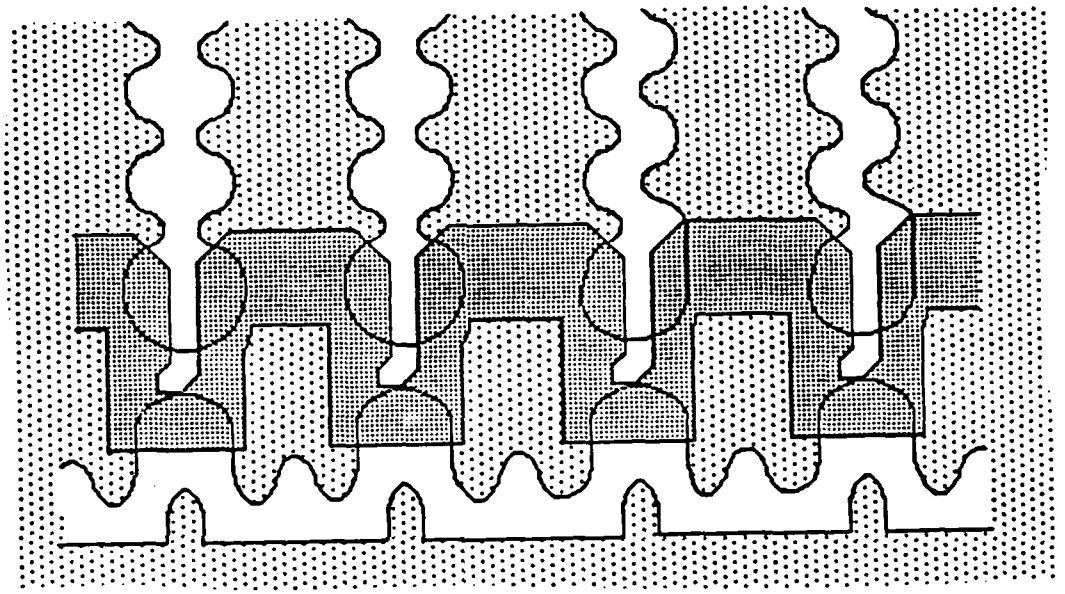

Figure 5: Trapping Transfer Gate[1]

4 Results

Preliminary testing of propagation has been completed on two wafers. Good margins (10%) have been obtained from each wafer. A representative margin from one of the minor loop diamond patterns is shown in Fig. 6. Each wafer also had areas which exhibited spontaneous nucleation at higher drive fields. The relationships between material parameters, implantation conditions, device design and device performance are still under investigation.

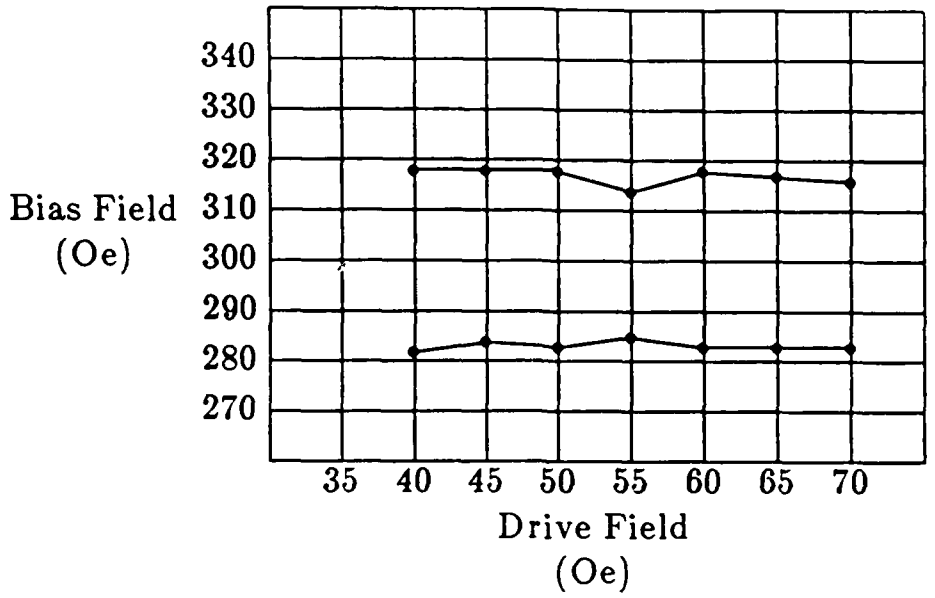

Figure 6: Propagation Margin - Minor Loop

References

1. John R. Wullert II, "Analysis and Design Of Ion-Implanted Contiguous Disk Bubble Memory Devices", Master's thesis, Carnegie Mellon University, 1986.

2. Ryo Suzuki, "Recent Development in Magnetic Bubble Memory", *Proceedings of the IEEE*,Vol. 74November 1986, pp. 1582-1590.

3. Eschenfelder, A. H., *Magnetic Bubble Technology*, Springer-Verlag, Springer Series in Solid State Sciences , 1981.

4. T.J. Nelson, V.J. Fratello, D.J. Muehlner, B.J. Roman and S.E.G. Slusky, "Four Micron Period Ion-Implanted Bubble Test Circuits", *IEEE Transactions on Magnetics*,March 1986, pp. 93-100.

5. Y.S. Lin, G.S. Almasi and G.E. Keefe, "Manipulation of 1μm Bubbles with Coarse (>4μm) Overlay Patterns", *Journal of Applied Physics*,Vol. 48December 1977, pp. 5201-5208.

6. T.J. Nelson and D.J. Muehlner, "Circuit Design and Properties of Patterned Ion-Implanted Layers for Field Access Bubble Devices", AT&T Bell Laboratories Technical Memorandum.

7. Soonchul Jo, *Propagation in Submicron Ion Implanted Magnetic Bubble Computer Memory Devices*, PhD dissertation, Carnegie Mellon University, 1987.

8. Y.S. Lin, G.S. Almasi, D.B. Dove, G.E. Keefe and C.C. Shir, "Orientation Dependence of Propagation Margin of 1μm Bubble Contiguous Disk Devices - Clues and Cures", *Journal of Applied Physics*,Vol. 50March 1979, pp. 2258.

9. R. Wolfe and T.J. Nelson, "Crystal Symmetry Effects in Ion-Implanted Propagation Patterns for Magnetic Bubbles", *IEEE Transactions on Magnetics*,Vol. MAG-15 , 1979, pp. 1323.

10. T.J. Nelson, R. Wolfe, S.L. Blank, P.I. Bonyhard, W.A. Johnson, B.J. Roman, and G.P. Vella-Coleiro, "Design of Bubble Device Elements Employing Ion-Implanted Propagation Patterns", *The Bell System Technical Journal*,Vol. 59February 1980, pp. 229-257.

Propagation in Submicron Ion Implanted Magnetic Bubble Computer Memory Devices

A Thesis
Submitted to the Graduate School
in Partial Fulfillment of the Requirements

for the Degree of

Doctor of Philosophy
in
Electrical and Computer Engineering

by

Soonchul Jo

Carnegie Mellon University
Pittsburgh, Pennsylvania
July, 1987

Table of Contents

1. Introduction 3
1.1. Magnetic Bubble Memory Devices 3
1.1.1. Magnetic Bubbles 3
1.1.2. Permalloy Devices 5
1.1.3. Ion Implanted Devices 5
1.1.4. Current Access Devices 8
1.1.5. Memory Chip Organization 9
1.1.6. Current Controlled Functions 10
1.1.6.1. Generator 10
1.1.6.2. Transfer Gates 11
1.1.6.3. Detector 12
1.2. Objectives of the Research 13
2. Theory of Bubble Domain Propagation 14
2.1. Magnetic Energies in Garnet Films 14
2.1.1. Exchange Energy 14
2.1.2. Demagnetization Energy 15
2.1.3. Perpendicular Anisotropy 16
2.1.4. Magnetocrystalline Anisotropy 17
2.1.5. Magnetostrictive Energy 18
2.1.6. Magnetic Field Energy 19
2.2. Bubble Domains 19
2.2.1. Domain Wall 19
2.2.2. Stability 20
2.2.3. Bubble Size 24
2.2.4. Bias Field Margin 27
2.2.5. Collapse Field Variation with Temperature[20] 29
2.3. Motion of a Bubble Domain 29
2.4. Ion Implantation and Annealing 31
2.4.1. Mechanisms of Ion Implantation 31
2.4.2. Determination of Ion-Implantation Conditions 32
2.4.2.1. Ion Species 33
2.4.2.2. Implantation Energy 34
2.4.2.3. Dosage 34
2.4.2.4. Multiple Implantation 36
2.4.3. Annealing 39
2.5. Charged Wall Formation 40
2.5.1. Stresses at the Pattern Boundary 40
2.5.2. Magnetostrictive Anisotropies at the Pattern Boundary 42
2.5.3. Charged Wall Formation 45
2.6. Charged Wall (Bubble) Circulation Around an Unimplanted Disk 48

2.6.1. Determination of Magnetization Directions and Critical Curves 48
2.6.2. Critical Curve for Crystalline Anisotropy 51
2.6.3. Critical Curve for Uniaxial Magnetostrictive Anisotropy 52
2.6.4. Critical Curve for Mixed Anisotropies 54
2.6.5. Critical Curve for Charged Wall 57
2.6.6. Minimum Circulation Field 58
2.6.7. Anisotropic Charged Wall Behavior Around a Disk 59
2.6.8. Isotropic Propagation 62
2.7. Bubble Propagation Bias Margin 66
2.7.1. Minimum In-Plane Drive Field 66
2.7.2. Bubble Collapse Fields 67
3. Experimental Methods 69
3.1. Design and Fabrication of Devices 69
3.1.1. Magnetic Garnet Films 69
3.1.1.1. Garnet Film Design 69
3.1.1.2. Characterization[45] 71
3.1.2. Device Layout and E-Beam Mask 80
3.1.2.1. Computer-Aided Design of Device Layout 80
3.1.2.2. Fabrication of E-Beam Mask 82
3.1.3. Device Processing 82
3.1.3.1. Wafer Cleaning 85
3.1.3.2. Wafer-Thinning and Back Film Removal 86
3.1.3.3. Deposition of Spacer and Electroplating Base 86
3.1.3.4. Photolithography 87
3.1.3.5. Electroplating of Ion-Implantation Mask 87
3.1.3.6. Ion Implantation 92
3.1.3.7. Reflecting Layer 92
3.2. Device Testing 93
3.2.1. Testing Set-Up 93
3.2.2. Bubble Domain and Charged Wall Observation 95
3.2.2.1. Magneto-Optic Method 95
3.2.2.2. Bitter Pattern Method[33] 97
3.2.3. Device Performance Measurements 99
3.2.3.1. Propagation Bias Margins 99
3.2.3.2. Bubble Position vs. In-Plane Field Direction 100
3.2.3.3. Tolerance to Ambient Temperature Variation 100
4. Experimental Results 101
4.1. Typical Bias Margins 101
4.2. Propagation Failure Modes 101
4.2.1. Skidding 103
4.2.2. Stripeout 103
4.2.2.1. Stripeout Across Adjacent Tracks 104
4.2.2.2. Stripeout Along the Track 106
4.2.3. Skip 107
4.2.4. Trap at Cusp (Hang Up) 108
4.3. Ion Implantation and Annealing of Devices 108
4.3.1. Ion Implantation 108
4.3.2. Annealing 114
4.4. Variation of Propagation Track Shape and Size 115
4.4.1. Variation of Propagation Track Shape 115

4.4.1.1. Isolated Elements 115
4.4.1.2. Propagation Tracks 118
4.4.2. Variation of Propagation Track Size 118
4.4.2.1. Isolated Disks 118
4.4.2.2. Propagation Tracks 118
4.5. Variation of Magnetostriction Coefficients - Nearly Isotropic Propagation 121
4.5.1. Comparison of Conventional and Nearly Isotropic Films 121
4.5.1.1. Propagation Bias Margins 123
4.5.1.2. Bubble Position vs. In-Plane Field Direction 125
4.5.1.3. Bubble Collapse Fields Along Propagation Tracks 128
4.5.2. Variation of Magnetostriction Coefficients - Nearly Isotropic Films 128
4.6. Variation of Ambient Temperature 134
5. Discussion **140**
5.1. Typical Bias Margins 140
5.2. Propagation Failure Modes 141
5.3. Ion Implantation and Annealing of Devices 144
5.3.1. Ion Implantation 144
5.3.2. Annealing 146
5.4. Variation of Propagation Track Shape and Size 146
5.4.1. Variation of Propagation Track Shape 146
5.4.1.1. Isolated Elements 146
5.4.1.2. Propagation Tracks 148
5.4.2. Variation of Propagation Track Size 150
5.4.2.1. Isolated Disks 150
5.4.2.2. Propagation Tracks 152
5.5 Variation of Magnetostriction Coefficients - Nearly Isotropic Propagation 152
5.5.1 Comparison of Conventional and Nearly Isotropic Films 152
5.5.1.1 Propagation Bias Margins 153
5.5.1.2 Bitter Pattern Observation 153
5.5.1.3 Bubble Position vs. In-Plane Field Direction 153
5.5.1.4 Bubble Collapse Fields Along Propagation Tracks 153
5.5.2 Variation of Magnetostriction Coefficients - Nearly Isotropic Films 156
5.6 Variation of Ambient Temperature 156
6. Conclusions **158**
6.1 Summary of Contributions 158
6.2 Suggestions for Future Research 160
Appendix A. Ion Implantation Range Statistics for Deuterium **161**
Appendix B. Garnet Film Characteristics **164**
Appendix C. Ion Implantation Conditions **168**

AD-A190 169 HIGH DENSITY ION IMPLANTED CONTIGUOUS DISK BUBBLE TECHNOLOGY(U) CARNEGIE-MELLON UNIV PITTSBURGH PA DEPT OF ELECTRICAL AND COM... M H KRYDER ET AL. 31 OCT 87 2/3

UNCLASSIFIED AFOSR-TR-87-2044 AFOSR-84-0341 F/G 9/1 NL

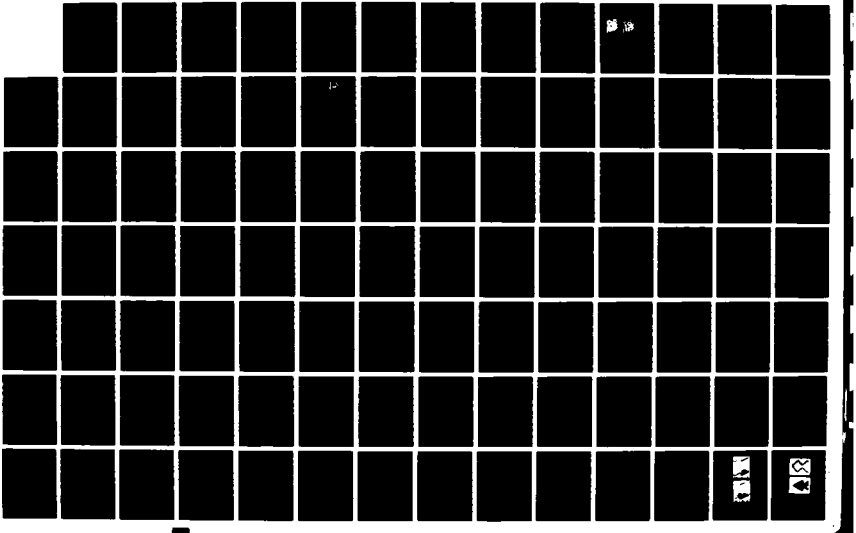

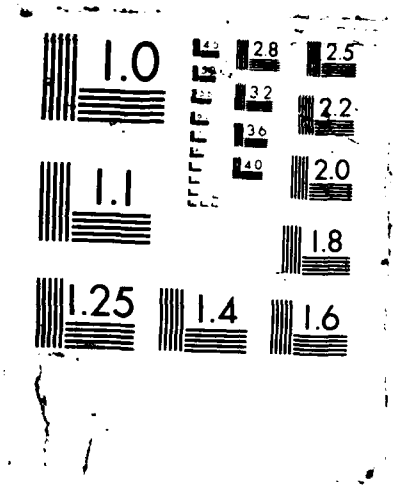
1.0
1.1
1.25
1.4
1.6
1.8
2.0
2.2
2.5
2.8
3.2
3.6
4.0

List of Figures

Figure 1-1:	Creation of magnetic bubbles	4
Figure 1-2:	Bubble propagation along permalloy tracks	5
Figure 1-3:	Bubble propagation along ion implanted tracks	6
Figure 1-4:	Comparison of cell sizes of permalloy and ion implanted devices	7
Figure 1-5:	(a) Dual-conductor propagation patterns, (b) disturbance of current by a hole in the current sheet and vertical magnetic field thus created, and (c) current waveforms	9
Figure 1-6:	Schematic diagram of ion implanted bubble memory chip	10
Figure 1-7:	Bubble generator	11
Figure 1-8:	Bubble transfer gates	12
Figure 1-9:	Bubble detector	13
Figure 2-1:	Demagnetizing field due to magnetization	15
Figure 2-2:	Cylindrical cordinate system	18
Figure 2-3:	Magnetic bubble cross section	19
Figure 2-4:	Domain configuration	20
Figure 2-5:	Graphical determination of d vs. H_b	24
Figure 2-6:	Extremes of bubble size vs. h/l	25
Figure 2-7:	d_{so}/d_{co} and $2W_s/(d_{so} + d_{co})$ vs. h/l	26
Figure 2-8:	Variation in bubble size, d vs. bias field, H_b for film thickness, h/l	27
Figure 2-9:	H_b margins vs. h/l	28
Figure 2-10:	Requirement for a field gradient	30
Figure 2-11:	The effects of ion implantation on a magnetic garnet crystal. The damage expands the lattice, resulting in lateral compression.	31
Figure 2-12:	ΔH_k vs. damage level after annealing at 350 ° C for 30 minutes[23]	33
Figure 2-13:	Anisotropy field change (ΔH_k) vs. dose[24]	36
Figure 2-14:	Implant-induced change in uniaxial anisotropy field ΔH_k and magnetostrictive field ΔH_σ vs. implant strain ϵ_{max} for film 84[21]	37
Figure 2-15:	Maximum implant strain vs. dose for 40 KeV and 88 KeV deuterium implantation[21]	38
Figure 2-16:	Double-implanted He^+ concentration profile on samples with SiO_2 (4000 A) on Cr (500 A) on garnet[26]	38
Figure 2-17:	Lattice distortion at boundary between implanted region ($x>0$) and unimplanted region ($x<0$)	40
Figure 2-18:	Stress and strain at edge of implantation region	41
Figure 2-19:	Coordinate system	43
Figure 2-20:	Qualitative representation of magnetostrictive anisotropies induced by stresses around a nonimplanted disk. Easy magnetization directions of uniaxial anisotropies are illustrated by double-ended arrows. Easy	44

directions of unidirectional anisotropies are shown by single-ended arrows (axial symmetry is broken by the presence of bubble biasing field perpendicular to film).

Figure 2-21: Perspective view of an ion implanted device 45

Figure 2-22: (a) The formation of charged walls under the influence of a uniaxial anisotropy with the preferred axis parallel to the implantation edge. (b) Contrasted with the essentially stray-free free-flow pattern possible without that anisotropy. 46

Figure 2-23: Wall in high anisotropy region becomes charged as it reduces its length 47

Figure 2-24: Three-fold critical curve for crystalline anisotropy 52

Figure 2-25: Uniaxial astroid of boundary anisotropy, H_{kb} 53

Figure 2-26: Propagation of charged wall around an unimplanted disk 54

Figure 2-27: Critical curve for mixed anisotropy 56

Figure 2-28: Critical curve for charged wall 58

Figure 2-29: Interpretation of domain patterns 60

Figure 2-30: Orientation of charged wall ϕ_{cw} vs. that of H_{xy}, ϕ_H for H_{xy}/H_{k1}=1/3 62

Figure 2-31: Average quasistatic operating margins for propagating 1 μm bubbles based on large amount of experimental data. Bias margin is normalized to 4πM (600 G). The in-plane field is normalized to an effective crystalline field H_{k1}[11] 63

Figure 2-32: Permalloy and ion implanted hybrid devices 64

Figure 2-33: Bubble potential well as a function of in-plane field direction 68

Figure 3-1: The required Q as function of bubble diameter for ion implanted contiguous disk devices[44] 70

Figure 3-2: The required $4\pi M_s$ as function of bubble diameter for ion implanted contiguous disk devices[44] 70

Figure 3-3: Typical film's optical interference trace 72

Figure 3-4: Plot of l/h versus P_o/h 73

Figure 3-5: FMR apparatus and minibox 74

Figure 3-6: Typical resonance curves for stressed and unstressed film[21] 76

Figure 3-7: Resonance spectra for an implanted film[21] 77

Figure 3-8: X-ray configuration to measure mismatch 78

Figure 3-9: X-ray diffraction rocking curve 79

Figure 3-10: Bubble propagation patterns (a) snake (b) diamond (c) circle (d) triangle 80

Figure 3-11: CAD flow chart 81

Figure 3-12: Computer printout of propagation patterns 83

Figure 3-13: Ion implanted propagation pattern processing steps 85

Figure 3-14: A schematic diagram of gold electroplating apparatus 88

Figure 3-15: Scanning electron micrographs of gold ion implantation masks for 0.5 μm bubbles (Period: 2 μm) 90

Figure 3-16: Scanning electron micrographs of gold ion implantation masks: (a) contiguous diamond shaped devices for 1 μm bubbles (period: 5 μm) (b) contiguous triangular shaped devices for 2 μm bubbles (period: 4 μm) 91

Figure 3-17: Testing set-up 94

Figure 3-18: Kilotest system 96

Figure 3-19: Fine magnetic particles attracted to stray flux emanating from magnetic poles 98

Figure 3-20: Bitter pattern of domain around nonimplanted disk[33] 98

Figure 4-1: Bias field margins for diamond shaped element, isolated track and close-packed tracks : Track period : 2.5 μm, wafer CA 72, Chip 12, Region 4, 4πM = 910 G 102

Figure 4-2:	Skidding failure mode	103
Figure 4-3:	Bubble stripeout across adjacent tracks: Bubble moving up [(a)-(b)-(c)] or moving down [(d)-(e)-(f)] can occur	104
Figure 4-4:	Bubble stripeout between bad and super tracks	105
Figure 4-5:	Stripeout along the track	106
Figure 4-6:	First cusp skip	107
Figure 4-7:	Anisotropy change versus implantation dose	110
Figure 4-8:	Maximum lattice strain vs. dose	111
Figure 4-9:	(a) Bias margin width vs. dose and (b) minimum drive field vs. dose for "good" track : 2.5 μm period diamond tracks, 32 KeV implant	112
Figure 4-10:	(a) Bias margin width vs. dose and (b) minimum drive field vs. dose for "bad track" : 2.5 μm period diamond tracks, 32 KeV implant	113
Figure 4-11:		114
Figure 4-12:	(a) Bias margin width vs. annealing temperature and (b) minimum drive vs. annealing temperature : AK 92, 2.5 μm period good diamond tracks, 32 KeV implant	116
Figure 4-13:	Bias margins of circle, diamond, triangle and reverse triangle : CA 72, Region 4, 2 μm size	117
Figure 4-14:	Bias margins of various shaped propagation tracks : CA 72, Region 4, 2.5 μm period	119
Figure 4-15:	Margins for 2 μm period snake patterns with (a) cusp to period ratio of 0.44 (b) cusp to period ratio of 0.38 film CA72	120
Figure 4-16:	Bias margins of various sized unimplanted disks : CA 71, Region 4	121
Figure 4-17:	Bias margins of 1.75 μm and 2.5 μm period snake patterns : CA 71, Region 4	122
Figure 4-18:	Bias margins of two 2 μm period snake patterns: one with 0.75 μm unimplanted region width, the other 1 μm width : CA 73, Region 4	123
Figure 4-19:	(a) Bias margins for conventional film S74 (: 5 μm period diamond tracks , Region 2) and (b) bias margins for nearly isotropic film AH 27 (: 4 μm period diamond tracks)	124
Figure 4-20:	Bias margins for nearly isotropic film CA 72 : 2.5 μm period tracks	125
Figure 4-21:	(a) Bubble position vs. in-plane field direction for conventional films S 74and (b) bubble position vs. in-plane field direction for nearly isotropic film AH 27	126
Figure 4-22:	(a) Potential wells of good, bad and super tracks in a conventional film (: Wafer S 74 5 μm period diamond tracks, region 4, H_{xy} = 60 Oe, $4\pi M$ = 600 G) and (b) in a nearly isotropic film (: Wafer CA 72, 2.5 μm Period diamond tracks, Region 4, H_{xy} = 60 Oe, $4\pi M$ = 910 Oe)	129
Figure 4-23:	Minimum drive fields for unimplanted disks	130
Figure 4-24:	(a) Bubble position vs. in-plane field direction for wafer AKb1, (b) for wafer AKa8 and (c) for wafer AK 92 : 4 μm disk, H_{xy} = 40 Oe	131
Figure 4-25:	(a) Bias margins of 2.5 μm period diamond tracks from wafer AKb1, (b) from wafer AKa8 and (c) from wafer AK92 : region 4	135
Figure 4-26:	Temperature dependence of minimum drive field for (a) diamond and (b) circular patterns : CA 72, 2.5 μm Period	138
Figure 4-27:	Temperature dependence of bias margins at 60 Oe of drive field for (a) diamond and (b) circular patterns : CA 72, 2.5 μm	139
Figure 5-1:	Bubbles encountering repulsive charged walls in cusps in (a) a good track and in (b) a bad and super track	142
Figure 5-2:	Failure modes of triangular patterns	147
Figure 5-3:	Charged wall directions when the bubbles come out of the cusps	149

Figure 5-4: (a) Collapse field at 60 Oe drive field and (b) minimum drive fields of the various sized unimplanted disks 151

Figure 5-5: Magnetization directions and charged wall polarities in the cusps: (a) H_{zy} = 0, (b) conventional film (c) nearly isotropic film 154

List of Tables

Table 3-1:	Ion Implanted Propagation Pattern Processing Steps	84
Table 4-1:	Ion Implantation Conditions	109
Table 4-2:	Garnet Film Characteristics (CA71)	109
Table 4-3:	Magnetostriction Coefficients	122
Table 4-4:	Magnetostriction Coefficients	128
Table 5-1:	The Effects of Various Cusps and Close Packing of Propagation Tracks on Minimum Drive Fields (CA72)	149

Abstract

Submicron magnetic bubble propagation in ion implanted magnetic bubble computer memory devices is presented. The propagation structures are fabricated on magnetic garnet films of composition $\{DySmLuYBi\}_3[FeGa]_5O_{12}$ with nominal bubble diameter of 0.5 μm. To increase the perpendicular anisotropy necessary for smaller bubbles and the Faraday magneto-optic effect to enhance the bubble visibility, Bi is incorporated in the film. The devices are fabricated using mid-U.V. E-beam mask exposure and gold electroplating, realizing minimum lithographic feature of 0.5 μm. Device testing is performed with a polarizing microscope utilizing the Faraday magneto-optic effect and sets of electromagnets to supply magnetic fields which stabilize and propagate the bubbles. The magnification of the microscope is 3,500 for easy observation of the submicron bubbles and the magnets are controlled by a personal computer.

Double deuterium ion implantation with implantation depth of 230 nm and implantation dose of $7.5x10^{15}/cm^2$ gave good propagation margins for most of the 2.5 μm period devices employing 0.5 μm diameter bubbles. Annealing of these devices showed good bubble propagation until 200 °C anneal. The study of bubble propagation failure modes clarified a number of failure modes such as bubble collapse at cusps, bubble skidding along the track, bubble stripeout across and along the tracks and bubble position skip at the end of the tracks. Various propagation track shapes and sizes were compared for their performances. Overall, the diamond shaped tracks showed the best performance with the typical margin width of 15 % of the mid bias value and minimum drive field of 35 Oe for 2.5 μm period devices using 0.5 μm bubbles. The snake patterns exhibited the best bias margins with 15 % of margin width and 25 Oe of minimum drive field when only "good" tracks were considered. A very good margin of 13 % margin width and 35 Oe minimum drive field was obtained for 1.75 μm period snake patterns using 0.5 μm diameter bubbles. Nearly isotropic propagation was achieved for most of the 2.5 μm period propagation tracks tested using garnet films with nearly isotropic magnetostriction. The degree of isotropy Δ $[(\lambda_{111} - \lambda_{100})/\lambda_{111}]$ was varied from 0.5 to 0.1, which showed nearly isotropic propagation for all Δ values tested. Garnet films with Δ values lower than 0.3 exhit almost identical margin widths for good and bad tracks. Since Δ is reduced by adding Dy to the film and Dy increases the damping of the film, it may not be desirable to reduce Δ lower than 0.3. Temperature dependence of bias margins were studied from 0 ° C to 130 ° C. Good overlapping margins (at least 13 %) of good and bad tracks were obtained throughout the temperature range.

Acknowledgements

The author would like to thank his advisor, Mark H. Kryder for guidance and support for this research. Garnet films were grown by C. Krafft, R. Campbell, R. Mahadevan and S. Santhanam. Ion implantation was performed by J. Tabacchi with the guidance of A. Guzman. R. Tiberio, D. Costello and S. Burgess of the National Submicron Facility at Cornell University provided assistance in E-beam mask generation. The author appreciates helpful discussions with D. Saunders , M. Alex and J. Wu. C. Bowman and F. Bruno provided technical support. This research was supported by the Air Force Office of Scientific Research under grant 84-0341, the National Science Foundation under grant ECS-8307261, and the National Reaearch and Resource Facility for Submicron Structures under NSF grant ECS-8200312.

The author would also like to thank his family : father Kyuchan Jo and late mother Jaok Kim for their encouragement, and wife Meewon Lee, son Michael and daughter Stephanie for their endurance of hardships during the course of this research.

Chapter 1
Introduction

1.1. Magnetic Bubble Memory Devices

Magnetic bubble memory devices are non-volatile magnetic digital information storage units which do not employ mechanical parts such as electric motors that are used in other magnetic information storage devices such as magnetic disks or tapes. They are non-volatile in the sense that the stored information is not lost in the event of power failure unlike most semiconductor memory devices. The data are encoded as the presence or absence of magnetic bubbles which are cylindrical magnetic domains in thin epitaxial magnetic garnet films grown on non magnetic substrates. Bubbles are generated according to the write information and propagated to the storage area. Then they remain there until they are read out by a detector. Depending on how the bubbles are manipulated, there are several different kinds of bubble devices. Currently commercially available permalloy devices[1, 2, 3, 4, 5] use an in-plane rotating magnetic field to move bubbles along tracks defined by permalloy patterns. Ion implanted devices (which are also called contiguous disk devices)[6, 7] use the same rotating field, but different bubble propagation tracks, which are defined by ion implantation. Current access devices[8, 9] use electric currents instead of rotating magnetic fields to move bubbles around. Bubbles propagate along rectangular holes in two thin metal sheets which are insulated and stacked up one after another.

In the following sections, we will examine what bubbles are, how they are manipulated in different bubble memory devices, how the memory chips are organized and what functions besides propagation are required to implement the chip organization.

1.1.1. Magnetic Bubbles

Presently used magnetic bubbles are created in thin magnetic garnet ($RE_3\ Fe_5O_{12}$ where RE stands for rare earth elements) films epitaxially grown on non magnetic garnet substrates by liquid phase epitaxy crystal growing technique. Various rare earth elements and Bi are usually used to provide adequate perpendicular (to film surface) magnetic anisotropy which is essential to

create bubbles in the films. Some diluents are also used to reduce the magnetization of Fe so that the diameters of the bubbles can be adjusted.

The garnet films have perpendicularly oriented magnetic domains as shown in Fig.1-1 (a).

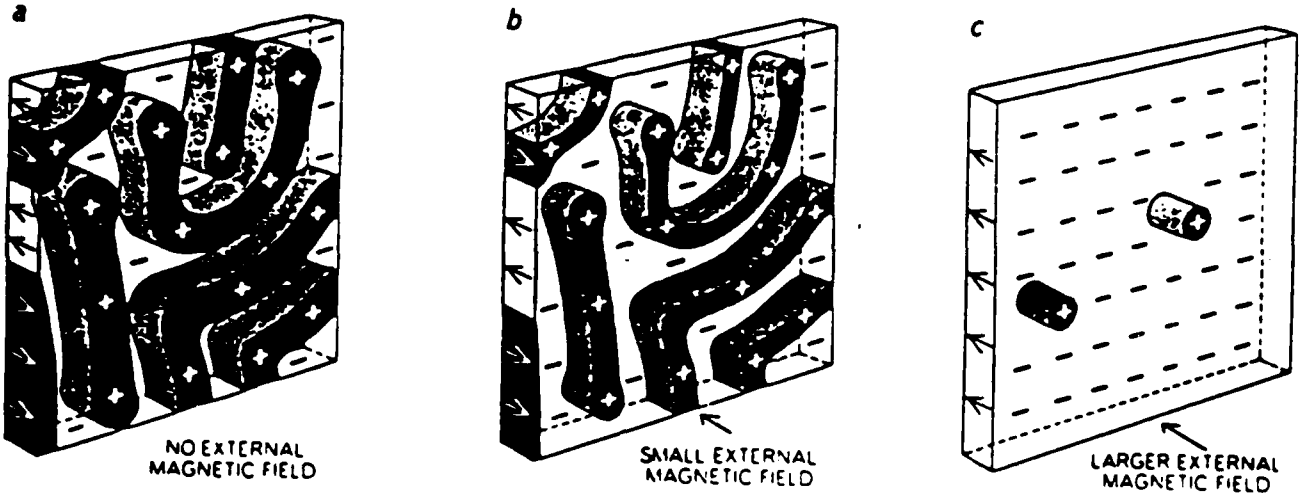

Figure 1-1: Creation of magnetic bubbles

The area of upward domains is the same as the downward domains as long as there is no external magnetic field. As soon as an external magnetic field is applied, the domains which have the same magnetization direction as the applied field grow at the expense of the others (Fig. 1-1 (b)). If the magnitude of the field is increased, the reversed (denoted as + in the figure) serpentine domains continue to shrink and at a certain critical field become cylindrical domains as shown in Fig. 1-1 (c). These domains are called magnetic bubbles because they looked like bubbles to initial researchers when viewed from the top with a microscope. If the external field is further increased, the bubble size becomes smaller and eventually the bubbles collapse, leaving the entire film magnetized in the direction of the external field. Therefore, bubbles exist in certain range of the external perpendicular magnetic field, which is called the bias field.

1.1.2. Permalloy Devices

Bubbles are moved in a bias field gradient. In permalloy devices, the field gradient is created by a permalloy structure overlay fabricated on top of the garnet film as shown in Fig. 1-2.

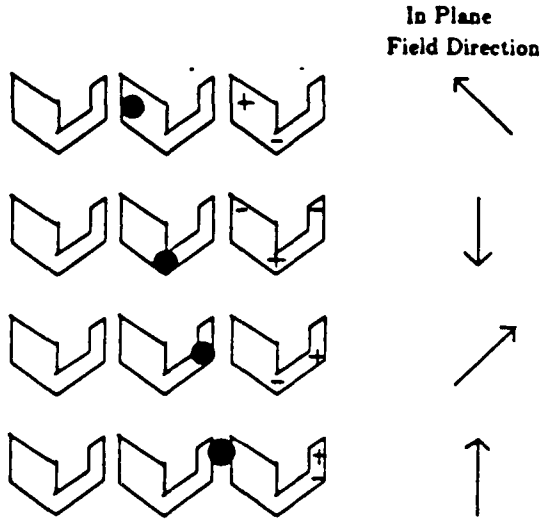

Figure 1-2: Bubble propagation along permalloy tracks

Permalloy is a Ni-Fe alloy which is easily magnetized upon application of a magnetic field. When a magnetic field which is in the plane of the film is applied as shown in Fig. 1-2, magnetic poles are created in the permalloy structures. Positive poles thus created are shown as plus signs and negative poles as minus signs. If the top of the bubbles are negatively charged, they will be attracted to positive poles. As the in plane field rotates, bubbles are attracted to the next positive poles, thus moving along the permalloy patterns.

1.1.3. Ion Implanted Devices

Ion implanted devices use ion implanted patterns to create the bubble moving drive force instead of permalloy patterns as in permalloy devices. Here, the same rotating in-plane field is applied to move bubbles. However, as the field is applied, so called charged walls are created at the boundary of the implanted patterns as shown in Fig. 1-3 in contrast to the magnetic poles in the permalloy patterns. The charged walls are positively or negatively charged and therefore attract bubbles whose tops are negatively or positively charged, respectively. As the in- plane field rotates, so do the charged walls dragging the bubbles along. The bubbles actually propagate along

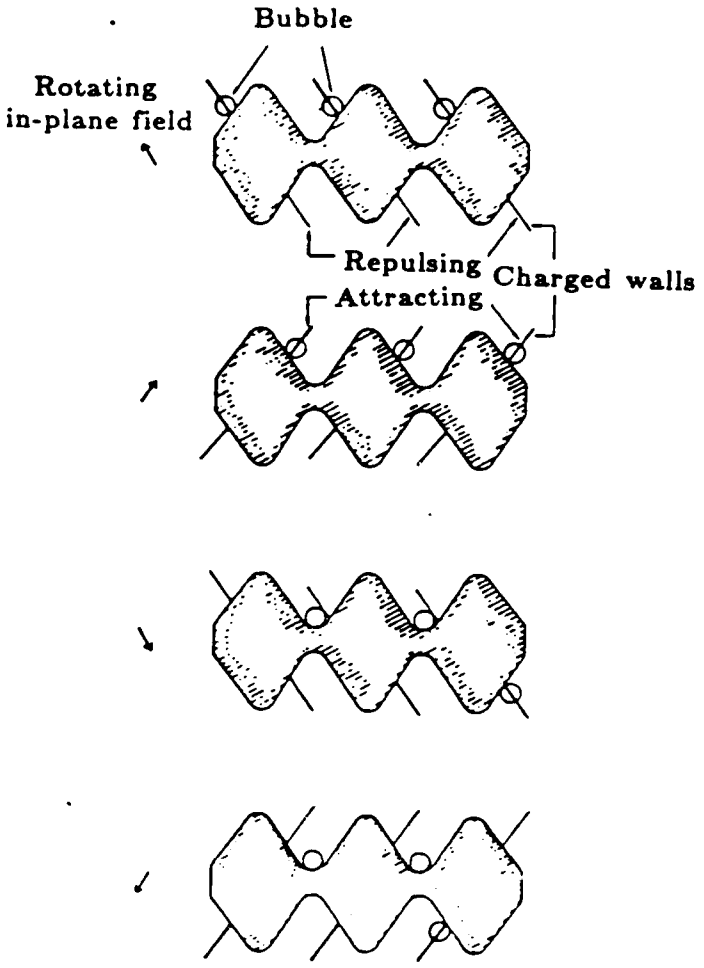

Figure 1-3: Bubble propagation along ion implanted tracks

the boundary for about one third to one fourth of a cycle of the rotating field and stay at the cusps of the patterns for the remainder of the cycle. Therefore, bubbles move from cusp to cusp or tip to tip during a cycle of the field. It is to be noted that the outside of the patterns are ion implanted and the patterns themselves are protected from the implantation by gold or photoresist during the implantation.

The ion implanted devices have important advantages over the permalloy devices which are explained in the following. The ion implanted devices give an order of magnitude higher memory density for a given minimum lithographic feature than the permalloy devices. Unit cell sizes of the permalloy device and the ion implanted devices are shown in Fig. 1-4. For a given minimum lithographic feature W, the cell size of the ion implanted device is 7.5 W^2, while that of the per-

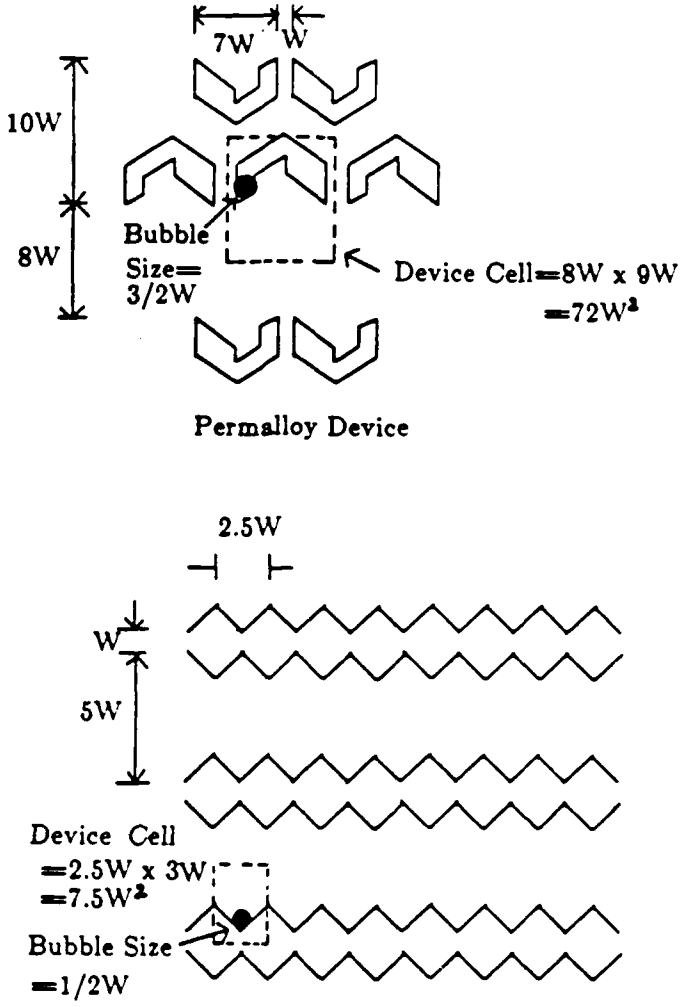

Figure 1-4: Comparison of cell sizes of permalloy and ion implanted devices

malloy device is 72 W^2. In other words, the ion implanted device can be fabricated an order of magnitude denser than the permalloy device using the same minimum feature.

Another advantage of using the ion implanted device is its lower drive current requirement. While the drive field for ion implanted devices does not increase very much as the bubble diameter is decreased, that of the permalloy devices increases inversely with the bubble diameter decrease[10].

The ion implanted devices have, however, one feature which has complicated the device design, i.e., anisotropic propagation of bubbles. Bubbles propagated in tracks oriented in some crystal

directions do not propagate as well as the bubbles propagated in tracks oriented in other directions. This is because of the three-fold anisotropy of the garnet films[11, 12]. The magnetization likes to lie in three preferred crystal directions, namely $[11\bar{2}]$ and its equivalent directions. There are two contributions to the three-fold anisotropy: one from the magnetocrystalline anisotropy which arises from the fact that the garnet films are cubic crystals and the magnetizations are elevated from the (111) film planes, and the other from the magnetostrictive anisotropy due to the partial relaxation of the stress at the boundary of the implanted patterns due to ion implantation. These will be explained in detail later in chapter 2.

1.1.4. Current Access Devices

Current access devices[9] use electric currents to move bubbles instead of a rotating magnetic field as in permalloy and ion implanted devices, which are also called field access devices. The propagation structure is fabricated by depositing two thin AlCu sheets, on top of the other separated by an insulator layer on the garnet film. In each AlCu sheet rectangular holes are etched. The holes are slightly offset from one layer to the other as shown in Fig. 1-5 (a). Cross-hatched holes are in one sheet and clear holes are in the other. When an electric current flows from the bottom to the top in the sheet around a hole, an upward magnetic field is generated on the right side of the hole and a downward field on the left side as shown in Fig. 1-5 (b). Then the bubble whose top is negatively charged will be attracted to the left side of the hole. Fig. 1-5 (c) shows a current timing diagram to move bubbles along the rectangles shown in Fig. 1-5 (a) from left to right. The current for the sheet with clear holes (i.e., top sheet) and for the sheet with crossed holes (bottom sheet) are denoted by J_1 and J_2, respectively. Initially the current flows in the top sheet in the direction indicated as J. Then, the bubble will be attracted to position 1. Next, the current on the top sheet is turned off and the current on the bottom sheet is turned on moving the bubble to position 2. The current in the top sheet is then reversed and the bubble moves to position 3. Finally, the current at the bottom is reversed and the bubble moves to position 4. Due to the low inductance of the conductor sheets, the current access device can be operated at much higher frequency ($>$ 1 MHz) than the field access devices which are typically operated at a few hundred KHz.

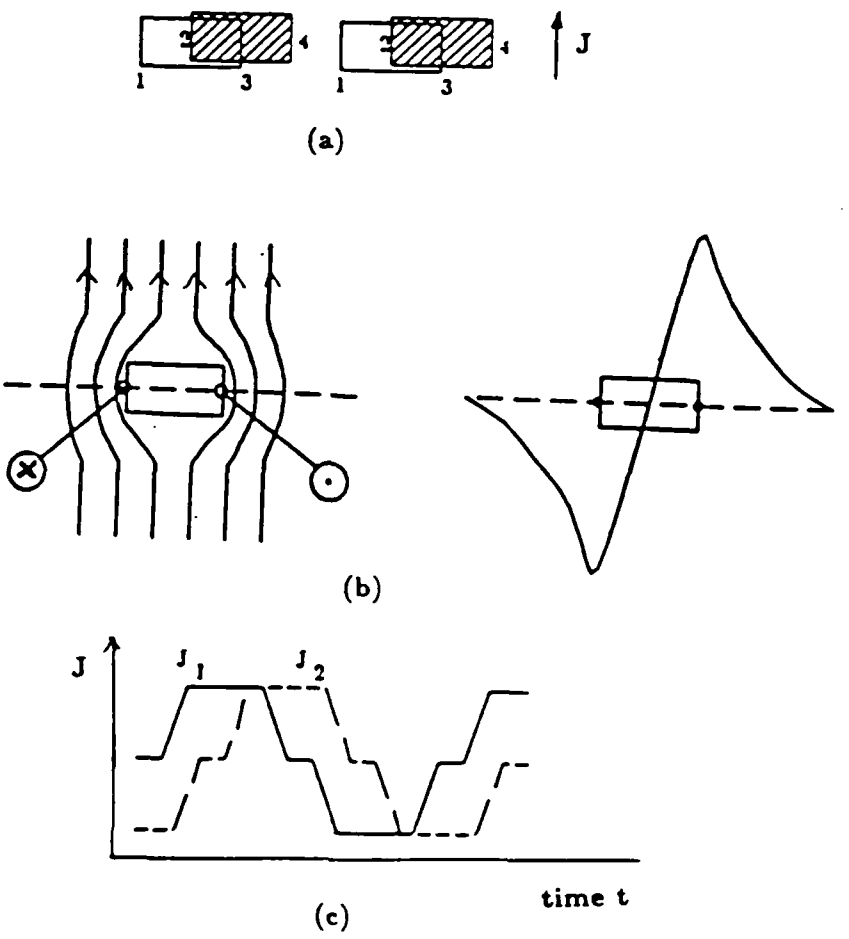

Figure 1-5: (a) Dual-conductor propagation patterns,
(b) disturbance of current by a hole in the current sheet
and vertical magnetic field thus created,
and (c) current waveforms

1.1.5. Memory Chip Organization

So far we have discussed how bubbles can be moved, i.e., bubble propagation in different kinds of device structures. Now we would like to consider bubble memory chip organization[3]. A typical bubble chip organization is shown in Fig. 1-6. Information to be stored is in the form of a string of electric current pulses and applied to the generator. The generator converts the electric current pulses to magnetic bubbles, whose presence or absence now represents the original information. The bubbles are then moved to the storage area via the major line. The storage area consists of a

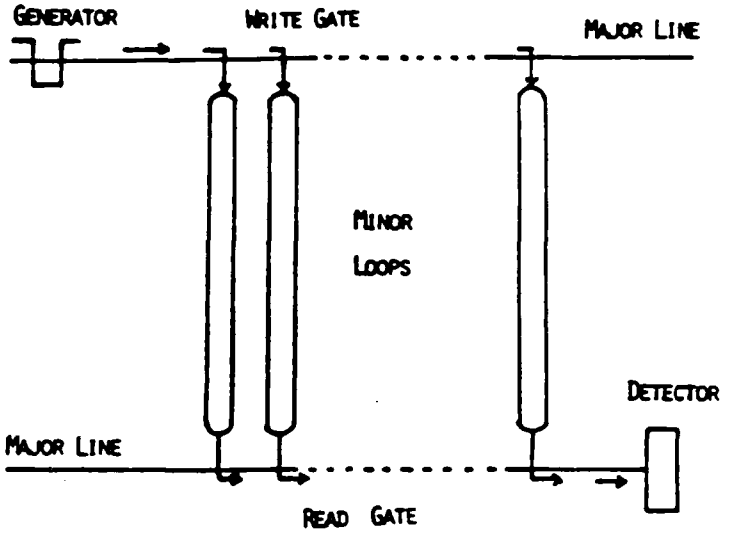

Figure 1-8: Schematic diagram of ion implanted bubble memory chip

number of bubble propagation loops called minor loops. Bubbles move from the major line to the minor loops through write gates when an electric pulse is applied to the gates. Bubbles reside in the minor loops until an external pulse is applied to the read gate to move them out of the storage minor loops to the read major line, then to the detector. The function of the detector is to re-convert bubbles to electric pulses to be sensed by external sensing circuits. The designs of the generator, write gate, read gate and detector are of course all different for the different propagation schemes which were discussed earlier. Since this thesis deals with the ion implanted devices, only the typical designs of memory chip functions for the ion implanted devices will be discussed in the following.

1.1.6. Current Controlled Functions

1.1.6.1. Generator

The generator[13] shown in Fig. 1-7 is fabricated by depositing a hairpin shaped conductor on top of the cusp of the write major line. A bubble is generated when an electric current pulse is applied to the conductor, which reverses the magnetization direction underneath the cusp and thus creates the bubble. In practice, the pulse is applied when the attractive charged wall is at the cusp. The charged wall supplies additional magnetic field thus reducing the magnitude of the electric pulse necessary to generate the bubble.

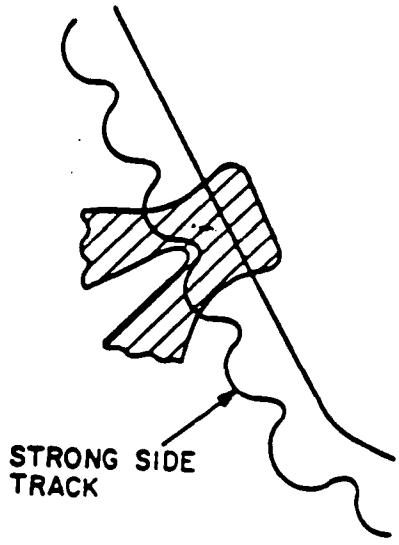

Figure 1-7: Bubble generator

1.1.6.2. Transfer Gates

Bubble transfer gates[13] between the major line and the minor loops are shown in Fig. 1-8. The gate is the hairpin shaped conductor deposited across the minor loop tip and the major line tip. Each gate serves one minor loop and the gates are all connected in series. Therefore, one electric pulse will transfer all the bubbles in the major line or minor loop tips. This gate can be used as either transfer in (write) and transfer out (read) gate. To transfer bubbles into the minor loops, the conductor is pulsed when the bubble is near the peak of the major loop. This bubble is then held in the conductor slot while the drive field rotates 180°, putting the attractive charged wall at the end of the minor loops. The pulse is then ended and the bubble follows the charged wall into the minor loops. The transfer out process is accomplished much like transfer in except the pulse begins when the bubble is near the end of the minor loop and held there until the charged wall makes the high peaks of the major loop attractive. This gate can be used as a bidirectional gate which performs both read and write functions. If a bidirectional gate is used, the chip organization (Fig. 1-6) is simplified incorporating only one major line which contains all the current controlled functions, i.e., the generator, the bidirectional gates for both read and write and the detector.

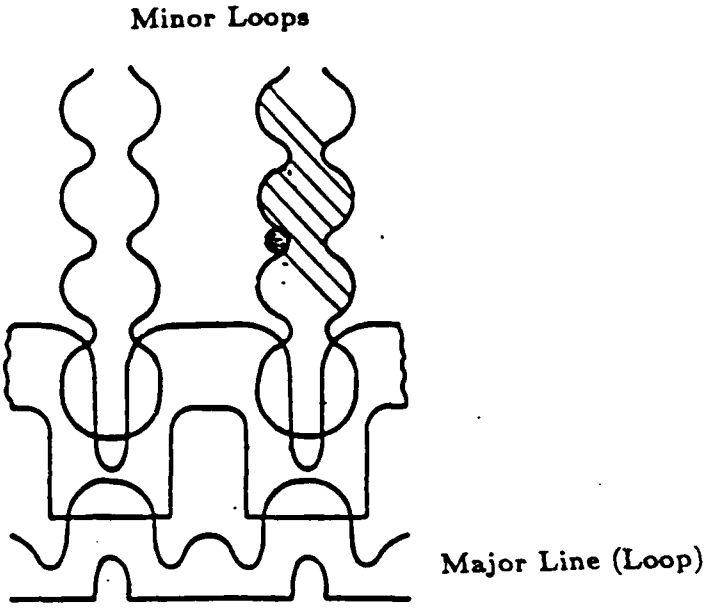

Figure 1-8: Bubble transfer gates

1.1.6.3. Detector

The bubble detector[13] converts the stray field of the bubble to a change of resistance of a permalloy strip via the magnetoresistive effect. Since the stray field of the bubble is small, the bubble is stretched by a long hairpin conductor in order to supply enough magnetic field change. As is shown in Fig. 1-9, the detector is formed by depositing a hairpin conductor on top of a strip of permalloy. By applying a current pulse to the conductor the bubble is stretched to form the long stripe domain whose stray field changes the resistance of the permalloy strip. A constant current is applied to the permalloy strip and the change in resistance changes the voltage across the strip which indicates the presence of the bubble. After detection, the stripe domain can either be reduced to a circular bubble domain or annihilated by turning off the stretch pulse or applying a proper reverse pulse.

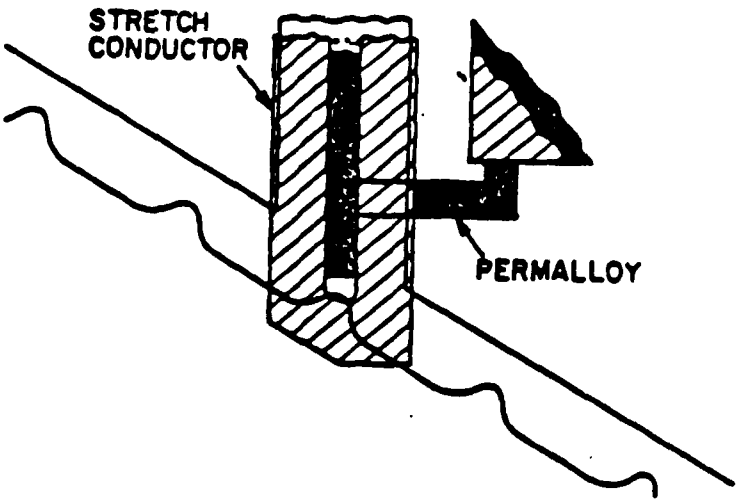

Figure 1-9: Bubble detector

1.2. Objectives of the Research

The main thrust of magnetic bubble memory research has been to increase the memory density, in order to decrease the cost per memory bit. At the beginning of this research, ion implanted bubble device research utilizing 1 μm bubbles was actively being pursued at leading laboratories. The objective of the research was set to design, fabricate, and understand bubble propagation devices using 0.5 μm bubbles which would lead to 16 to 64 Mbit chips. As the research progressed, a considerable amount of effort was given to understanding the three fold anisotropic behavior of bubble propagation and to making devices more isotropic. A theory was proposed by researchers[14, 15] to make devices isotropic by adjusting magnetostriction coefficients of the garnet films. Therefore an objective of the research was set to experimentally verify the theoretical predictions and to design and fabricate isotropic propagation devices. To achieve that goal, detailed examination and analysis of the bubble propagation behavior was performed.

Chapter 2
Theory of Bubble Domain Propagation

In this chapter theoretical aspects of bubble domain propagation in ion implanted devices are considered. First magnetic energies present in the bubble films are discussed. Discussions of bubble domains including domain walls, domain stability and domain motion follow. Next, ion implantation of devices, and charged wall formation and propagation are discussed. Finally, the bubble propagation bias margin which is a figure of merit of the bubble devices is considered.

2.1. Magnetic Energies in Garnet Films

The magnetic energies typically present in bubble garnet films[16, 17] are discussed in this section, which are exchange energy, perpendicular anisotropy energy, demagnetizing energy, magnetostrictive energy, magnetocrystalline energy and applied magnetic field energy.

2.1.1. Exchange Energy

The bubble film essentially constitutes a network of ions having spin and magnetic moments. The exchange energy between a pair of nearest neighbor spins S_i and S_j is

$$W_{ex} = -2J\ \mathbf{S}_i \cdot \mathbf{S}_j \tag{2.1}$$

which becomes $-2JS^2\phi_{ij}^2$ when the spins have the same magnitude and the angle between them, ϕ_{ij}, is small. A network of spins, therefore, tend to be aligned so that there is a net, bulk magnetization as long as the temperature is not high enough to break down the coupling. The temperature at which thermal agitation completely disrupts any long-range spin alignment and magnetization $4\pi M_s$ becomes zero is called the Curie temperature, T_c.

The exchange energy prevents abrupt discontinuities in the orientation of spins in a material

and there is a smooth transition in that orientation with small angles between adjacent spins. If the spins are located on a cubic array with spacing, a, then the exchange energy density in erg/cm^3 is

$$E_x = A[(\nabla\alpha_1)^2 + (\nabla\alpha_2)^2 + (\nabla\alpha_3)^2] \tag{2.2}$$

where $A = 2JS^2/a$ and α_1, α_2, α_3 are the direction cosines of the orientation of the local magnetization.

2.1.2. Demagnetization Energy

If a magnetic body of finite size is magnetized, magnetic poles are induced as shown in Fig. 2-1.

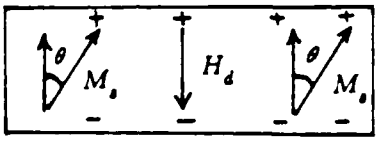

Figure 2-1: Demagnetizing field due to magnetization

These, in turn, give rise to a magnetic field in a direction opposite that of the magnetization. This field, called the demagnetizing field H_d , is proportional to the magnetization M_s. For thin film specimens shown in Fig. 2-1,

$$H_d = - NM_s \cos\theta \ , \tag{2.3}$$

where N is the demagnetizing factor (dimensionless quantity) which is a function of the shape of the specimen. For thin magnetic films magnetized normal to the film surfaces such as magnetic bubble films, the demagnetizing field is

$$H_d = -4\pi M_s \cos\theta \ , \tag{2.4}$$

which corresponds to a demagnetizing energy density

$$E_d = -\frac{1}{2}\,\mathbf{M}\bullet\mathbf{H}_d = 2\pi M_s^2 \cos^2\theta \ .$$

$$= 2\pi M_s^2(1 - \sin^2\theta) = constant - 2\pi M_s^2 \sin^2\theta$$

The demagnetizing energy is the lowest when the magnetization lies in the plane, i. e., $\theta = 90\ ^\circ$. The constant term may be dropped since it only affects the reference level of the energy. Then the demagnetizing energy is expressed as

$$E_d = -2\pi M_s^2 \sin^2\theta \ . \tag{2.5}$$

2.1.3. Perpendicular Anisotropy

As grown, garnet film exhibits a uniaxial anisotropy with preferred direction of magnetization perpendicular to the film plane, which can be expressed as

$$E_u = K_u \sin^2\theta \ , \tag{2.6}$$

where θ is the orientation of the magnetization with respect to the normal to the film. Without this perpendicular anisotropy, the magnetization in the film would lie in the plane of the film due to the demagnetizing energy. The net uniaxial anisotropy of the film is the sum of the perpendicular anisotropy and the demagnetizing energy :

$$E = (K_u - 2\pi M_s^2) \sin^2\theta \quad . \tag{2.7}$$

The perpendicular anisotropy in the film causes the magnetization to stand up as long as the anisotropy energy is larger than the demagnetizing energy of the film. The ratio of the perpendicular anisotropy to the demagnetizing energy is defined as quality factor

$$Q = \frac{K_u}{2\pi M_s^2} \quad . \tag{2.8}$$

For the magnetization to be perpendicular to the film, Q must be larger than 1.

The primary mechanism producing the perpendicular anisotropy in crystal garnet films is the preferential distribution of rare earth ions on certain lattice sites depending on the growth orientation, the deposition parameters and the identity of the ions.

2.1.4. Magnetocrystalline Anisotropy

The garnets are cubic materials and the first order expression for the cubic crystalline anisotropy energy density is[16]

$$E_1 = K_1 (\alpha_1^2 \alpha_2^2 + \alpha_2^2 \alpha_3^2 + \alpha_3^2 \alpha_1^2) \tag{2.9}$$

where the α's are the direction cosines of the magnetization with respect to the crystalline axes. The practical magnetic garnet crystals have a negative K_1, and the easy axes are along the cubic diagonals [1 1 1]. Therefore, the magnetization in the plane of the garnet film would prefer to lie in one of these directions. If Eq. (2.9) is rewritten as

$$E_1 = K_1 (1/4 \sin^4\theta + 1/3 \cos^2\theta + \sqrt{2}/3 \sin^3\theta \cos\theta \cos 3\phi) \tag{2.10}$$

where θ and ϕ represent the direction of the magnetization in cylindrical coordinates(Fig. 2-2), it is easy to see that the last term containing cos 3ϕ indicates a three-fold symmetry of the crystalline anisotropy for $\theta < \pi/2$.

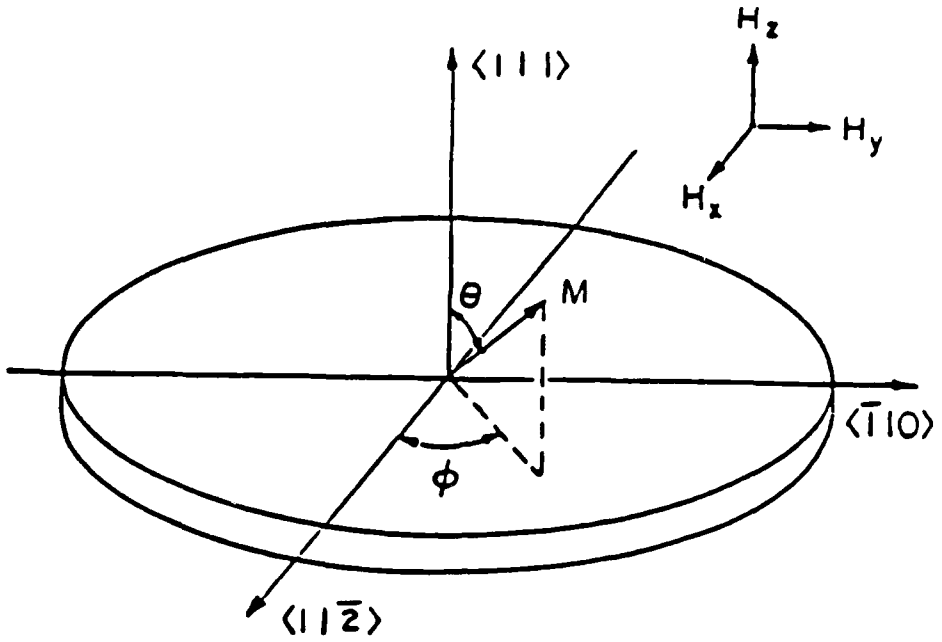

Figure 2-2: Cylindrical cordinate system

There are three easy directions for the magnetization corresponding to the projections of the cubic diagonals into the plane. This three-fold magnetocrystalline anisotropy, causes three-fold anisotropic behavior in the bubble devices.

2.1.5. Magnetostrictive Energy

A stress in the garnet film creates a magnetostrictive energy through the inverse magnetostrictive effect[16] which is given by

$$E = -\frac{3}{2}\,\sigma_p\,\lambda_{111}\,\sin^2\theta \tag{2.11}$$

where σ_p is the planar stress and λ_{111} is the magnetostriction coefficient along the [111] direction (the film normal). A compressive stress is present in the film due to ion implantation which will be discussed in detail later. Another stress normally present in the film is due to the lattice mismatch of the film and the substrate, which can be either compressive or tensile depending on the

film growth conditions. However, this stress is generally kept small by minimizing the lattice mismatch.

2.1.6. Magnetic Field Energy

In an applied field, H, the magnetization has a magnetic field energy density of

$$E_s = - \mathbf{M}_s \cdot \mathbf{H} \text{ or } - M_s H \cos\theta \tag{2.12}$$

where θ is the angle between the orientations of the field and magnetization. In a bubble device, an external applied field perpendicular to the film is always present to create bubbles. In addition, an in-plane field is also applied to propagate the bubbles.

2.2. Bubble Domains

2.2.1. Domain Wall

The magnetic configuration of a bubble domain[17] is shown in Fig. 2-3.

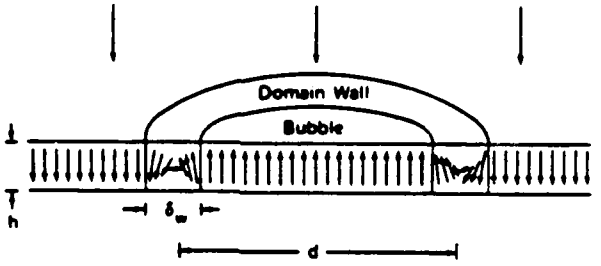

Figure 2-3: Magnetic bubble cross section

The magnetization does not reverse abruptly at the boundary of the bubble, but changes direction rather gradually across a finite transition region which is called the bubble domain wall. The

reversal in magnetization direction through the domain wall is not abrupt because the exchange energy E_x tends to keep the angles between adjacent spins small. Therefore, the exchange energy tends to make the domain wall wide. On the other hand, the (perpendicular) anisotropy energy tends to reduce the width of the wall to avoid the increase of the spins deviated from the easy (perpendicular) direction. There is an optimum domain wall width that minimizes the total energy. The wall width and the domain wall energy per unit area are given as follows[17]:

$$\delta_w = \pi \ (A/K_u)^{1/2} \tag{2.13}$$

and

$$\sigma_w = 4 \ (AK_u)^{1/2} \tag{2.14}$$

2.2.2. Stability

The bubble domain stability and its equilibrium configuration were analyzed by Thiele[18]. An isolated reverse magnetic domain in an infinite plane, i.e., $r_f = \infty$ is shown in Fig. 2-4.

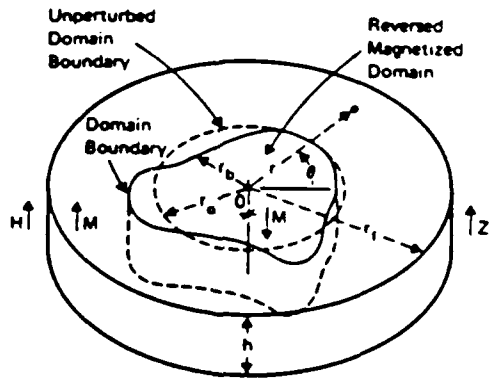

Figure 2-4: Domain configuration

The magnetization direction in the plane is restricted to be perpendicular to the plane, which is the case in bubble domain devices. A cylindrical coordinate system (r, θ, z) is used in this analysis and the origin of the system is at the center of the domain, denoted by 0. The domain is considered to be only slightly perturbed from a circular shape. The z-axis is parallel to the perpendicular to the plane and the domain shape is assumed not to change with z. The domain wall width is assumed to be negligible compared to the radius of the domain. Also, the wall energy density σ_w is assumed to be constant everywhere. The thickness of the domain is denoted by h. Now, the bubble domain boundary $r_b(\theta)$ is expressed in terms of Fourier Series coefficients, r_n and θ_n, giving the description of the shape of the bubble domain.

$$r_b(\theta) = \sum_{n=0}^{\infty} r_n \cos [n(\theta-\theta_n)] = r_o$$

$$+ \Delta r_o + \sum_{n=1}^{\infty} \Delta r_n \cos [n(\theta-\theta_n-\Delta\theta_n)] . \qquad (2.15)$$

The Δr_n and $\Delta\theta_n$ describe a variation from a circular domain, and θ_n gives the direction of the variation. The condition

$$|r_o| >> \sum_{n=1}^{\infty} n\ r_n \qquad (2.16)$$

assures that the domain is nearly circular and the function $r_b(\theta)$ is single-valued and smooth.

The total energy of the bubble domain is defined as the difference of the system energy with the domain and without the domain. The energies introduced by the presence of the bubble domain are the wall energy, E_w which increases the system energy, and the magnetostatic energy, E_m which tends to reduce the system energy by flux closure. In addition to these, external magnetic field energy E_h is present to stabilize bubble domains. The external field H is applied perpendicular to the film plane and opposite to the magnetization direction of the bubble domain as was mentioned in Chapter 1. The total energy of the domain[19] is:

$$E_t = E_w + E_m + E_h \tag{2.17}$$

where

$$E_w = \int_a \sigma_w \, da = h \, \sigma_w \int_0^{2\pi} \left[r_b^2(\theta) + \left(\frac{\partial r_b(\theta)}{\partial \theta} \right)^2 \right]^{1/2} d\theta, \tag{2.18}$$

$$E_m = \frac{1}{2} \int_V \int_{V'} \frac{\nabla \bullet \mathbf{M} \;\; \nabla' \bullet \mathbf{M}'}{| \mathbf{r} - \mathbf{r}' |} \, dV' dV \tag{2.19}$$

and

$$E_h = - \int_V \mathbf{M} \bullet \mathbf{H} \; dV = - \int_{-\infty}^{\infty} \int_0^{2\pi} \int_0^{\infty} M_z H r dr d\theta dz \; . \tag{2.20}$$

V denotes volume and the primes the second coordinate system used to cribe the internal magnetostatic interaction.

Thiele showed that for the configuration of Fig. 2-4, the variation of the total energy can be described as:

$$\frac{\Delta E_t}{2(4\pi M_s^2)(\pi h^3)} = \left[\frac{l}{h} + \frac{H_b}{4\pi M_s} \frac{d}{h} - F\left(\frac{d}{h}\right) \right] \frac{\Delta r_o}{h}$$

$$- \left[\frac{l}{h} - S_o\left(\frac{d}{h}\right) \right] \frac{h}{d} \left(\frac{\Delta r_o}{h} \right)^2$$

$$+ \frac{1}{2} \sum_{n=2}^{\infty} (n^2-1) \left[\frac{l}{h} - S_n \left(\frac{d}{h}\right) \right] \left(\frac{h}{d}\right) \left(\frac{\Delta r_n}{h} \right)^2 + O_3 \; , \tag{2.21}$$

where $l = \sigma_w / 4\pi M_s$ is the material characteristic length, O_3 is the collection of the third and higher order terms, and the functions F and S_n are called the force and stability functions, respec-

tively. The equilibrium diameter of the bubble is determined by setting the coefficient of the first order variation equal to zero so that:

$$\frac{l}{h} + \frac{H_b}{4\pi M_s}\frac{d}{h} = F\left(\frac{d}{h}\right) . \tag{2.22}$$

The domain is stable with respect to an arbitrary variation in shape when all of the coefficients of Δr_n^2 terms are positive, i.e.,

$$\frac{l}{h} - S_o\left(\frac{d}{h}\right) < 0 \tag{2.23}$$

and

$$\frac{l}{h} - S_n\left(\frac{d}{h}\right) > 0 \text{ for } n \geq 2 . \tag{2.24}$$

Since the stability functions have the property

$$S_{n+1}\left(\frac{d}{h}\right) < S_n\left(\frac{d}{h}\right) , \tag{2.25}$$

the domains are stable for

$$S_2\left(\frac{d}{h}\right) < \frac{l}{h} < S_o\left(\frac{d}{h}\right) . \tag{2.26}$$

If $S_2\,(d/h)$ is larger than l/h the bubble stripes out and if $S_o\,(d/h)$ is smaller than l/h the bubble collapses.

2.2.3. Bubble Size

The functions, F, S_0, S_2 versus d/h are plotted in Fig. 2-5. The figure also shows how the bubble diameter in the presence of the external magnetic field can be determined graphically as a function of the characteristic length and thickness of the film. First, the value of l/h *(.25)* for the film is plotted on the ordinate. Then two lines are drawn from this point, one horizontal and the other with a slope equal to $H_b/4\pi M_s$ where H_b denotes the external bias field. From Eq. (2.22) it can be seen that the equilibrium bubble size is determined by the intersection of the second straight line with the curve for F. In the case shown in Fig. 2-5, when $H_b/4\pi M_s$ is greater than 0.329 (the slope of the tangent to curve F), there is no intersection with the curve F, i.e., no bubble can exist at such a field.

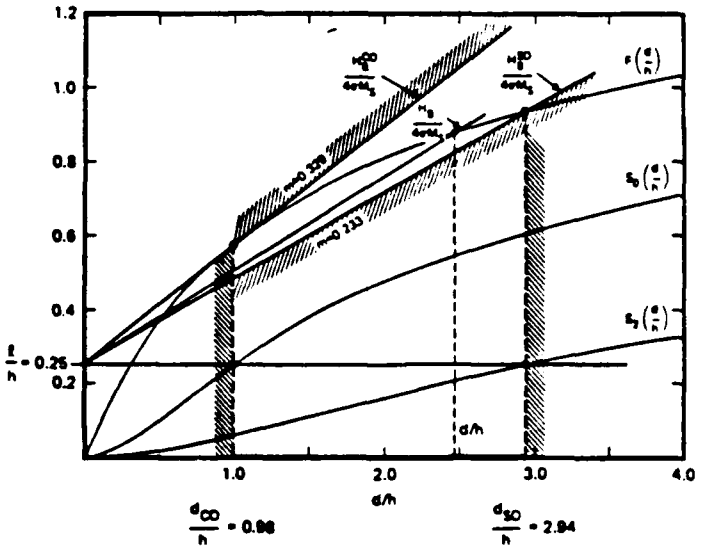

Figure 2-5: Graphical determination of d vs. H_b

Therefore, this is the bubble collapse, H_{co} of the film. When the applied field is smaller than H_{co}, there are two intersections with curve F. However, not all of the solutions are stable. From the stability criteria [Eq. (2.26)], it is clear that only the solutions are stable which are located between the two intersections obtained from the horizontal line drawn from the point indicating l/h

value on the ordinate. The smaller diameter limit represents the collapse diameter d_{co} and the larger limit the stripeout diameter d_{so}. The corresponding applied fields shown in the figure as H_b^{co} and H_b^{so} are then the collapse field and the stripeout field, respectively.

The bubble diameter variation with respect to the film thickness can be obtained as follows. First, Fig. 2-5 is used to obtain d_{co}/h and d_{so}/h values as a function of l/h by drawing a straight line from the point (l/h) on the ordinate as was explained earlier since these values are defined by

$$\frac{l}{h} = S_o\left(\frac{d_{co}}{h}\right) = S_2\left(\frac{d_{so}}{h}\right) . \tag{2.27}$$

Then by transposing the parameters the desired plot is obtained as is shown in Fig. 2-6.

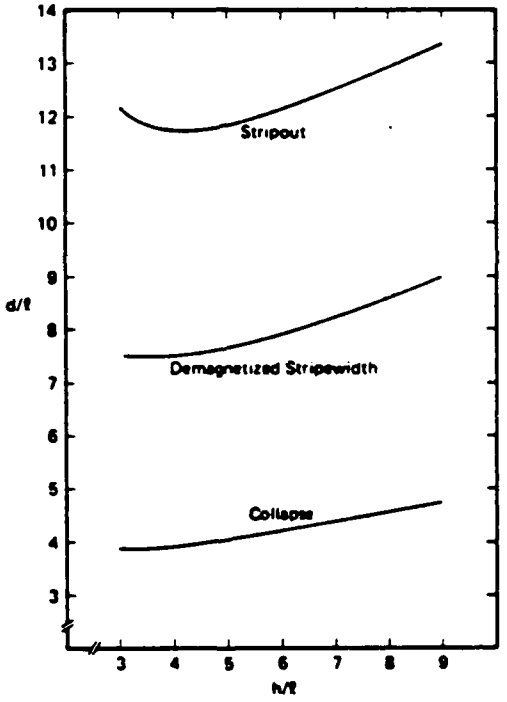

Figure 2-6: Extremes of bubble size vs. h/l

Notice that the zero-field demagnetized stripewidth is also plotted. The figure shows that the bubble diameter does not change appreciably as the thickness of the film is changed.

The ratio of bubble diameter at stripeout to the bubble diameter at collapse is about 3 and the ratio of stripewidth to the average of bubble diameter at stripeout and bubble diameter at collapse is about 1, and are shown in Fig. 2-7.

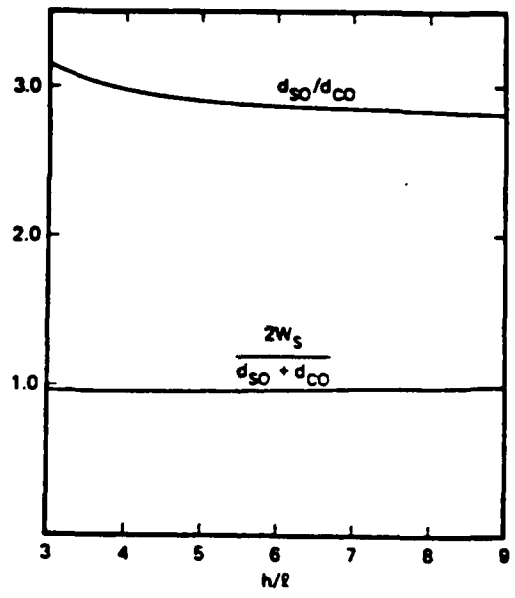

Figure 2-7: d_{so}/d_{co} and $2W_s/(d_{so} + d_{co})$ vs. h/l

The variations of the bubble diameter with bias field can be obtained from Fig. 2-5, and the results are shown in Fig. 2-8.

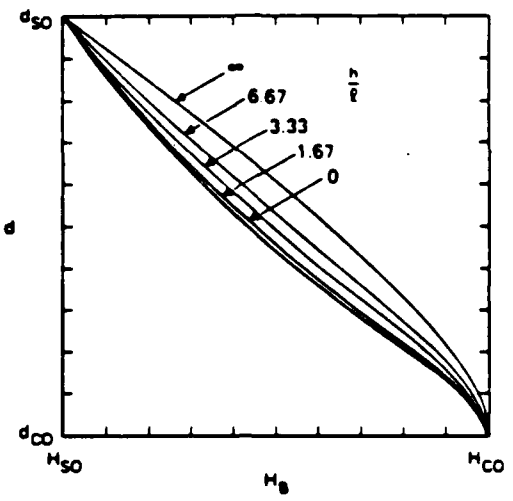

Figure 2-8: Variation in bubble size, d vs. bias field, H_b for film thickness, h/l

The parameter is the thickness of the films. These curves show that the diameter of the bubble decreases almost linearly as the bias field is increased and the effect of changes in thickness is not great.

2.2.4. Bias Field Margin

The collapse and stripeout fields $H_b^{co}/4\pi M_s$ and $H_b^{so}/4\pi M_s$ may be obtained from Eq. (2.22) and Eq. (2.27)

$$\frac{H_b^{co}}{4\pi M_s} = \frac{F\left(\frac{d_{co}}{h}\right) - \frac{l}{h}}{d_{co}/h} = \frac{F\left(\frac{d_{co}}{h}\right) - S_o\left(\frac{d_{co}}{h}\right)}{d_{co}/h}, \tag{2.28}$$

and

$$\frac{H_b^{\infty}}{4\pi M_s} = \frac{F\left(\frac{d_{\infty}}{h}\right) - \frac{l}{h}}{d_{\infty}/h} = \frac{F\left(\frac{d_{\infty}}{h}\right) - S_2\left(\frac{d_{\infty}}{h}\right)}{d_{\infty}/h} \tag{2.29}$$

These relationships are plotted in Fig. 2-9 for various h/l.

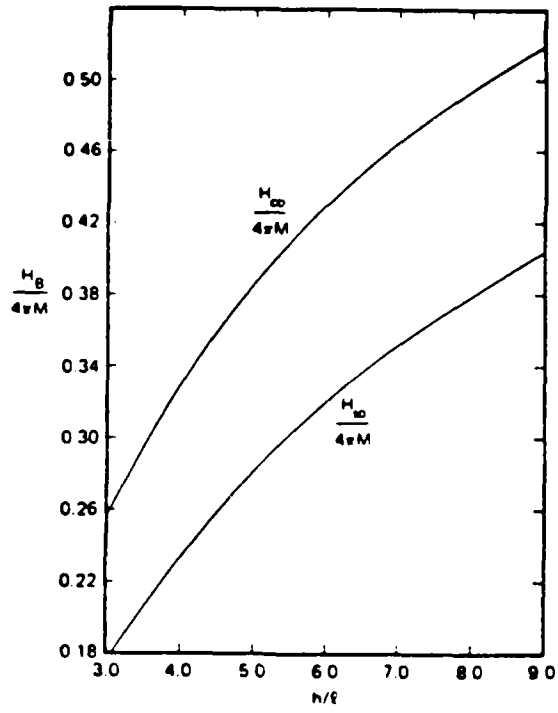

Figure 2-9: H_b margins vs. h/l

It is seen that both collapse fields and stripeout fields decrease steadily as the height of the bubble decreases. The bias field margin width defined by the difference of the collapse field and the stripeout field also decreases as the bubble height decreases. It is expected from the plots that the bubble will have a bias margin width of about $0.11 \times 4\pi M_s$ when the bubble height is $9l$

2.2.5. Collapse Field Variation with Temperature[20]

The exact treatment of bubble statics does not yield a simple closed form expression for the collapse field. Callen and Josephs introduced a good approximation which is useful for understanding thermal behavior:

$$H_c = 4\pi M_s + \frac{3\sigma_w}{4hM_s} - \left(\frac{12\pi\sigma_w}{h}\right)^{1/2} \tag{2.30}$$

where $4\pi M_s$ is the saturation magnetization, h is the bubble height, and σ_w is the domain wall energy per unit area.

The normalized temperature derivative of the collapse field is of interest because it is desirable that the dependence of the bubble collapse field on temperature is as closely matched as possible to that of the bias magnet field, to achieve wide temperature operation of magnetic bubble devices. Assuming that the thermal expansion is negligible, from Eq. (2.30),

$$\frac{H_c'}{H_c} = \frac{\left(4\pi M_s - \frac{3\sigma_w}{4hM_s}\right)\frac{M_s'}{M_s} + \left[\frac{3\sigma_w}{4hM_s} - \left(\frac{3\pi\sigma_w}{h}\right)^{1/2}\right]\frac{\sigma_w'}{\sigma_w}}{4\pi M_s + \frac{3\sigma_w}{4hM_s} - \left(\frac{12\pi\sigma_w}{h}\right)^{1/2}} \tag{2.31}$$

where a prime indicates a derivative with respect to temperature.

2.3. Motion of a Bubble Domain

As discussed in the previous section, a static bias field H_B is necessary to stabilize the bubble in conjunction with the demagnetizing energy and wall energy. If the bias field is changed, the bubble size is changed, i.e., the bubble wall moves radially inward or outward (Fig. 2-10).

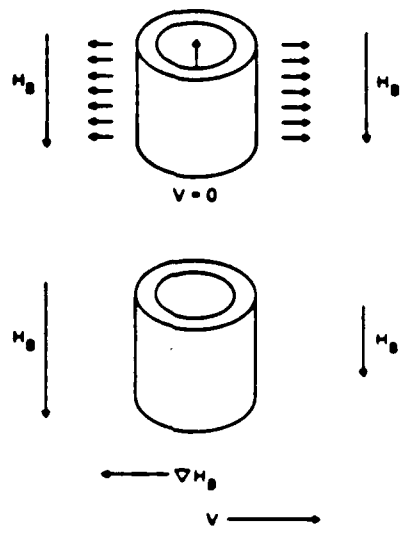

Figure 2-10: Requirement for a field gradient

The domain wall motion will stop when the bubble reaches its new equilibrium diameter. The uniform change in bias field does not cause a net translation of the bubble. However, a gradient in bias field will cause a translation of the bubble. Thiele[18] showed that the equation of motion for a circular bubble with diameter d is:

$$V = -\mu_b \left(\Delta H_b - 8H_c/\pi\right) , \tag{2.32}$$

where $\mu_b = \mu_w/2$ and $\Delta H_b = d \bullet dH_b/dy$.

Thus the bubble mobility (μ_b) is one-half the wall mobility(μ_w), the difference in bias field across the bubble diameter acts as the driving field and the coercivity for bubbles is $8H_c/\pi$.

2.4. Ion Implantation and Annealing

In ion implanted devices, ion implantation changes the magnetization direction of the garnet film from perpendicular to parallel to the surface, thus enabling the creation of charged walls which are the driving forces of the bubbles. The charged wall characteristics, thus the bubble driving force, depend on the characteristics of the implanted layers. In this section, the mechanism of ion implantation and the way to create proper implantation layers for device operation will be discussed. Variations of implantation layer characteristics with ambient temperature and annealing will also be considered.

2.4.1. Mechanisms of Ion Implantation

When the magnetic film is implanted with energetic ions (few tens to few hundreds KeV) such as hydrogen, deuterium, helium, neon or oxygen, the ions collide with the nuclei and electrons of the host material, lose their energy and, finally, come to rest. The collisions cause the displacement of the constituent atoms resulting in the lattice expansion of the film. The film can expand freely perpendicular to the surface but is constrained from expanding in the film plane by the thick GGG substrate (3 orders of magnitude thicker than the film) as shown in Fig. 2-11.

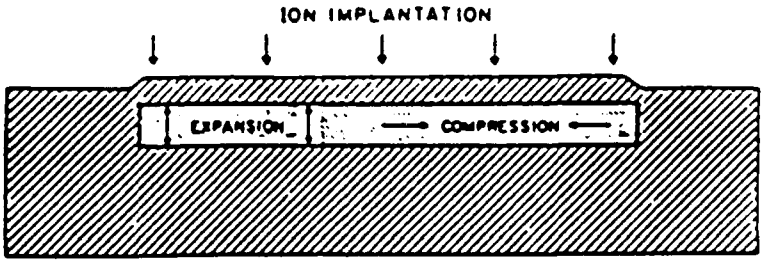

Figure 2-11: The effects of ion implantation on a magnetic garnet crystal. The damage expands the lattice, resulting in lateral compression.

Therefore, there exists compressive stress in the film plane as shown in the figure. Notice that there is no stress in the direction normal to the film because the stress is relieved by the lattice expansion in that direction.

Since λ_{111} is typically negative in bubble films and σ_p is also negative in case of compression, Eq. (2.11) shows that the minimum magnetostrictive energy is achieved when the magnetization lies in the plane of the film, i.e., the easy magnetization direction is in the plane as can be seen in Fig. (2.11). The total energy of the film is the sum of the energies expressed in Eqs. (2.7) and (2.11). So, if the magnetostrictive energy induced by the ion implantation is greater than the sum of the perpendicular uniaxial energy and the demagnetizing energy, the easy direction of magnetization will change from perpendicular to parallel to the film plane. In contiguous disk ion-implanted devices, enough ion implantation is applied so that the magnetization lies in the plane of the film.

So far we have discussed the anisotropy energy change of the film due to the lattice expansion by ion implantation. But there are other mechanisms which also cause the anisotropy change. One is the destruction of the growth induced anisotropy by the implantation[21]. This is induced by the displacement of rare-earth ions. The other is a change of the anisotropy not explained by the above two mechanisms, but obscured for light ions such as hydrogen and deuterium. The researchers have suggested that the ions form metastable compounds with the host ion nuclei[22, 21], and that these compounds are responsible for this change of the anisotropy.

2.4.2. Determination of Ion-Implantation Conditions

The purpose of ion implantation is to overcome the perpendicular magnetic anisotropy [Eq. (2.7)] of the bubble film so that the magnetic anisotropy lies in the plane of the film. Therefore the anisotropy change necessary to create an adequate in-plane anisotropy is first determined. It is found empirically that an in-plane Q_i of at least 3 is necessary to insure adequate bubble propagation. Since a perpendicular $Q_u\left((H_k-4\pi M)/4\pi M\right)$ of about 1 is necessary for reasons of bubble stability, the change of Q necessary is 4. For 0.5 μm bubble materials with $4\pi M$ of 1,000 Oe, the anisotropy change ΔH_k needed is therefore 4,000 Oe. Another important factor to consider is the depth of the implanted layer. This determines the depth of the charged wall. It is well known that too thin a charged wall will not propagate bubbles and too thick a charged wall interferes with the charged wall of the adjacent propagation track, thus impeding bubble propagation. In this section, proper implantation conditions such as ion species, implantation energy and dosage will be discussed.

2.4.2.1. Ion Species

The considerations to be made in determining the ion species are the depth of penetration and the change of anisotropy that each ion species produces. Only light ions can penetrate an adequate distance into garnet with easily available acceleration energy. Therefore H^+, He^+ and Ne^+ have mostly been used. Heavier He^+ and Ne^+ cause lattice damage which produces anisotropy change with less dosage of ions, but the achievable anisotropy change saturates before producing adequate anisotropy change for small submicron bubble materials. Ions of H need much higher dosage to produce adequate anisotropy change but the anisotropy change does not saturate at high dose[23]. This is shown in Fig. 2-12.

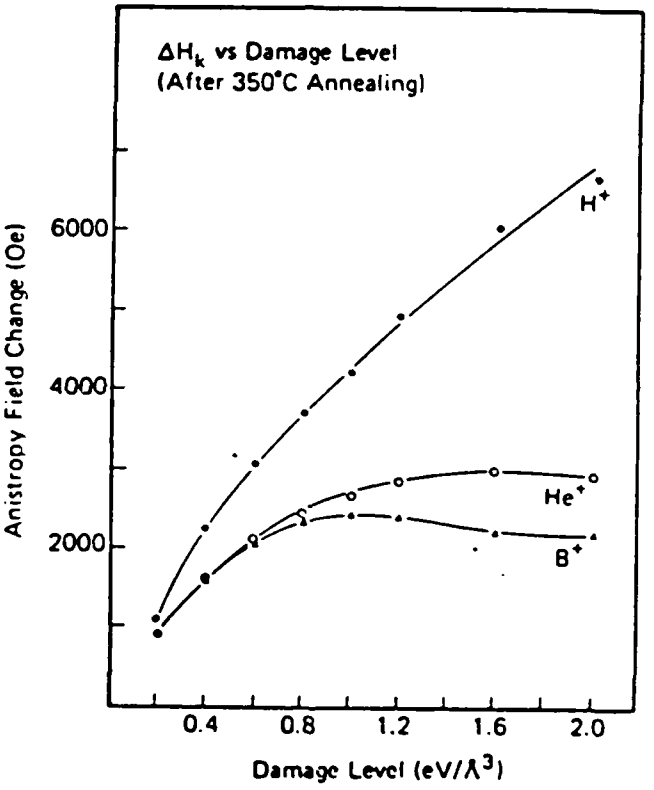

Figure 2-12: ΔH_k vs. damage level after annealing at 350 ° C for 30 minutes[23]

Here, the anisotropy changes are plotted with respect to damage level which is related to the ion dosage. Because smaller bubble materials require higher anisotropy changes, hydrogen is most widely used nowadays. Another advantage of using hydrogen is that since it does not damage the garnet crystal excessively, the material parameters such as damping parameter, gyromagnetic ratio, etc. also do not degrade significantly. Recently, it was found that deuterium implantation exhibits similar advantages[21]. Moreover, the dosage required is about half that required for hydrogen, which reduces the implantation time. Therefore deuterium implantation was exclusively used for this study.

2.4.2.2. Implantation Energy

The acceleration energy of ions determines the depth of ion penetration into garnet films. The depth distribution of implanted ions is roughly Gaussian and can be characterized by a mean projected range R_p and a projected standard deviation ΔR_p. Tabulations of these values according to ion species are available and the estimates for the implanted layer thickness ($\sim R_p + \Delta R_p$) are obtained from these tabulations. An estimate of the desired thickness of the implanted layer can be obtained by considering the magnetic flux matching of a charged wall and an underlying bubble[6]. It is assumed that to attract a bubble effectively, the average magnetic flux of a charged wall ($\sim 8\pi M\, \Delta h d$) should be large enough to couple with the circulating bubble flux ($\sim 1.4 \times 4\pi M\, \pi/4d^2$), where Δh is the depth of the implantation layer and d is the bubble diameter. From this relationship, Δh should be approximately 0.5 d. A thicker ion-implanted layer provides longer and stronger charged walls, which tend to interact with the charged walls from the adjacent track, thus impeding bubble propagation.

2.4.2.3. Dosage

As mentioned above the anisotropy energy change caused by ion implantation is composed of two parts, one due to magnetostriction and the other due to nonmagnetostrictive effects. The magnetostrictive anisotropy change is described (see Eq. (2.11))as

$$\Delta E = -\frac{3}{2}\,\lambda_{111}\sigma_p \tag{2.33}$$

where

$$\sigma_p = \frac{Y}{1-\nu}\,\frac{\Delta a}{a} \simeq 3 \times 10^{12}\,\frac{\Delta a}{a}\ \text{dyne/cm}^2 \ . \tag{2.34}$$

Therefore

$$\Delta E = -\frac{9}{2} \times 10^{12} \lambda_{111} \frac{\Delta a}{a} \text{ erg/cm}^2 \tag{2.35}$$

$$\Delta H_k = \frac{2\Delta E}{M} = -9 \times 10^{12} \frac{\lambda_{111}}{M} \frac{\Delta a}{a} . \tag{2.36}$$

Here, λ_{111} is the magnetostriction coefficient along the [1 1 1] axis of the garnet crystal, σ_p is the stress induced in the film plane due to ion implantation, Y is Young's modulus, ν is Poisson's ratio, a is the lattice constant of the film, Δa is the change of lattice constant due to ion implantation, and M is the magnetization of the implanted layer. The anisotropy field change can therefore be estimated by Eq. (2.36) once the magnetostriction coefficient and the magnetization of the implanted layer and the lattice strain are known. This works reasonably well for ions like He^+ and Ne^+ since the anisotropy change comes mostly from the inverse magnetostive effect. However, for ions like H^+ and D^+, the contributions from nonmagnetostrictive effects have to be added. Krafft[21] determined that only about 1/3 to 1/2 of the entire anisotropy change comes from the magnetostrictive effect. The proper amount of implantation dosage for best device performance is generally determined by empirical methods. The dose of ions necessary to create the anisotropy change is obtained from experimental curves[24, 21] such as the one shown in Fig. 2-13 or a set of curves like Fig. 2-14 and Fig. 2-15.

In Figs. 2-14 and 2-15, the desired implant dose is obtained by first obtaining the implant strain from Fig. 2-14 and then the implant dose from Fig. 2-15. Fig. 2-14 includes a curve indicating the magnetostrictive portion of the anisotropy change. This is obtained from Eq. (2.36). Notice that all these curves are for specific values of the implantation energy, i.e., the implantation depth. Obviously the ions confined in a smaller area (smaller energy) will cause higher lattice strain than the same number of ions in a larger area (larger energy).

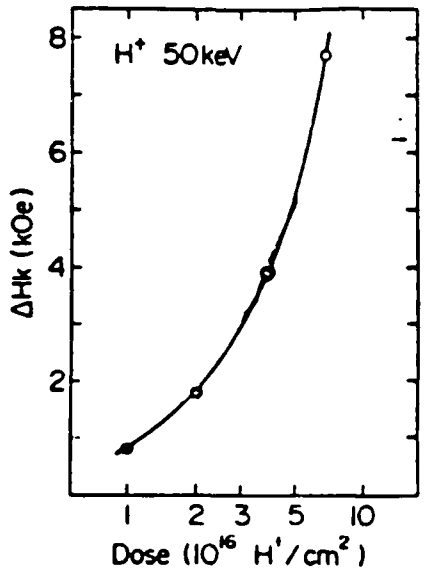

Figure 2-13: Anisotropy field change (ΔH_k) vs. dose[24]

2.4.2.4. Multiple Implantation

Ion implantation creates a Gaussian like distribution of ions into the depth of the film, which is roughly correlated to the damage and strain of the lattice and the anisotropy change in the implanted layer. It is not clear what constitutes the optimum implantation profile for best device operation. However, some researchers suggest that a uniform anisotropy change profile through the depth of the film gives good device operation[25]. Since a single implantation gives roughly a Gaussian profile (of anisotropy change) multiple implantation (generally double or triple) is used to make the profile more uniform. An example of an ion concentration profile created by double implantation is shown in Fig. 2-16.

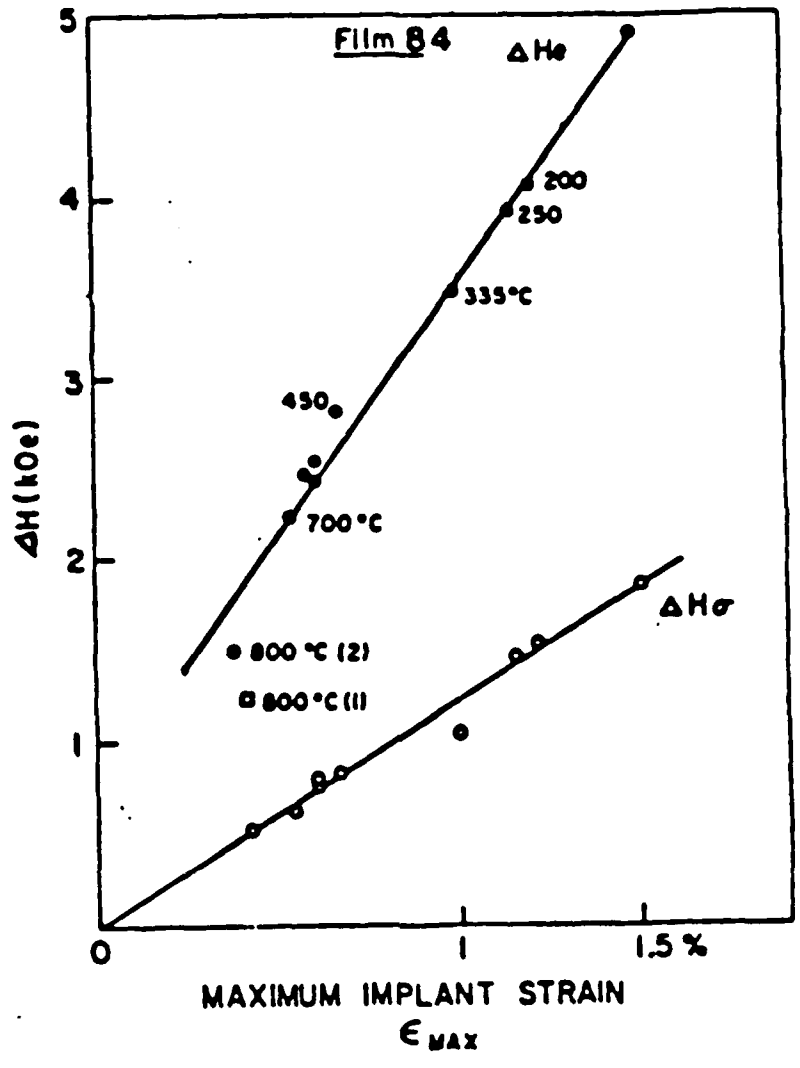

Figure 2-14: Implant-induced change in uniaxial anisotropy field ΔH_k and magnetostrictive field ΔH_σ vs. implant strain ϵ_{max} for film 84[21]

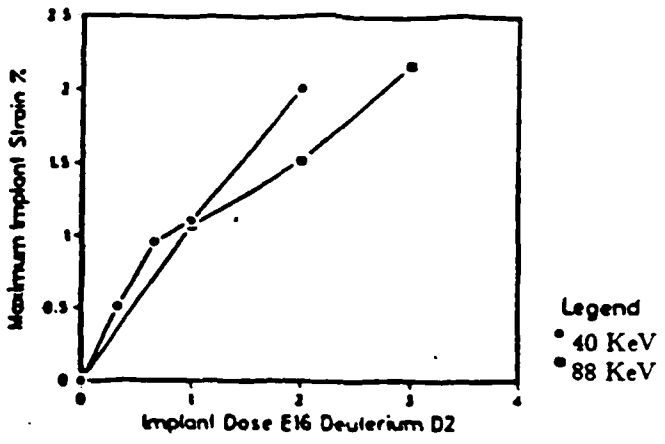

Figure 2-15: Maximum implant strain vs. dose for 40 KeV and 88 KeV deuterium implantation[21]

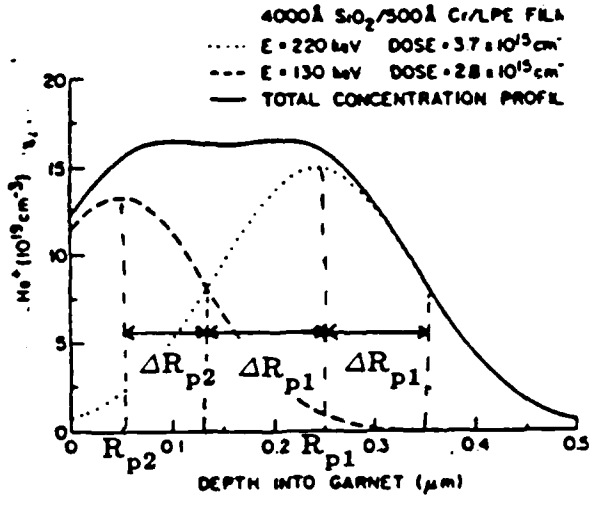

Figure 2-16: Double-implanted He^+ concentration profile on samples with SiO_2 (4000 A) on Cr (500 A) on garnet[26]

In this study, double implantation was exclusively used. The methods to determine the ion-implantation conditions used in this study are described in the following. The deep main implantation determines the thickness of the implanted layer and the thickness of the layer is $R_{p1} + \Delta R_{p1}$ where R_{p1} is the projected range and ΔR_{p1} the standard deviation in range of the first implant. The second implantation depth (R_{p2}) is chosen as $R_{p1} - (\Delta R_{p2} + \Delta R_{p1})$ where R_{p2} is the projected range and ΔR_{p2} the standard deviation in range of the second implant.

Krafft[21] indicated that ratio of doses (dose of the second implant to that of the first implant) of about one-half to one-third produced a relatively uniform implant. However, Saunders showed that an implant uniform in depth does not lead to magnetization uniform in depth near to the mask edge[27]. If uniform magnetization is desired and if Δ $(=(\lambda_{111}-\lambda_{111})/\lambda_{111}) = 0$, the implant should be uniform throughout most of the depth and then taper off into the bulk. If $\Delta \neq 0$, the implant should peak slightly near the surface to increase the reduced "stress-relief anisotropy". In this study Saunders' suggestion was tried, so that the ratio of the doses was chosen to be 2/3, which was expected to give a slight peak near the surface due to the higher dose used for the shallow implant.

2.4.3. Annealing

Annealing of the implanted layers generally lowers the anisotropy change of the layer. This is in part due to the restoration of the damage which is associated with the implantation to the garnet crystal. Another contributing factor is thought to be the desorption of the ions (especially hydrogen and deuterium) from the surface of the implanted layer[28, 21]. A sudden decrease of the anisotropy change in hydrogen and deuterium implanted samples near 200 °C~250 °C is commonly observed and believed to be an indication of the desorption of the ions. A thin coating of SiO_2 (several tens of nm) before the implantation prevents this sudden decrease of anisotropy change and maintains adequate anisotropy change for proper device operation after annealing[1]. The annealing simulates the heat treatment associated with the device processing after the implantation. Typical annealing conditions range from 200 °C~400 °C of temperature and from 0.5 to 1 hr. of time depending on the processing steps employed.

To account for the annealing process, the curves for the anisotropy change vs. ion dose and lattice strain (Figs. 2-13, 2-14, 2-15) which were discussed in the preceding subsection should be obtained after the pertinent annealing process to estimate the necessary dose of ions more realistically.

---

[1] It is observed that the total anisotropy change and the magnetostriction part of the anisotropy change decrease linearly with the decrease of the lattice strain.

2.5. Charged Wall Formation

As was briefly mentioned in Chapter 1, the driving force of the bubble in ion-implanted devices is the charged wall. We will discuss in this section the mechanisms of the charged wall formation. Partial stress relaxation at the boundary of the implanted patterns and the resultant magnetostrictive anisotropy will be discussed first. Then the charged wall formation will be explained based on the preceding discussions.

2.5.1. Stresses at the Pattern Boundary

In the previous section, we discussed the results of ion implantation in a magnetic film with no boundaries. Now we will discuss what happens at the boundary of an implanted and non-implanted region. As was mentioned earlier, charged walls are created at such a boundary. A diagram of such a boundary between implanted and nonimplanted regions is shown in Fig. 2-17.

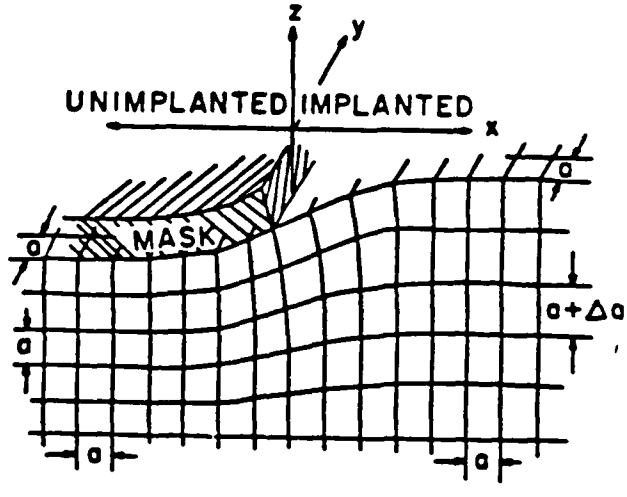

Figure 2-17: Lattice distortion at boundary between implanted region ($x>0$) and unimplanted region ($x<0$)

The lattice constant is denoted as a in the figure. The implanted region is covered by the mask which stops the penetration of ions. As was explained in the previous section, the lattice constant in the implanted region far from the boundary expands by Δa in the direction perpendicular to the film (z-direction), but remains unchanged in the plane (x,y plane). It is assumed that the boundary is parallel to the y coordinate. This reduces the analysis to a two-dimensional problem.

At the interface, the implanted region presses into the unimplanted region, partially relieving the stress in the direction perpendicular to the edge. Thus, the lattice constant in the x direction in the implanted region is expanded while that in the unimplanted region is reduced. Fig. 2-18 shows qualitatively lattice constants and stresses at the edge of the implantation region shown in Fig. 2-17.

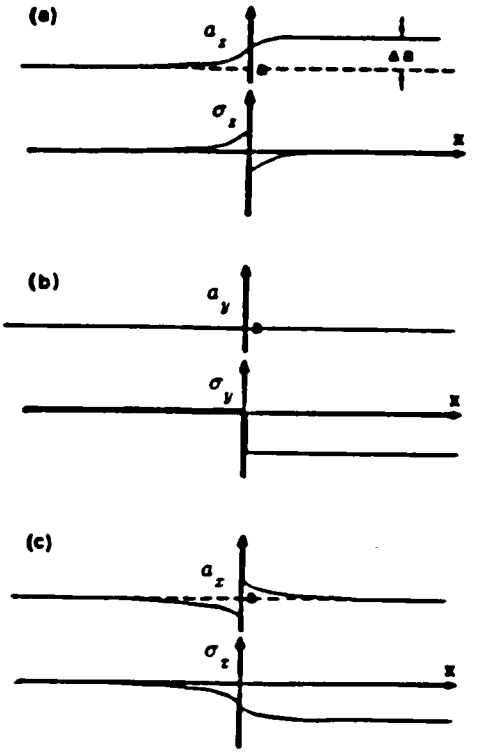

Figure 2-18: Stress and strain at edge of implantation region

At the interface of the implanted and unimplanted regions, the lattice constants and the stresses must satisfy boundary conditions. Since two adjacent cells of the lattice, one on each side of the boundary, must share a common face at the boundary, the dimensions of that face must be continuous across the boundary. Therefore the lattice constants in the y and z directions, a_y and a_z, must be continuous in x. The lattice constant a_y is constrained by the substrate to be constant in x [Fig. 2-18 (b)] while a_z gradually increases from a in the unimplanted area to $a+\Delta a$ in the implanted area. The lattice constant perpendicular to the interface a_x has no boundary conditions to meet, and changes abruptly at the boundary as was mentioned earlier.

Now consider the boundary conditions of the stresses at the boundary. The stress in the x direction σ_x must be continuous in x so that the forces acting on the boundary are balanced. The stress in the implanted region is partially relieved by the expanding of the lattice into the unimplanted region at the same time creating the residual compressive stress in the unimplanted region [Fig. 2-18 (c)]. No boundary conditions are directly imposed on σ_y and σ_z. However, because the implanted lattice would prefer to expand while the unimplanted lattice would prefer to retain its dimensions, the stresses σ_y and σ_z change discontinuously at the interface to maintain the continuity of the lattice constants a_y and a_z. At $x = 0$, σ_y increases suddenly to compress the implanted lattice so that it conforms to the dimensions of the substrate and the unimplanted lattice [Fig. 2-18 (b)]. Meanwhile, the stress normal to the film σ_z changes sign at the interface: the smaller unimplanted lattice is stretched (tensile stress) to fit the larger implanted lattice which, in turn, is compressed [Fig. 2-18 (a)]. There is significant shearing stress σ_{xz} at the interface as indicated by the distortion of the cubic cells in Fig. 2-17. However, since the shearing stress does not seem to contribute to the formation of the charged walls[15], it will be ignored in the following analysis.

Far from the edge in the implanted region, the stresses along the axes x and y are equal and negative while the stress along z is zero as was the case of the thin magnetic film with no boundary discussed in the previous section. As the implantation edge is neared, the stress relief perpendicular to the boundary becomes significant and the magnitude of σ_x decreases, leaving σ_y the most negative principal stress. Due to negative magnetostriction, the y axis becomes the easiest axis of magnetization. Even though σ_x becomes significant at the very near edge of the boundary, it does not contribute much to the formation of the charged wall. The dominant contributing factor in the formation of charged walls turns out to be the stress relief defined as the difference between σ_y and σ_z.

2.5.2. Magnetostrictive Anisotropies at the Pattern Boundary

The magnetostrictive anisotropies at the pattern boundary due to ion implantationare expressed in the following equation using a coordinate system which is referenced to the boundary as illustrated in Fig. 2-19[15].

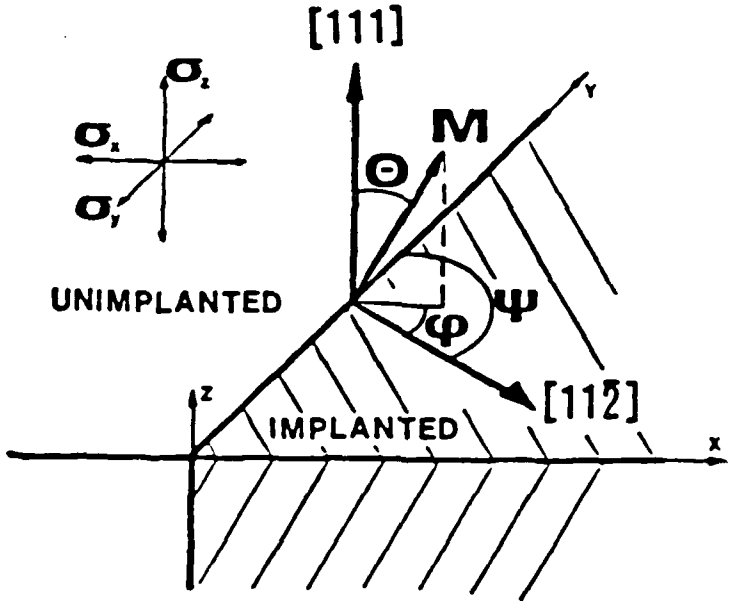

Figure 2-19: Coordinate system

$$E_{us} = -\frac{3}{2}\lambda_{111}\{[(\sigma_x-\sigma_z) + \Delta(\sigma_y-\sigma_z)/6]\cos^2\theta$$

$$+ [(\sigma_y-\sigma_z)(1-\Delta/3)]\sin^2\theta\sin^2\phi$$

$$+ [(\sigma_y-\sigma_z)\sqrt{2}\Delta/6]\sin 2\theta\sin(\phi+3\psi)\}$$

$$= -K_{us}\{[S_3-S_2(\Delta/6)]\cos^2\theta$$

$$+ [S_2(1-\Delta/3)]\sin^2\theta\sin^2\phi$$

$$+ [S_2(\sqrt{2}\Delta/6)]\sin 2\theta\sin(\phi+3\psi)\} \quad (2.37)$$

where θ is the polar angle of the magnetization from the film normal, ϕ is the azimuthal angle of the magnetization from the edge normal (the x-axis), ψ is the angle between the $[1\ 1\ \bar{2}]$ direc-

tion and the implantation edge (the y-axis), $S_2 = (\sigma_y - \sigma_z)/\sigma_p$, $S_3 = (\sigma_z - \sigma_x)/\sigma_p$, $\Delta = (\lambda_{111} - \lambda_{100})/\lambda_{111}$, σ_p is the planar stress far from the edge, λ_{111} and λ_{100} are the magnetostriction coefficients of the cubic garnet film and $K_{us} = 3/2\ \lambda_{111}\ \sigma_p$.

The first term is the uniaxial anisotropy which causes the magnetization to be planar far from the boundary where $\sigma_z = \sigma_y = \sigma_p$. The second term is a uniaxial anisotropy parallel to the y-axis, i.e., parallel to the implantation boundary as shown in Fig. 2-20 (a), where anisotropy directions around an unimplanted disk is shown.

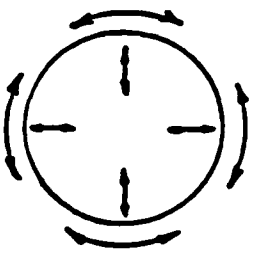

$[S_2\ (1-\Delta/3)]\ \sin^2\theta\ \sin^2\phi$

(a)

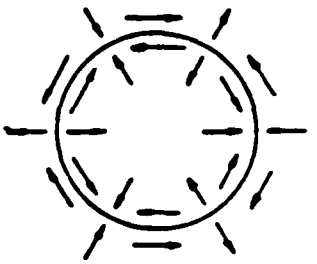

$[S_2\ (\sqrt{2}\ \Delta/6)]\ \sin 2\theta\ \sin(\phi+3\psi)\}$

(b)

Figure 2-20: Qualitative representation of magnetostrictive anisotropies induced by stresses around a nonimplanted disk. Easy magnetization directions of uniaxial anisotropies are illustrated by double-ended arrows. Easy directions of unidirectional anisotropies are shown by single-ended arrows (axial symmetry is broken by the presence of bubble biasing field perpendicular to film).

As will be shown later, this anisotropy is chiefly responsible for the formation of charged walls. Notice that the anisotropy is proportional to the stress relief, $\sigma_y - \sigma_z$. The third term is also proportional to the stress relief and describes a unidirectional anisotropy which varies with orientation of the boundary as illustrated in Fig. 2-20 (b). Due to this anisotropy, a charged wall will prefer to remain at one of the three locations around a nonimplanted disk. This anisotropy is

partially responsible for the three-fold nonuniform motion of the charged wall in bubble devices and will be discussed in detail in the next section.

2.5.3. Charged Wall Formation

Charged walls are formed on both sides of an unimplanted disk as shown in Fig. 2-21.

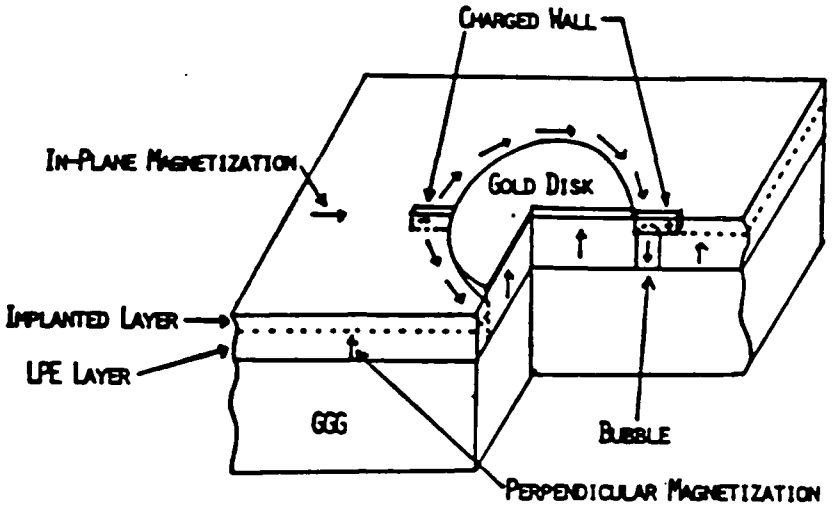

Figure 2-21: Perspective view of an ion implanted device

On the right-hand side of the disk, a positive charged wall is created by the convergence of the magnetization and across the disk on the left-hand side, a negative-charged wall is created by the divergence of the magnetization. A bubble is attracted to an oppositely polarized charged wall. As the applied in-plane field is rotated, the charged wall rotates dragging along the bubble. Actual propagation tracks are formed by contiguously joining many of these propagation elements together as was shown in Fig. 1-3.

Even though researchers were aware that the charged walls were responsible for the propagation of bubbles from early on, the mechanisms of the charged wall formation were not clear for a long time. Initially, Almasi, et al.[29] suggested that the walls form as a result of the magnetization flowing around the nonpermeable disk, i.e., due to demagnetizing effects. This theory was generally accepted until Hidaka and Matsutera[30] and, independently, Backerra[31], et al. indicated that stress gradients due to partial relaxation of the stress at the implanted pattern edges were important to the formation of charged walls. Hidaka and Matsutera found out that demagnetiz-

ing forces around nonpermeable disks were not sufficient to produce charged walls and concluded that the uniaxial anisotropy along the boundary due to stress relaxation normal to the boundary was responsible for the formation of the charged walls. Saunders and Kryder[32] observed domains in a (100) garnet film which indicated that magnetostrictive anisotropies were large enough to overcome demagnetizing effects and that charged walls formed only at points where the magnetostrictive anisotropy was parallel to the boundary.

Hubert explained in hindsight that if only the demagnetizing energy were responsible for the formation of the walls, noncharged walls as shown in Fig. 2-22 (b) would be formed in conjunction with the three-fold crystalline anisotropy[14]. The magnetization directions favored by the anisotropy are shown as arrows in the figure. He reasoned that only if there is a strong uniaxial anisotropy parallel to the boundary, charged walls as shown in Fig. 2-22 (a) would be formed.

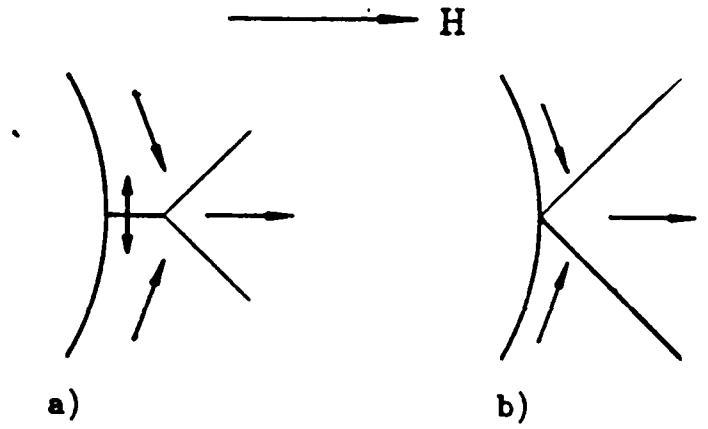

Figure 2-22: (a) The formation of charged walls under the influence of a uniaxial anisotropy with the preferred axis parallel to the implantation edge. (b) Contrasted with the essentially stray-free free-flow pattern possible without that anisotropy.

Saunders explains more clearly in his Ph. D. thesis[33] why a strong anisotropy is necessary to form a highly charged wall. The large uniaxial anisotropy arising from the stress relaxation decreases with distance from the boundary. Such a high anisotropy region is shown in Fig. 2-23. The anisotropy direction is along the y axis. Now consider an isolated 180° domain wall which separates two antiparallel domains and which lies at an angle β to the easy direction. In general, a 180° wall will be oriented parallel to the easy direction ($\beta = 0$) to avoid the formation of free poles on the wall. The wall energy density is proportional to $\sqrt{K}$ and a wall transversing a high

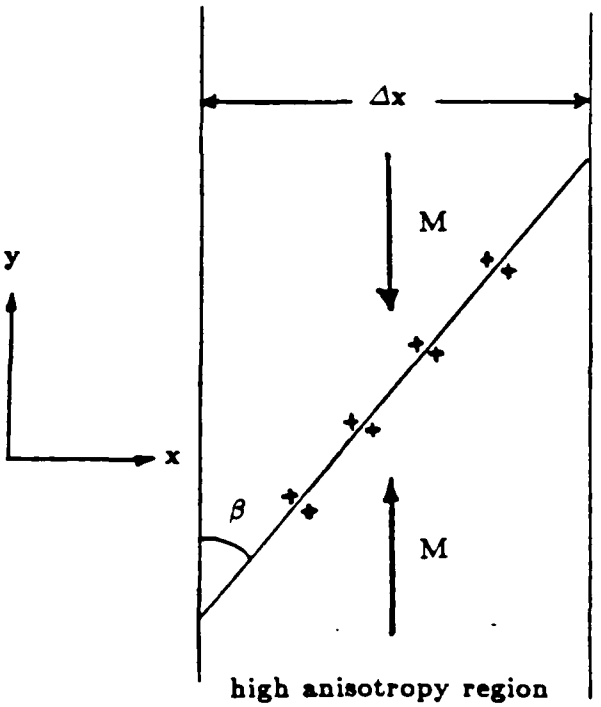

Figure 2-23: Wall in high anisotropy region becomes charged as it reduces its length

anisotropy region (high K) as in Fig. 2-23 will bend (increase β) to reduce the length of the wall in that high anisotropy region to reduce the total wall energy. However, by bending, more free poles are created on the wall thus increasing magnetostatic energy. Therefore, the equilibrium angle of the wall angle β, and the length of the charged wall, is determined by the balance of the magnetostatic energy and the wall energy. The higher the wall energy, the shorter and the stronger the charged wall will become. The pole strength per unit area is described as $Mt \sin\beta$ where t is the thickness of the charged wall, i.e., the depth of the ion implantation. Since the anisotropy decreases with distance from the edge, the wall bends back (decreased β) to reduce the charge as it extends further from the edge. The preceding analysis considered only the wall energy and the magnetostatic energy due to the magnetic charges induced on the wall to explain the formation of the charged wall. In practice, the demagnetizing effect of the boundary, the applied field energies, the magnetocrystalline anisotropy, the three-fold uniaxial magnetostrictive energy and the energy due to the free poles of the bubble should be included to describe the charged wall more accurately.

2.6. Charged Wall (Bubble) Circulation Around an Unimplanted Disk

In the preceding section (2.5), the mechanism of the charged wall formation was described assuming that there were no applied fields and no three-fold anisotropies. In actual bubble devices, there always exists a bias field to stabilize bubbles as was described in Section 2.2. In addition, to manipulate bubbles around, an in-plane rotating drive field has to be applied. The crystalline and magnetostrictive three-fold anisotropies affect the motion of the charged wall greatly and cause nonuniform movement along the propagation tracks. In this section, the charged wall motion under the influence of the applied fields and the three-fold anisotropies will be examined and ways to minimize the three-fold anisotropic propagation will be explored.

2.6.1. Determination of Magnetization Directions and Critical Curves

The stable magnetization orientations ϕ and θ (Fig. 2-2) are obtained by minimizing the total energy of the system. The total energy can be written as the sum of the energy due to the perpendicular uniaxial anisotropy E_u, thin film demagnetizing field E_d, the planar magnetostrictive anisotropy from ion implantation E_{us} [Eq. (2.37)], the planar uniaxial anisotropy also due to ion implantation but which is not magnetostrictive in nature E_{uc}, cubic crystalline anisotropy [Eq. (2.10)] E_1 and applied fields E_a as follows:

$$E = E_u + E_d + E_{us} + E_{uc} + E_1 + E_a \tag{2.38}$$

where

$$E_u = - K_u \cos^2\theta$$

$$E_d = 2\pi M^2 \cos^2\theta$$

$$E_{uc} = K_{uc} \cos^2\theta$$

$$E_{us} = K_{us}\{[- S_3 + S_2 (\Delta/6)] \cos^2\theta - [S_2 (1-\Delta/3)] \sin^2\theta \sin^2\phi$$

$$- [S_2 (\sqrt{2}\Delta/6)] \sin 2\theta \sin(\phi+3\psi)\}$$

$$E_1 = K_1 \{\sin^4\theta/4 + \cos^3\theta/3 + (\sqrt{2}/3) \sin^3\theta \cos\theta \cos 3(\phi+\psi)\}$$

$$E_a = - M \{H_x \sin\theta \cos\phi + H_y \sin\theta \sin\phi + H_z \cos\theta\} .$$

K_u, K_{us} and K_{uc} are the growth-induced anisotropy, the stress-induced anisotropy due to ion implantation and nonstress-related anisotropy (believed to be due to chemical effects), also due to ion implantation. The applied in-plane field and components are H_x and H_y, while the applied bias field is H_z. The coordinate system used is shown in Fig. 2-2.

The stable equilibrium magnetizations are obtained by minimizing the total energy[34]:

$$\frac{\partial E}{\partial \theta} = 0 \text{ and } \frac{\partial^2 E}{\partial \theta^2} > 0 ,$$

$$\frac{\partial E}{\partial \phi} = 0 \text{ and } \frac{\partial^2 E}{\partial \phi^2} > 0 . \qquad (2.39)$$

Due to the complexity of the energy equation, actual calculation of the magnetization distribution, i.e., θ and ϕ is done by computer. However, far away from the implantation edge where the stress relaxation does not have to be included, the polar angle of the magnetization is large, i.e., the magnetization is in the plane if the ion implantation energy (K_{us} + K_{uc}) is large. In that case the polar angle of the magnetization can be approximated as follows:

$$\cos\theta \simeq \frac{H_z}{(H_{us} + H_{uc}) - (H_u - 4\pi M)} \tag{2.40}$$

where $H_{us} = 2K_{us}/M$, $H_{uc} = 2K_{uc}/M$ and $H_u = 2K_u/M$.

The salient features of the domains and charged walls near nonimplanted patterns can be qualitatively explained by investigating the critical curves. The critical curves are the loci of applied field points (H_x, H_y) which satisfy the critical equilibrium conditions

$$\frac{\partial E_\phi}{\partial \phi} = 0 \text{ and } \frac{\partial E_\phi^2}{\partial \phi^2} = 0 \ , \tag{2.41}$$

where E_ϕ represents the collection of terms of Eq. ((2.38)) which depend on ϕ as shown below:

$$\begin{aligned} E_\phi = & - K_{us}\{[S_2(1-\Delta/3)]\sin^2\theta \ \sin^2\phi + [S_2(\sqrt{2}\Delta/6)]\sin 2\theta \ \sin(\phi+3\psi)\} \\ & + \frac{\sqrt{2}}{3} K_1 \ \sin^3\theta \ \cos\theta \ \cos 3 \ (\phi+\psi) \\ & - M \ (H_x \ \sin\theta \ \cos\phi + H_y \ \sin\theta \ \sin\phi) \end{aligned} \tag{2.42}$$

If we rewrite E_ϕ as follows:

$$E_\phi = E_k \ (\phi) - (MH_x \sin\theta \ \cos\phi + MH_y \sin\theta \ \sin\phi) \ , \tag{2.43}$$

E_k is the sum of the anisotropies which include three-fold magnetocrystalline anisotropy, three-fold magnetostrictive anisotropy and uniaxial anisotropy.

In the following subsections, critical curves with various anisotropies will be considered and the magnetization directions under the influence of the in-plane field will be graphically determined using the critical curves.

2.6.2. Critical Curve for Crystalline Anisotropy

If Eq. (2.43) is substituted into Eq. (2.41), the following parametric equations result:

$$H_x = -[E_k'(\phi)\ \sin\phi + E_k''(\phi)\ \cos\phi]/M\ \sin\theta \tag{2.44}$$

$$H_y = -[-E_k'(\phi)\ \cos\phi + E_k''(\phi)\ \sin\phi]/M\ \sin\theta\ . \tag{2.45}$$

For the magnetocrystalline anisotropy of Eq. (2.10) with $K_1 < 0$ and $\theta < 90^\circ$, the parametric equations become

$$h_x = -(2\ \cos 2\phi + \cos 4\phi)\ 3 \tag{2.46}$$

$$h_y = -(-2\sin 2\phi + \sin 4\phi)/3 \tag{2.47}$$

where h_x and h_y are the applied field components H_x and H_y normalized to the effective magnetocrystalline anisotropy field,

$$H_{k1} = 3\sqrt{2}\ |\ K_1\ \sin^2\theta\ \cos\theta\ |/M\ . \tag{2.48}$$

These equations describe a hypocycloid of three cusps as shown in Fig. 2-24.

The vertices point in the hard magnetization directions with the easy directions being antiparallel or pointing out of the cusps (i.e., at $\phi = 0^\circ$, 120° and 240°). The stable magnetization directions are found for an applied in-plane field by drawing tangent lines from the curves to the applied field point, (h_x, h_y). The orientation of the tangent lines is toward the direction of the magnetization. Among the three magnetization directions shown in Fig. 2-24 by three tangent lines, M_3 is metastable since it opposes the direction of the applied field, and M_1 is more energetically favorable than M_2 because its direction is closer to the direction of the applied field. If the applied field lies outside the critical curve only one line can be drawn tangent to the curve, and hence, only one stable magnetization direction exists.

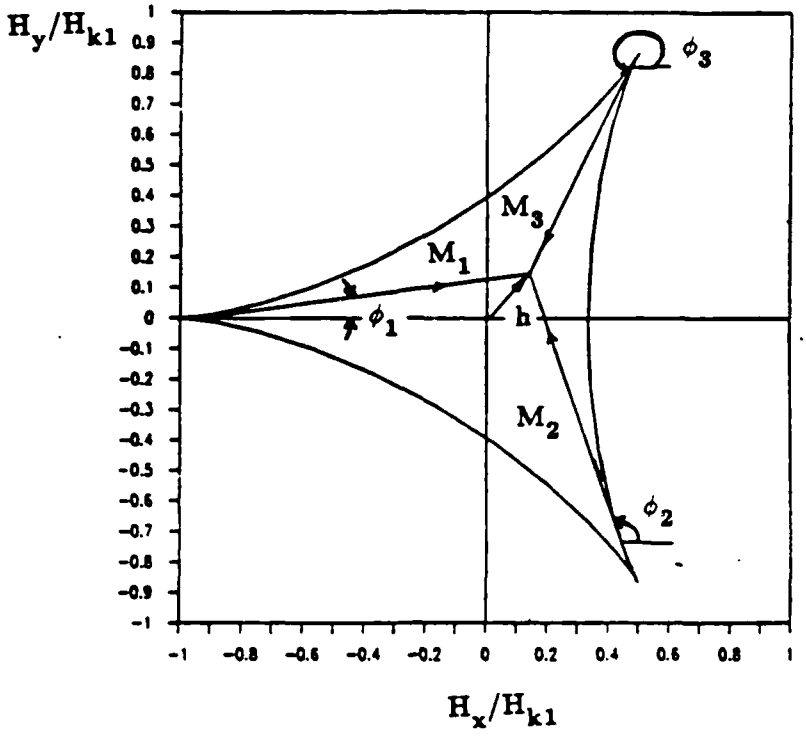

Figure 2-24: Three-fold critical curve for crystalline anisotropy

2.6.3. Critical Curve for Uniaxial Magnetostrictive Anisotropy

For the uniaxial magnetostrictive anisotropy,

$$E_k(\phi) = - K_{us} S_2 (1-\Delta/3) \sin^2\theta \sin^2\phi \quad . \tag{2.49}$$

Employing the same method used for the magnetocrystalline anisotropy, the critical curve turns out to be the well known Stoner-Wolfarth astroid[35] as shown in Fig. 2-25, however with the easy axis at an angle ψ to the $[\bar{1}\ \bar{1}\ 2]$ axis[33]. Two easy magnetization directions which are parallel to the boundary are shown in the figure for the applied field. The effective unaxial magnetostrictive field, H_{kb}, is given as :

$$H_{kb} = H_{us} S_2 (1-\Delta/3) \sin\theta \quad . \tag{2.50}$$

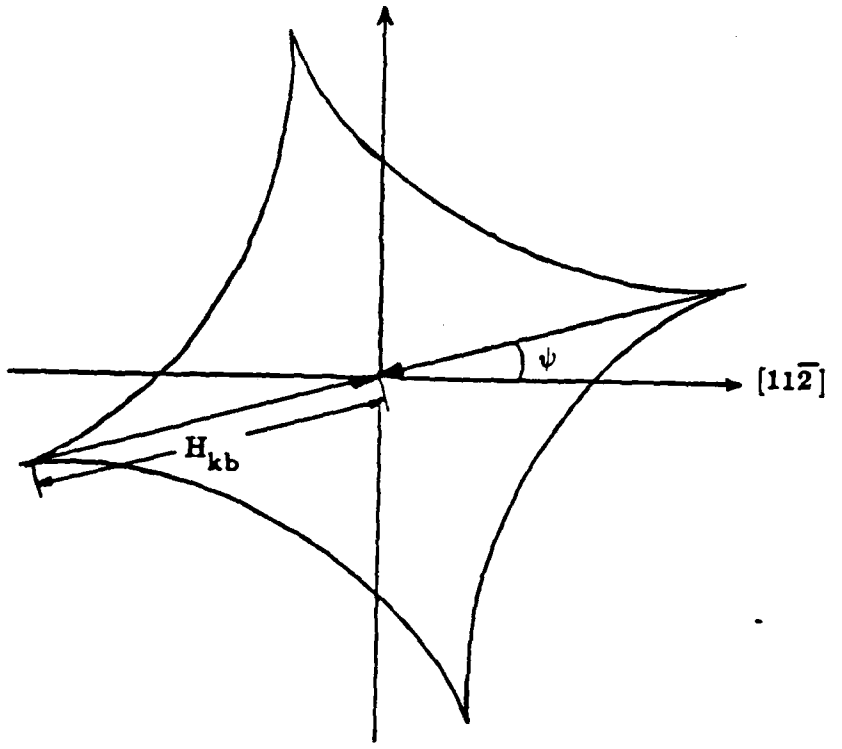

Figure 2-25: Uniaxial astroid of boundary anisotropy, H_{kb}

Near the boundary the magnitude of the effective anisotropy field is generally considered to be much larger than the applied in-plane field and the effect of the applied field is to switch the magnetization from one easy direction to the other in the direction of the in-plane field. A rotating in-plane field thus causes the magnetization at successive locations around a nonimplanted disk to switch from clockwise to counterclockwise (or vice versa) as the field rotates, resulting in the circulation of the charged walls around the disk which is explained with the help of Fig. 2-26.

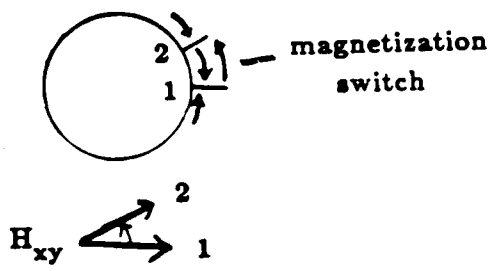

Figure 2-26: Propagation of charged wall around an unimplanted disk

When the in-plane field is pointing to direction 1, a charged wall resides at position 1 of the disk as shown in Fig. 2-26. As the field rotates to direction 2, the magnetizations between position 1 and position 2 switch from clockwise to counterclockwise as shown in the figure to form a charged wall at position 2, thereby circulating a charged wall around the disk (from position 1 to position 2). If the media had no other anisotropy and no coercivity, the walls would closely follow the rotating field. If the in-plane field becomes larger and comparable to the anisotropy field, it will cause the magnetization direction to rotate, from the direction of the boundary and, thus, reduce the strength of the charged wall.

2.6.4. Critical Curve for Mixed Anisotropies

When both magnetocrystalline and magnetostrictive anisotropies are present,

$$E_k(\phi) = \frac{\sqrt{2}}{3} K_1 \sin^3\theta \cos\theta \cos3(\phi+\psi) - K_{us}\{[S_2(1-\Delta/3)] \sin^2\theta \sin^2\phi + [S_2(\sqrt{2}\Delta/6)] \sin2\theta \sin(\phi+3\psi)\} \quad (2.51)$$

For $[1\ 1\ \overline{2}]$ along the x-axis and constant θ, $E_z(\phi)$ normalized to the magnetocrystalline anisotropy can be written as

$$\frac{E_k(\phi)}{MH_{k1} \sin\theta} = \frac{1}{9} \cos3\phi - \frac{h_{kb}}{4} \cos2(\phi-\psi) - h_d \cos(\phi+2\psi) \quad (2.52)$$

where

$$h_{kb} = \frac{H_{kb}}{H_{k1}}, \tag{2.53}$$

h_d is the effective three-fold magnetostrictive anisotropy (H_d) divided by H_{k1},

$$h_d = \frac{H_d}{H_{k1}} = \frac{H_{us} S_2 \ (\sqrt{2}\Delta/6) \ \cos\theta}{H_{k1}} \tag{2.54}$$

and ψ is the angle of the boundary from the $[1 \ 1 \ \overline{2}]$ direction. Using the same method as before, the critical curve is described by

$$\begin{aligned} h_x = H_x/H_{k1} = & - (2 \ \cos 2\phi + \cos 4\phi)/3 \\ & + h_{kb} \ [\sin\phi \ \sin 2(\phi-\psi) + 2\cos\phi \ \cos 2(\phi-\psi)]/2 \\ & + h_d \ \cos 2\phi \end{aligned} \tag{2.55}$$

$$\begin{aligned} h_y = H_y/H_{k1} = & - (-2 \ \sin 2\phi + \sin 4\phi)/3 \\ & + h_{kb} \ [-\cos\phi \ \sin 2(\phi-\psi) + 2\sin\phi \ \cos 2(\phi-\psi)]/2 \\ & + h_d \ \sin 2\phi \ . \end{aligned} \tag{2.56}$$

This curve is very complicated and only a couple of cases of interest, where the boundary is parallel to the x-axis ($\psi = 0^\circ$ or 180°) and the boundary is parallel to the y-axis ($\psi = -90^\circ$

or 90°) are considered[33]. In both cases, the critical curves have the same shape as shown in Fig. 2-27 for $h_{kb} = 1$ and $h_d = 0$.

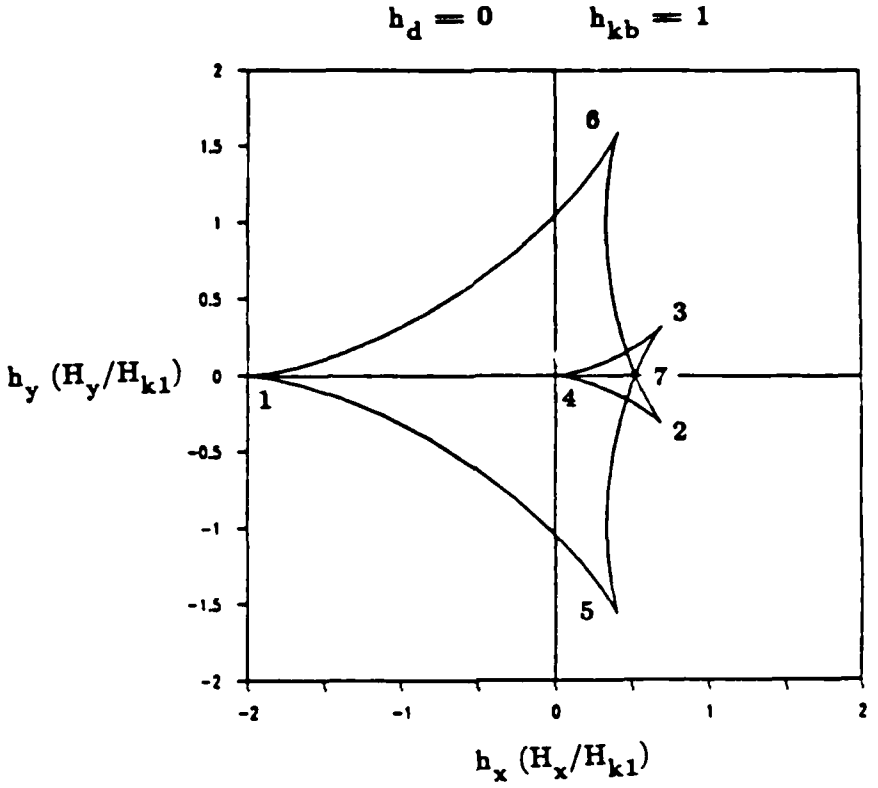

Figure 2-27: Critical curve for mixed anisotropy

As in other critical curves, the stable magnetization directions are found by drawing tangent lines from the vertices to the applied field point (h_x, h_y). For the case where the boundary is parallel to the x-axis, the stable magnetization directions are found by using the three vertices marked 1, 2 and 3. When the boundary is parallel to the y-axis, the vertices 4, 5 and 6 are used. For field points inside the curve, there are at least two stable magnetization directions, sometimes three. Outside of the curve, only one magnetization direction is stable.

2.6.5. Critical Curve for Charged Wall

Saunders in his Ph.D. thesis[33] proposed a critical curve for charged walls (not for magnetization). He constructed the curve the same way as the other critical curves were drawn. First, the energy difference across a stable wall in the presence of a field h along ϕ_h is obtained using Eq. (2.52):

$$\frac{\Delta E}{MH_{k1}\ \sin\theta} = (h_d+1/9)\ \sin 3d\ +\ h\ \sin(\alpha-\phi_h) \tag{2.57}$$

where α is the angle of the normal of the boundary from the $[1\ \ 1\ \ \bar{2}]$ direction ($\alpha = \psi - 90^\circ$). The magnetization directions on either side of the wall are $\alpha + 90^\circ$ and $\alpha - 90^\circ$. They are assumed to be parallel to the boundary due to the strong uniaxial magnetostrictive anisotropy along the boundary. Noticing that ΔE is normalized to E_ϕ [Eq. (2.43)], Eq. (2.57) is substituted into Eq. (2.41) as usual and the critical curve for the charged wall is obtained in Fig. 2-28 (for a negative charged wall).

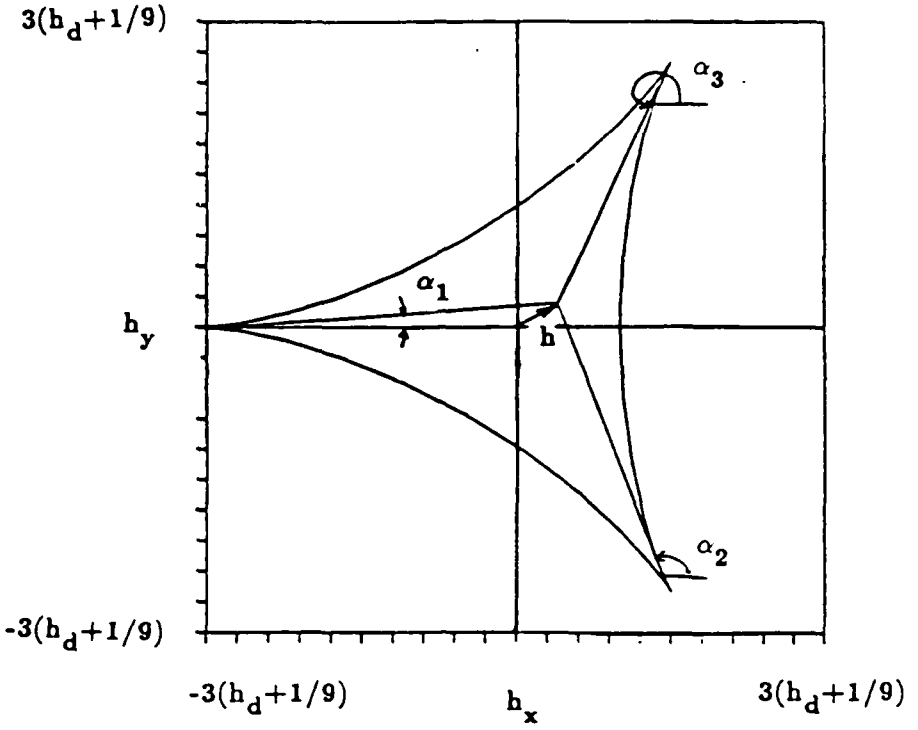

Figure 2-28: Critical curve for charged wall

This is the same shape as the critical curve for the crystalline anisotropy (Fig. 2-24) except the size of the curve. The position of the charged wall is found by drawing a tangent from the curve to the applied field point. There are three stable charged wall positions when the field is inside the curve and only one outside of the curve. For zero field the stable positions are at 0°, 120° and 240°. The locations of the positive charged walls are 180° apart from the negative charged walls. Therefore the stable positions for positive charged walls are at 60°, 180° and 300°.

2.6.6. Minimum Circulation Field

The bubble attached to a charged wall circulates around a nonimplanted disk nonuniformly jumping from one of the three stable positions to the next at low drive field. If the rotating field is lowered still further, the bubble ceases to circulate. The rotating field where the bubble starts to circulate is called the minimum circulation field. The minimum circulation field has been

deduced using the critical curve for the magnetocrystalline anisotropy (Fig. 2-24). This calculation is based on the fact that once the drive field is large enough that the field lies outside the critical curve, there exists only one stable magnetization direction and there cease to exist three favored directions of magnetization. Therefore, the magnetizations switch freely under the influence of the drive field and the charged walls thus created move freely around the disk. The critical curve crosses the h_x axis at 1/3, i.e., 1/3 H_{k1} which was designated to be the minimum circulation field, because the field lies mostly outside the curve during the circulation if the circulation field is larger than this.

Recently, as the importance of the magnetostrictive anisotropy due to the stress relaxation was recognized, Saunders included this effect in obtaining the minimum circulation field. As was shown in the previous subsection, he constructed the critical curve for the charged wall which has the same shape as the critical curve for crystalline anisotropy. From the curve, the minimum circulation field is deduced to be h_d + 1/9, (i.e., 1/9 H_{k1} + H_d). It turns out that this formula gives higher estimates than the experimental results in many cases. The reason is believed to be at least partly due to the fact that the domain configurations near the minimum drive are influenced by the magnetizations far from the implantation pattern edge (see the next subsection) where the influence of the magnetostrictive anisotropy is negligible. Therefore, the contribution of the magnetostrictive anisotropy is exaggerated at low drive field. At higher drive, the domains around the disk that determine the charged wall shrink and most of the magnetization is under the strong influence of the three-fold magnetostrictive anisotropy. It is then expected that both the magnetocrystalline and magnetostrictive anisotropy contribute substantially in determining the domain shapes and the charged wall behavior.

2.8.7. Anisotropic Charged Wall Behavior Around a Disk

Propagation of charged walls around a nonimplanted disk is shown in Fig. 2-29. These are artist's renditions of the actual Bitter patterns of domain walls in the ion-implanted layer (see Chapter 3 for Bitter pattern), which are formed by fine magnetic particles suspended in colloidal solution. The particles are attracted to the stray flux emanating from the domain walls and the walls are made visible by the presence of the particles. The directions of the magnetization in the domains are interpreted with the help of the critical curve for the crystalline anisotropy (Fig. 2-24). As mentioned in the previous subsection, the directions of the magnetization in the domain are mostly determined by the magnetocrystalline anisotropy except those of the magnetizations very near to the edge. Due to magnetocrystalline anisotropy, there are three easy magnetization directions, m_1, m_2, m_3 which are along [1 1 $\bar{2}$], [$\bar{2}$ 1 1] and [1 $\bar{2}$ 1] crystalline directions.

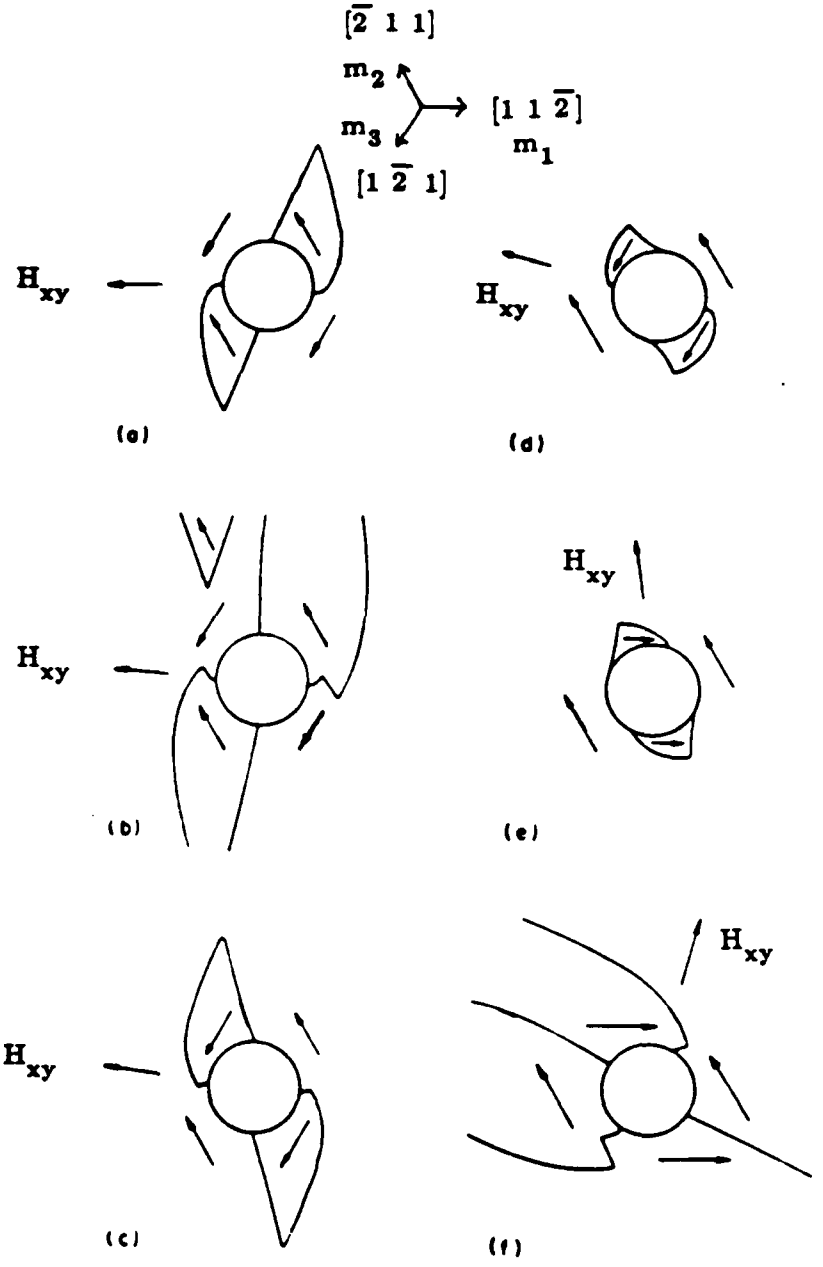

Figure 2-29: Propagation of charged walls around a nonimplanted disk

When an in-plane field is applied in a hard magnetization direction (antiparallel to $[1\ 1\ \bar{2}]$) the implanted region is divided into two domains, one with magnetization m_3 and the other with m_2. If the applied field is slightly closer to the m_3 direction, the m_3 domains are favored and most of the implanted layer will be m_3 domains. However, m_2 domains are also present where magnetostrictive anisotropy and demagnetizing effects favor their formation. Near the non-implanted disk, the magnetization conforms to the disk edges and charged walls form. As the charged walls extend from the disk, they bend to decrease their net charge as was explained in Subsection 2.3.5. Because the m_3 domain is favored over the m_2 domain, the walls bend to encase the m_2 domain and a propeller domain is formed. As the field is rotated counterclockwise toward the m_2 direction, the m_2 domains become favored over the m_3 domains and the propeller domains grow at the expense of the ambient domain as shown in Fig. 2-29 (b). After much wall motion, m_3 domains become propeller domains and m_2 domains become ambient domains. While all of this is happening the portions of the charged walls attached to the disk remain relatively stationary. This motion of the walls is known as whipping. As the field is further rotated clockwise toward the m_2 direction, the m_3 propeller domain becomes less favored and contracts. As the domain contracts, the charged wall is moved in the direction of the field. However, the rotation of the wall around the disk lags the rotation of the field because of the impediment of the still-stable propeller domain. When the field is rotated through the m_2 direction, the propeller domain switches its magnetization direction to the m_1 direction as shown in Fig. 2-29 (e). This sudden reversal of the magnetization in the propeller domain is known as flipping. As the field is further rotated, the whipping motion again occurs, followed by the flipping. This cycle of whipping and flipping is repeated three times for each rotation of the charged wall and the charged wall lags and leads the in-plane field alternatively. The orientation of the charged wall with respect to the in-plane field is depicted in Fig. 2-30 for $H_{xy} = H_{k1}/3$ using the crystalline anisotropy critical curve (Fig. 2-24).

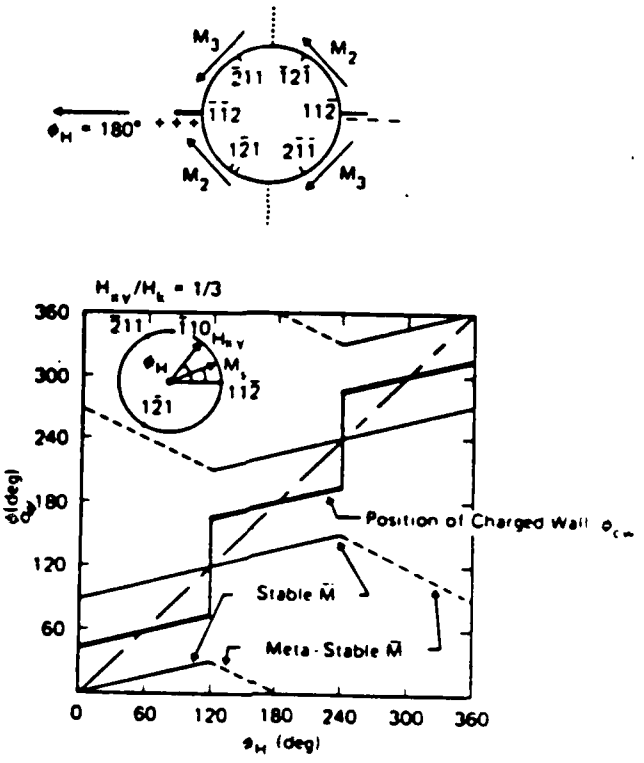

Figure 2-30: Orientation of charged wall ϕ_{cw} vs. that of H_{xy}, ϕ_H for H_{xy}/H_{k1}=1 3

The position of the charged wall is midway between the two stable magnetization directions as shown in the figure. It is to be noted that the position of the charged wall depicted here is obtained considering only the magnetocrystalline anisotropy for $\theta < \pi/2$ and the magnetostrictive anisotropy might affect the position of the charged wall somewhat as was noted above.

2.6.8. Isotropic Propagation

One of the major difficulties that has confronted the designers of the ion implanted devices has been the anisotropic propagation of bubbles. Unlike in permalloy devices, bubble propagation in ion implanted devices is much more difficult in certain crystal orientations than in other directions. Typical bias margins[11] for propagation tracks oriented in $[\bar{1}\,\bar{1}\,2]$ and $[\bar{1}\,10]$ directions are shown in Fig. 2-31.

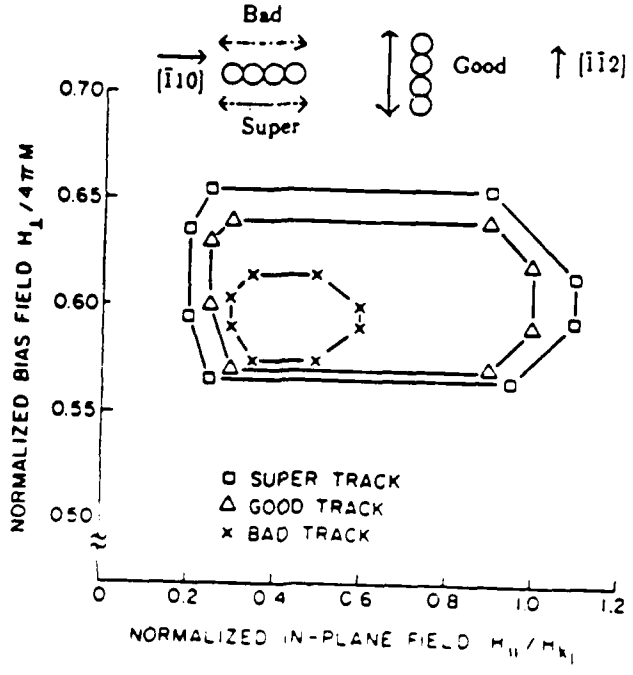

Figure 2-31: Average quasistatic operating margins for propagating 1 μm bubbles based on large amount of experimental data. Bias margin is normalized to $4\pi M$ (600 G). The in-plane field is normalized to an effective crystalline field H_{k1} [11]

The bias margin is the figure of merit of the bubble device. It indicates the bubble device operating range in the bias field - drive field plane. If both applied fields are located inside the curve, the bubbles propagate properly. As is shown in Fig. 2-31, the bubbles propagated on one side of the tracks (bad tracks) oriented in $[\bar{1}10]$ direction have a much smaller bias margin than the bubbles on the other side of the tracks (super tracks) . The bubbles on the tracks oriented in $[\bar{1}\,\bar{1}\,2]$ direction propagate equally well on both sides of the tracks and those tracks are called good tracks. As is clear from the figure, we have to avoid bubble propagation in bad tracks to have reasonably good overall bias margins. This has posed a considerable difficulty to bubble device designers as was indicated earlier. For example, with the double major line architecture shown in Fig. 1-6, where minor loops are aligned as good tracks, one side of the major line is a super track and the other a bad track. Therefore we are limited to using only one side of the major lines. Then the bubbles have to be transferred across the unimplanted region of a major line which decreases the bias margin. Another example is the folded minor loop design shown in

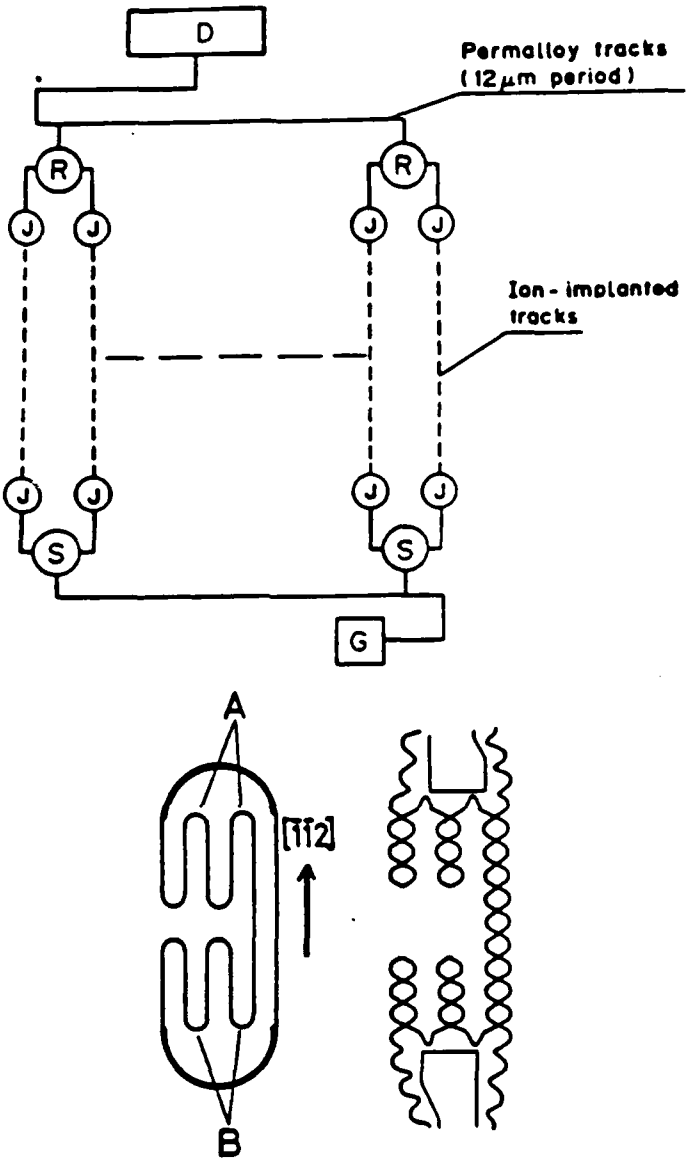

Figure 2-32: Permalloy and ion implanted hybrid devices

Fig. 2-32. This was once considered for minor loops for permalloy and ion implanted hybrid devices[36] which use permalloy major tracks and ion implanted minor loops, but quickly abandoned. The reason was that the *bottom* bubble path as aligned in the figure, constitutes a bad track, and the bias margin there was unacceptable.

The three-fold anisotropic propagation of the charged wall and, hence, the bubbles were initially believed to be due to the three-fold magnetocrystalline anisotropy. However, later findings suggest that three-fold magnetostrictive anisotropy also plays an important role in determining the charged wall motion. According to Hubert[14] and Saunders and Kryder[15], isotropic propagation can be achieved by adjusting the magnetostriction coefficients λ_{111} and λ_{100} to cancel out the effect of the cubic crystalline anisotropy. Hubert made calculations of position and shape of charged walls attached to the unimplanted disks as a function of rotating in-plane field direction. These indicated that the magnetocrystalline anisotropy causes only a small part of the three-fold phase lag and lead of the charged wall with respect to the applied field. The majority of the phase difference is attributed to the magnetostrictive anisotropy which arises due to the anisotropic magnetostriction (unequal λ_{111} and λ_{100}, i.e., $\Delta \neq 0$).

Attempts have been made to make the charged wall propagation more isotropic by decreasing $\Delta \left(= (\lambda_{111}-\lambda_{100})/\lambda_{111}\right)$ which is proportional to the magnetostrictive anisotropy $H_d\left(= H_{ss}\ S_2\ \Delta\ \sqrt{2}/6\ \cos\phi\right)$. Makino, et al.[37] grew garnet films with $\Delta = 0.6$ and $\Delta = 1.3$ and compared the difference of the propagation behavior. They reported about 10 Oe decrease in the minimum drive field of an isolated disk (from 20 Oe to 10 Oe) and a similar decrease for close-packed minor loops for the more isotropic films ($\Delta = 0.6$) compared with more conventional films ($\Delta = 1.3$). This result seems to be quite encouraging since the factor of two decrease of Δ resulted in the same decrease of minimum drive. However, the results by Fratello, et al.[38] showed almost no change in minimum drive field when Δ was changed from 1.2 to 0.2. They also reported that the Ferrofluid Bitter patterns around unimplanted circles did not change noticeably in spite of the substantial reduction of Δ, i.e., the magnetostrictive anisotropy. These results are similar to our experimental results which will be discussed in Chapter 5. We did not observe significant changes in minimum drive field or Ferrofluid Bitter patterns of unimplanted disks. This may not be that surprising if the domain magnetizations, thus, charged walls especially at low drive fields are substantially determined by the cubic magnetocrystalline anisotropy and the three-fold magnetostrictive contribution becomes substantial at high drive fields as was suggested earlier. The effect of the change of Δ is manifested more clearly in the increase of the collapse field of the "bad" propagation tracks, which will be discussed in Chapter 5. By decreasing Δ to one-third, nearly isotropic bubble propagation in closed packed propagation tracks was obtained[39].

2.7. Bubble Propagation Bias Margin

A bias margin is a curve in the $H_b - H_{xy}$ plane (Fig. 2-31) bounded by a minimum drive field H_{xy} (min) on the left side, bubble collapse fields on the top side and bubble stripeout fields on the bottom side. The right side of the curve is usually open for practical in-plane fields used but closed out for higher in-plane drive fields. The wider the bias field range and the smaller the minimum in-plane drive field, the better the bubble devices are. Devices with wider bias margins can withstand bias field variations due to ambient temperature variations, chip to chip performance variations, etc. Lower drive field means lower current necessary to operate the device, which amounts to lower power consumption essential to portable equipment, space and military applications, etc. In this section, theoretical models to estimate the bounding field values of the bias margin will be presented.

2.7.1. Minimum In-Plane Drive Field

In Subsection 2.6.6, the minimum circulation field for a nonimplanted disk was considered and estimated to be

$$H_{xy}\ (\min)_{disk} = \frac{H_{k1}}{9} + H_d \tag{2.58}$$

where H_{k1} is the effective magnetocrystalline anisotropy field and H_d is the contribution from the three-fold magnetostrictive anisotropy field. For implanted propagation tracks whose typical patterns are shown in Fig. 1-3, the minimum drive field is larger than that of a simple disk. As the long adjacent tracks are placed closely together to increase the memory density, the magnetization in the ion-implanted region experiences additional shape anisotropy due to the demagnetizing fields. Best[40] first considered this problem. He modeled the propagation pattern edges as straight lines and the ion-implanted region between two tracks as a long ellipsoid. Using the shape anisotropy energy of a long ellipsoid, a critical curve similar to Fig. 2-27 was obtained. Employing the argument that the applied in-plane field should lie outside of the curve most of the time to insure smooth charged wall propagation, the additional in-plane field needed to move bubbles in the close-packed tracks was estimated to be $2\pi Mt/(t+W)$ where W is the average distance between the tracks. Thus the minimum drive field of the close-packed tracks is

$$H_{xy}\ (\min) = H_{xy}\ (\min)_{disk} + 2\pi Mt/(t+w)\ . \tag{2.59}$$

B. A. Calhoun and I. L. Sanders[41] surveyed 11 published papers giving data for the minimum drive fields of the close-packed tracks and found that the minimum drive fields follow the above relationships (Eq. (2.59)) reasonably well, but not without considerable deviations (about 7 Oe) from the best fit straight line.

2.7.2. Bubble Collapse Fields

The bubble experiences a potential well from the charged wall H_{cw}, the edge affinity[6] H_{ed} and the surface magnetic charges H_{sc} (when there exists an in-plane field) at the edge of the unimplanted pattern. The potential wells due to the charged wall, the edge affinity and the surface magnetic charges are obtained from the distributions of the perpendicular magnetic field components produced by the charged wall, the magnetization in the unimplanted pattern of thickness equal to the thickness of the implanted layer and the demagnetizing boundary surface magnetic charges induced by the in-plane field, respectively. The collapse field for a bubble circulating around an unimplanted disk is given by the sum of the collapse field of a free bubble $H_{o,f}$ and the potential wells due to the charged wall $H_{cw}{}^{+}$, the edge affinity $H_{ed}{}^{c}$ and surface magnetic charge $H_{sc}{}^{c}$, as follows[42]:

$$H_{o,c} = H_{o,f} + |H_{cw}{}^{+}| + |H_{ed}{}^{c}| + |H_{sc}{}^{c}| \ . \tag{2.60}$$

Now consider the collapse field of the bubbles that propagate along a propagation track. During propagation, bubbles are actually in motion only about one-third to one-fourth of the rotating field cycle and remain in the cusp for the rest of the propagation period. While a bubble is residing in a cusp it not only loses the attractive potential well from the charged wall which carried it along, but has to survive the interaction with an opposing charged wall. At high bias field, this results in collapse of the bubble in the cusp. This is generally the case when the propagation tracks are aligned as bad tracks. For good tracks, the opposing charged wall is not as strong as for bad tracks and the bubble collapse may actually happen while the bubble is moving along the tracks. In most cases, the bubble collapses when it crosses the easy magnetization direction, i.e., the flip direction. This is because the charged wall is the weakest when it is in the flip direction. The minimum collapse field of the bubble in the propagation track when the bubble collapses at the cusp can be expressed as

$$H_{o,p} = H_{o,f} + |H_{cw}| + |H_{ed}| + |H_{sc}| \tag{2.61}$$

$$= H_{o,f} - |H_{cw}^{-}| + |H_{ed}^{c}| + |H_{ec}^{c}| \tag{2.62}$$

where $H_{o,p}$ is the minimum bubble collapse fields during propagation, H_{cw}^{-} is the potential well due to a repulsive charged wall, H_{ed}^{c} is the edge affinity in the cusp and H_{ec}^{c} is the potential well due to the surface magnetic charge in the cusp.

Fukushima and Hayashi[43] calculated the potential well of a bubble for a cycle of the in-plane field from the distribution of the magnetizations around a continuous disk ion-implanted propagation track. They obtained the magnetization distribution by numerical integration of the Landan-Lifshitz-Gilbert equation[16]. The energy terms included were exchange, uniaxial anisotropy, crystalline anisotropy, stress-induced anisotropy, external field, and demagnetizing field. The calculated collapse fields along with the measured values for bubbles on the good track are plotted in Fig. 2-33.

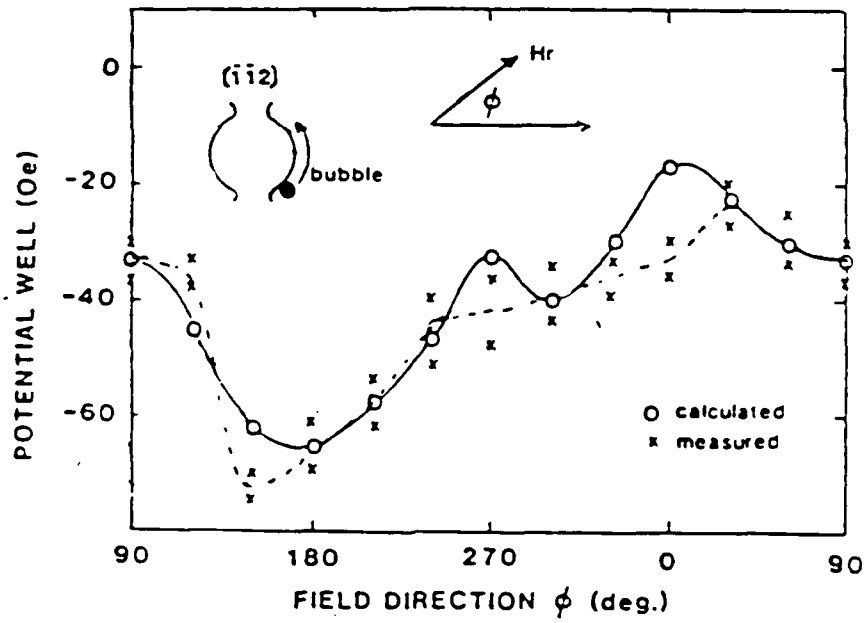

Figure 2-33: Bubble potential well as a function of in-plane field direction

The shallowest potential well, thus, the minimum bubble collapse field occurs when the bubble is moving along the track near the charged wall flip direction (30°) as was mentioned earlier.

Chapter 3
Experimental Methods

3.1. Design and Fabrication of Devices

3.1.1. Magnetic Garnet Films

3.1.1.1. Garnet Film Design

Material design of magnetic garnet films is simplified by the fact that the garnet system will accept a large range of substituted ions into the basic $\{RE_3\}$ $[Fe]$ (Fe_3) O_{12} formula, here { } stands for the dodecahedral, [ ] for the octahedral and ( ) for the tetrahedral lattice sites. To design a garnet film of bubble diameter d, the minimum quality factor Q for the bubble diameter is first chosen from Fig. 3-1[44]. The characteristic length of the film l is chosen to be $d/9$. Bubble height has usually been chosen to be $9l$, but a recent trend is toward shorter bubbles. From Q and l, the values of $4\pi M$ and K_u are calculated. The composition is designed to meet these requirements with the condition that the lattice constant of the film is reasonably well matched to that of the GGG substrate. The amount of iron and iron substitutes, such as Al and Ga in octahedral.and tetrahedral positions control the magnetization, exchange constant, and Curie temperature.

Rare-earth or other substituent ions are incorporated into dodecahedral sites to achieve the desired anisotropy energy, lattice match and magnetostriction constants. To increase the memory density, the bubble size and the propagation element dimensions have to be decreased, As the bubble size becomes smaller, it is increasingly difficult to achieve the necessary magnetic anisotropy of the garnet films. According to the scaling rules developed by Kryder[44], the requirements of Quality Factor Q and $4\pi M_s$ are approximately 2 and 1100 Gauss, respectively for 0.5 μm bubbles as shown in Figs. 3-1 and 3-2.

Therefore, the H_k needed is about 2200 Oe. Films containing Bi provided the necessary anisotropy for the studies here . In addition, they give excellent visibility of bubbles due to the

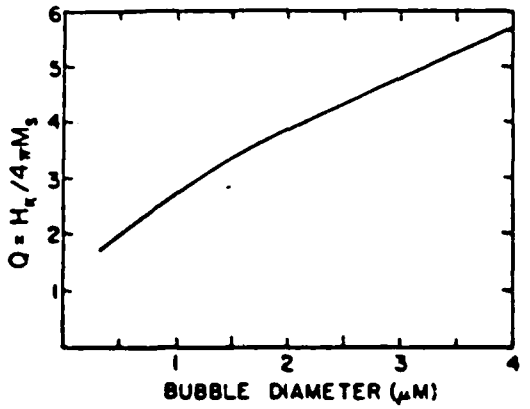

Figure 3-1: The required Q as function of bubble diameter for ion implanted contiguous disk devices[44]

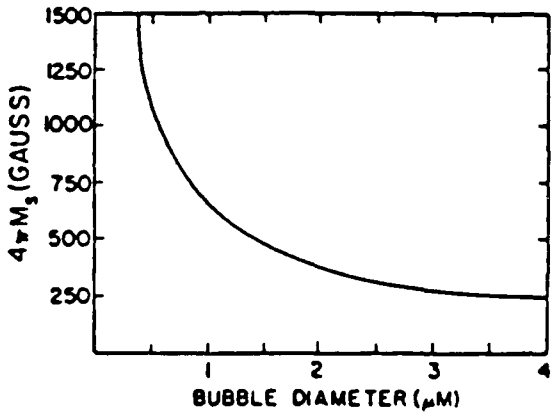

Figure 3-2: The required $4\pi M_s$ as function of bubble diameter for ion implanted contiguous disk devices[44]

high Faraday rotation which is extremely important in observing small bubbles. Another advantage of Bi incorporation was the wide temperature range of the devices fabricated with these films.

To develop isotropic material Dy (dysprosium) is incorporated. Both bismuth and dysprosium iron garnet have

$\lambda_{100} < \lambda_{111}$ while most other rare-earth iron garnets have $\lambda_{111} < \lambda_{100}$. By careful selection of film constituents it was possible to obtain nearly isotropic films. Another requirement for λ_{111} is that it should be negative and large to make large negative anisotropy change possible by ion implantation.

To aid in the film development, a computer program written by Robert Campbell[45] was used to estimate the magnetic parameters of films of various compositions. The program is based on the assumption that properties of films containing several constituents can be calculated from the known properties of single constituent rare-earth iron garnets such as $Sm_3Fe_5O_{12}$, $Y_3Fe_5O_{12}$, $Dy_3Fe_5O_{12}$ and $Lu_3Fe_5O_{12}$. Computer analysis provided several acceptable compositions from the $\{DySmLuYBi\}_3$ $[FeGa]$ $(O)_{12}$ film system that would have isotropic magnetostriction, desired bubble diameter, and an acceptable quality factor Q.

3.1.1.2. Characterization[45]

Film Thickness

A very important measurement of film characteristics is to determine the film's thickness, because it is the basis for determining other important parameters of the films. High accuracy in film thickness measurement is therefore desired. The method used to determine thickness makes use of the difference of the indices of refraction in the GGG substrate and in the LPE film. Because the index of refraction of the film depends nonlinearly on wavelength and is suitably different from that of the GGG substrate, the interfaces of air-to-film and film-to-substrate reflect light. These two reflected beams of light interfere constructively or destructively depending upon the wavelength of the light and the thickness of the film. By scanning the wavelength of light and making an interference trace, the thickness may be calculated from

$$t = \Delta N/2 \; [(n_1/\lambda_1) - (n_2/\lambda_2)] \tag{3.1}$$

where ΔN is the number of maxima or minima between λ_1 and λ_2, and n_1 and n_2 are the refractive indices at their respective wavelengths. An interference curve from a 3.25 μm thick Bi – Dy film is shown in Fig. 3-3.

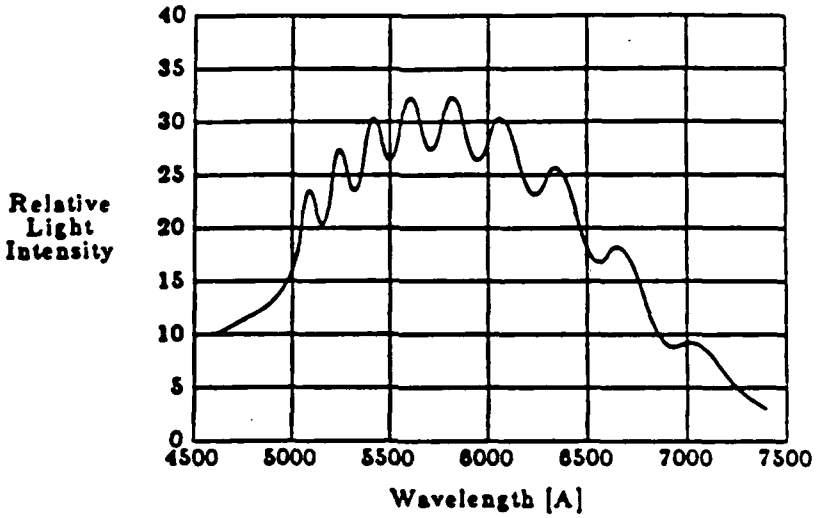

Figure 3-3: Typical film's optical interference trace

Characteristic Length and Magnetization

The characteristic length (l) and the magnetization ($4\pi M$) are determined from measurements of the stripe domain width and the bubble collapse field once the film thickness is known. The stripe domain width and the bubble collapse field are measured using a polarizing microscope (see Section 3.2) with which stripeout and bubble domains can be optically seen due to the Faraday magneto-optic effect. Actually a period of stripe domains (P_o) which is defined as the combined width of an up domain and a down domain as shown in Fig. 1-1 is measured. The relationship between P_o and l are plotted in Fig. 3-4 where h is the thickness of the film.

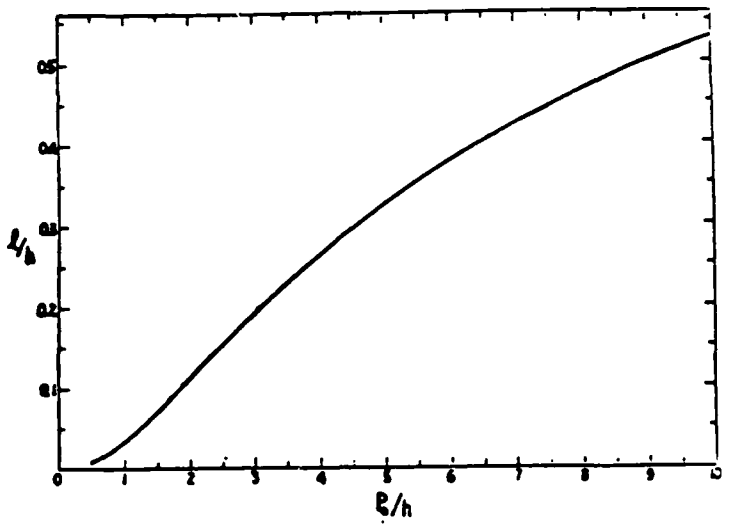

Figure 3-4: Plot of l/h versus P_o/h

The magnetization is determined to high accuracy from the following equation by Fowlis and Copeland[46]:

$$4\pi M_S = H_o/[1+3l/4h - (3l/h)^{1/2}] \quad (3.2)$$

Magnetic Anisotropies, Magnetostriction Coefficients, Gyromagnetic Ratio and Damping Parameter Using FMR

Ferromagnetic resonance (FMR) is used to measure magnetic anisotropies such as uniaxial anisotropy (H_k) and cubic crystalline anisotropy (H_1), and magnetostriction coefficients. The samples for FMR measurements are usually diced into small chips (typically 1 cm x 1 cm) and are put in a resonant cavity[47]. However, a stripline minibox[21] is used instead of a cavity if a whole wafer is desired to be used. The FMR apparatus is shown in Fig. 3-5. It includes a wide band microwave spectrometer for the stripline or the stripline measurements or a klystron microwave generator for the resonant cavity measurements, and a DC magnetic field generator capable of up to 10K Gauss. Microwave frequencies of 4.5 GHz to 7.5 GHz were used for the stripline measurements and 9.36 GHz for the resonant cavity measurements.

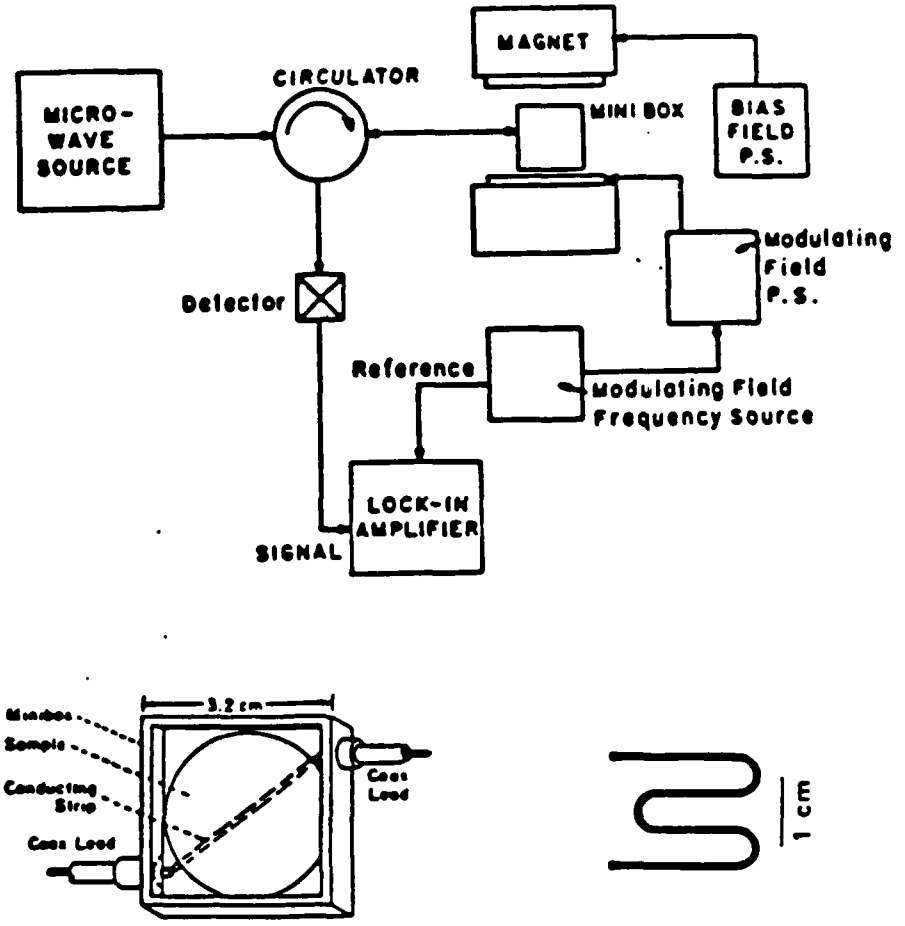

Figure 3-5: FMR apparatus and minibox

The ferromagnetic resonance condition for resonance about an applied DC field H_{dc} perpendicular to the plane of the film is given as

$$w/\gamma = H_{dc} + H_{eff} , \tag{3.3}$$

where $H_{eff} = H_k - 4\pi M_s$, ω is the microwave exciting frequency, γ is the gyromagnetic ratio, H_{eff} is the effective anisotropy field of the film and H_{dc} is the applied perpendicular field. Both γ and H_{eff} can be determined from the measurements of resonance fields H_{dc} at two or more different frequencies. From these measurements, a straight line plot of ω vs. H_{dc} is made. From the

slope of the line and the intercepting point of the H_{dc} axis by the line, γ and H_{eff} are, respectively, determined. The magnetic damping can also be determined from FMR. The damping λ' is directly related to α, the Gilbert damping parameter, where α is experimentally measured using the FMR linewidth at resonance:

$$\alpha = (3)^{1/2} \Delta H_{p-p}/(2\omega/\gamma) \tag{3.4}$$

where ΔH_{p-p} is the full width at half maximum of the resonance absorption curve.

The use of a minibox allows a simple nondestructive measurement (use of a whole wafer instead of a small piece of it) of the magnetostriction coefficients by placing the sample on a teflon O-ring and applying vacuum to the nonfilm side of the sample causing compressive stress in the film. The stress in the film creates an induced magnetostrictive anisotropy which shifts the resonance field. From this shift, λ_{111}/M_s can be determined as follows:

$$\lambda_{111}/M_s = 2\ \delta H_{111}/(\sigma_v) \tag{3.5}$$

where δH_{111} is the shift of the resonance peak between the vacuum and normal pressure conditions and σ_v is the stress. An example of absorption derivative resonance curves for the measurement of the magnetostriction coefficient is shown in Fig. 3-6.

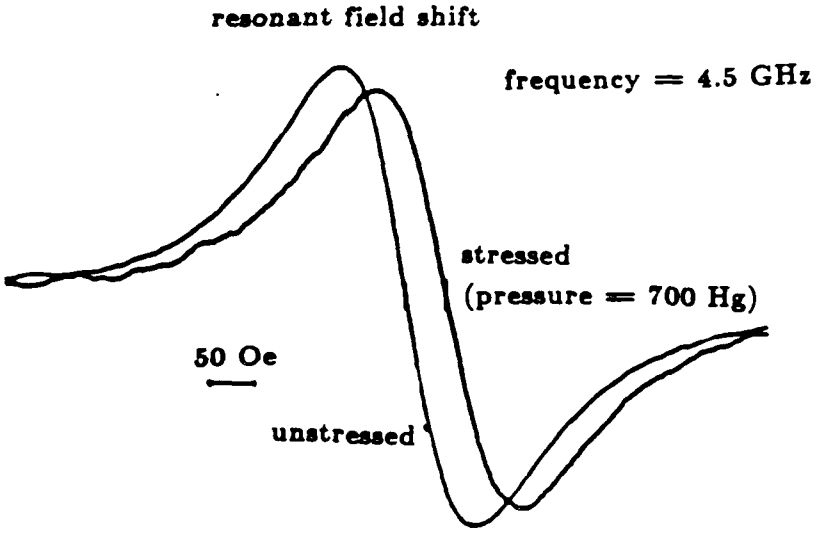

Figure 3-6: Typical resonance curves for stressed and unstressed film[21]

The magnetostriction coefficients along [1 1 1] and [1 0 0] directions of the garnet crystal are determined using films grown on [1 1 1] and [1 0 0] oriented substrates, respectively.

The cubic crystalline anisotropy field in magnetic garnets is obtained by measuring the resonance field at several selected angles. The film is aligned so that the field is applied in the $[\bar{1}\,10]$ plane. The sample is rotated about the $[\bar{1}\ \ \bar{1}\ \ 2]$ direction. The value of H_1 is obtained by comparing resonance fields at the measured angles with those calculated based on an assumed H_1 value. Wang et al.[48]. developed a graphical method for determining H_1 from the resonance fields at 0°, 70°, 90° and 110° applied field angles. This method was used to determine the H_1 value.

The uniaxial anisotropy change ΔH_K by ion implantation is also measured by the FMR measurement. The ion-implanted layer typically supports several spin wave modes. The mode with the largest resonance field is the uniform spin wave mode of the layer with in-plane anisotropy. The difference between this spin wave resonance field and that of the perpendicular uniaxial resonance field of the unimplanted layer of the film is the uniaxial anisotropy field change ΔH_k. An example of such resonance spectra is seen in Fig. 3-7.

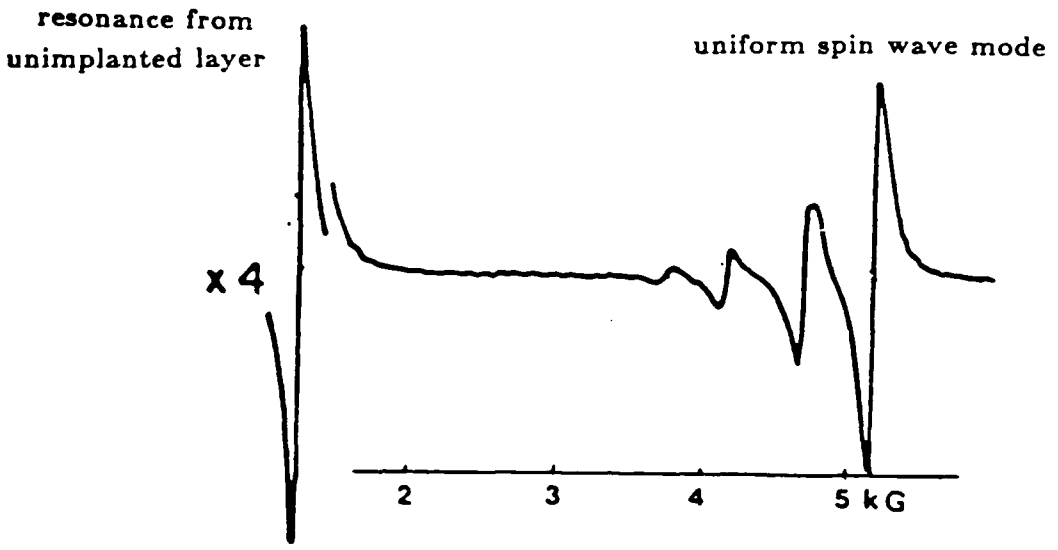

Figure 3-7: Resonance spectra for an implanted film[21]

Lattice Mismatch and Strain

A double crystal x-ray diffractometer was used to measure the lattice mismatch and the strain in the implanted layer. Normally, zero mismatch is desired because the mismatch introduces stress into the film. Too much stress can make the film very fragile to handle. The stress also creates stress-induced anisotropy which can either be perpendicular to or parallel to the film depending on the sign of the lattice mismatch and the sign of the magnetostriction constant λ_{111}.

The double crystal diffractometer is shown schematically in Fig. 3-8.

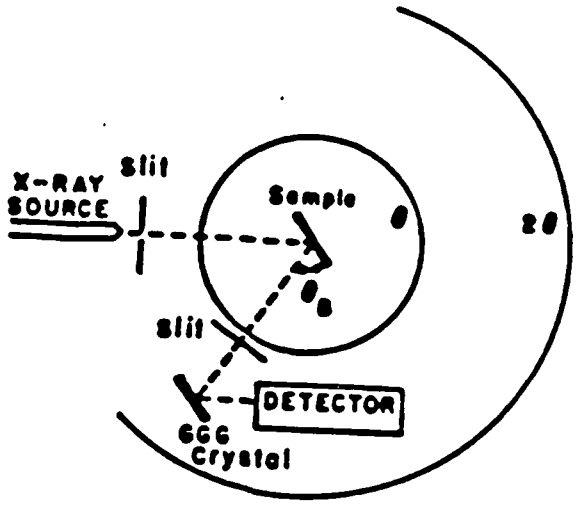

Figure 3-8: X-ray configuration to measure mismatch

Here the sample crystal is placed in the sample position for single crystal diffraction, on the θ rotation circle. The second crystal, which is a $Gd_3 Ga_5 O_{12}$ (GGG) substrate with no epitaxial film, is placed at the normal detector position, on the 2θ rotation circle. The detector is fixed with respect to the second crystal, such that when the Bragg condition for the incident x-rays are satisfied, the diffracted x-rays will reach the detector. The Bragg angle for a particular reflection (hkl) in a cubic crystal is determined from

$$\sin^2\theta_B = \frac{\lambda^2}{4a^2}(h^2+k^2+l^2) \tag{3.6}$$

where h, k and l are the indices for the reflection, λ is the wave length of the x-ray, and a is the lattice parameter. The x-ray source used was Cu $K\alpha_1$ radiation. The reflected x-ray beam used is from the [888] direction in the film. The angular difference between the peaks from the GGG substrate and the film's lattice ($\Delta\theta$) are related to the lattice mismatch by

$$\frac{\Delta a}{a} = \frac{\Delta\theta}{\tan\theta_B} \tag{3.7}$$

where θ_B is the Bragg angle given by Eq. (3.6).

The maximum lattice strain by ion implantation is measured by the same method. A typical x-ray diffraction curve for ion-implanted films is shown in Fig. 3-9.

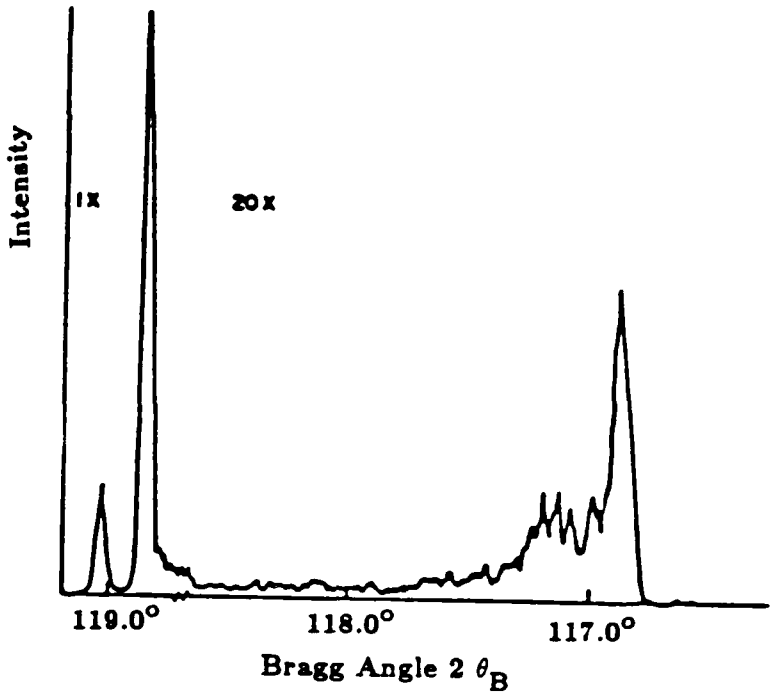

Figure 3-9: X-ray diffraction rocking curve

The left-most peak is from the GGG substrate. The next peak is from the unimplanted portion of the layer and the right-most peaks are from the ion-implanted layer. Notice that the vertical intensity scale of the substrate was reduced by a factor of 20. The maximum lattice strain due to the implantation is obtained using Eq. (3.7). The diffraction angle difference $\Delta\theta$ is the difference of the angle of the lowest angle diffraction peak of the implanted layer and the unimplanted LPE layer.

3.1.2. Device Layout and E-Beam Mask

Various shapes of bubble propagation tracks were designed and fabricated to study bubble propagation in ion-implanted devices. The shapes of the tracks studied in this thesis, which were generated by a computer, are shown in Fig. 3-10.

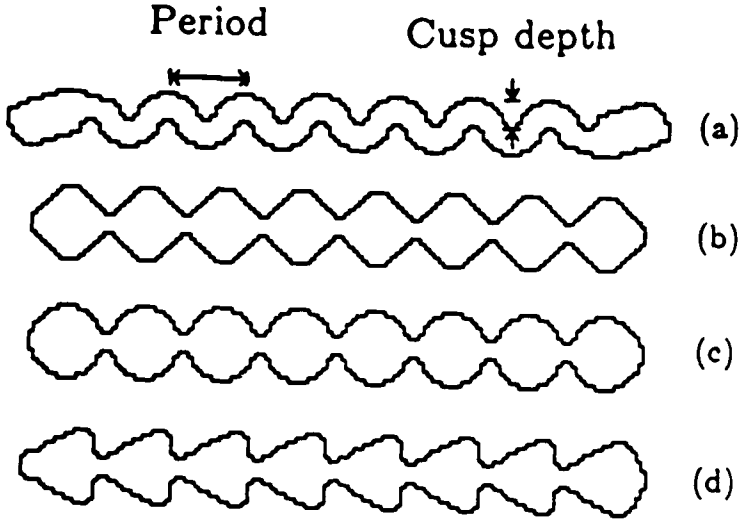

Figure 3-10: Bubble propagation patterns (a) snake (b) diamond (c) circle (d) triangle

In this subsection, the computer-aided design process of the propagation device layout is described first. Then the description of the actual fabrication process of the electron beam mask is followed.

3.1.2.1. Computer-Aided Design of Device Layout

The computer-aided design process of the device layout is depicted in Fig. 3-11. A graphic design editor called Piglet, which is an internal Hewlett-Packard product and which runs on an HP 9836 model computer, is used to translate device design into a high-level descriptive language called IGS[49]. It is then translated into CIF (Caltech Intermediate Form) which is again translated into DIP. The patterns described in DIP are converted into appropriate shapes on the mask by vector scanning of an electron beam using a Cambridge electron beam pattern generator which is located at National Research and Resource Facility for Submicron Structures at Cornell University.

The basic design rule of the propagation tracks is that the distance between the bubble posi-

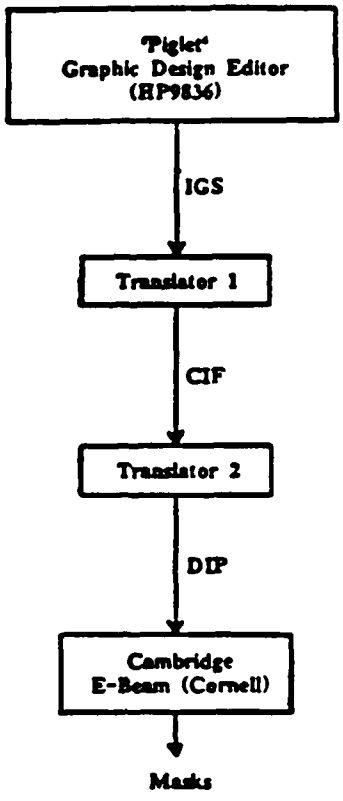

Figure 3-11: CAD flow chart

tions should be at least four times the bubble diameter to avoid bubble-bubble interaction. The ratio of the cusp depth to the period (Fig.3-10) is generally held at about 1/3. If the ratio is too small (i.e., the cusp too shallow), the bubble does not propagate reliably, often skidding to the next bubble positions. The edges of the patterns should be smooth and the cusp should have a sufficient width.

The mask contains four basic shapes of patterns, i.e. snake, diamond, circle and triangle as shown in Fig. 3-10. The pattern geometries tested varied in many ways such as track period, track spacing, cusp depth, unimplanted pattern width, etc. Two identical sets of patterns were oriented perpendicular to each other to test the effect of track orientation with respect to the crystal orientation. Also, various-sized building blocks of the propagation tracks such as circles, diamonds and triangles were included. Overall more than 60 different patterns were put on the mask. The track period was varied from 1.75 μm to 2.5 μm and this mask was intended for 0.45

μm to 0.65 μm bubble materials. A portion of the computer-generated mask pattern is shown in Fig. 3-12. Some of the devices were fabricated on 1 μm bubble films, and a different earlier fabricated mask which contains propagation patterns having periods of 4, 5 and 6 μm was used.

3.1.2.2. Fabrication of E-Beam Mask

The mask was exposed with the Cambridge mask pattern generator (EBFM-2-150) at Cornell University. The mask blank used has 1000 Å of chrome (40.8% reflectivity) and 2000 Å of PMMA resist on a Borosilicate glass substrate. For the exposure of the track patterns, an electron beam current of 1 nA, a beam spot size of 1/16 micron, and a clock speed of about 500 KHz were used. The best results for the smaller-sized patterns were obtained at a clock speed of 450 KHz and for the larger-sized patterns at 550 KHz. Much higher currents and scanning rates were used on large coarse shapes to reduce exposure time.

The resist was developed in a developing solution (mixture of equal volume of methyl isobutyl ketone and isopropyl alcohol) for 2 minutes, and rinsed in deionized water. The underlying Cr layer was then etched for 45 seconds in Cr etchant (ceric ammonium nitrate and glacial acetic acid solution), and thoroughly rinsed in DI water.

3.1.3. Device Processing

The processing steps of ion-implanted propagation pattern devices are listed in Table 3-1 and also illustrated in Fig. 3-13.

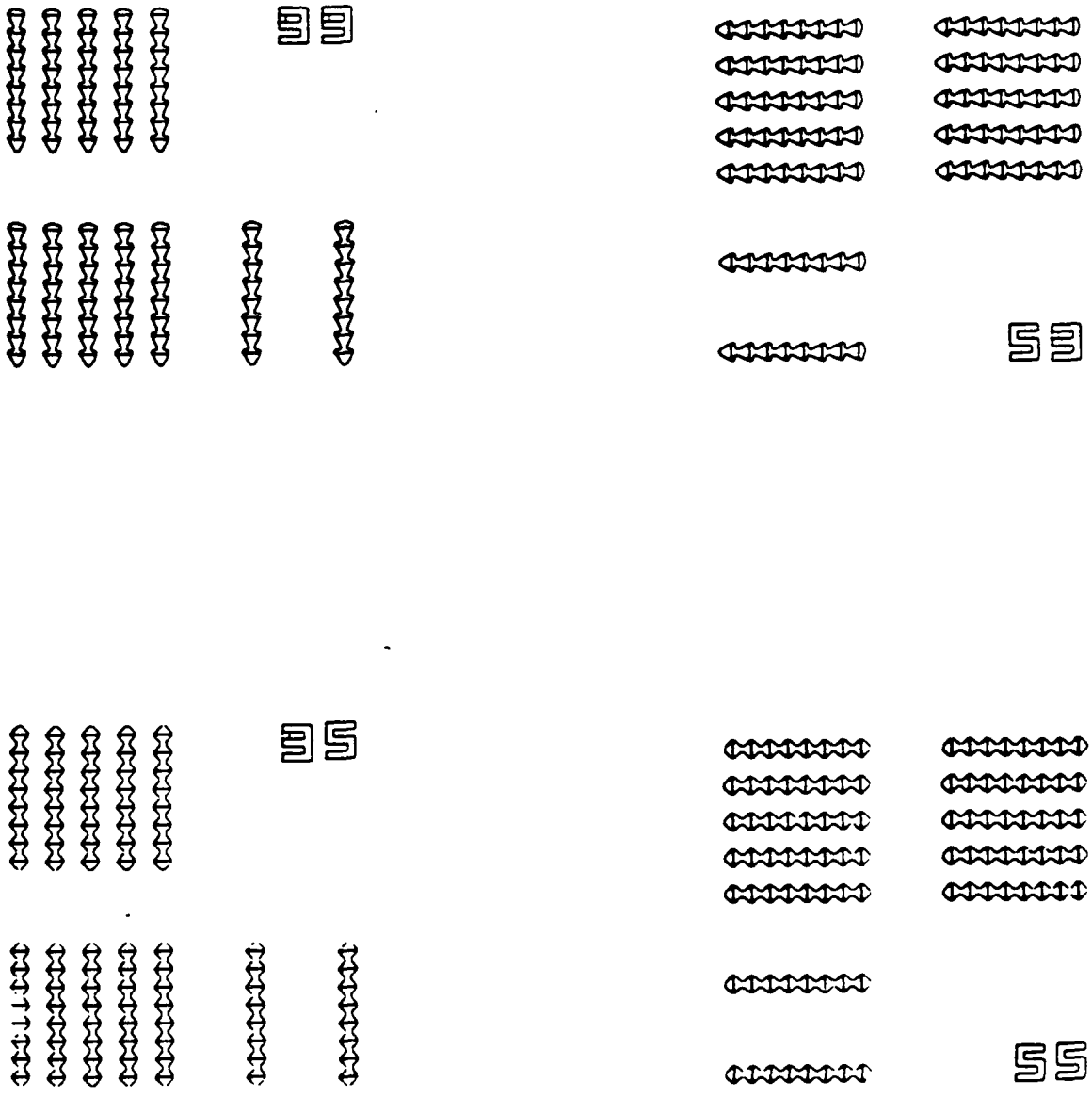

Figure 3-12: Computer printout of propagation patterns

Table 3-1: Ion Implanted Propagation Pattern Processing Steps

Purpose of Step	Material	Process	Thickness
Bubble Layer Growth	$(DyBiSmLuY)_3(FeGa)_5O_{12}$	LPE	0.7μm
Spacer	SiO_2	Sputter	800 Å
Plating Base	Mo/Au	Sputter	50 Å/300 Å
Propagation Pattern Delineation	AZ-4070		0.5 μm
Ion Implantation Mask	Au (BDT 510)	Electroplating	0.4 μm
Ion Implantation	Deuterium		
Plating Base Removal	Mo/Au	Chemical Etch	50 Å/300 Å
Reflection Layer	Al	Sputter	2500 Å

After sputter depositing the SiO_2 spacer and the plating base Mo and Au, propagation patterns are delineated with photoresist. The mask is exposed after a layer of photoresist is spin-coated and developed. Then gold is electroplated to fill the openings created by the resist process. The remaining photoresist is then removed and the device is ion-implanted with deuterium. The gold patterns provide protection from the ion bombardment and the garnet film area underneath the gold patterns become unimplanted propagation patterns. After the implantation, the gold implantation mask is removed and an Al layer is deposited (to serve as a reflector) for the magneto-optical observation of the bubbles. Photoresist patterns instead of gold patterns can be used as masks for ion implantation. However, the drawback of the photoresist is that it changes pattern shapes when it is exposed to the ion implantation due to elevated temperature during the process. Therefore for small, submicron features that are required for submicrometer devices, the use of gold was believed to be advantageous in spite of the added processing steps. In the remainder of the section, each processing step will be discussed in more detail.

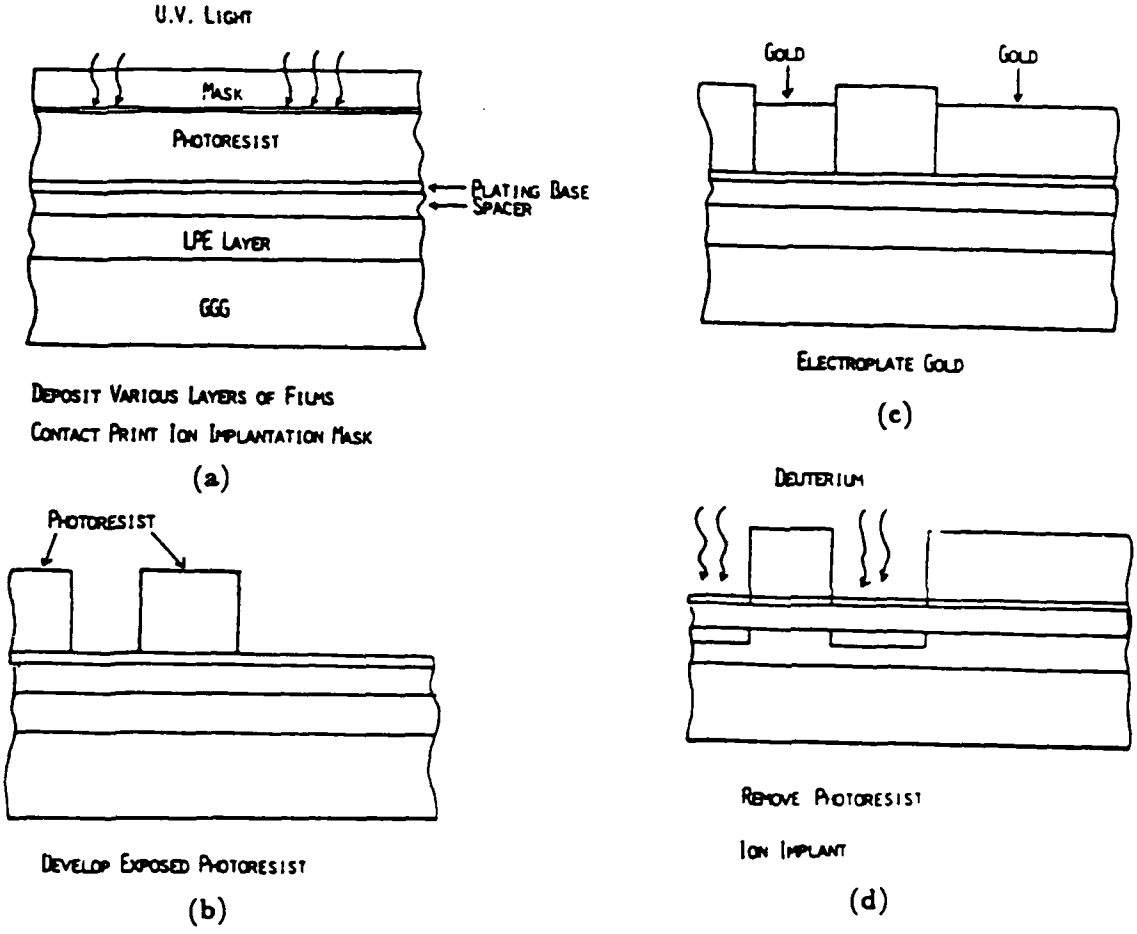

Figure 3-13: Ion implanted propagation pattern processing steps

3.1.3.1. Wafer Cleaning

Garnet wafer cleaning is of great importance to insure good contact with the mask during the mask exposure. If any sizable dust particles are not removed before the next processing step takes place, those particles will remain there throughout the entire process because sputter-depositing of spacer and plating base will trap the particles and preserve them.

The cleaning process begins by inspecting the wafers visually. If they look dirty, they are

scrubbed with cotton applicators (Q-Tips) using plenty of DI water, or a scrubber is used to remove coarse particles. Then the wafers are immersed in RT-2 solution which is a mixture of sulfuric and nitric acids for 15 to 30 minutes to remove any remaining inorganic particles. Subsequently, boiling solvents are used to remove any organic materials. The wafers are first put in trichloroethylene for three minutes, then in acetone for three minutes, and then in isopropyl alcohol for three minutes. Lastly, they are rinsed with DI water. These steps are repeated until the wafer is clean. It is important to scrub the wafers with a Q-Tip to remove stubbornly adhering particles.

3.1.3.2. Wafer-Thinning and Back Film Removal

The thickness of the garnet films was fine-tuned by thinning in hot phosphoric acid whenever necessary. Since the growth rate of Bi films was sometimes high, it was difficult to control the thickness of the film accurately as thinner (0.5 $\sim$ 0.7 μm) films were grown for 0.5 μm bubble devices. Therefore some of the films were thinned to the desired thickness by etching them. The etching rate of the garnet by phosphoric acid sharply increases with the acid temperature. To accurately control the thickness, low temperature was used, thereby slowing down the etching rate. At 100 $^\circ$C, the rate was about 200 $\mathring{A}$ /min. A temperature of 100 $^\circ$C was chosen since it is the boiling point of the water. The phosphoric acid and the sample were put in a beaker, and the beaker in turn was placed in boiling water to maintain the temperature.

Since garnet films are grown by dipping in a melt, both sides of the substrate are coated with films even though only one side is used for device fabrication. It is sometimes desirable to remove the back film because either it adds noise signal to the magneto-optic detection signal from the top film or an undesirable FMR signal to the measurement of the magnetostriction coefficients. To remove the back film[50], the top side of the wafer is first coated with RTV silicon rubber and dried for 30 minutes. The wafer is then immersed in boiling phosphoric acid ($\sim$165 $^\circ$C) to etch off the unwanted film. A couple of minutes is enough to remove about 1 μm of the garnet film. After the etching, the silicon rubber is removed by soaking in a 20:40:40 mixture of acetic, nitric acid and DI water for 20 minutes at 100 $^\circ$C.

3.1.3.3. Deposition of Spacer and Electroplating Base

A SiO_2 spacer is deposited to prevent interactions between the garnet film and the next layer (in our case, the plating base), and to protect the garnet film from further device processing steps. The electroplating gold base is needed for the subsequent electroplating process. It serves as an electrical contact to the propagation patterns. As an adhesion layer,Mo is used. It promotes adhesion of the Au to the SiO_2 layer. All three layers are sputter-deposited in one pumpdown,

which enhances adhesion. When the sample was taken out with one layer deposited, and then resputtered with another layer in a later pumpdown, the adhesion was poor and the layer was peeled off in subsequent processing. A Perkin Elmer 2400 series RF sputterer with three targets was used at 10 milliTorr of Ar pressure. The sputtering time and forward power for 800 Å of SiO_2, 25 Å of Mo and 300 Å of Au were 8 minutes and 500 W, 23 seconds and 150 W and 57 seconds and 150 W, respectively. The SiO_2 and Mo targets had to be presputtered before film deposition because they formed oxides on the surfaces of the targets. Typical presputter conditions were 500 W and 30 minutes for the SiO_2 target and 300 W and 30 minutes for the Mo target after long exposure (overnight or longer) to air and 300 W and 3 minutes for the Mo target after a short (few to few tens of minutes) in-between run exposure.

3.1.3.4. Photolithography

The photoresist AZ 4070 which is sensitive to mid UV light of 310 nm wavelength was used to delineate most of the devices fabricated. The minimum features of the devices are 0.7 μm for 2 μm period devices and 0.5 μm for 1.75 μm period devices. Because of these small features deep UV exposure was initially considered. However, mid UV exposure with the available Karl-Suss contact aligner provided adequate resolution for most of the device runs. The resist was spin-coated at 6000 rpm or 7000 rpm which gave 5700 Å or 4000 Å of resist thickness. Then it was prebaked at 90 °C for 25-30 minutes. Typical exposure time was 45 seconds at 5 mW/cm^2 of UV intensity. Development time was fixed at one minute in diluted AK 400 developer (AK 400 : DI = 1 : 4). A plasma asher was sometimes used to remove any remaining resist from the pattern openings (200 W for 5 minutes). Resist residue prevents the current flow necessary for the subsequent electroplating. However, the effectiveness of the asher was not totally satisfactory. Instead, deliberate slight overexposure was used to insure the absence of any resist residue. The pattern shapes obtained were very sensitive to exposure and development conditions and the contact established between the mask and the wafer during the exposure. The mask was cleaned with acetone and rinsed with DI water using cotton applicators (Q-Tip) after each exposure to remove any resist residue adhering to the mask from the wafer as well as any dust particles.

3.1.3.5. Electroplating of Ion-Implantation Mask

The electroplating of gold through a photolithographic pattern requires very simple equipment, but gives excellent pattern definition and a good implantation mask. The plating method used was a variation of barrel plating as shown in Fig. 3-14. The barrel is stationary and serves as the anode. The sample in a holder is attached to the shaft of an agitating motor which is connected to the negative terminal of a constant current source. This plating cell was built along with a motor control unit which automatically changes the direction of the rotation of the agitating motor at desired intervals. Sel-Rex Corporation's gold bath BDT 510 was used.

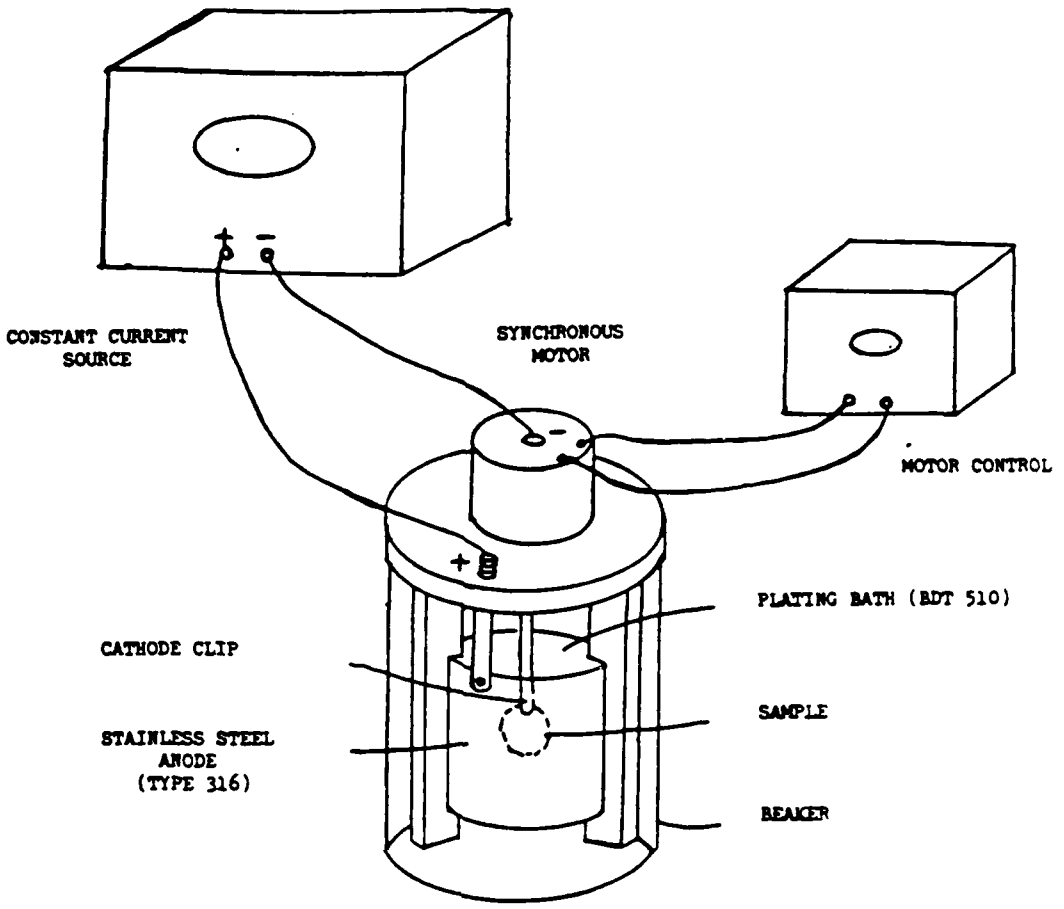

Figure 3-14: A schematic diagram of gold electroplating apparatus

The total amount of the gold plated is proportional to the electric charge that passed through the plating bath, i.e.,

$$V = S\ t \propto J\ T \tag{3.8}$$

where V is the volume of the gold plated, S is the surface area of the sample (plus holder) that the electric current passes through, t is the thickness of the plated gold, J is the current density and T is the time for which the electric current was applied. The pattern area is negligible compared to the exposed sample holder area. Therefore S is the area of the sample holder (plus

motor shaft) immersed in the bath. Generally S and J are kept constant, then the thickness of the plated gold is proportional to the plating time. The recommended current density J for this bath is 5 mA/cm^2, but it was learned that a smaller current density ($\sim$3 mA/cm^2) gave a better quality of gold (shiny and golden colored).

The thickness of the gold necessary was determined by the implantation ion species and energy. Since the gold patterns serve as protection from the implantation, the thickness of the gold should be thicker than the penetration depth into gold of the ions. The deuterium distribution data due to implantation calculated from the Lindhard-Scharff-Schiott statistics in gold substrates as well as SiO_2 and garnet were made available to us by IBM, which are in tabular form and listed in Appendix A. The ion penetration depth is considered to be the sum of the projected range and the projected standard deviation.

Gold does not adhere well to the stainless steel (#316) that was used for the sample holder. Therefore the entire holder was sputter-deposited with Mo to enhance adhesion. One earlier problem encountered is worth mentioning. If the holder is left in the air for an extended period of time, the plating rate increases dramatically and the quality of the gold plate is very poor. Therefore the holder was kept in a jar (with calcium chloride) to reduce the adsorption of particles and moisture in the air, which alleviated the problem considerably. Another thing to remember is that BDT brightener should be periodically added ($1\sim2$ ml/l) every few months to the bath to maintain the quality of the plated gold.

A typical plating rate was 50 nm/min. at 3 mA/cm^2 current density. The thickness of gold needed for 0.5 μm bubble devices is about 250 nm and that for 1 μm bubble devices is about 450 nm. Generally about 350 nm of gold was electroplated for 0.5 μm bubble devices and 500 nm for 1 μm bubble devices.

After electroplating, the photoresist pattern is removed by immersing the device in RT-2 solution for 3 minutes. The devices were then rinsed in running DI water for at least 2 minutes. Some scanning electron micrographs of gold implantation masks thus fabricated are shown in Figs. 3-15 and 3-16. The pictures in Fig. 3-15 were taken by tilting the samples 30° to show the sidewalls of the patterns, which exhibit virtually no undercutting.

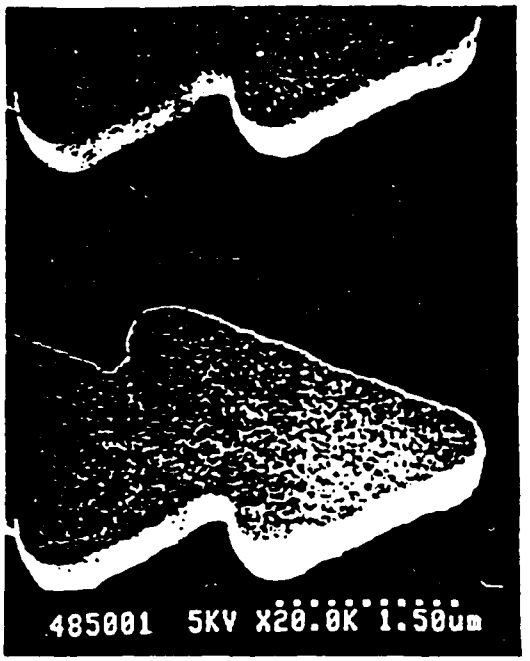

(a)

(b)

Figure 3-15: Scanning electron micrographs of gold ion implantation masks for 0.5 μm bubbles (Period 2 μm)

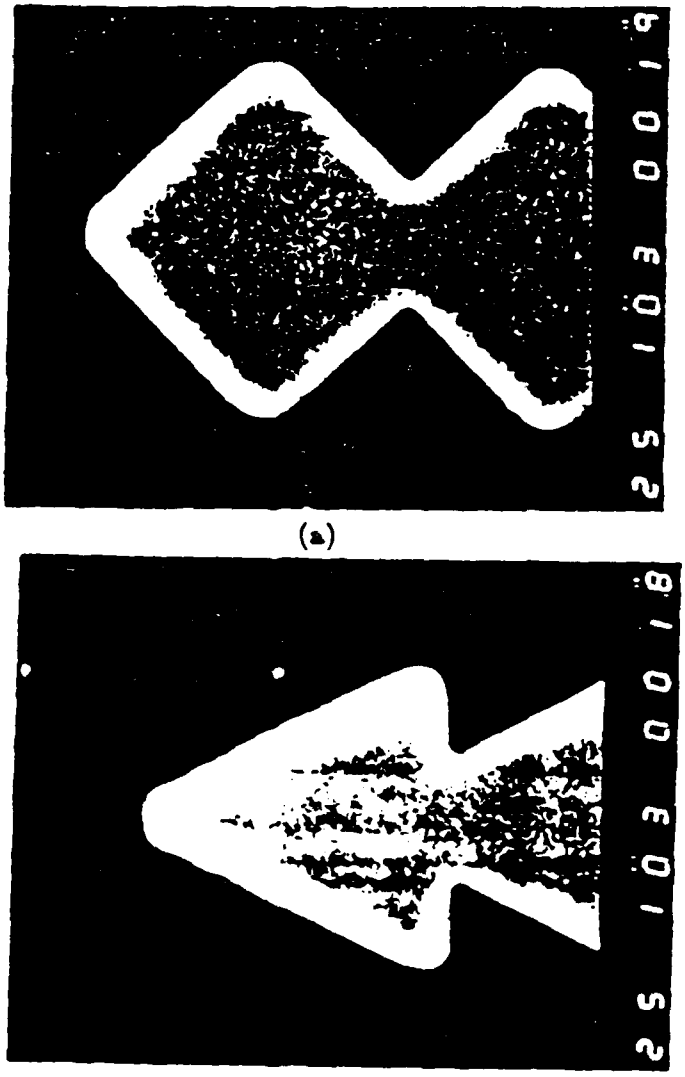

Figure 3-18: Scanning electron micrographs of gold ion implantation masks: (a) contiguous diamond shaped devices for 1 μm bubbles (period 5 μm) (b) contiguous triangular shaped devices for 2 μm bubbles (period 4 μm)

AD-A190 169 HIGH DENSITY ION IMPLANTED CONTIGUOUS DISK BUBBLE TECHNOLOGY(U) CARNEGIE-MELLON UNIV PITTSBURGH PA DEPT OF ELECTRICAL AND COM.. M H KRYDER ET AL. 31 OCT 87 3/3

UNCLASSIFIED AFOSR-TR-87-2044 AFOSR-84-0341 F/G 9/1 NL

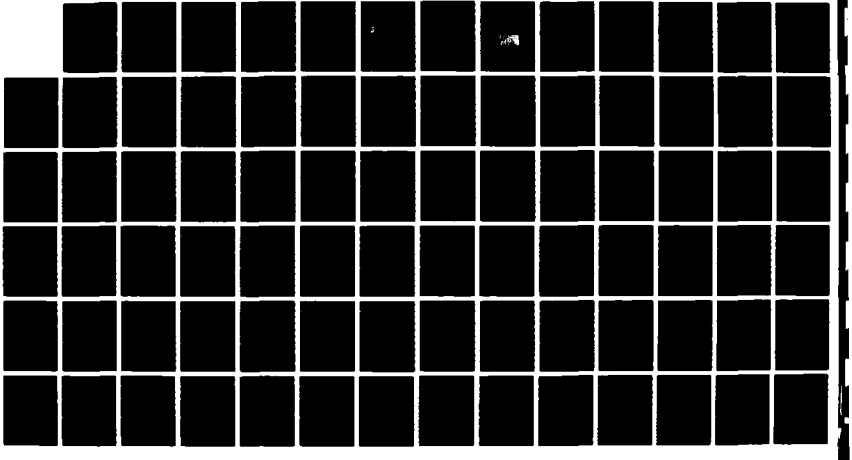

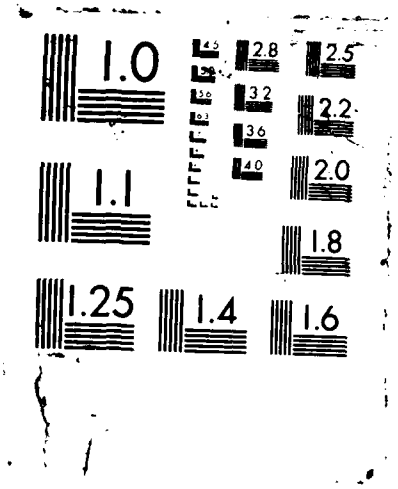
1.0
2.8
2.5
3.2
2.2
3.6
4.0
2.0
1.1
1.8
1.25
1.4
1.6

3.1.3.6. Ion Implantation

The implanter used was an Accelerators Incorporated Model 200, which has maximum acceleration voltage capability of 200 KV. A low beam current density (0.35 $\mu A/cm^2$) was used to avoid wafer heating which could cause self-annealing since the wafer stage was not cooled. Double implantation of singly-ionized deuterium molecules (D_2^+) was used throughout the study.

Each wafer was divided into four regions and implanted using different combinations of ion-implantation conditions to study the effects of different ion-implantation conditions on device operations and to save wafers. For nominal 0.5 μm bubble devices, the range of implantation depth tried was from 230 nm to 310 nm and the range of estimated in-plane Q was from -2.5 to -5. For 1 μm bubble devices, a depth range of 350 nm to 450 nm and an in-plane Q range of -4 to -8 were tried. The initial estimations of in-plane Q values for 0.5 μm bubbles were obtained from Figs. 2-14 and 2-15 using the methods described in Section 2.4. Since the thickness of the implanted layers intended in this study was about 1/2 of the thickness of the layer studied in Figs. 2-14 and 2-15, a higher estimation of the anisotropy change (1.5 times the plotted value) was used to determine the dose. The implantation energies were determined using the method presented in Section 2.4. Since the ions were implanted through the plating base and the spacer, the energy necessary to penetrate these layers was added (14 KeV for 80 nm of SiO_2, 2.5 nm of Mo and 30 nm of Au) to the energy which would have been needed for bare garnet film. The doses ranged from $6 \times 10^{15}/cm^2$ to $1.23 \times 10^{16}/cm^2$ and energies from 26 KeV (which is the stable minimum acceleration energy of the implanter) to 80 KeV.

3.1.3.7. Reflecting Layer

After ion implantation the gold implantation masks together with the plating base are stripped with Au etchant (mixture of 250 g of KI, 50 g of I and 200 ml of deionized water) by dipping the wafer in the etchant for one minute and rinsing in DI water for one minute. Then an aluminum layer is deposited to be used as a mirror for the magneto-optical observation of bubbles by a polarized light microscope. Without a mirror it is almost impossible to see the bubbles. Initially Cr ($500 \sim 1000$ Å) was used as a mirror, but later, Al replaced Cr because Al has higher reflectivity than Cr. However Al has its own drawbacks. For example, it is vulnerable to many chemicals used in the processing such as the SiO_2 etchant, Au etchant, electroplating solution and photoresist developer. Initially the Al mirror was deposited along with the plating base before the electroplating and the ion implantation, but later it was deposited after those processes since the chemicals used in the process produced pin holes in the Al layer or thinned the layer.

The Al layer was deposited either by a thermal evaporator or a DC magnetron sputterer (Leybold Hereaus Z 400). The Ar pressure for the sputtering process was 7.3 mTorr, and 100 W of power was used. At this power level and Ar pressure, the deposition rate was 500 Å/minute and 5 minutes of deposition produced 2500 Å of excellent quality aluminum. The quality of the Al deposition by the thermal evaporation which was used in the early phase of the study was poor in the sense that the adhesion of the layer was not good and the layer possibly contained trapped air particles. These were deduced from the fact that the Al layer was locally lifted, forming dome-shaped areas and eventually "popped" creating snowflake-like ruptures when it was heated above 120°C. Therefore DC magnetron sputtering was exclusively used for the latest device processing.

3.2. Device Testing

3.2.1. Testing Set-Up

Device testing was performed with a microscope-bubble exerciser (called Kilotest) set-up, which is diagramed in Fig. 3-17. The microscope is a Leitz Orthoplan equipped with polarizer and an analyzer, a 100 W mercury arc lamp (which has the strongest intensity) housed in a 250 W mirror housing, a MTI 66 silicon-intensified target TV camera, (improved version of Dage 650 SIT), Audiotronic 14" monitor, 50 × bubble objective and a 125 × oil immersion objective. By placing the camera high on top of the microscope using a long extension tube (14"), very high magnification of 3500 was achieved, which enabled easy observation of small (0.5 μm) bubbles. A 250 W mirror housing was used instead of a 100 W housing because the optics of the former is better than the latter. The bias field is applied by a custom-made double donut shaped electromagnet capable of generating 1.5 KOe (manufactured by Stonite). The cooling water is provided by a refrigerated recirculator manufactured by Neslab (Model CFT-75) which keeps the temperature of the water at a set temperature. The power supply for the magnet is a model TCR 30T100 made by Electronic Measurements with DC current and voltage specifications of 100 A and 25 V, respectively. Two sets of near Helmholtz coils attached perpendicularly to each other are inserted at the center opening of the bias magnet to provide the in-plane circulating drive field. The maximum in-plane field obtainable is about 200 Oe and the magnets are powered by a Crown DC-300 stereo power amplifier. The coil constant is 15 Oe/ampere. The bias field is monitored by a digital panel meter calibrated to indicate field strength in Oersteds. The in-plane field is monitored by an oscilloscope, which shows the magnitude and the direction of the field.

The Kilotest system which is used to test the bubble chips controls the in-plane rotation field

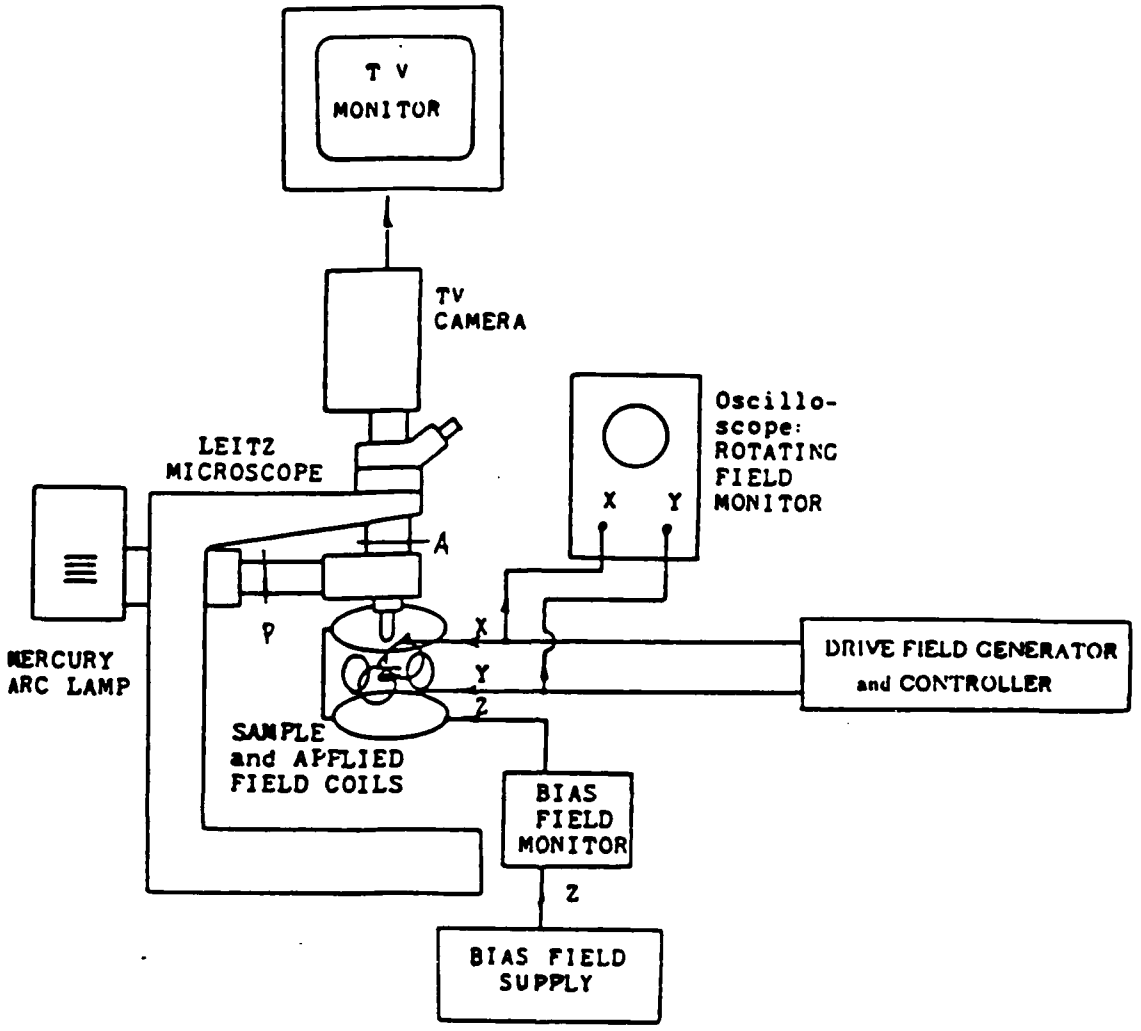

Figure 3-17: Testing set-up

strength and cycles and the bias field strength using an IBM XT personal computer. The Kilotest was donated by Bell Labs and the computer program to run it was written by John Wullert. A block diagram of the Kilotest system[51] is shown in Fig. 3-18. The system is capable of testing all bubble device functions, i.e., generation propagation, transfer, and detection although only the propagation testing function was used for this study. The drive field frequency range of the system is from 0.1 Hz to 50 KHz. The system is complimented by a manual circular drive field generator and a bias field control. The drive field is generated by a Sine/Cosine potentiometer. The output of the manual drive field generator is summed with the output of the Kilotest drive field generator and amplified by the aforementioned Crown stereo power amplifier to drive the drive field magnets.

The ambient temperature of the test sample was changed by enclosing the bias magnet openings with pieces of duct tape after inserting the sample at the center of the magnet, and by blowing in hot air or cold nitrogen gas into a hole. The nitrogen gas was cooled by passing it through a copper tube which was immersed in a dewar of liquid nitrogen and subsequently passed through a resistive electric heater which controlled the temperature. To raise the temperature, air was passed through the heater at low temperature. Nitrogen gas instead of air was used to prevent condensation and ice from appearing on the sample, which prohibited the observation of the magnetic bubbles. The temperature was controlled by an Omega Series 4200 RTD temperature controller. The accuracy of the temperature control was $\pm 1\,^{\circ}C$. The temperature of the sample was monitored by placing a thermocouple temperature probe near the sample. Since the probe is magnetic, it was not located too close to the sample. Otherwise, it would affect the magnetic fields applied to the sample.

3.2.2. Bubble Domain and Charged Wall Observation

3.2.2.1. Magneto-Optic Method

Magnetic bubble domains are observed with a polarized light microscope (Fig.3-17) using the Faraday magneto-optic effect. The Faraday effect is exhibited when light is transmitted through a magnetic medium. When polarized electromagnetic waves travel through a magnetic medium, the plane of polarization is rotated by an angle ρ_f due to the Faraday effect:

$$F = F\, t\, \mathbf{m} \cdot \mathbf{k} \tag{3.9}$$

where F is the Faraday coefficient of the medium, t is the path length of the waves through that

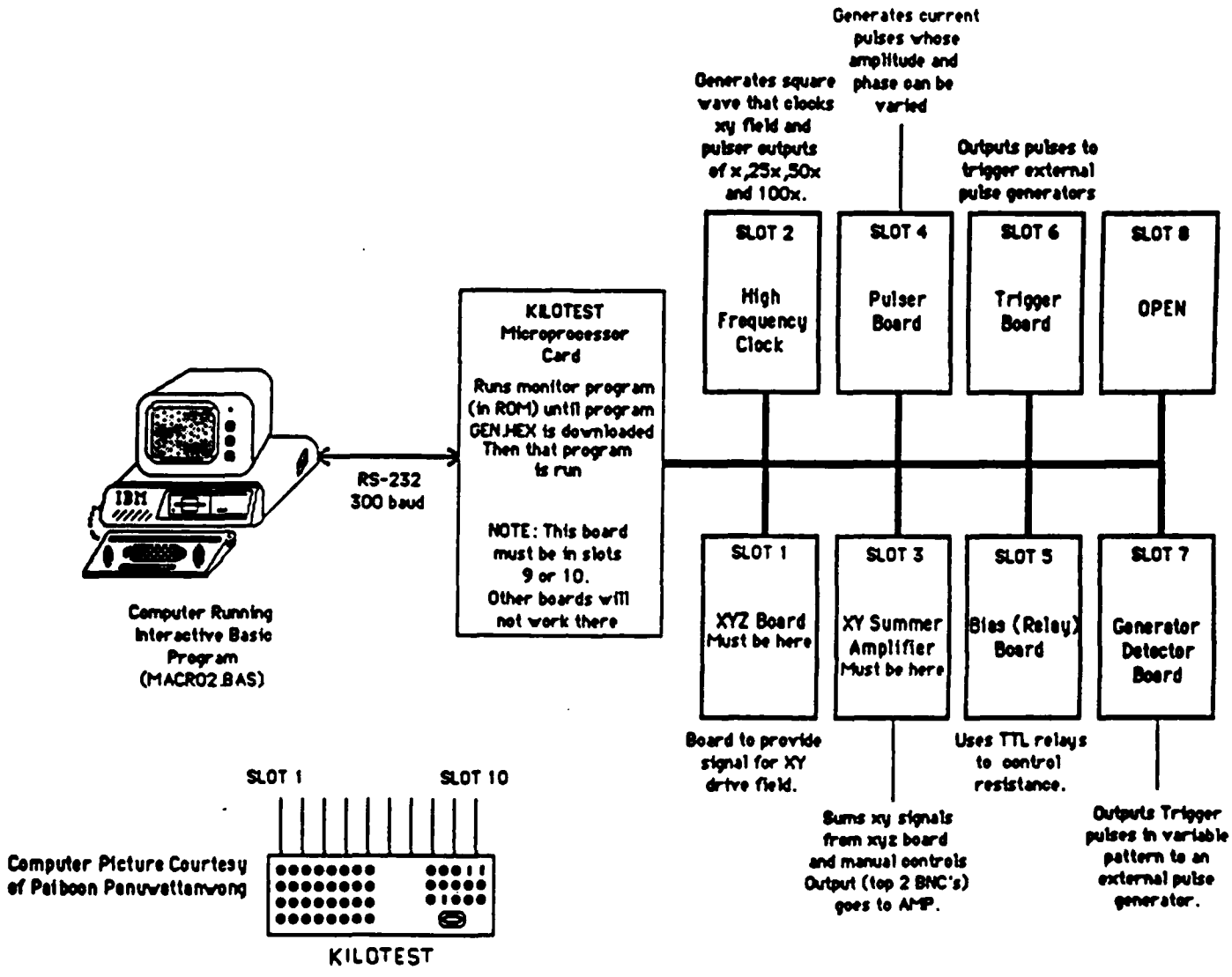

Figure 3-18: Kilotest system

medium, m is a unit vector in the direction of magnetization, and k is a unit vector in the direction of the light travel.

To see the bubble domains (perpendicularly polarized), the sample is placed on the stage face down on top of a mirror and the polarized light is illuminated on the sample. The light travels through the sample and is reflected by the mirror, goes through the objective and the analyzer (a polarizer in the out-path of the light), and viewed by eyepieces or a TV monitor through a TV camera. Bubble domains and the surrounding area are oppositely magnetized. Therefore the polarization of the light from the bubble is rotated in one sense (say clockwise) by ρ_f and the polarization of the light from the surrounding area is rotated in the other sense (then counterclockwise) by ρ_f. If the angle of the polarizing plane of the analyzer (the analyzer angle) is set at $90^\circ + \rho_f$ clockwise relative to the angle of the polarizer, the light from the bubble is completely blocked, while the light from the surrounding area has a component of polarization parallel to the analyzer angle and therefore is not completely blocked. Then the bubble is viewed as a dark disk with light surroundings. This method cannot be used to see the in-plane domains (thus, charged walls) because the Faraday rotations from the in-plane domains are small.

3.2.2.2. Bitter Pattern Method[33]

Domain walls may be made visible by the application of a colloidal suspension of very fine magnetic particles to the surface of the magnetic specimen. This colloid is known as Bitter solution or ferrofluid. The fine magnetic particles ($100 \sim 200$ Å) in the solution are attracted to the stray flux emanating from the domain walls at the sample surface and migrate to these regions. Thus the walls are made visible by the presence of the particles. With a cover glass placed over the colloid and sample, the domain configuration can be viewed through a microscope. Generally, the use of an optical microscope affords one the space to place field coils near to the sample under observation. Then, changing domain configurations due to applied fields can be observed as they happen.

To view the walls in the ion-implanted layer, it is necessary to apply a field perpendicular to the film plane. When a magnetic field is applied perpendicular to the sample plane, such as in Fig. 3-19, the acicular magnetic particles in the ferrofluid align with this field and, in the case of Fig. 3-19, are polarized with their negative poles downward.

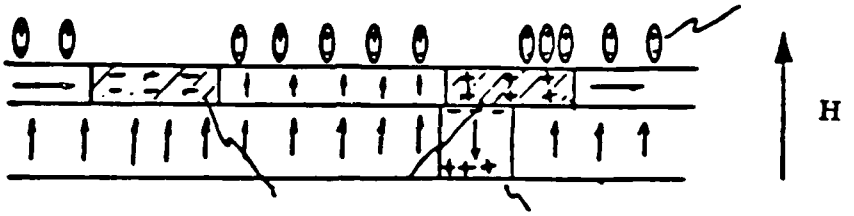

Figure 3-19: Fine magnetic particles attracted to stray flux emanating from magnetic poles

Subsequently, the downward negative poles of the particles are attracted to regions of positive magnetic poles within the film and are repelled by regions of negative poles. This causes regions of positive magnetic charge to appear black due to the collection of particles and regions of negative charge to appear white due to the absence of particles. A Bitter pattern of the domain around a nonimplanted disk is shown in Fig. 3-20.

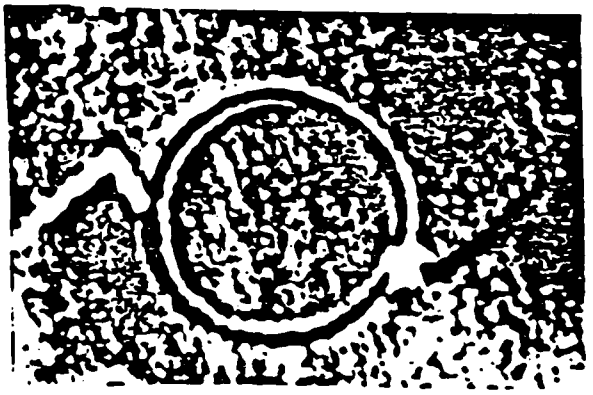

Figure 3-20: Bitter pattern of domain around nonimplanted disk[33]

In this illustration, the perpendicular field is pointed upward (out of the page), aligning the particle's negative poles down. Therefore, the particles are attracted to positively charged structures and repelled by negatively charged structures. The positive charged wall extending from

the right of the disk in Fig. 3-20 thus appears black, while the negative wall on the left appears white. A bubble can be seen attached to the positive wall and shows up as a bright spot on the dark wall because the top of the bubble domain is negatively charged.

The samples are usually diced to about 0.5 cm square and are encapsulated in a glass envelope with ferrofluid. Detailed sample preparation steps are found elsewhere[33]. The ferrofluid solutions tried were 500 and 600 Series manufactured by Ferrofluidics Corporation.

3.2.3. Device Performance Measurements

3.2.3.1. Propagation Bias Margins

Most of the bias margins were measured at 1 Hz rotating in-plane field frequency. The in-plane field magnitude was first set and the field was rotated. The bias field was then slowly raised from zero by manually rotating a knob for current output of the bias field current supply. The low limit of the bias was recorded when there ceased to exist stripe domains. The bias field was increased further, and the high limit of the bias margin was recorded when the bubbles on the tracks collapsed. For close-packed propagation tracks which were shown in Fig. 3-12, all five tracks were watched simultaneously. The bubble collapse fields recorded were those of the inner three tracks. Generally bubbles in the outer two tracks started to collapse first. Since there were no bubble generators, bubbles were generated randomly by the above mentioned process. However, care was given to insure at least a few bubbles on each track. The in-plane field was increased or decreased typically in 10 Oe increments and sometimes in 5 Oe increments.

For observations of propagation failure modes, bubbles were moved manually (without the benefit of the Kilotest) using a Sine/Cosine generator. The in-plane field rotating frequency of the bias margins reported here are 1 Hz unless otherwise noted. The visibility (contrast) of the bubbles was very good for most of the nominally 0.5 μm bubbles in the devices fabricated with the garnet films containing Bi. Bubbles were clearly seen up to collapse, where the size of the bubble is three times smaller than that near stripeout [Fig. 2-7], for many of the devices. Using devices having non-Bi films, it was impossible to see the collapse of even 1 μm bubbles. Non-Bi 0.5 μm bubbles were only barely seen at low bias fields where bubble sizes are large. The Al mirror improved the visibility of the bubbles compared with the Cr mirror.

The thickness of the bubble also influences the visibility since the Faraday rotation is proportional to the bubble film thickness [Eq. (3.9)]. Other factors which influence the visibility are the conditions of the implantation. The higher the dose, the more the implantation layer absorbs the light (becomes darker), thereby reducing the available signal light. Of course, deeper implants also reduce the bubble height, thereby decreasing the contrast.

3.2.3.2. Bubble Position vs. In-Plane Field Direction

Bubble position around various sized unimplanted disks were measured as a function of the in-plane drive field. The measurement procedure is as follows: On a transparent plastic sheet a circle and lines were drawn from the center to the circumference of the circle in increments of 10°. The plastic circle was attached to the screen of the TV monitor and the center of the implanted disk was then moved to the center of the marked plastic circle by moving the microscope stage. Another of these plastic circles are attached to the oscilloscope (x,y in-plane field monitor), coinciding the center of the circle at the center of the circle drawn by the rotation of the beam spot.

The direction of the in-plane field was obtained from the angle of the beam spot on the oscilloscope and the corresponding bubble position was obtained from the angle of the bubble position on the TV monitor. Since it is desired to know the position of bubbles with respect to the crystal orientation, the in-plane magnets, the TV camera, the monitor and the samples all had to be aligned carefully.

3.2.3.3. Tolerance to Ambient Temperature Variation

Bias margins were measured as the ambient temperature of the chip was changed from 0°C to 130°C. The temperature was changed in increments of 20°C. Sufficient time was allowed for the chip to reach equilibrium temperature between each measurement. The visibility of the bubble became worse as the temperature was increased since the magnetization (of the bubble) decreases with increasing temperature, thus decreasing the Faraday rotation.

Chapter 4
Experimental Results

4.1. Typical Bias Margins

Results of bias margin measurements for typical diamond propagation patterns are presented here. Bias margins of an isolated element, an isolated track and close packed tracks with 2.5 μm period oriented in [1 1 $\bar{2}$] direction (good tracks) fabricated on wafer CA72 are shown in Fig. 4-1. The minimum drive field of an isolated diamond pattern (width of 4 μm) is seen to be 10 Oe. The minimum drive field of a close-packed track was 35 Oe. The margin width of the isolated element is 25 % (of the mid bias value at 60 Oe drive field), that of the isolated track is 18 % and that of the close-packed tracks is 15 %. The low end of the bias margin of a close-packed track is higher than that of the isolated track and the low end margin of the isolated track is in turn higher than that of the isolated element.

4.2. Propagation Failure Modes

Various bubble propagation failure modes are observed. At high bias, bubbles collapse in most cases, but bubbles can also propagate more than one period of the track (typically two periods) during one cycle of the rotating drive field, which is defined as skidding. These failure modes define the upper end of the bias margin. At low bias fields, bubbles typically stripe out across to the adjacent track and sometimes stripeout along the track boundary. These modes determine the low end of the bias margin for most in-plane field ranges. At low drive field, the predominant failure mode is bubble trapping at the cusps. Bubbles simply fail to move out of the cusps. They are typically trapped at the ends of the propagation track. Another failure mode at low drive field is the skipping of bit positions (cusps). Most frequently seen is the skipping of the first cusp as the bubble rounds the end of a track. These failure modes basically determine the minimum drive field and the low bias end at low drive field. The failure modes mentioned so far are for bubbles which propagate, i.e., which have bias margins. When bubbles do not propagate properly due to improper ion implantation, the most frequently seen failure modes are bubble jumping between tracks and bubble trapping in the cusps.

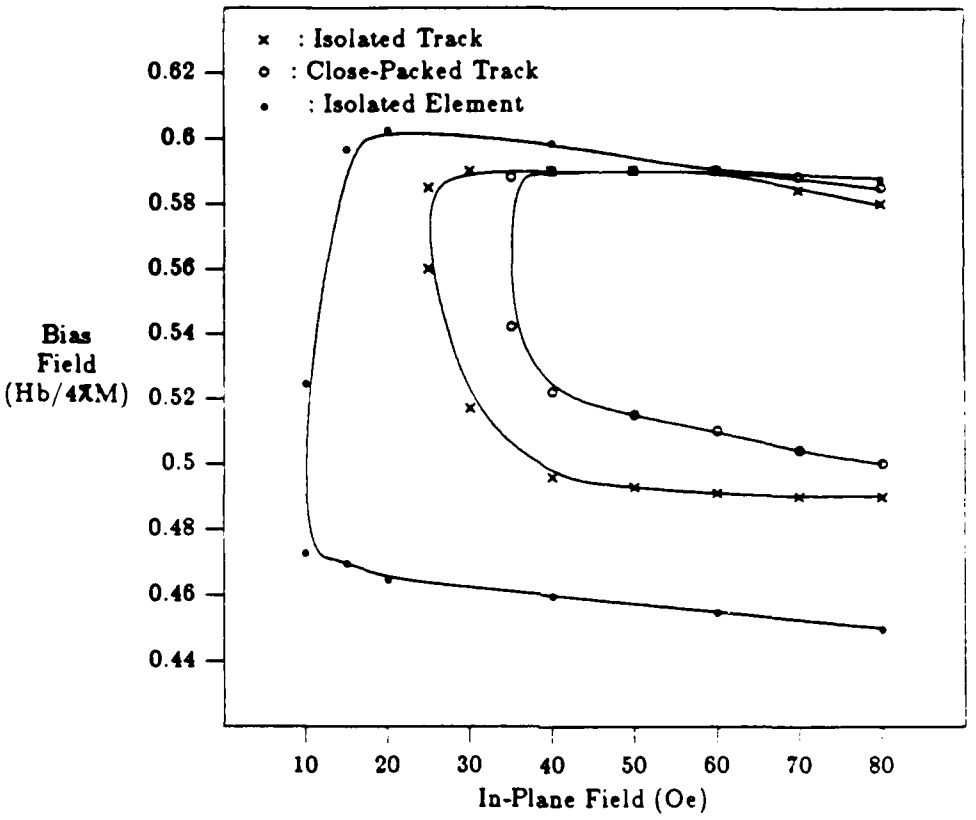

Figure 4-1: Bias field margins for diamond shaped element, isolated track and close-packed tracks : Track period : 2.5 μm, wafer CA 72, Chip 12, Region 4, $4\pi M$ = 910 G

4.2.1. Skidding

Skidding is a failure mode in which a bubble moves generally two periods of a propagation track during one period of rotating in-plane field cycle, which is explained in Fig. 4-2.

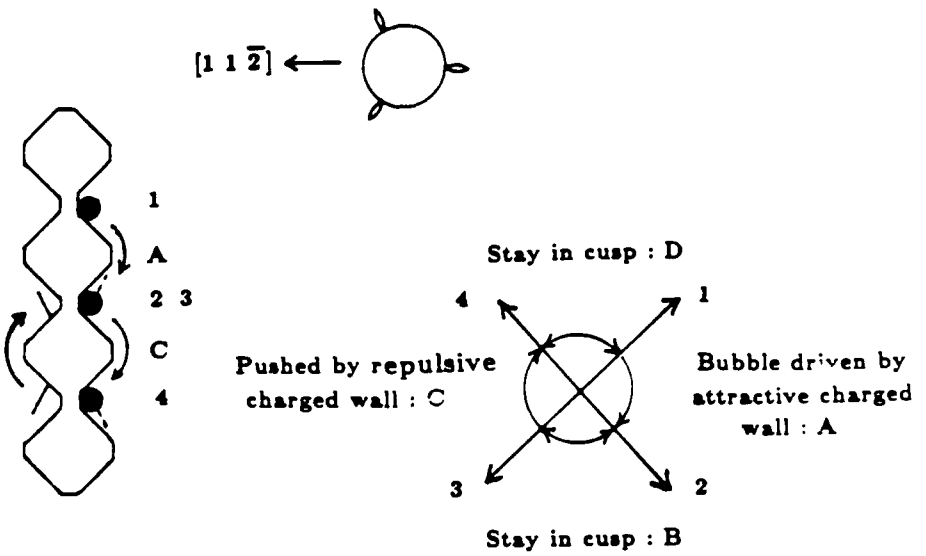

Figure 4-2: Skidding failure mode

The bubble positions on the track and the corresponding in-plane field (H_{xy}) directions are shown in the figure. During the Phase A, the bubble is driven by an attractive charged wall (normal propagation mode) from the top cusp to the center cusp. The bubble stays in the cusp during the Phase B. During a normal propagation cycle, the bubble would stay in the cusp through Phases B, C and D and would be picked up by an attractive charged wall when the in-plane field points in direction 1. However, during skidding the bubble is pushed along the track by a repulsive charged wall and arrives at the bottom cusp during the Phase C. The bubble then stays in the cusp during the Phase D until an attractive charged wall drives it out of the cusp.

4.2.2. Stripeout

As the bias field is lowered, bubbles start to stripe out. There are two modes of stripeout. The first is bubble stripeout across the adjacent tracks. The second is stripeout along the pattern edge. The former is more common and the latter occurs when the charged wall is not strong compared with the edge affinity along the pattern edge. Bubbles then stripe along the pattern edge rather than along the charged wall which is approximately perpendicular to the edge.

4.2.2.1. Stripeout Across Adjacent Tracks

Bubble stripeout failure modes across adjacent good tracks are shown in Fig. 4-3.

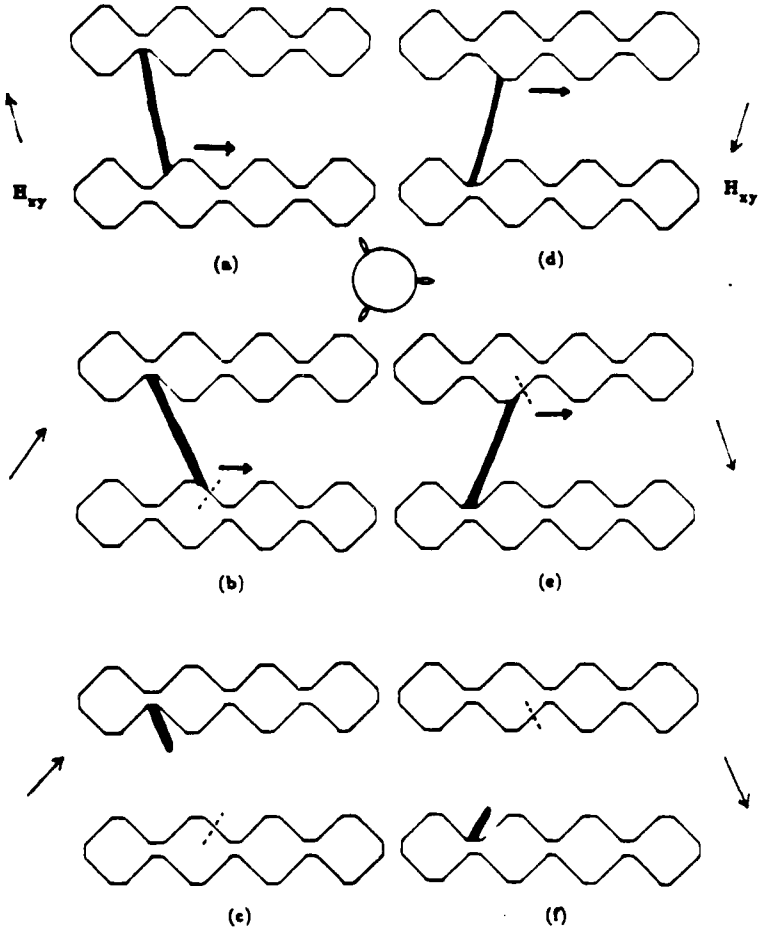

Figure 4-3: Bubble stripeout across adjacent tracks: Bubble moving up [(a)-(b)-(c)] or moving down [(d)-(e)-(f)] can occur

Diagrams (a), (b) and (c) show the failure mode when the in-plane field rotates clockwise and (d), (e) and (f) show the failure mode when the in-plane field rotates counterclockwise. When the in-plane field points near one of the easy stripe directions in (a), the bubble on the bottom track stripes out and is stretched all the way to the cusp of the top track because at this field direction the cusp has an attractive charged wall. As the field rotates the bottom side of the stripe rotates to the direction of the hard stripeout direction (b). At this point, the stripe shrinks to the cusp of the top track if the cusp is much more attractive to the bubble than the bottom track. In most conventional devices (highly anisotropic), bubbles move up which indicates that the attractive charged wall strength at the hard stripeout charged wall (flip) position is weak. In nearly

isotropic devices it is often observed that the stripe shrinks back to the bottom track which indicates that the charged wall strength of the bottom track even in the flip position is quite strong. If the field rotates clockwise in diagram (a) the stripe shrinks back to the bottom track, because the cusp of the top track encounters a repulsive charged wall.

Diagrams (d), (e) and (f) show the failure mode when the in-plane field rotates counterclockwise. The processes are similar to what happens in case of the clockwise rotating field. This time the stripe shrinks to the bottom cusp and the bubble thus moves down to the adjacent track.

Similar propagation failure occurs between good and super tracks as shown in Fig. 4-4.

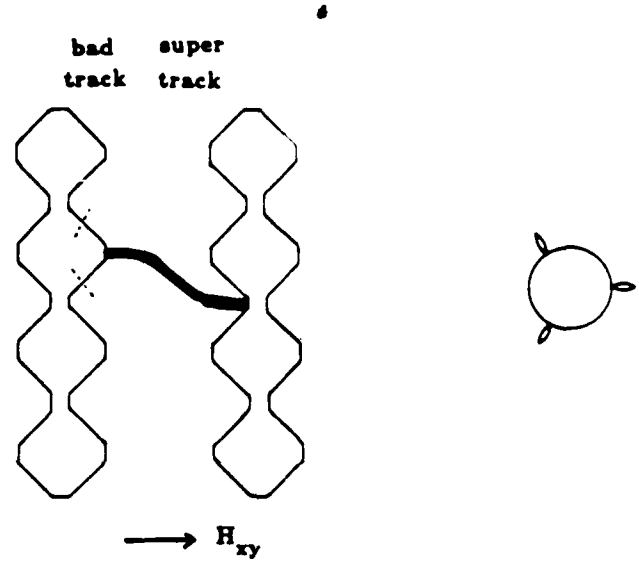

Figure 4-4: Bubble stripeout between bad and super tracks

When the field points into the cusp of the super track, the attractive charge wall is formed there and the bubble on the bad track is striped out and stretched into the cusp. However this time the rotating field sense does not make a difference. As the field rotates in either direction, the stripe end on the bad track side encounters charged wall flip positions shown as dotted lines and shrinks to the cusp on the super track in most cases. Therefore, the bubble moves mostly to the right (super) track.

4.2.2.2. Stripeout Along the Track

This failure mode occurs when the bubble is in the cusp at low bias field and generally at high in-plane field. At high in-plane field, the charged wall influence over the bubble (stripe) domain is diminished and the effect of edge affinity therefore becomes relatively stronger. When the in-plane field is directed along the boundary of the pattern as shown in Fig. 4-5 (a), the bubble stripes out along that boundary.

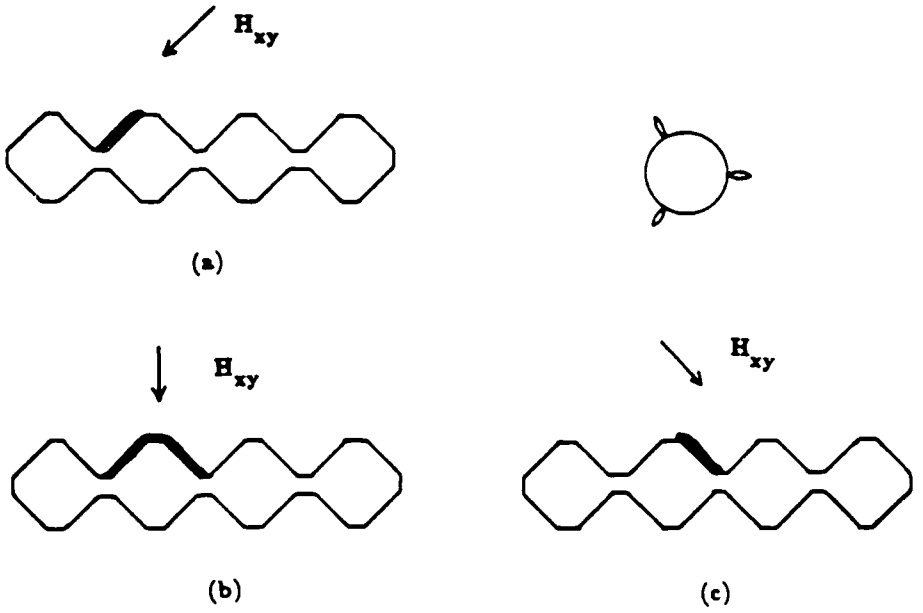

Figure 4-5: Stripeout along the track

As the field rotates counterclockwise as shown in Fig. 4-5 (b), the stripe generally shrinks back to the cusp and forms a bubble again. However, the stripe can also stretch out from one cusp to the next as shown in the figure. As the field further rotates [Fig. 4-5 (c)], the stripe shrinks back to the next cusp and eventually forms a bubble there. Thus the bubble moves one bit position to the right while it is supposed to stay at the cusp.

4.2.3. Skip

This failure mode happens when the bias field is low and the drive field is also low. In most cases a bubble skips the first cusp as it turns around (clockwise) the end of the track as shown in the bottom track of Fig. 4-6 (a).

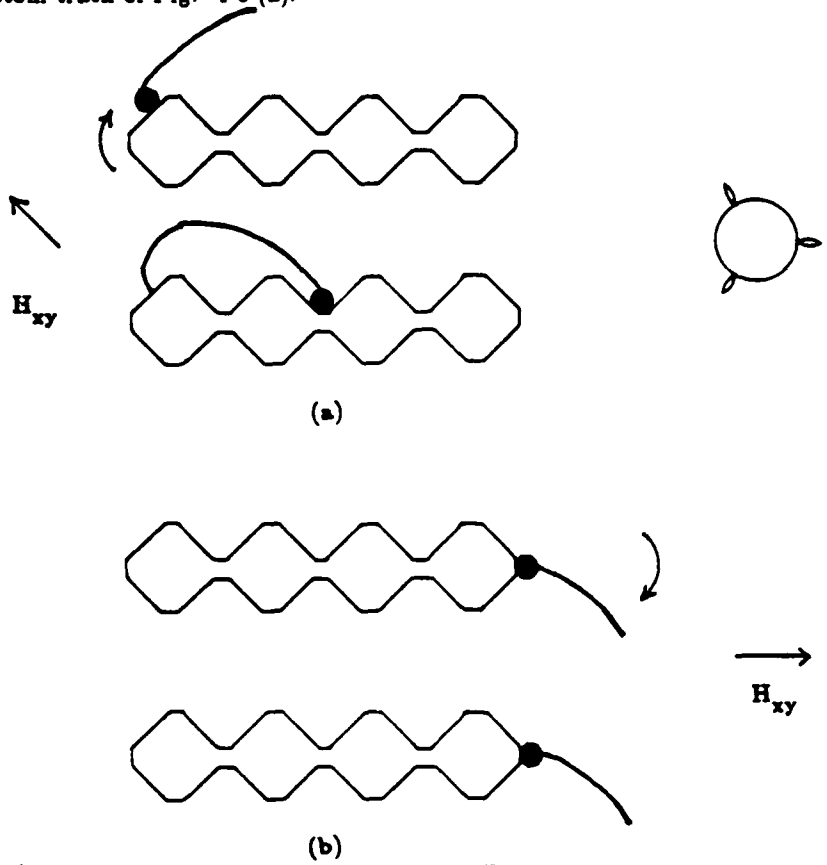

Figure 4-6: First cusp skip

It happens more frequently in close-packed tracks than in isolated tracks[52]. Most interestingly, it does not happen on the right side of the track when the track is oriented with respect to the crystal orientation as shown in the figure.

4.2.4. Trap at Cusp (Hang Up)

This is the most common failure mode at low drive field. At low drive field the charged wall does not move smoothly and jumps at the flip directions leaving the bubbles in the cusps. As the bias field is increased, the bubble size shrinks and the bubbles can move easily and follow the charged wall, giving the negative slope at the lower left corner of the bias margin as seen in Fig. 4-1. The bubbles are most often trapped in the cusps of the end of the track.

4.3. Ion Implantation and Annealing of Devices

4.3.1. Ion Implantation

The ion implantation conditions of devices were chosen based on the general rules presented in Chapter 2. The ion species used were initially deuterium and oxygen: deuterium for main implantation and oxygen for shallow surface implantation to make the damage profile uniform. However, later implantations were performed with only deuterium ions, the reason being that the oxygen implantation deteriorates the material properties and the anisotropy change induced by the oxygen implantation saturates at a lower value than the deuterium implantation[21]. The energies of the main implantation chosen were 40 KeV and 32 KeV which would give implantation layer depths of .27 μm and .23 μm, respectively, for nominal 0.5 μm diameter bubble films. Implantation doses were varied widely from $5.7 \times 10^{15}/cm^2$ to $12.3 \times 10^{15}/cm^2$ considering the material characteristics of the garnet films. Due to the limited supply of garnet films, most of the wafers (1" diameter) were divided into four regions and implanted with different conditions; two regions with 40 KeV of energy and the other two with 32 KeV of energy. The implantation current used was 20 μA which amounts to a current density of 0.35 $\mu A/cm^2$. With this current it took 7.4 minutes to implant 10^{15} ions/cm^2. Five of the one-inch diameter wafers could be implanted simultaneously. The experimental results obtained from eight representative wafers with a nominal bubble diameter of 0.5 μm (CA71, 72, 73, 77, AK91, 92, *a*8 and *b*1) are reported here. Some of the results obtained from wafers with nominal bubble diameter of 1 μm (S59, S74 and AH 27) are also reported. The implantation conditions of wafers CA71 and CA72 are summarized in Table 4-1 and those of the others are in Appendix C. The important material characteristics of wafer CA71 are listed in Table 4-2. Those of the others are also listed in Appendix B.

Table 4-1: Ion Implantation Conditions

Wafer ID	Region	First Implant		Second Implant	
		Energy (KeV)	Dose ($\times 10^{15}$)	Energy (Kev)	Dose ($\times 10^{15}$)
CA71 and 72	1	40	12	16	8
	2	40	8.5	16	5.7
	3	32	11.3	12	7.5
	4	32	7.5	12	5

Table 4-2: Garnet Film Characteristics (CA71)

Composition	$\{Bi_{0.4}Dy_{0.7}Sm_{0.2}Lu_{1.5}Y_{0.2}\}[FeGa]_5\ (0)_{12}$	
Thickness	t	0.65 μm
Collapse Field	H_c	580 Oe
Material Length	l	0.054 μm
Magnetization	$4\pi M$	960 G
Uniaxial Anisotropy	H_k	1850 Oe
Quality Factor	Q	1.9
Bubble Diameter	d	0.5 μm
Magnetostriction Coeff.	λ_{111}	-3.1×10^{-6}
	λ_{100}	-2.1×10^{-6}

It is to be noted that the implantations were performed through the SiO_2 spacer and the electroplating base so the implantation energies listed in Table 4-1 are 14 KeV less than actual to account for the energy needed to penetrate the SiO_2 spacer (800 Å) and Mo/Au (50 Å /300 Å) electroplating base. All the implantations performed were double implantations.

The anisotropy changes induced by the ion implantation were measured for the chips diced from the wafers CA72, CA77, AK92 and AKa8, and AK91. Except AK91, all the other wafers underwent device fabrication processes and had unimplanted propagation track patterns on the wafers. The wafers were diced into 16 chips, four chips in each region and the anisotropy change was measured using the FMR method with the resonant cavity (see section 3.1.1.2). Wafer AK91 did not undergo device processing steps and was not diced. The anisotropy change of AK91 was measured with the stripeline FMR method using the minibox. The results of the measurements, separated into two energy values (32 KeV and 40 KeV) used for the implantation are shown in Fig. 4-7. Anisotropy changes for both implantation energies are proportional to the implantation doses.

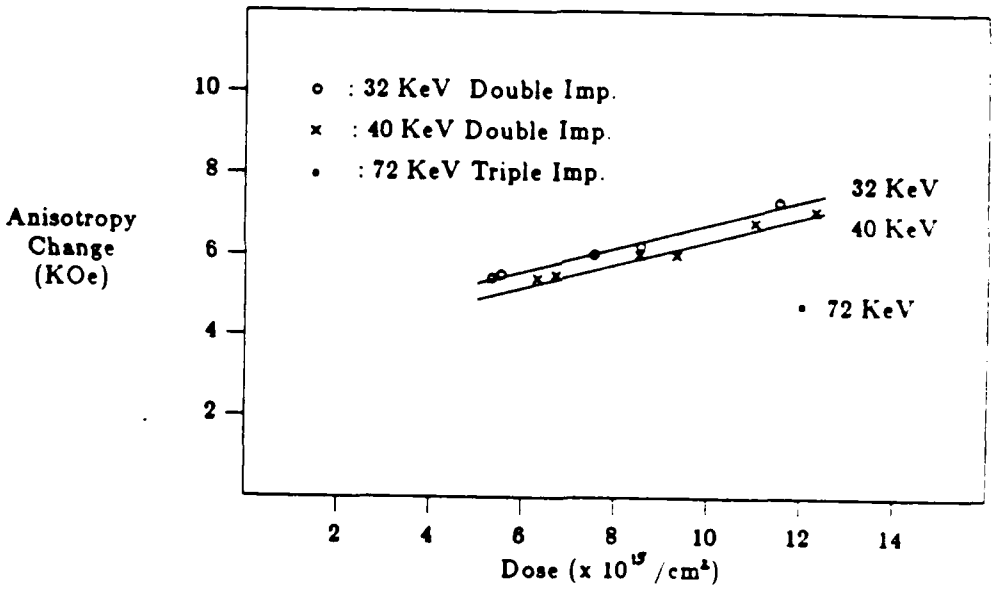

Figure 4-7: Anisotropy change versus implantation dose

The maximum lattice strain was measured using the double crystal x-ray diffraction method. The results for S59 is shown in Fig. 4-8 along with the result for AK91. The strain data for S59

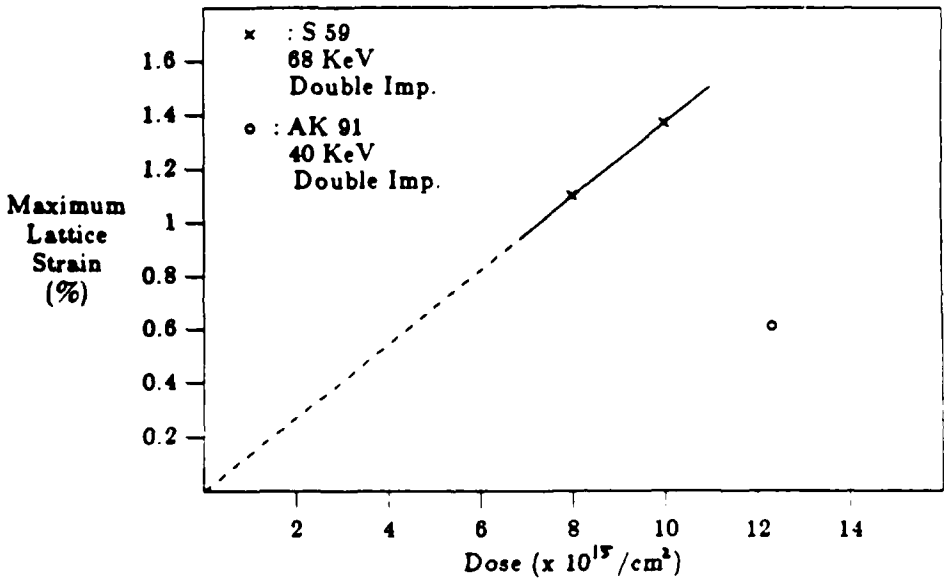

Figure 4-8: Maximum lattice strain vs. dose

is proportional to the implantation dose as expected and the maximum lattice strain values are similar to those of other researchers[21].

The variations of bias margin width in terms of the percentage of the mid-bias value and the minimum drive field as a function of the implantation dose are shown in Figs. 4-9 and 4-10 for "good" and "bad" tracks, respectively.

The margin width data of both good and bad tracks is somewhat scattered, but shows a definite trend. At the dose range studied, the margin width increases for the good tracks and decreases for the bad tracks as the dose is increased. The minimum drive field did not change very much as the dose changed. The data were obtained from the bias margins measured for 2.5 μm period diamond tracks of wafer AK92, CA72 and AKa8. The implantation energy used was 32 KeV which gave good bias margins for 2.5 μm period propagation tracks fabricated from all wafers.

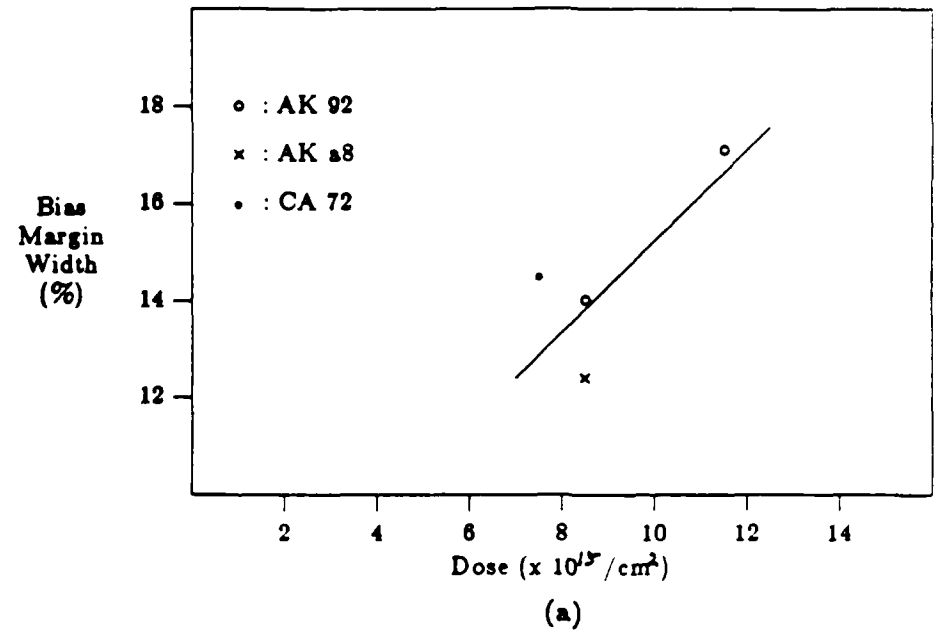

(a)

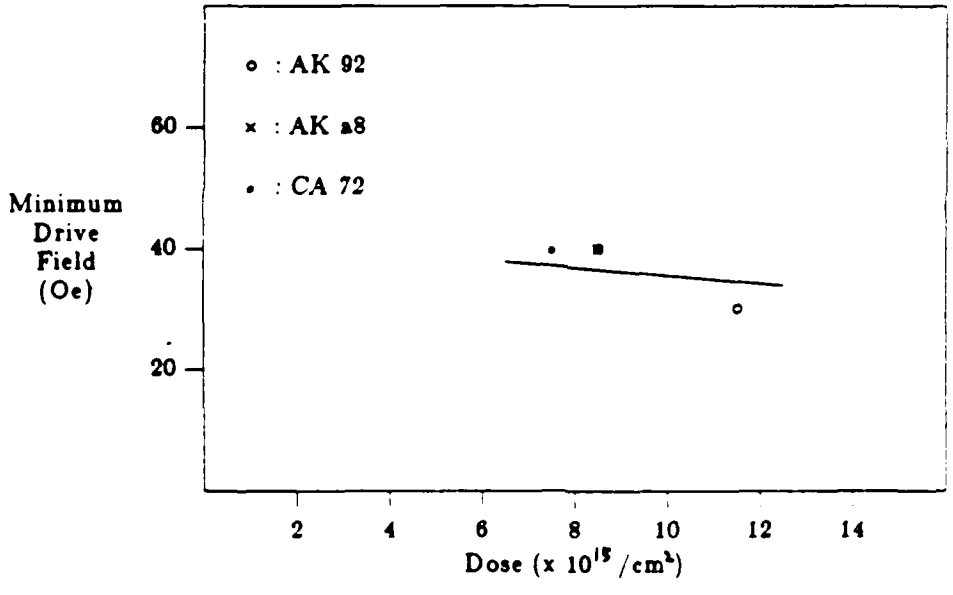

(b)

Figure 4-9: (a) Bias margin width vs. dose and (b) minimum drive field vs. dose for "good" track : 2.5 μm period diamond tracks, 32 KeV implant

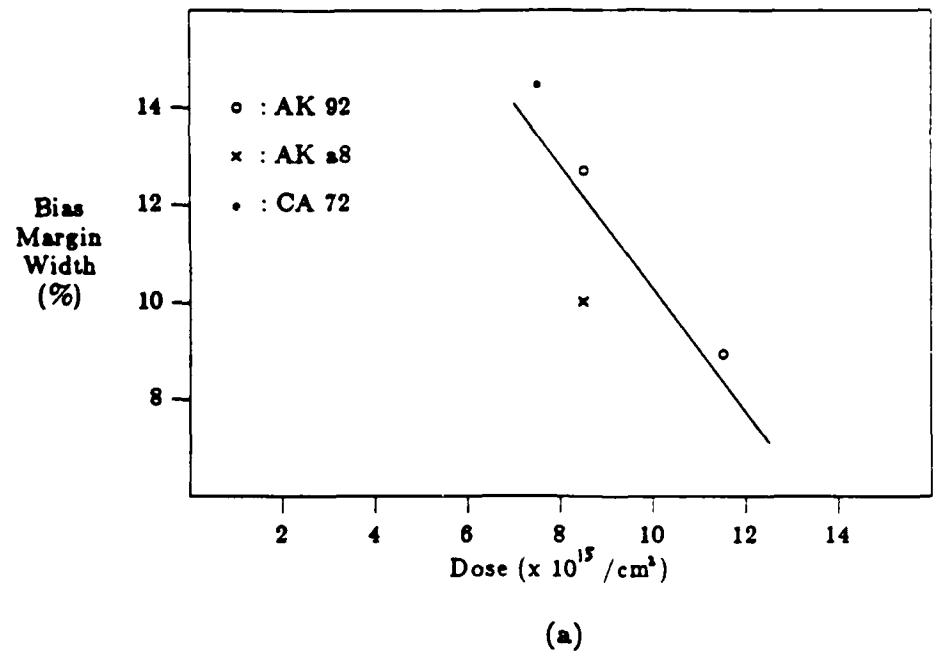

(a)

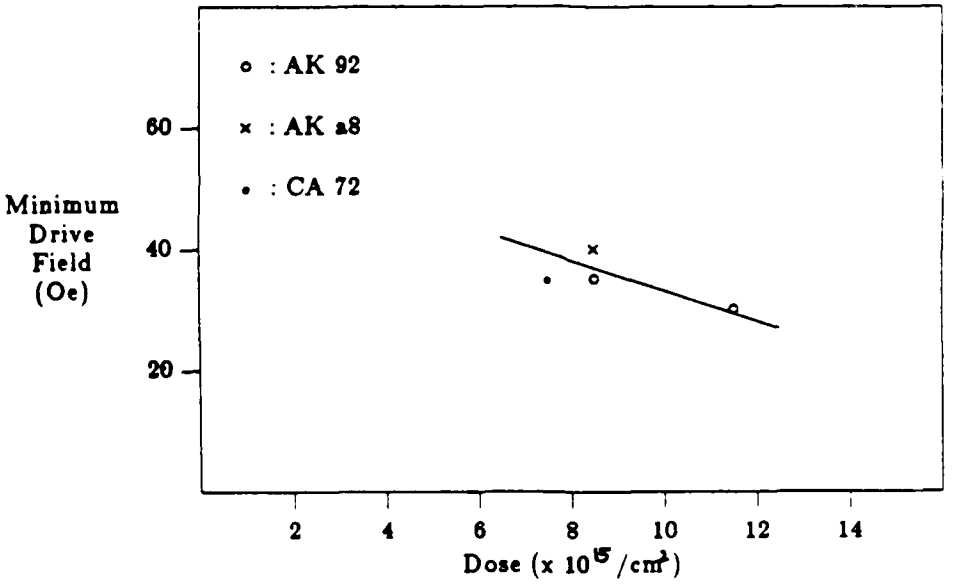

(b)

Figure 4-10: (a) Bias margin width vs. dose and (b) minimum drive field vs. dose for "bad track" : 2.5 μm period diamond tracks, 32 KeV implant

4.3.2. Annealing

An annealing test was performed with 2.5 μm period diamond shaped tracks fabricated on the wafer AK92. The same chips were used by successively annealing at 200 °C, 250 °C and 300 °C for 30 minutes each. The bias margin width, the minimum drive field, and the anisotropy change were measured after each annealing. Two chips implanted with 32 KeV of energy and 11.5 $\times$ $10^{15}/cm^2$ of dose and another two chips with 32 KeV of energy and 8.5 $\times$ $10^{15}/cm^2$ of dose were used. Two chips each were used to enhance the FMR signal, which is proportional to the area of the sample. The anisotropy change with annealing temperature is shown in Fig. 4-11.

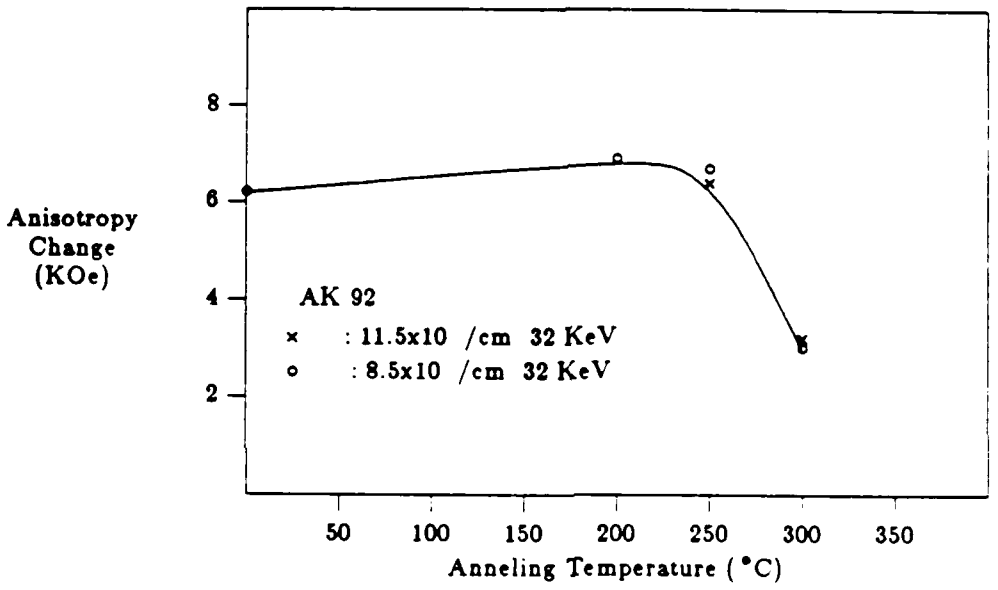

Figure 4-11:

Anisotropy change vs. annealing temperature for wafer AK 92 (Chip 12, Region 4)

The anisotropy change drops precipitously between 250 °C and 300 °C annealing, which is believed to be due to the desorption of deuterium discussed in Chapter 2. The difference of anisotropy changes between the two doses is not substantial after 250 °C and 300 °C anneals. The data for high dose as - implanted and after 200 °C anneal are not present because the FMR signal was too weak to be detected. The ion implantation damages the lattice and the FMR signal is therefore weak if the dosage is high. The FMR signals from as-implanted chips were very weak, and only one strongest mode was generally observed. As the chips were annealed at

higher temperatures the signals got stronger and several surface modes were observed. The anisotropy change actually increases somewhat after a 200 °C anneal. The bias margin width at 60 Oe of drive field vs. annealing temperature and the minimum drive field vs. annealing temperature are shown in Fig. 4-12. The variations of the average values of the bias margin width and the minimum drive field obtained from the two chips implanted with different doses are plotted in Fig. 4-12 (a) and (b) which can be considered as the responses of the chips implanted with the average values of the two doses, $11.5 \times 10^{15}/cm^2$ and $8.5 \times 10^{15}/cm^2$. Until a 200 °C anneal the device performance does not change appreciably (Even though the data was not taken below 200 °C anneal for these chips, the measurements taken for chips fabricated from other wafers confirm this remark.). After the 250 °C anneal, the minimum drive increases and the margin width decreases noticeably.

4.4. Variation of Propagation Track Shape and Size

4.4.1. Variation of Propagation Track Shape

4.4.1.1. Isolated Elements

Four propagation track shapes were chosen to compare their performance in propagating bubbles. They are shown in Fig. 3-10, which are snake, diamond, circular and triangular patterns. The triangular patterns were oriented both parallel to and antiparallel to the $[1\ 1\ \bar{2}]$ direction, so that the effect of bubble propagation on the track orientation could be studied. The triangular patterns were originally proposed by Shir[53] to help compensate for the three-fold crystal anisotropy by the shape anisotropy. If the pointed end of the track (left end as shown in the figure) is oriented to the $[1\ 1\ \bar{2}]$ direction, the triangular shape anisotropy is supposed to counteract the crystal three-fold anisotropy and make the bubble propagation smoother around the track. The circular patterns have been most widely used and the name contiguous disk device comes from this track shape. The diamond patterns have also been used by many researchers partly due to the ease of the mask design: only straight lines need be used, thus avoiding "stepping" of the patterns even though stepping was used in this study. The snake patterns were tried recently because the intertrack distance is longer for these patterns than others for a given cell size.

The bias margins of the isolated building blocks (circle, diamond, triangle and reverse triangle which points antiparallel to $[1\ 1\ \bar{2}]$ direction) were first measured. The results are shown in Fig. 4-13.

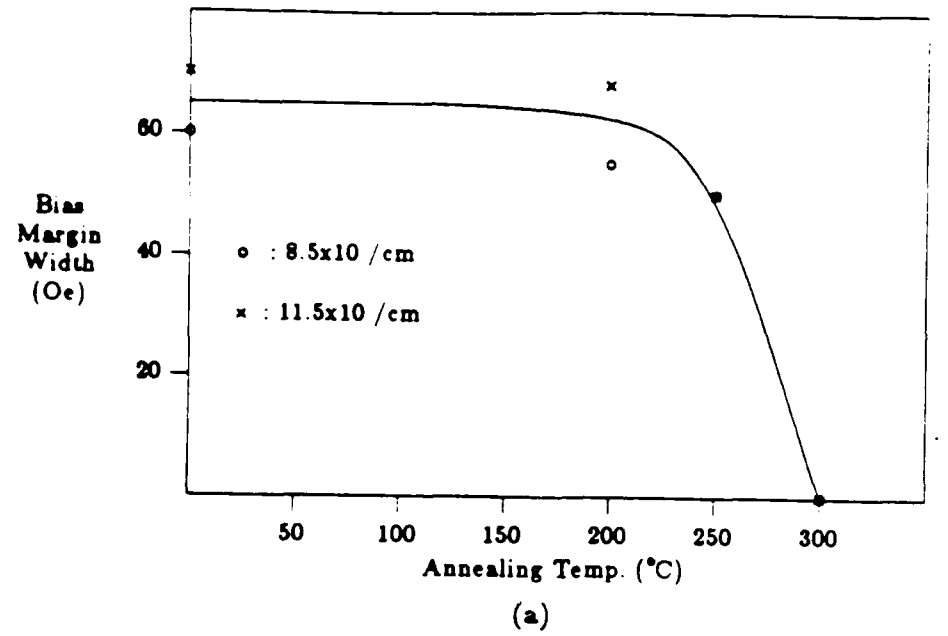

(a)

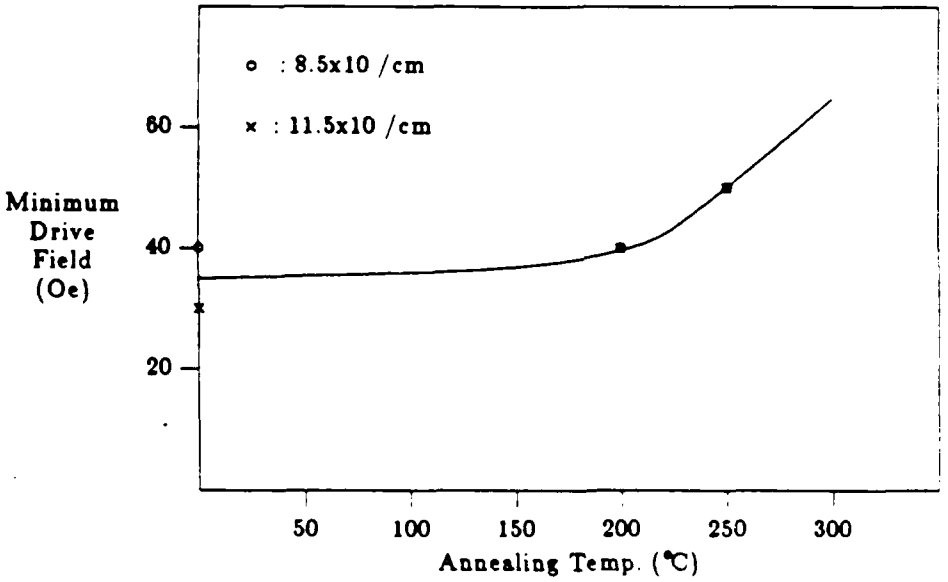

(b)

Figure 4-12: (a) Bias margin width vs. annealing temperature and (b) minimum drive vs. annealing temperature : AK 92, 2.5 μm period good diamond tracks, 32 KeV implant

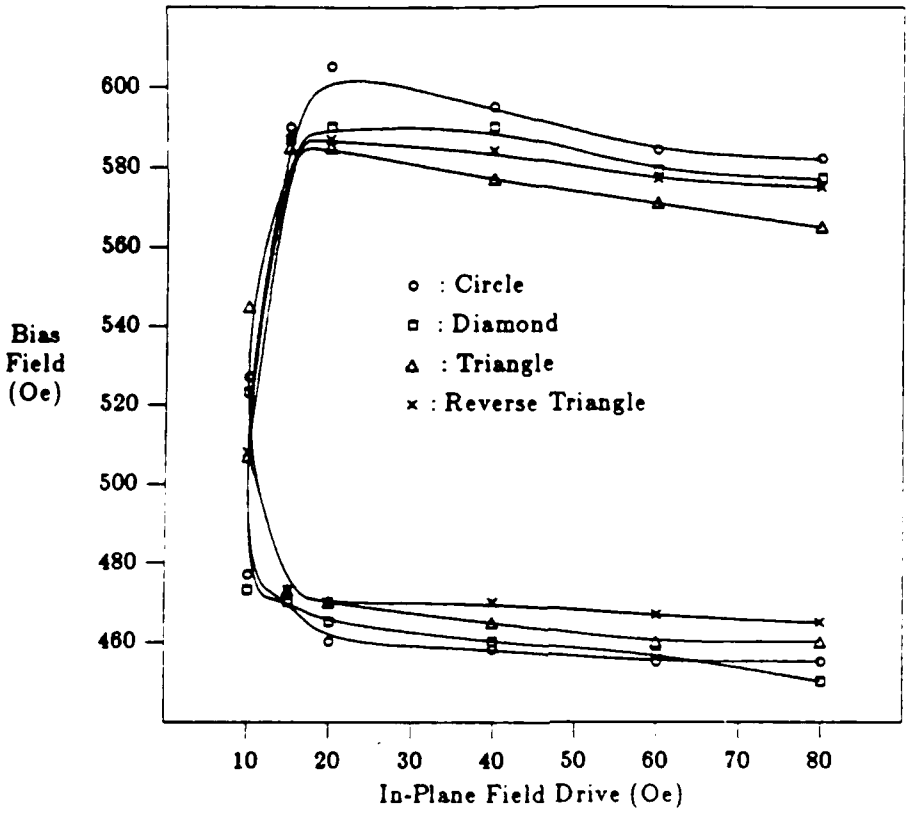

Figure 4-13: Bias margins of circle, diamond, triangle and reverse triangle : CA 72, Region 4, 2 μm size

The patterns were building blocks for 2 μm period good propagation tracks, and the ambient temperature was 40 °C. The patterns were all fabricated from the same wafer CA72 and were parts of the same chip which belongs to region 4 of the wafer. The ion implantation conditions for the region is listed in Table 4-1. The minimum circulation field for all the patterns are 10 Oe. The widest bias margin width belongs to the circle. The next is the diamond and the triangles are the last. The measurements of the minimum circulation fields for the larger sized elements show some variations (Only the minimum circulation fields were measured.). For 4 μm sized elements, the minimum circulation fields are 11 Oe for a circle, 12 Oe for a reverse triangle, 14 Oe for a diamond and 16 Oe for a triangle.

4.4.1.2. Propagation Tracks

The bias margins for the five different propagation tracks are shown in Fig. 4-14. These were obtained from the same chip explained in the previous subsection. The tracks are all oriented in the [1 1 $\bar{2}$] direction ("good" track orientation). The snake shaped tracks show the best margin. The minimum drive field (30 Oe) is the lowest and the margin width (80 Oe at 60 Oe drive field) is the largest. The next best margins are for the diamond tracks with the next lowest minimum drive field (40 Oe) and as large a margin width as the snake shaped tracks. The triangular patterns are the third best and surprisingly, the circular patterns are the worst along with the reverse triangular patterns.

The effect of the cusp depth change is shown in Fig. 4-15. The bias margins for good and bad snake tracks with 2 μm period, and the cusp depth to period ratio of 0.44 are shown in Fig. 4-15 (a) and the margins for the similar tracks with the cusp depth to period ratio of 0.38 are shown in Fig. 4-15 (b). The difference in good track margins is mainly the increase (by 10 Oe) of the minimum drive field for the tracks with shallower cusps. However, the difference in bad track margins is rather remarkable. The minimum drive increases and the collapse field decreases due to skidding for the tracks with shallower cusps. For the tracks with deeper cusps, the deterioration of the bad track margins is less spectacular.

4.4.2. Variation of Propagation Track Size

4.4.2.1. Isolated Disks

To find out the dependence of the propagation bias margin on the track size, the bias margins of the various sized unimplanted disks (from 1.5 μm diameter to 16 μm diameter) were measured and are shown in Fig. 4-16. The device chip used is from region 4 of the wafer CA71. It is seen that the bias margin is widest for large disks, but that the minimum drive field is lowest for small disks.

4.4.2.2. Propagation Tracks

The bias margins for 1.75 μm and 2.5 μm period snake patterns are shown in Fig. 4-17. The tested chip is from region 4 of the wafer CA71. The collapse fields are lower for smaller period (smaller sized) patterns as was the case for isolated disks as are shown in Fig. 4-17. However, here the bias margin of the smaller period devices is reduced.

The bias margins for two different 2 μm period snake patterns are shown in Fig. 4-18. The difference is with the width of the unimplanted snake patterns. One has the width of 0.75 μm

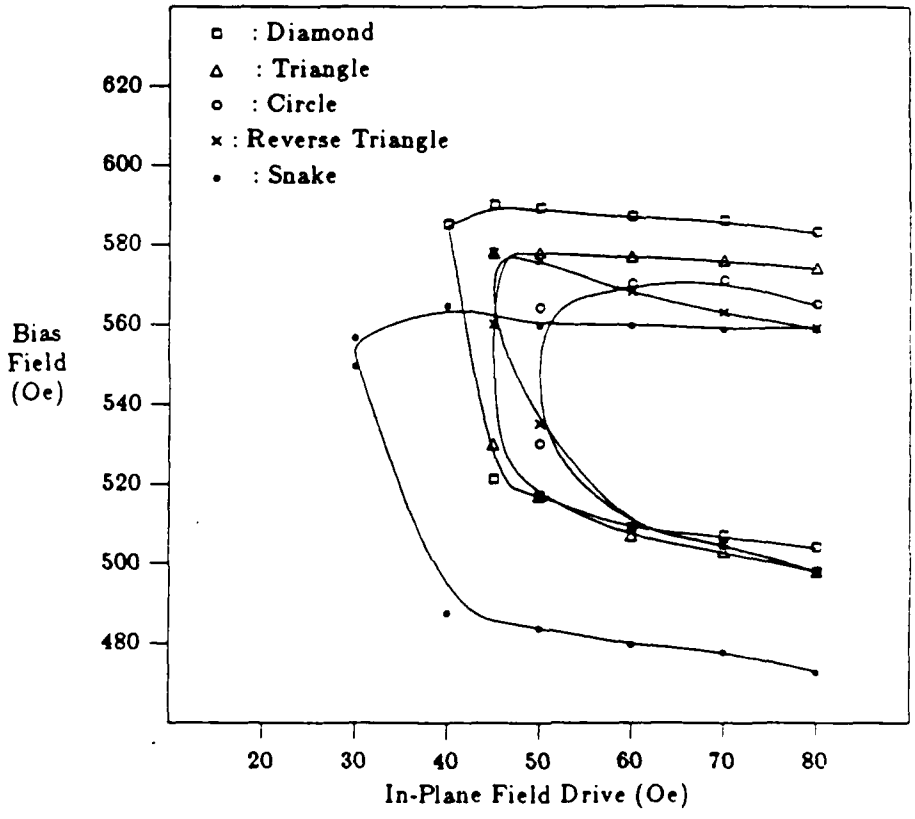

Figure 4-14: Bias margins of various shaped propagation tracks : CA 72, Region 4, 2.5 μm period

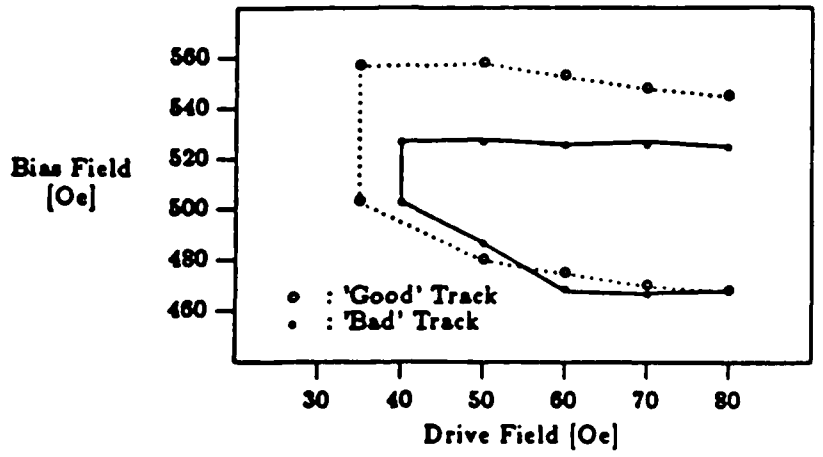

(a)

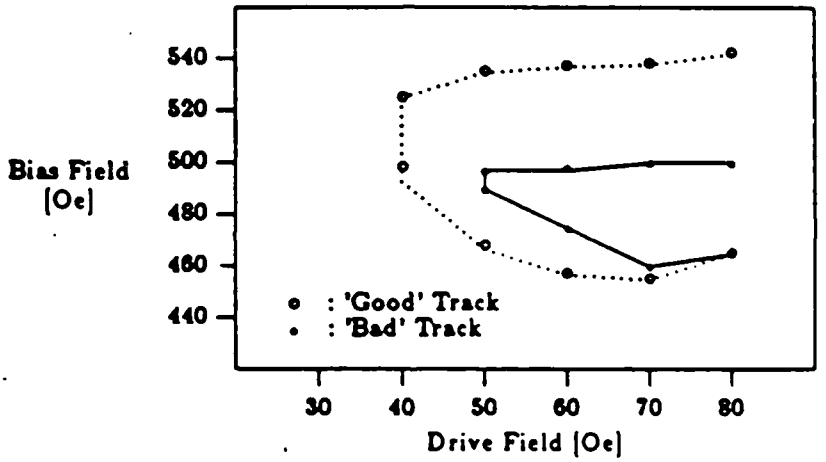

(b)

Figure 4-15: Margins for 2 μm period snake patterns with (a) cusp to period ratio of 0.44 (b) cusp to period ratio of 0.38 film CA72

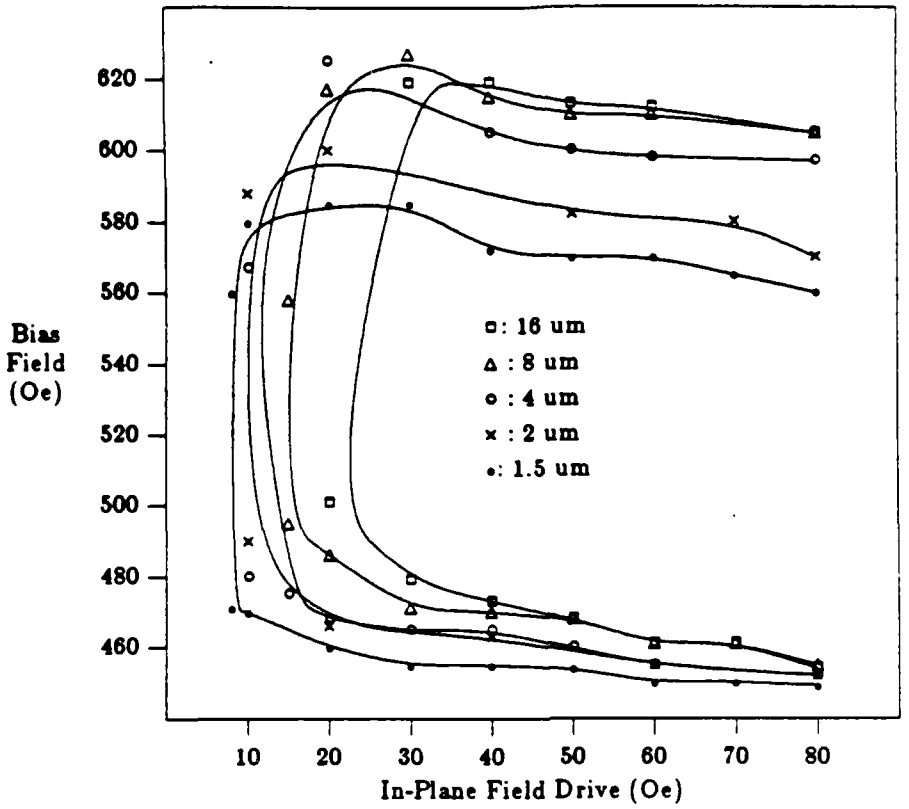

Figure 4-16: Bias margins of various sized unimplanted disks : CA 71, Region 4

and the other 1 μm. The propagation tracks with the smaller width have lower collapse fields and stripeout fields. It also has smaller minimum drive field.

4.5. Variation of Magnetostriction Coefficients - Nearly Isotropic Propagation

4.5.1. Comparison of Conventional and Nearly Isotropic Films

Bubble propagation around unimplanted disks and propagation tracks fabricated with conventional films ($\lambda_{100} > 0$ and $\lambda_{111} < 0$) and nearly isotropic films ($\lambda_{111} \sim \lambda_{100}$ and $\lambda_{111} < 0$) is compared here. The magnetostriction coefficients of the garnet films used for this study are shown in Table 4-3.

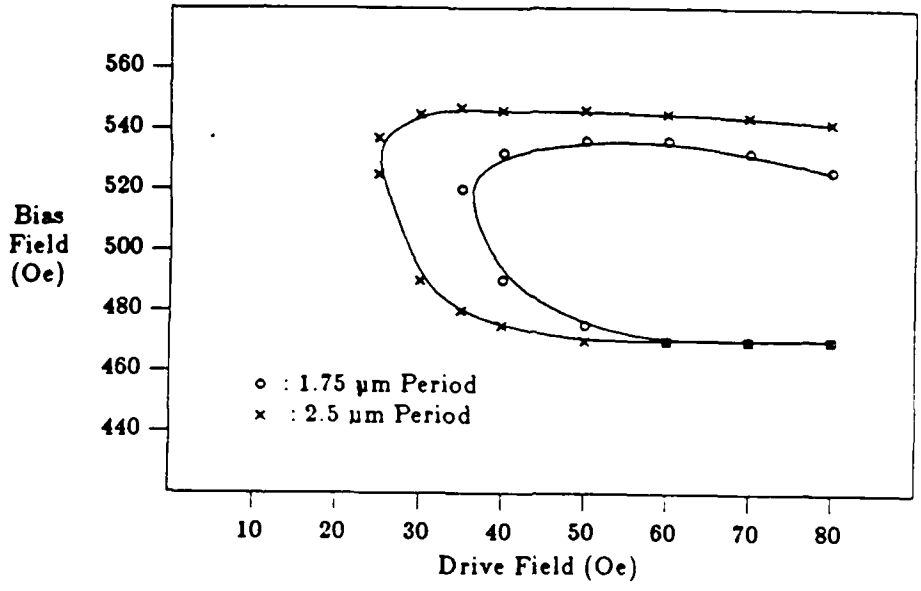

Figure 4-17: Bias margins of 1.75 μm and 2.5 μm period snake patterns : CA 71, Region 4

Table 4-3: Magnetostriction Coefficients

	λ_{111}	λ_{100}	$\Delta=(\lambda_{111}-\lambda_{100})/\lambda_{111}$
S74	−2.5	+1 (est.)	1.4
AH27	−3.7	−2.5	0.33
CA72	−2.9	−2.0	0.31

The conventional film used is wafer S74 with nominal 1 μm bubble diameter and the nearly isotropic films are AH27 with nominal 1 μm bubble diameter and CA72 with nominal 0.5 μm bubble diameter.

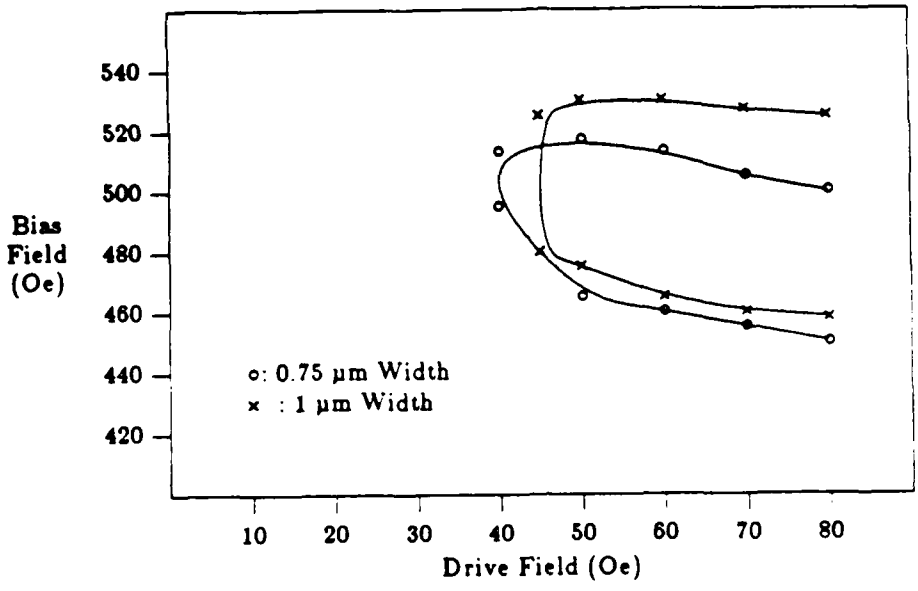

Figure 4-18: Bias margins of two 2 μm period snake patterns: one with 0.75 μm unimplanted region width, the other 1 μm width : CA 73, Region 4 .

4.5.1.1. Propagation Bias Margins

Bias margins for 5 μm period diamond patterns from S74 (conventional film) and bias margins for 4 μm period diamond patterns from AH27[2] (nearly isotropic film) are shown in Figs. 4-19 (a) and (b), respectively. Also shown are the bias margins of good and bad tracks obtained from 2.5 μm period diamond patterns fabricated with wafer CA72 (nearly isotropic, nominal 0.5 μm bubble diameter) in Fig. 4-20. The bias margin of the bad tracks of the conventional film shows much lower collapse fields than that of the good tracks, which is typical of conventional films. On the other hand, the bias margins for good and bad tracks from nearly isotropic films are nearly identical.

[2]This wafer was processed by M. Alex.

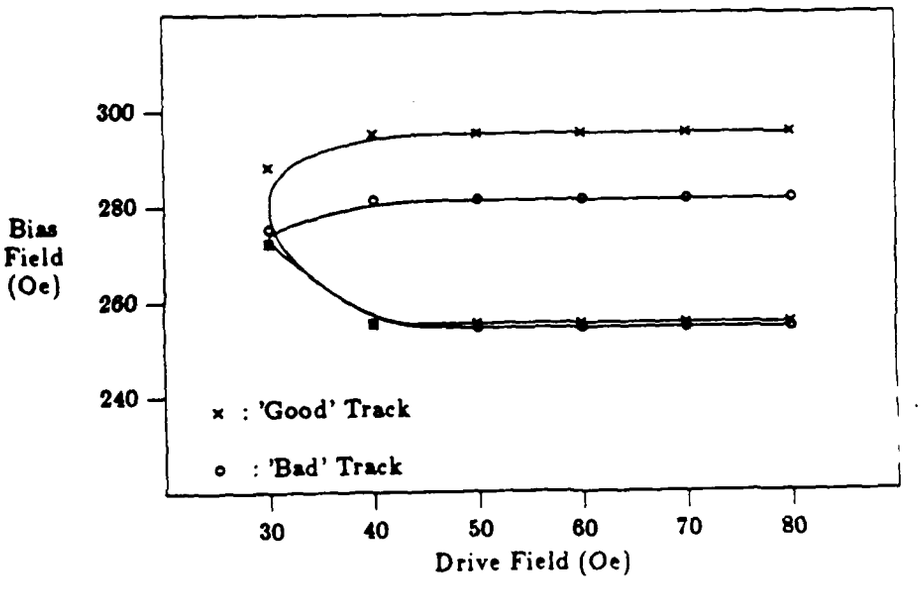

(a)

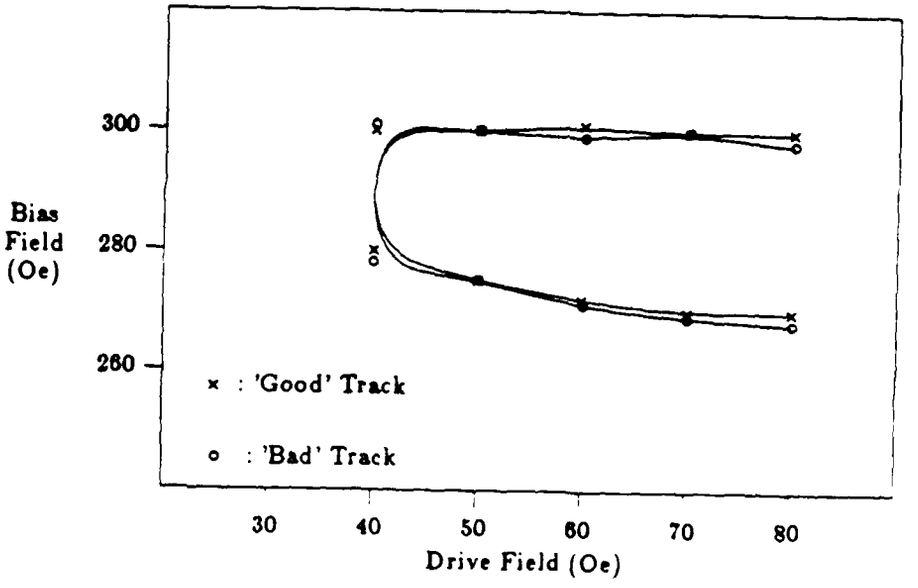

(b)

Figure 4-19: (a) Bias margins for conventional film S74 (: 5 μm period diamond tracks , Region 2) and (b) bias margins for nearly isotropic film AH 27 (: 4 μm period diamond tracks)

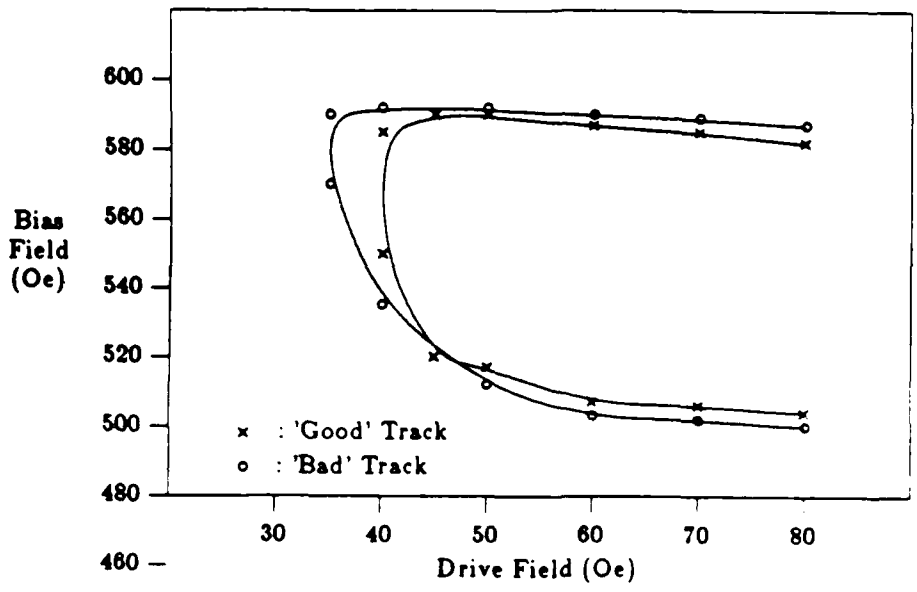

Figure 4-20: Bias margins for nearly isotropic film CA 72 : 2.5 μm period tracks

4.5.1.2. Bubble Position vs. In-Plane Field Direction

Bubble positions around unimplanted disks as the in-plane field is rotated, were measured for the conventional film (S74) and the nearly isotropic film (AH27) which are shown in Figs. 4-21 (a) and (b), respectively.

The in-plane drive field strength was fixed at 24 Oe. The diameters of the disks were 4 μm for S74 and about 3.5 μm for AH27. The straight lines drawn in the figures are for comparison. The straight lines indicate perfect synchronization of the in-plane field and the bubble position which would occur if the films are perfectly isotropic. The comparison of the two bubble positions vs. the in-plane field direction curves [Figs. 4-21 (a) and (b)] indicates that the bubble follows the in-plane field more closely in the nearly isotropic film than in the conventional film. In the conventional film, the bubble jumps (from 60° to 80°) at the three charged wall flip positions (near 60°, 190° and 290° of in-plane field directions), whereas in the nearly isotropic film, the bubble really does not abruptly jump at the three charged wall flip positions.

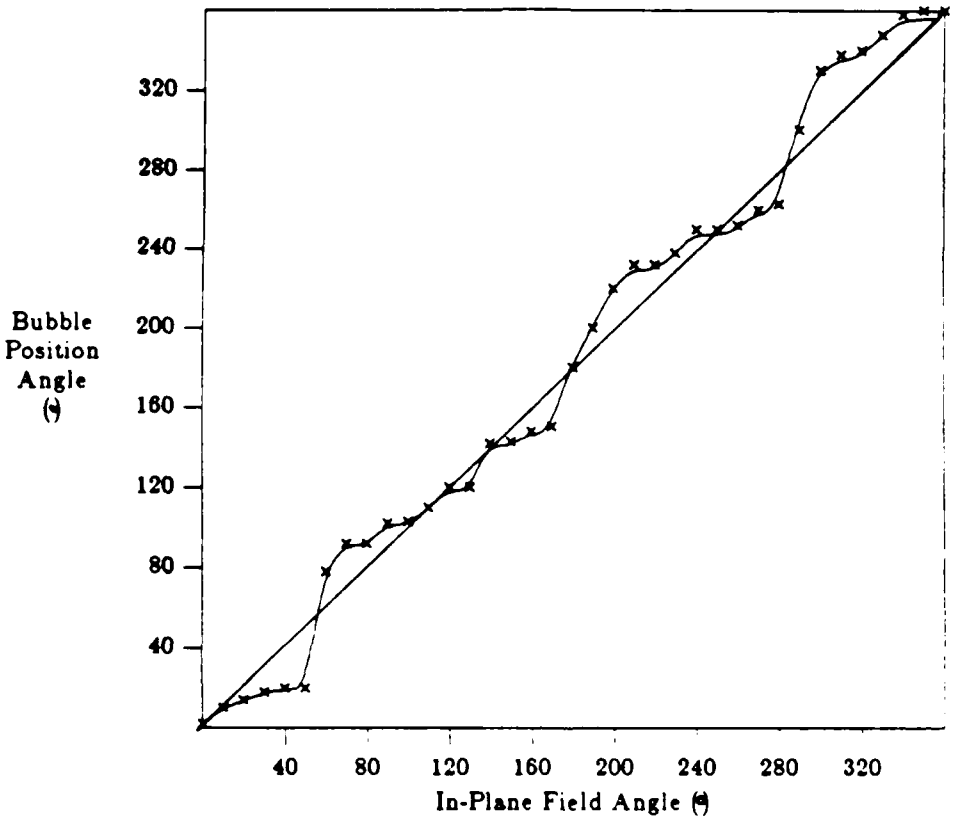

Figure 4-21: (a) Bubble position vs. in-plane field direction for conventional films S 74and

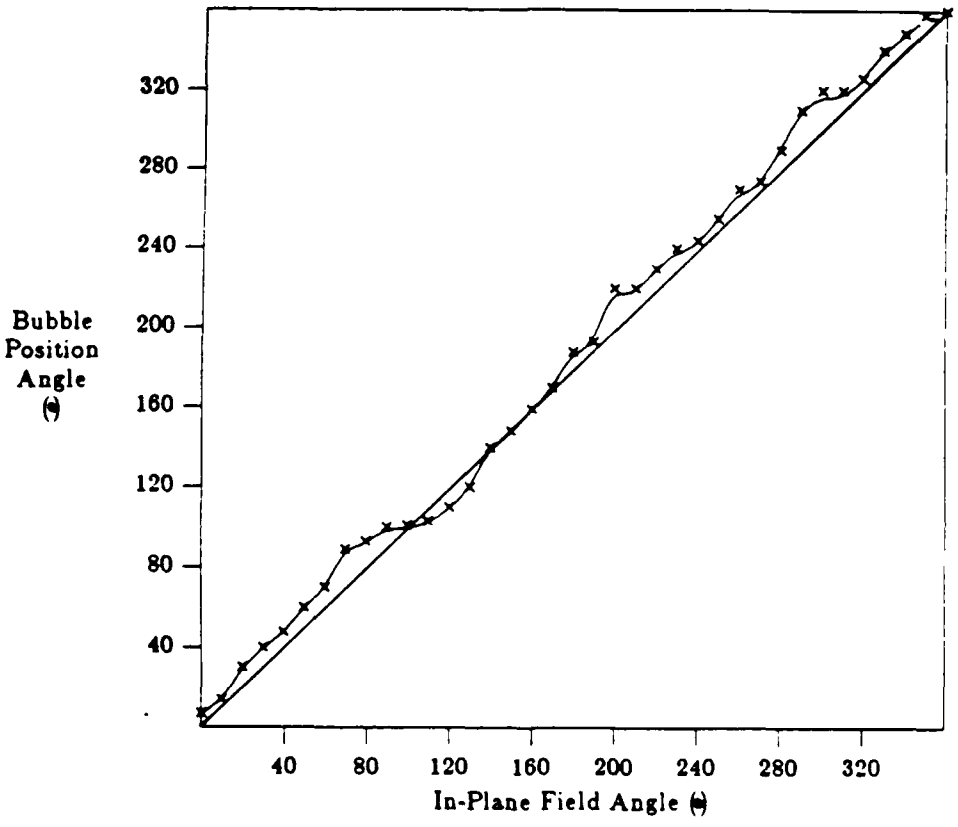

(b) bubble position vs. in-plane field direction for nearly isotropic film AH 27

4.5.1.3. Bubble Collapse Fields Along Propagation Tracks

Bubble collapse fields as a function of in-plane field directions along good, bad and super tracks for one cycle of the in-plane field rotation were measured for the conventional film S74 and the nearly isotropic film CA72. The curves of bubble collapse fields then were converted to curves of the bubble potential wells. The depth of the bubble potential well (H_w) at a certain direction of the in-plane field is obtained by subtracting the bubble (adhered to the pattern boundary) collapse field at that direction from the free bubble collapse field. The bubble potential wells for the conventional film are shown in Fig. 4-22 (a) and those for the nearly isotropic film are shown in Fig. 4-22 (b). The potential well depths are normalized to $4\pi M$ for ease of comparison since the two films have different magnetizations (600 Oe for S74 and 910 Oe for CA72) and the potential well depth scales with $4\pi M$. Propagation tracks measured were 5 μm period diamond shaped tracks for the conventional film and 2.5 μm period diamond shaped tracks for the nearly isotropic film. The in-plane field applied was 60 Oe. It is to be noted that some of the potential well curves were translated so that the in-plane field points into the cusps at 180° of the in-plane direction regardless of the track orientations (good, bad or super) for ease of comparison. The portion of the in-plane field cycle when the bubble resides in the cusp or when the bubble is on the move along the track, is indicated in the figures. The main difference between the two sets of potential well curves is that the potential well in the cusps of bad tracks in the conventional film is much shallower than that in the nearly isotropic film.

4.5.2. Variation of Magnetostriction Coefficients - Nearly Isotropic Films

In an effort to create more isotropic films the magnetostriction coefficients were varied to obtain lesser and lesser Δ $[(\lambda_{111} - \lambda_{100})/\lambda_{111}]$ values. The magnetostriction coefficients and Δ values for three nearly isotropic films presented here are shown in Table 4-4.

Table 4-4: Magnetostriction Coefficients

	λ_{111}	λ_{100}	$\Delta=(\lambda_{111}-\lambda_{100})/\lambda_{111}$
AK92	−3.1	−1.5	0.52
AKa8	−3.5	−2.5	0.29
AKb1	−3.8	−3.4	0.11

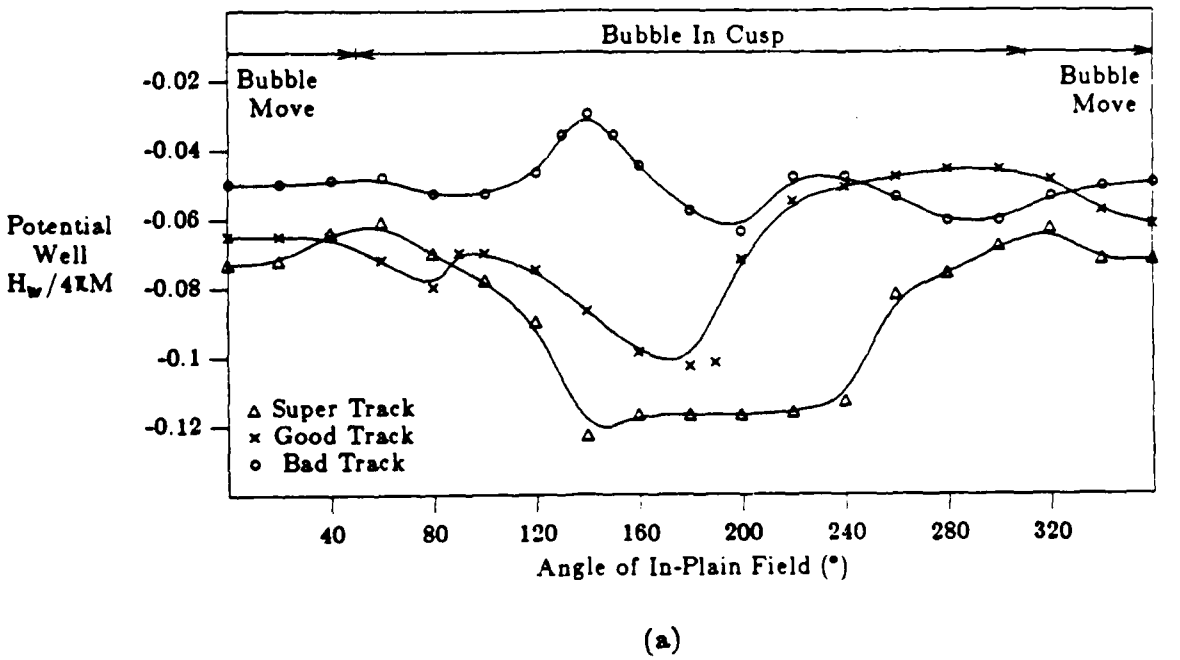

(a)

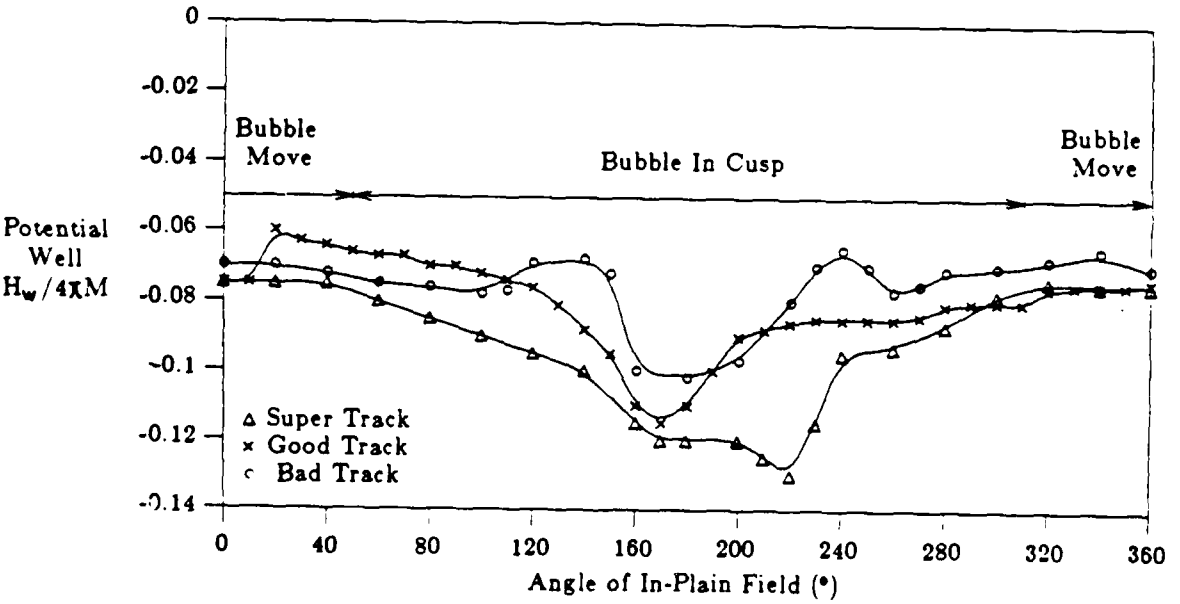

(b)

Figure 4-22: (a) Potential wells of good, bad and super tracks in a conventional film (: Wafer S 74 5 μm period diamond tracks, region 4, H_{xy} = 60 Oe, $4\pi M$ = 600 G) and (b) in a nearly isotropic film (: Wafer CA 72, 2.5 μm Period diamond tracks, Region 4, H_{xy} = 60 Oe, $4\pi M$ = 910 Oe)

These three films were grown from the same melt by changing the Dy contents. Adding Dy increases the magnitude of λ_{100} faster than that of λ_{111}, therefore decreasing Δ. In this subsection, comparison is made for the three nearly isotropic films in the bubble circulation around the implanted disks, in the plots of bubble position vs. in-plane field direction and in the propagation bias margins.

The minimum drive fields were measured for circulation around nonimplanted disks fabricated with the three films. The measurements were made for 2 μm diameter and 8 μm diameter disks from the same chips. The results are shown in Fig. 4-23. For 2 μm disks there is not much difference (from 8 Oe to 10 Oe) in the minimum drive fields as Δ varies from 0.11 to 0.52. However, the difference is more pronounced for the larger 8 μm disks. The minimum drive field changes from 10 Oe to 15 Oe.

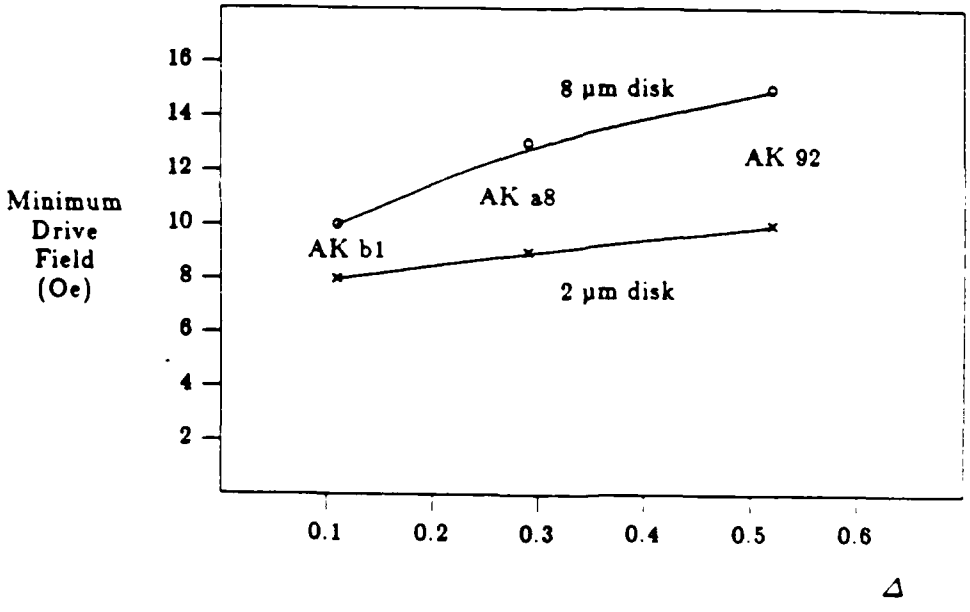

Figure 4-23: Minimum drive fields for unimplanted disks

The bubble position vs. in-plane field direction curves were measured for wafers AKb1, AKa8 and AK92 and are shown in Figs. 4-24 (a), (b) and (c), respectively.

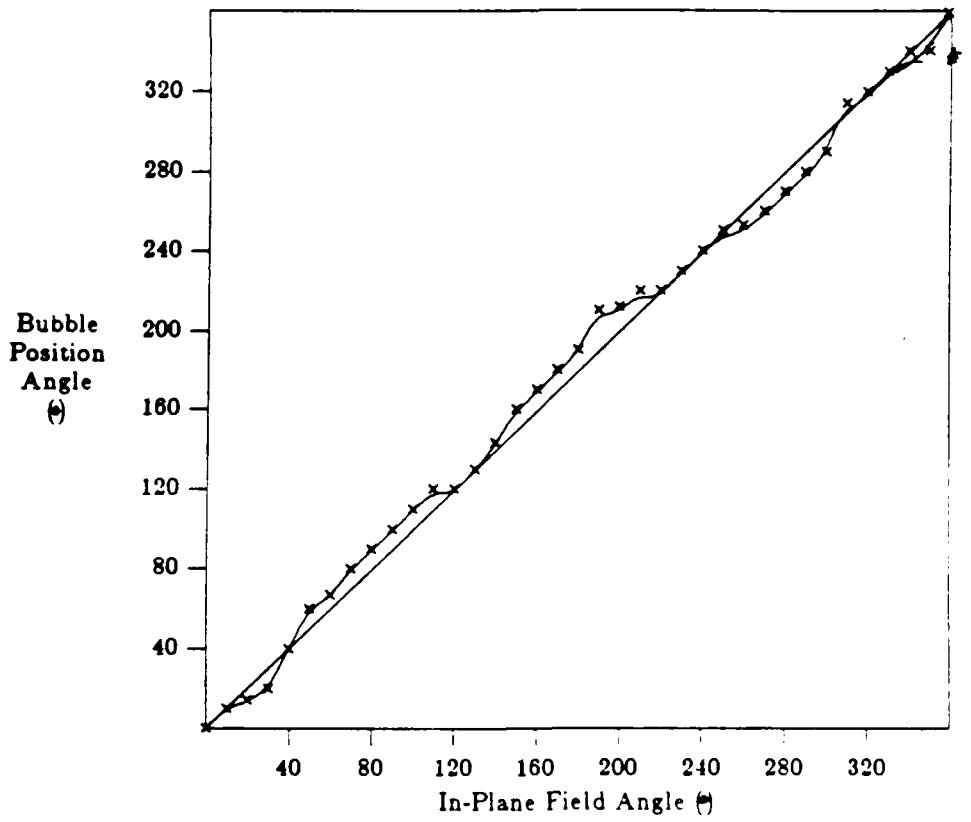

Figure 4-24: (a) Bubble position vs. in-plane field direction for wafer AKb1.

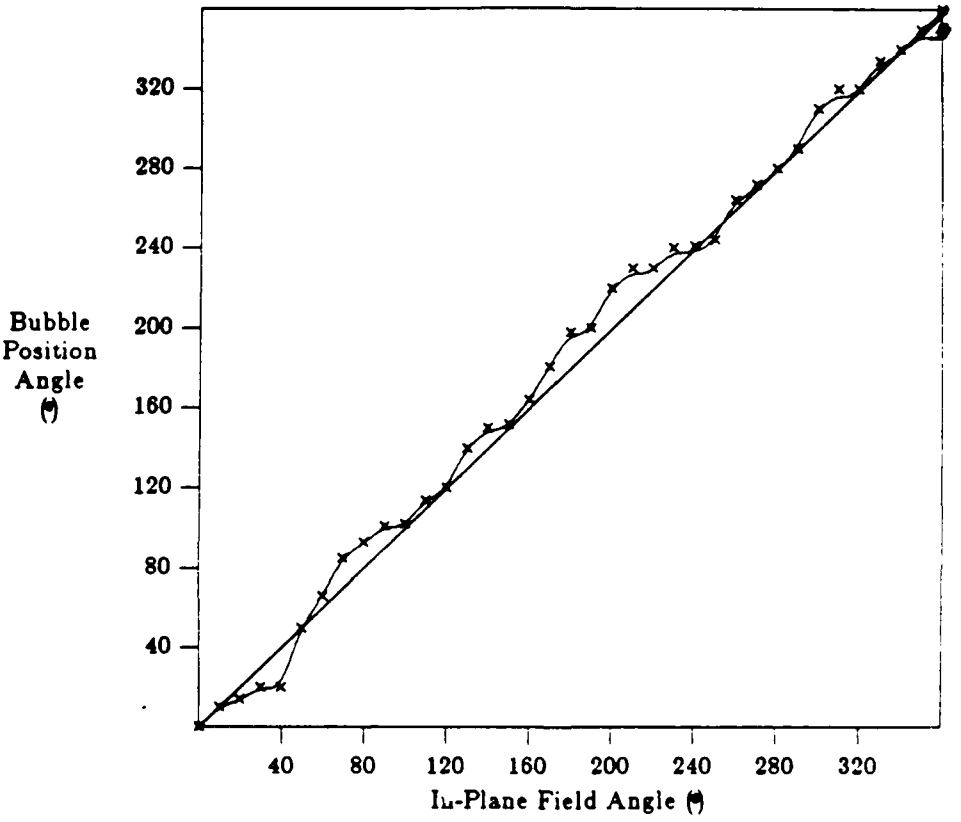

(b) for wafer AKa8 and

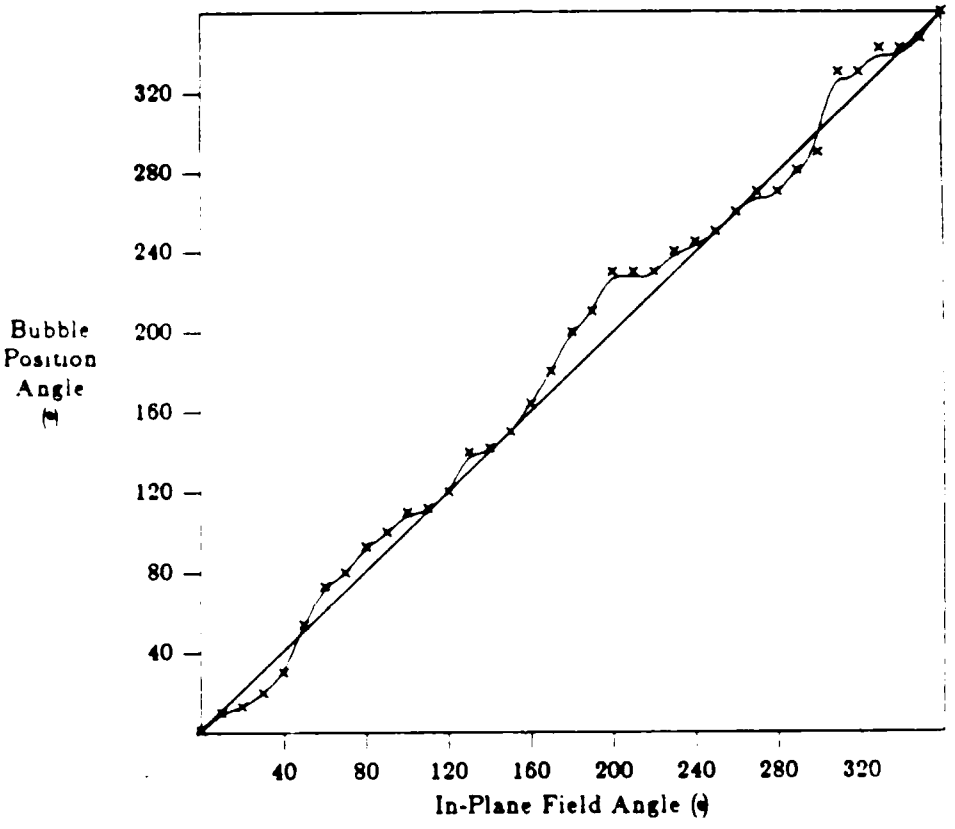

(c) for wafer AK 92

The diameter of the disks for the measurements was 4 μm and the in-plane field was 40 Oe. The curves (Fig. 4-24) do not differ much from each other, but do show a tendency toward increasing three-fold anisotropy as Δ is increased, which can be seen in decreased synchronization of bubble positions with the directions (angles) of the in-plane field.

The bias margins of good and bad diamond tracks (2.5 μm period) from wafers AKb1, AKa8 and AK92 are shown in Figs. 4-25 (a), (b) and (c), respectively.
The bias margins for all wafers (Fig. 4-25) exhibit nearly isotropic propagation. The collapse fields of good and bad tracks measured from the wafers AKb1 and AKa8 are nearly identical, while those from the wafer AK92 show minor differences.

4.6. Variation of Ambient Temperature

In this section, the temperature dependence of propagation margins for 2.5 μm period diamond and circular propagation tracks from the nearly isotropic wafer CA72 is presented. The temperature range tested was from 0 °C to 130 °C.

The temperature dependence of the minimum drive fields of diamond and circular propagation patterns as a function of temperature is shown in Fig. 4-26. The curves in Fig. 4-26 show a monotonic decrease of the minimum drive as the temperature is increased. Diamond patterns showed lower drive fields for both good and bad tracks (less than 40 Oe). The propagation bias margins at 60 Oe drive field as a function of chip temperature are shown in Fig. 4-27 for diamond and circular patterns. The margins in Fig. 4-27 shift downward monotonically as the temperature increases with a coefficient [Eq. (2.31)] of approximately $-0.27\%/^\circ$C at 50 °C. Diamond patterns showed the wider overlapping margin of good and bad tracks (80 Oe or 15% of mid-bias value at 40 °C). Circular patterns showed almost no margin width variation throughout the temperature range tested. At 130 °C, they still showed 55 Oe (14% of mid-bias) of overlapping bias margin.

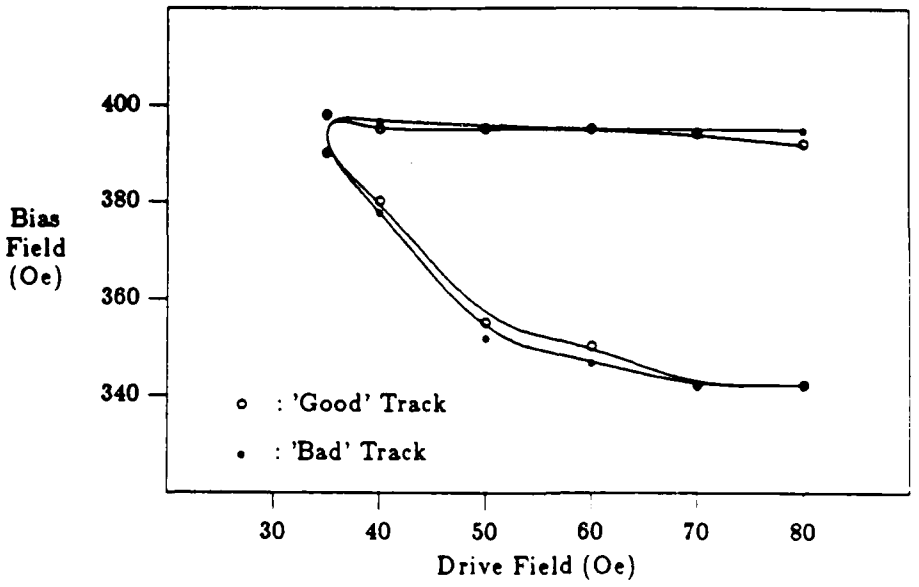

Figure 4-25: (a) Bias margins of 2.5 μm period diamond tracks from wafer AKb1,

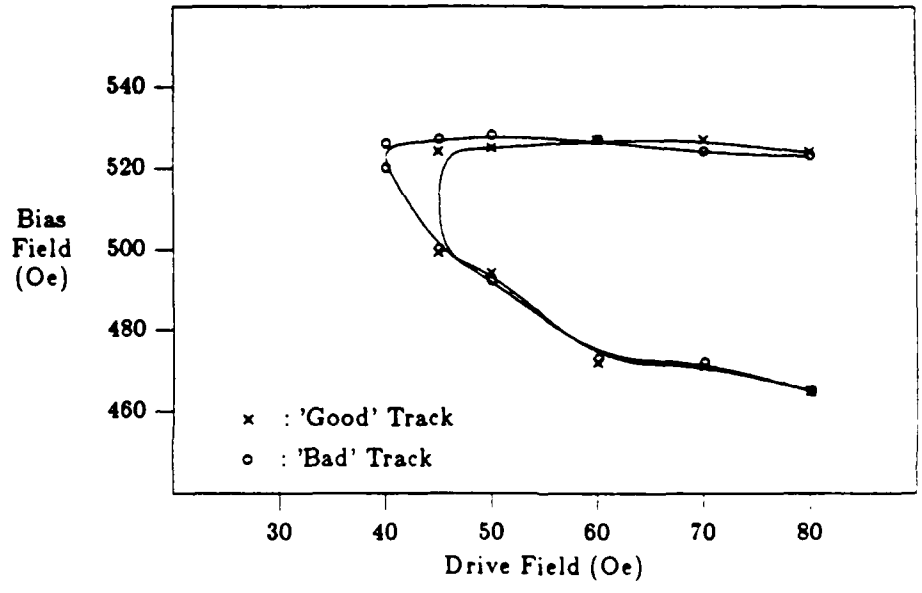

(b) from wafer AKa8 and

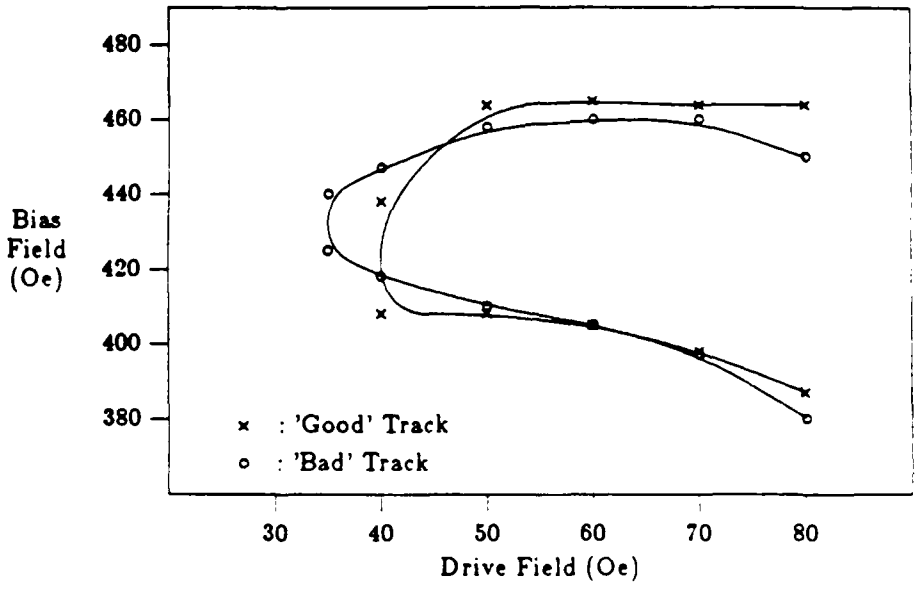

(c) from wafer AK92

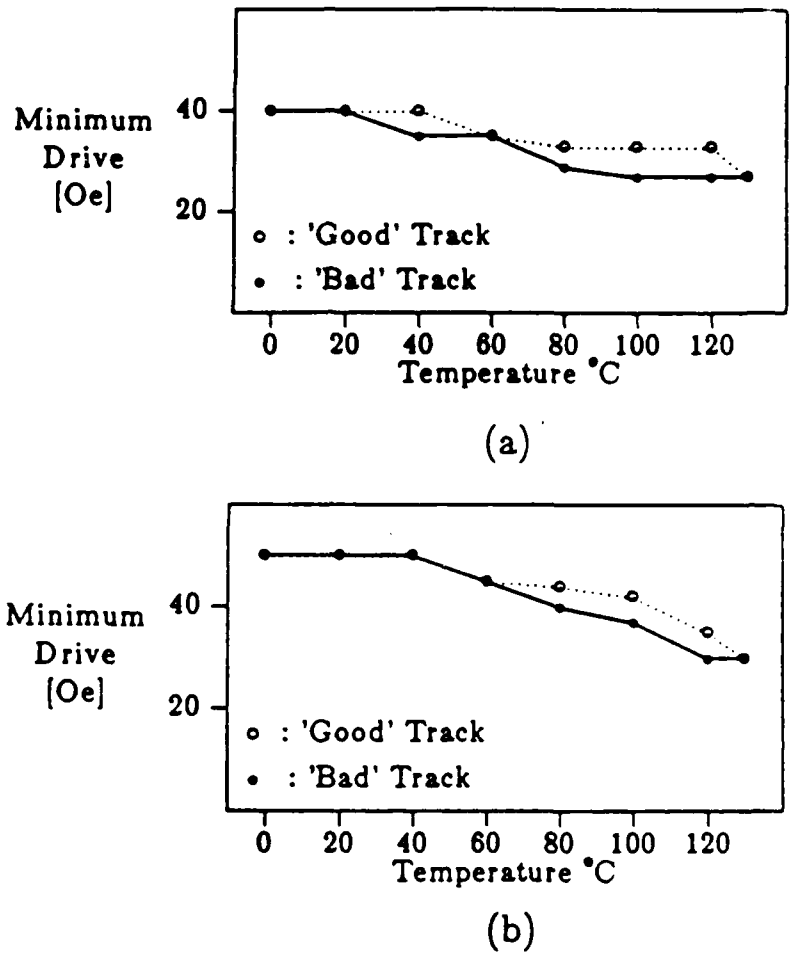

Figure 4-28: Temperature dependence of minimum drive field for (a) diamond and (b) circular patterns : CA 72, 2.5 μm Period

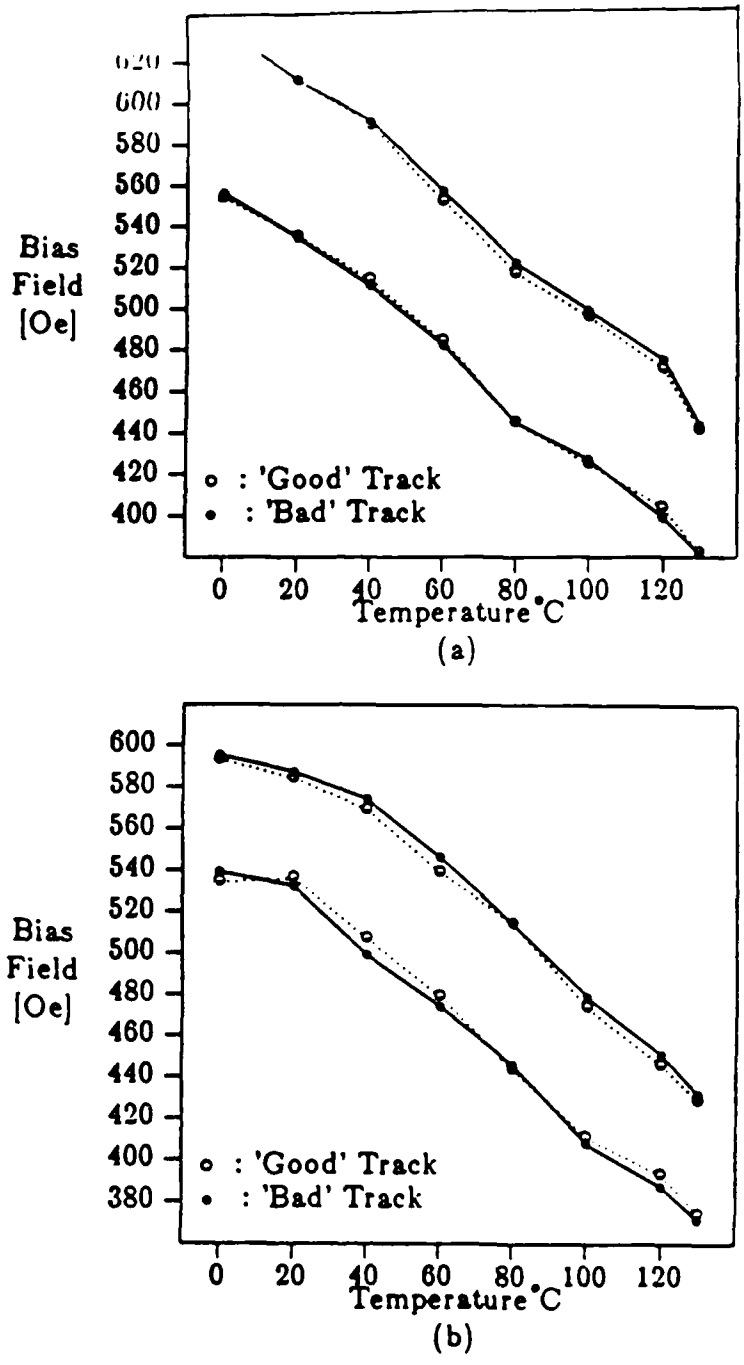

Figure 4-27: Temperature dependence of bias margins at 60 Oe of drive field for (a) diamond and (b) circular patterns : CA 72, 2.5 μm

Chapter 5
Discussion

5.1. Typical Bias Margins

The typical bias margin of the 2.5 μm period propagation devices (Fig. 4-1) is discussed here. The minimum circulation field of an isolated diamond pattern is discussed first. As is shown later, the minimum circulation field of a diamond pattern is not much different from that of a circular pattern if there is any difference at all. Therefore the theory developed for the circular pattern in chapter 2 will be used for the diamond pattern to discuss the minimum circulation field.

The crystalline anisotropy field, H_{k1}, is calculated to be 18 Oe using Eqs. (2.48) and (2.40), where 2 K_1/M is estimated to be 55 Oe in the implanted layer ([2 K_1/M]/2 of the unimplanted garnet), $4\pi M$ is estimated to be 750 Oe in the implanted layer (3/4 of $4\pi M$ in the unimplanted garnet), H_z = 560 Oe, H_{us} = 2000 Oe, H_{uc} = 4000 Oe, H_u = 2000 Oe. The values of the magnetization M and the crystalline anisotropy constant K_1 in the implanted layer were estimated according to the results obtained by Krafft[21] in a thicker (0.5 μm) implanted layer. With the thin (0.23μm) implanted layer used here, the FMR signals were not strong enough to determine K_1 values. To obtain M values in the implanted layer, the magnetization depth profile has to be obtained[21]. The process to obtain the profile is very elaborate and time consuming, which is not suited for routine wafer charaterization. If we use $H_{k1}/3$ as the theoretical minimum circulation field value (conventional theory ignoring the contribution from the demagnetizing field), the minimum circulation field is 6 Oe which is not far from the experimental value (10 Oe in Fig. 4-1). On the other hand, if Saunders' theory [Eq. (2.58)] is applied using Eq. (2.54) and (2.48), H_{uc} = 4000 Oe, H_{us} = 2000 Oe, S_2 = 1/2, Δ = 1/3, H_u = 2000 Oe, $4\pi M$ = 750 Oe and H_z = 560 Oe and H_{k1} = 18 Oe, $H_{k1}/9 + H_d$ = 2 Oe + 10 Oe = 12 Oe, which is very close to the actual value. Saunders' theory holds pretty well for heavy hydrogen or deuterium implantations since those implantations give high H_{uc} values, thus making the magnetization polar angle θ large [see Eq. (2.40)]. However, if H_{uc} becomes small, θ becomes smaller and the predicted magnetostriction contribution (H_d), Eq. (2.54) becomes too large compared to the experimental

value. The reason that this is the case could be that the charged wall motion may be governed more by the crystalline anisotropy at low drive field than the magnetostrictive anisotropy since the wall is long and therefore its behavior is largely determined by magnetization considerably far from the immediate vicinity of the pattern edge where the influence of the magnetocrystalline anisotropy is dominant, as was mentioned in Chapter 2.

The minimum drive field of a close-packed track, 35 Oe (Fig. 4-1), is fairly close to the predicted value of 37 Oe obtained by using Eq. (2.59), $H_{zy}(\min)_{disk} = 12$ Oe (Saunder's Theory) $W = 3.3$ μm and $t = 0.23$ μm. The average intertrack distance W is obtained by adding the cusp depth of 0.8 μm to the intertrack peak to peak distance (the distance between the peak of one track to the peak of the adjacent track) of 2.5 μm. The ion implantation depth t was 0.23 μm for the sample discussed here. The minimum drive field of an isolated track is shown to be 25 Oe. It is to be noted that the effect of "close-packing" is only 10 Oe (difference of minimum drive field between close-packed and isolated tracks) out of 35 Oe of minimum drive field.

The low end of the bias margin of a close-packed track is higher than that of the isolated track because of the charged wall interaction between tracks. The low end margin of the isolated element is in turn considerably lower than that of the isolated track mainly because of the way the low end margin was defined for the isolated element. To determine the low end margin of the isolated track the bias field was lowered until after the bubble actually striped out (no longer a bubble domain but a stripe domain) somewhat as long as the stripe circulated. When the low end of the bias margin for the isolated element was defined to be the bias field value where the bubble starts to stripe out, there was not much difference in low end of the bias margin between the isolated element and the isolate track.

The bias margin width predicted for an isolated bubble for $h=8l$ (which is the case for the present sample) is about 0.12 x 4πM (Fig. 2-9). The measured margin width of the isolated track (and the isolated element when the low end of bias margin was defined as the bubble stripeout field value) is 0.1 x 4πM, which is close to the predicted value.

5.2. Propagation Failure Modes

It is observed that bubbles collapse typically in cusps in bad tracks ,but they do not always collapse in cusps in good and super tracks. The reason is explained in the following. Bubbles residing in cusps encounter repulsive charged walls (twice in one cycle of in-plane field rotation) regardless of track orientations, which raise potential wells. However, the strength of the potential well depends on the track orientation due to three fold anisotropies. In Fig. 5-1 in-plane

field directions (arrows) and approximate charged wall directions are shown for bubbles encountering repulsive charged walls (dotted lines) in cusps.

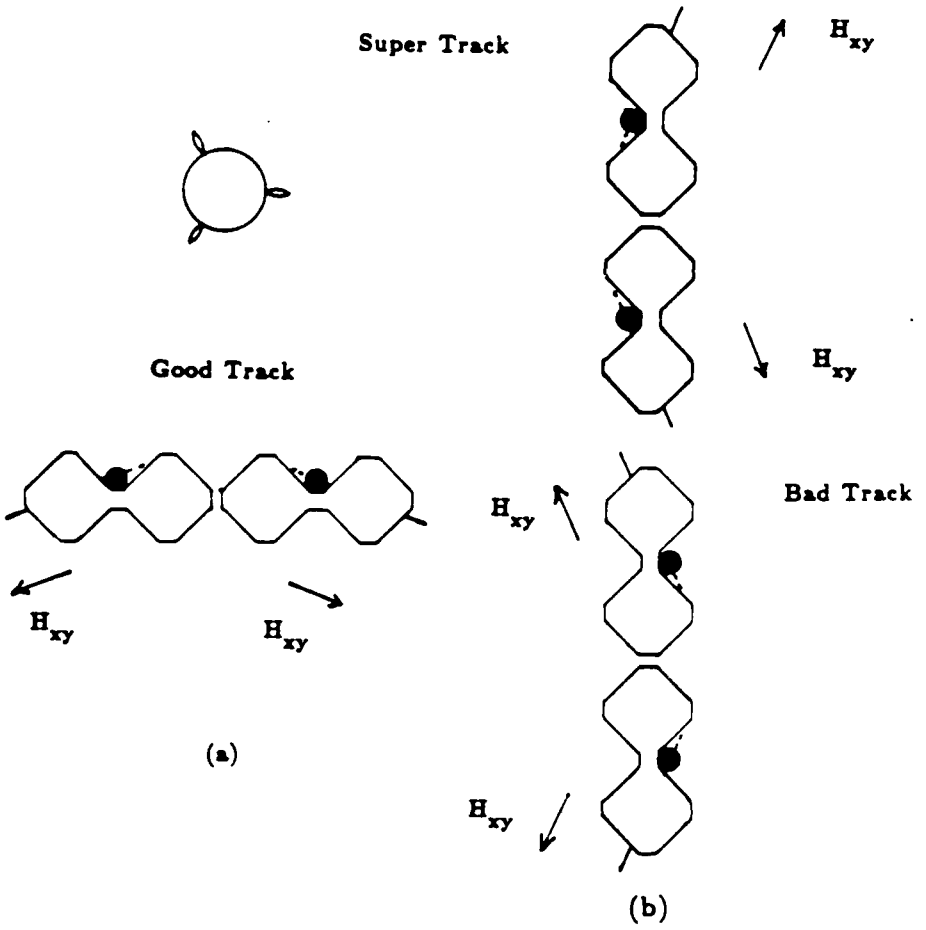

Figure 5-1: Bubbles encountering repulsive charged walls in cusps in (a) a good track and in (b) a bad and super track

It is to be reminded that the repulsive charged wall is also the strongest when the attractive charged wall is the strongest , i. e., when the in-plane field points in the three easy stripeout directions which are shown in the upper left corner of the figure, and the weakest when the in-plane field points opposite to those directions (easy magnetization directions). In a good track [Fig. 5-1 (a)] the repulsive charged wall strength is moderate when the repulsive walls encounter the bubble because the in-plane field directions are between the easy stripeout and the easy magnetization directions. In bad tracks a bubble encounters strong repulsive charged walls since the charged wall is over the bubble when the in-plane field points in the easy stripeout direction. In

super tracks, the repulsive charged walls are weakest since the charged wall is over the bubble when the in-plane field points in the easy magnetization directions. The potential well is raised when the repulsive charged walls are over the bubbles in the cusps, and, since the repulsive charged wall is strong in bad tracks, the potential well is raised considerably and the bubble collapses usually in the cusps in bad tracks. In good and super tracks, bubbles can and sometimes do collapse out of the cusps because the bubble potentials in the cusps is not raised as much. More about the bubble collapse will be discussed later in conjunction with the isotropic propagation.

The above reasoning is based on the assumption that the bubble stripeouts occur 120° apart at the indicated directions shown in the figure and that the charged wall strengths in these three directions are the same. In reality, bubble stripeout directions are not exactly 120° apart and in many cases, the charged wall strengths are not the same. The pattern and cusp shapes also influence the direction of the in-plane field in which the repulsive charged wall is created over the bubble, thus, the strength of the charged wall. Therefore, the detailed potential well shapes are different from wafer to wafer and from propagation track shape to shape, and it is not a simple matter to predict where the bubble collapse would occur. However, it is fairly safe to predict that bubbles collapse in cusps in bad tracks.

The skidding failure mode happens basically because the affinity of the cusp is not strong enough to hold the bubble in the cusp against the pushing of the repulsive charged wall. The snake pattern is the most susceptible to this kind of failure mode, which is believed to be due to the fact that its unimplanted region is smaller than that of the other patterns (see Fig. 3-10) causing the edge affinity to be not as strong as the other pattern shapes. Also, it happens most often in bad tracks because the repulsive charged wall is strong. It is often observed that the bubble wiggles in the cusp before it starts to move out of the cusp under the influence of the repulsive charged walls as the bias field is increased. The bubble wiggles in the cusp because of the pushing of the repulsive charged walls. If the bubble does not succeed in moving out, it falls back to the cusp. Every time a repulsive wall passes over the bubble, it is pushed and moved in the direction of the wall movement, then once the size of the bubble becomes small enough due to increased bias field, the bubble finally moves out of the cusp. Usually the skidding bubble collapses soon after it comes out of the cusp as the bias field is increased. The collapse field of a skidding bubble is quite low compared with other bubbles because it is under the influence of a repulsive charged wall instead of an attractive charged wall.

It is often observed that the stripeout bias fields for good tracks are a few Oe higher than those for bad-super tracks, which can be explained as follows: The bubble stripeout direction of

the good track is approximately into the adjacent track cusp (see Fig. 4-3 (a)) because strong charged walls are formed on both sides of the tracks when the in-plane field points into the cusp (easy stripeout direction). On the other hand, the stripeout direction of the bad track is toward the peak of the super track and not the cusp (Fig. 4-4) because strong charged walls are formed on both sides of the tracks when the in-plane field points to the peak of the super track (easy stripeout direction). The stripe starts out toward the peak of the super track, then bends toward the cusp because a strong attractive charged wall resides in the cusp. Therefore the effective distance between the bad track peak and the super track cusp is longer than that between the good track peak and the adjacent good track cusp, which lowers the low end margin of the bad-super track.

At low bias and low drive field, the charged wall can become very long during the whip motion which occurs when the in-plane drive field points in the easy stripeout direction. As is shown in the bottom track of Fig. 4-6 (a), the long charged wall bends in between two adjacent tracks and reaches the second cusp from the end of the track causing the bubble to jump to the cusp if it has lower potential well, skipping the first cusp. This failure happens mostly at the end of the track, because further inside, the charged wall during the whip motion does not grow so long because of the adjacent track. In the top track of Fig. 4-6 (a), the charged wall is not forced to bend by the adjacent track and it more often does not reach a cusp. Then the bubble propagates normally. The reason the same failure mode does not occur on the right side of the track is shown in Fig. 4-6 (b). Here, the whip motion occurs when the field direction points to the right and by the time the charged wall enters the region between the tracks it actually undergoes a flip motion. Therefore there does not exist a long charged wall which could reach the second cusp and the bubble does not skip the first cusp as it rounds the end of the track.

5.3. Ion Implantation and Annealing of Devices

5.3.1. Ion Implantation

The difference of anisotropy change between 32 KeV implantation and 40 KeV implantation (~500 Oe in Fig. 4-7) is not as much as one would have expected from the difference of the penetration depth (0.23 μm vs. 0.27 μm). The anisotropy change for a triple implantation with implantation depth of 0.5 μm (72 KeV) observed by Krafft[21] is shown for comparison in the same figure. The implantation of a given dose ($12 \times 10^{15}/cm^2$) in thinner layers (.23 μm and 0.27 μm vs. 0.5 μm) resulted in much higher anisotropy changes (7300 Oe and 7000 Oe vs. 4800 Oe), but the anisotropy change was not proportionally related to the implantation depth at a given dose as

mentioned above. It is not clear why this is the case. The reason may be explained once the ion implantation induced anisotropy in the garnet films is fully understood in the future.

The maximum lattice strain value of 0.6% for wafer AK91 at the implantation dose of 12.3 $\times$ $10^{15}/cm^2$ in Fig. 4-8 is considerably lower than the measurement of Krafft ($\sim$1.3%). Measurements of other nominal 0.5 μm diameter bubble garnets showed similar low values of the maximum lattice strain. It is not clear whether this difference is due to the different film compositions (Bi was substituted for our 0.5 μm diameter films) or for other reasons.

To find out optimum implantation dose for diamond tracks, bias margin widths and minimum drive fields were plotted as functions of implantation dose for both good and bad tracks. From the margin data of good tracks shown in Fig. 4-9, it looks like an even higher dose than the maximum dose used will be better because the margin width keeps increasing and the minimum drive field keeps decreasing as the dose is increased. However the bad track margin deteriorates at high dose due to the stronger repulsive charged wall as shown in Fig. 4-10. The bubbles start to skid at lower and lower bias field, reducing the margin width. Therefore, for most of the wafers tested, region 4 (5.7 $\times$ $10^{15}/cm^2$ to 8.5 $\times$ $10^{15}/cm^2$) showed better bad track margins than region 3 (higher dose).

For deeper implantation (40 KeV, 0.27 μm depth), the minimum drive field becomes higher because the charged walls become stronger and interact with the charged walls of adjacent tracks. Also, the skidding failure mode in the bad tracks occurs at a lower bias field. It is noted that the nominal 0.5 μm diameter bubble films tested are all nearly magnetostrictively isotropic and most bubbles skid before they collapse. Skidding is more likely if the bubble is relatively short compared with the depth of the implanted layer. The deeper implant shortens the bubble and, thereby, promotes the skidding.

Considering both good and bad track margins, a dose of about 7.5 $\times$ $10^{15}/cm^2$ and 32 KeV of implantation energy seems to be good compromise for 2.5 μm period propagation patterns fabricated from the above mentioned garnet wafers. These conditions produce a Q of -5 and an implantation depth of 0.23 μm. The ratio of the implantation depth to the bubble height is approximately 0.5, which confirms the theory presented in Chapter 2, that the ratio should be around 0.5 for good propagation.

5.3.2. Annealing

After the 250 ° C anneal in Fig. 4-12, the minimum drive field increases and the margin width decreases noticeably. This is somewhat unexpected because the anisotropy change actually does not decrease appreciably after the 250 ° C annealing. The margin width vanishes after the 300 ° C anneal which is also unexpected because the anisotropy change is still substantial (3000 Oe which would give in-plane anisotropy of approximately −2). The explanation for this behavior may lie in the small lattice strain of these films mentioned earlier. It is plausible that after the 300 ° C anneal, the lattice strain became too small to produce adequate stress relaxation needed for the formation of charged walls (Chapter 2). This could also explain the device performance decline after the 250 ° C anneal even though the anisotropy change did not decrease much (200 Oe). The lattice strain may already have decreased to affect the charged wall formation after the 250 ° C anneal. It is to be noted that if the small lattice strain observed is indeed correct, the estimated anisotropy change due to the lattice strain before anneal is only about 1000 Oe.

The annealing study indicates that a 200 ° C anneal is safe after ion implantation of 8 × $10^{15}/cm^2$ to 11.5 × $10^{15}/cm^2$ with 32 KeV of implantation energy for garnet films similar to AK92 tested here. Another annealing study by Michael Alex[54] with nearly isotropic, Bi incorporated 1 μm diameter bubble films which were implanted with higher dose (up to 1.75 × $10^{16}/cm^2$) shows adequate bias margins after a 380 ° C anneal. Therefore it is expected that with higher dose, nearly isotropic 0.5 μm bubble devices would be able to perform after higher temperature annealing.

5.4. Variation of Propagation Track Shape and Size

5.4.1. Variation of Propagation Track Shape

5.4.1.1. Isolated Elements

The reason that the minimum circulation fields are the same (10 Oe) for various shaped elements of 2 μm size (Fig. 4-13) is that the bubbles do not see much difference in shapes of elements because their size (0.5 μm) is comparable to the size of the elements (2 μm). As the sizes of the elements are increased to 4 μm, the bubbles see the difference in shapes and the minimum drive fields vary with the shapes of the elements. The triangular patterns have high minimum circulation fields (16 Oe) because the bubble collapses at the tips of the pattern [Fig. 5-2 (a)] which are oriented in a hard stripeout direction(, i.e., flip direction).

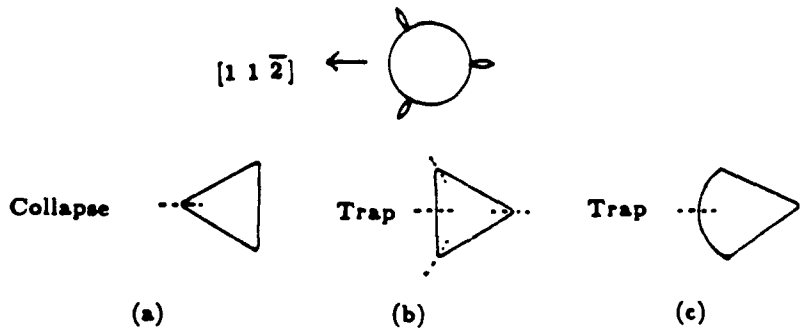

Figure 5-2: Failure modes of triangular patterns

At the tips the charged walls are weak and the edge affinity is small, which allows the collapse of the bubbles. The reverse triangle [Fig. 5-2 (b)] has a lower minimum circulation field (14 Oe) than the triangle (16 Oe) because its tips now point to the easy stripeout directions, which provide strong charged walls. The failure mode for the reverse triangle was bubble trapping at the charged wall flip position as shown in Fig. 5-2 (b). Here, again the charged walls are weak, but the bubble does not collapse due to higher edge affinity. The bubble simply cannot come out of the position due to the weak driving force provided by the weak charged walls. If the straight edge is rounded [Fig. 5-2 (c)], the minimum circulation field decreases because the bubble can come out of the trapped position (flip position) more easily. This is because the bubble does not have to move all the way to the corner [Fig. 5-2 (b)] to get out of the trapped position. On the rounded edge the charged wall direction continuously changes as the bubble moves along the edge, and the bubble does not therefore have to move far to get out of the flip position. The minimum circulation fields were measured for both rounded and straight edge triangular patterns fabricated from an earlier garnet film with different in implantation conditions than the samples discussed here. The results show that the minimum circulation field decreased from 25 Oe to 15 Oe as the edge was rounded.

From the bias margins of the isolated elements, it is seen the circular pattern is the best and the diamond pattern is the next best. The triangular pattern is not as good as expected. The corners in the patterns impede the bubble propagation and the circle thus exhibits the best bubble circulation as was also pointed out by Lin et al.[6]. At high bias fields the bubbles collapse at the corners of the triangular patterns and at low bias fields large bubbles do not turn the corners and get trapped in the straight edges. The sharper the corners, the lower are the collapse fields.

5.4.1.2. Propagation Tracks

The minimum drive field for propagation along a track is largely influenced by the shape of the cusps. The important factors are the slope, the width and the depth of the cusps, which influence the charged wall formation at the cusps and the strength of edge affinity. The snake shaped tracks have wide and rounded cusps and thus, the lowest minimum drive. The circular patterns were designed to have the same cusp shapes, but the actual E-beam mask patterns show shallower cusps than the snake patterns. This is because the circular patterns were a little bit overexposed while the snake patterns were properly exposed. Therefore, it is believed that with a properly exposed mask, the circular patterns would show a lower minimum drive field, but not as low as the snake patterns because the intertrack distance of the snake patterns is longer than that of the circular patterns. The triangular patterns have higher minimum drive than the diamond patterns because the triangular patterns have sharper cusps (60° vs. 90° of the diamond patterns) It seems to be important that the cusps provide enough space for the domains to form strong and adequately long charged walls to pick up bubbles when the charged walls move out of the cusps Also, sharper cusps provide larger edge affinity which protects bubbles from the repulsive charged walls, but which tends to trap bubbles unless the outgoing charged walls are strong. Rounded edges of patterns generally provide more uniform propagation because the charged wall direction changes rather continuously along the track compared with the straight edges. Therefore the bubble does not have to move for a long distance at a time. In general, the cusps with rounded edges (circle and snake patterns) give smaller minimum drive as long as the lithography is good However, as was proven in this study, the diamond patterns are easier to resolve and give good margins Therefore, if the lithography is a problem, the diamond patterns may turn out better than the circular or snake patterns.

It is also noted that the triangular patterns provide better bias margin than the reverse triangular patterns in the case of propagation tracks as opposed to the other way around in isolated elements. This is due to the cusp shape difference As shown in Fig. 5-3, the triangular patterns (Fig. 5-3 (a)) have strong charged walls (easy stripeout positions indicated in dotted lines for both senses of the rotating drive fields) when the bubbles get out of the cusps, while the reverse triangular patterns (Fig. 5-3 (b)) have weak charged walls (flip positions indicated in solid lines) when the strong charged walls are needed to overcome the strong affinity of the cusps.

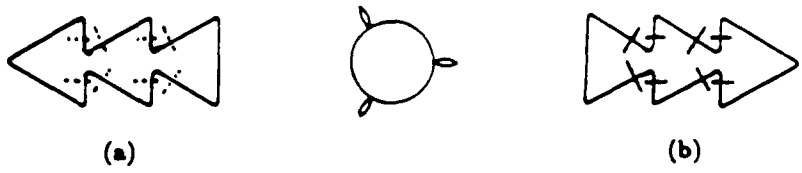

Figure 5-3: Charged wall directions when the bubbles come out of the cusps

This is an example of the fact that the bias margins of pattern elements are not proper indications of the bias margins of propagation tracks. The important difference comes from the shapes of the cusps. The increase in minimum drive field as a result of the cusps and as a result of close-packing of adjacent tracks are shown in Table 5-1.

Table 5-1: The Effects of Various Cusps and Close Packing of Propagation Tracks on Minimum Drive Fields (CA72)

Track Shape	Effect of Cusp (Oe)	Effect of Close Packing (Oe)
Snake	10	10
Diamond	15	10
Triangle	20	10
Circle	25	15
Reverse Triangle	30	10

The effect of the cusp is defined as the minimum drive field difference between the isolated element and the isolated propagation track. The effect of the close packing is defined as the minimum drive field difference between the isolated track and the close-packed tracks. As was mentioned earlier, the snake pattern cusp provides the least impediment to the bubble propagation, and the reverse triangle cusp the most. The effect of the cusp of the circular patterns would be smaller if the pattern cusp had come out as designed. It is noted that the effects of the close packing of the different patterns do not vary noticeably except in the case of the circular patterns. The circular patterns have shorter track to track distance because the cusp depths came

out shallower than originally designed, which explains the larger effect of the close packing than with other patterns.

The collapse field and the stripeout field of the snake patterns are much lower than those of the other patterns. The collapse field (the potential well) is determined by the charged wall, the edge affinity and the surface demagnetizing charge at the pattern boundary as was shown in Eq. (2.61). Another factor that has to be considered as the unimplanted area becomes smaller is the influence of the oppositely charged wall across the unimplanted pattern (see Fig. 2-21). The snake pattern has a particularly thin unimplanted region, of which the width is 0.75 μm for 2.5 μm period track, and overall smaller unimplanted region than other patterns. Therefore it is expected that the oppositely charged wall across the pattern (the width is only 1.5 times the bubble diameter) would effectively reduce the collapse field, and the smaller edge affinity due to the smaller unimplanted region also would reduce the collapse field. The stripeout field is also lowered because of the same reasons. In addition, since the intertrack distance is longer for the snake patterns than the other patterns, the stripeout field becomes even lower. The diamond patterns have the highest collapse fields among the rest of the patterns due to the stronger and more uniform charged walls formed by the wider and deeper cusps, relatively rounded pattern edges and larger unimplanted region.

Overall the diamond patterns seem to be the good choice since they have an advantage in margins over the snake patterns if the bad tracks are included in the device design, and they also have an advantage over the circular patterns if the pattern resolution becomes a limiting factor.

5.4.2. Variation of Propagation Track Size

5.4.2.1. Isolated Disks

The features of the margins in Fig. 4-16 are that the collapse fields of the disks increase as the diameters of the disks are increased and so do the minimum drive fields, which are plotted in Fig. 5-4. The collapse field (at 60 Oe drive field) increases until the diameter of the disk reaches 8 μm, then it levels off.

As was explained earlier, the decrease of the collapse field at smaller diameters of disks can be attributed to the smaller edge affinity and the adverse interaction of the oppositely charged wall across the disk. It is also conceivable that the charged wall strength becomes weaker as the disk becomes smaller because the implanted regions on both sides of the disk push against the small unimplanted disk so that the stress in the implanted regions does not relax significantly to produce a strong charged wall. There is some evidence for this explanation. Omi, et al.

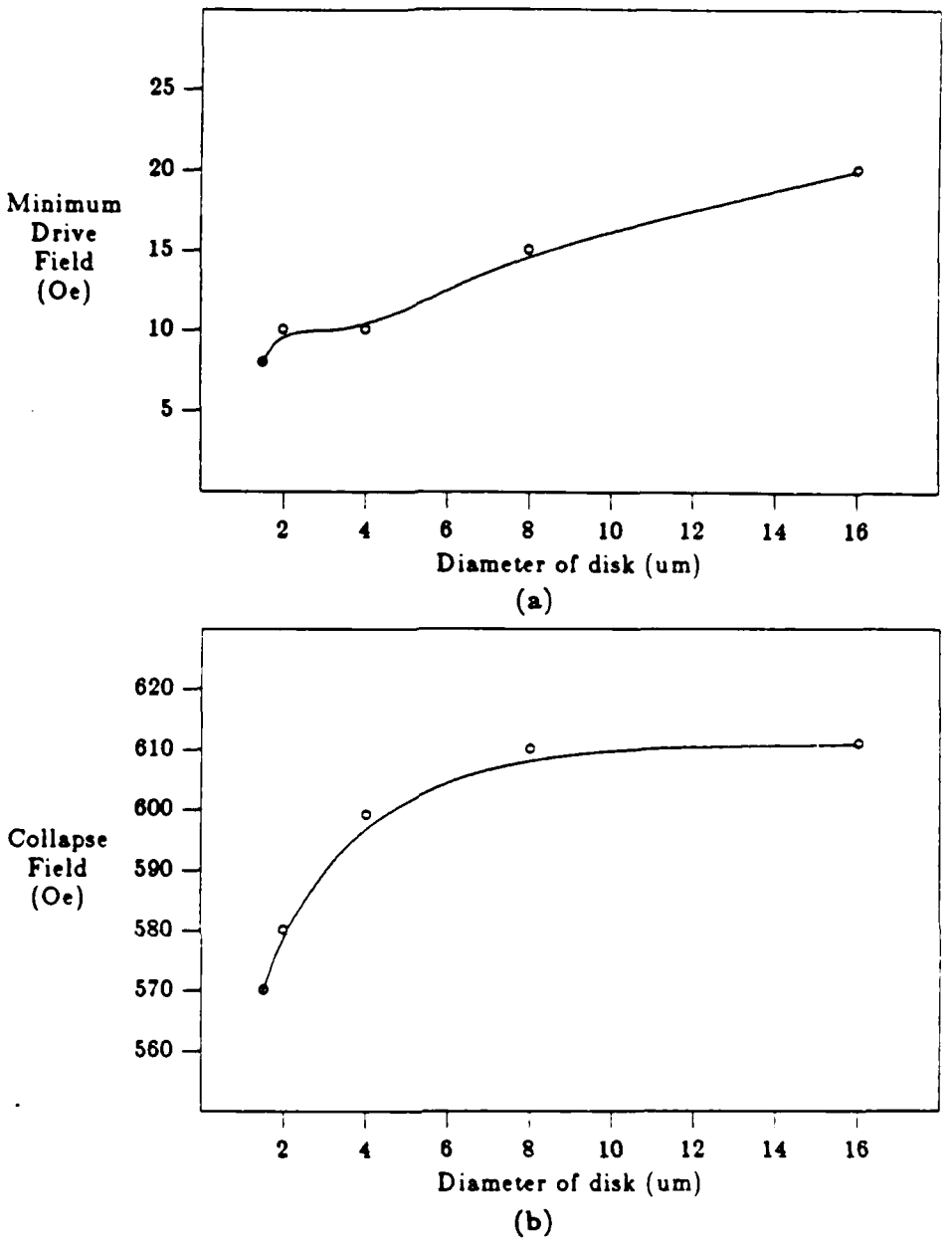

Figure 5-4: (a) Collapse field at 60 Oe drive field and (b) minimum drive fields of the various sized unimplanted disks

reported[55] that the distance that the stress relaxation (and lattice constant variation) occurs at the edges of 10 μm diameter disks is at least 1 μm. Therefore it is possible that if the diameter of the disk becomes a few μm, there may be smaller stress relaxation which would lead to a weaker charged wall.

The increase of the minimum drive field with the increase of the disk diameter is not surprising because the bubble has to travel further during the charged wall flip motion which causes the

charged wall to jump. Unless the drive field is increased so that the charged wall motion becomes less jerky, the bubble will be left behind during the charged wall flip motion.

5.4.2.2. Propagation Tracks

The lower collapse fields of propagation tracks with smaller patterns shown in Fig. 4-17 may be explained with the same arguments as for the isolated elements. As the pattern becomes smaller, the distance across the pattern becomes smaller. Therefore the oppositely charged wall across the pattern starts to reduce the collapse field. The smaller edge affinity due to the smaller unimplanted region also reduces the collapse field. The lower minimum drive fields of the larger patterns may be explained by their better cusp definition (wider and deeper cusps) and larger intertrack distance. It is to be noted that the bias margin for the 1.75 μm period snake propagation tracks employing 0.5 μm bubbles shown in Fig. 4-17 is excellent with 35 Oe of minimum drive field and 13.5% of bias margin.

The propagation tracks (Fig. 4-18) with smaller width have lower collapse fields and stripeout fields because they have smaller unimplanted regions. It also has smaller minimum drive field because the intertrack distance is larger.

It is better to have larger patterns because of higher collapse fields unless the larger patterns cause reduced intertrack distance, which increases the minimum drive field for a given cell size.

5.5. Variation of Magnetostriction Coefficients - Nearly Isotropic Propagation

5.5.1. Comparison of Conventional and Nearly Isotropic Films

The bias margins of bad tracks obtained from the nearly isotropic films show marked improvement of the margin widths, equaling those of good tracks. The reason why this is so will be explained using the results obtained from Bitter pattern observations, bubble position vs. in-plane field direction measurements and bubble collapse field measurements along the propagation tracks.

5.5.1.1. Propagation Bias Margins

Bias margins from the nearly isotropic films (Fig. 4-19 (b) and Fig. 4-20) show substantial increase of the collapse fields of the bad tracks. Since the pattern periods of the propagation tracks of both films are not identical (4 μm and 5 μm) and the ion implantation conditions (see Appendix C) are different, it is difficult to ascertain the effect of the differing magnetostrictions on the minimum drive fields of the propagation tracks. However, as will be explained later, the minimum drive fields do not change greatly as the magnetostriction coefficients change. The typical change observed from the more isotropic films is the increase of the collapse fields of the bad tracks.

5.5.1.2. Bitter Pattern Observation

Bitter patterns of magnetic domain walls around unimplanted disks fabricated with the nearly isotropic films were observed, to show familiar charged wall whip and flip motions commonly seen in conventional films as were described in section 2.6.7. This is not surprising since the film is still three-fold anisotropic, even though the degree of anisotropic tendency has been reduced. The observation was made at low drive fields which give longer domain walls for better visibility. As was mentioned in Chapter 2, these longer domain walls are formed largely by magnetizations away from the pattern boundary where the magnetocrystalline anisotropy is dominant over the magnetostrictive anisotropy. Therefore, the effect of the reduced magnetostrictive anisotropy due to the reduced Δ is not readily observable.

5.5.1.3. Bubble Position vs. In-Plane Field Direction

The bubble position vs. in-plane field direction curves in Fig. 4-21 show how strong the three-fold anisotropy is for each bubble garnet film. The more closely the bubble follows the in-plane field, the less strong the anisotropy is. Of course, the three-fold anisotropy comes from the two sources, the magnetocrystalline anisotropy and the magnetostrictive anisotropy. The magnetocrystalline anisotropy constants (K_1) of the two films do not differ much (both have K_1 values of approximately 5000 erg/cm^3); therefore, it is believed that the difference in the bubble behavior comes from the difference in the magnetostrictive anisotropy of the films.

5.5.1.4. Bubble Collapse Fields Along Propagation Tracks

The potential well shapes of Fig. 4-22 are explained in the following. The magnetization directions and polarities of the charged walls in the cusps estimated from the three-fold critical curves and the pattern boundaries are illustrated for good, bad and super tracks in Fig. 5-5. As Lin, et al. illustrated with the ferrofluid patterns[11], a repulsive charged wall (shown in the figure as minus signs) is formed in the cusps of bad tracks when there is no applied field in conventional

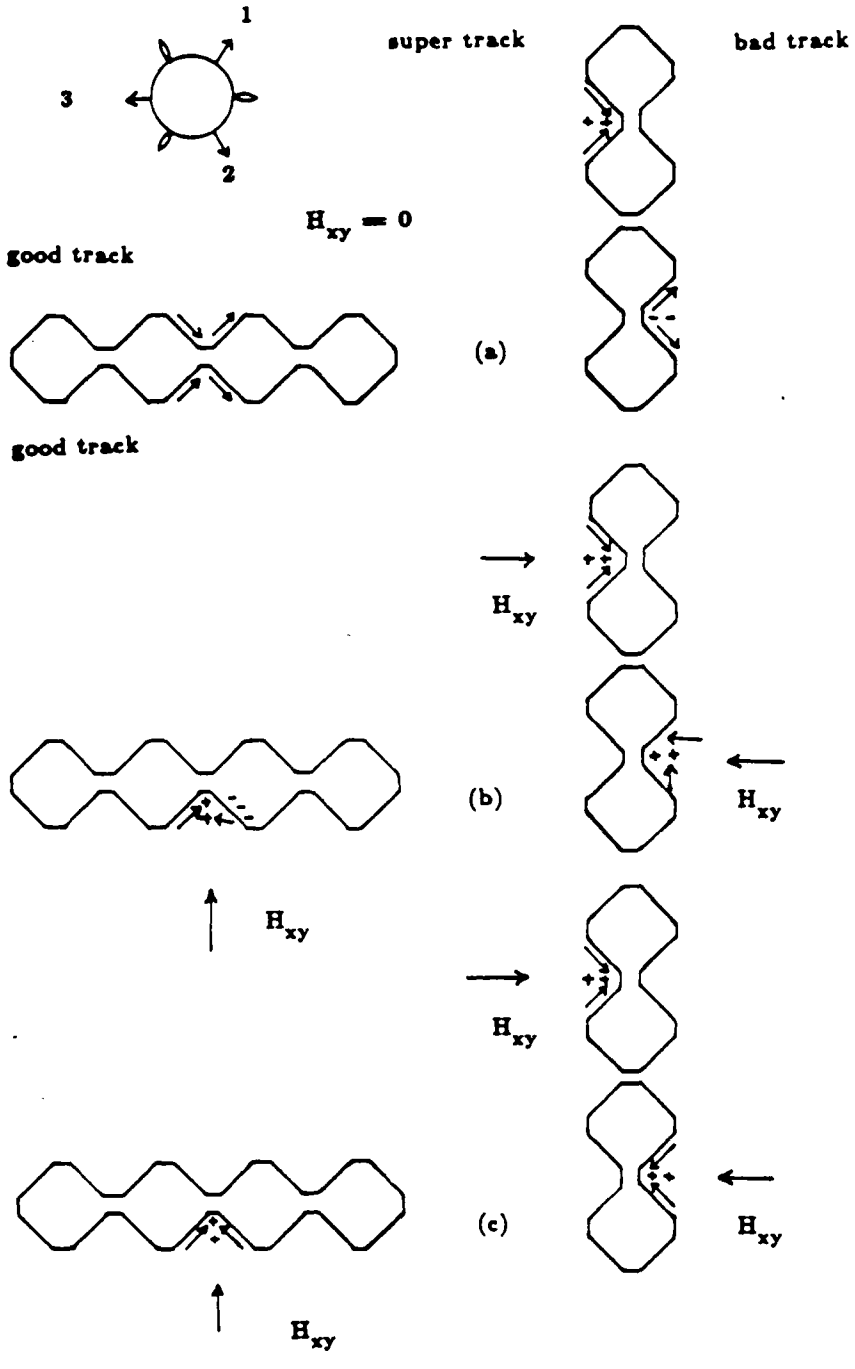

Figure 5-5: Magnetization directions and charged wall polarities in the cusps: (a) $H_{xy} = 0$, (b) conventional film (c) nearly isotropic film

films as shown in Fig. 5-5 (a). The easy magnetization directions of the film are shown as arrows (1, 2, and 3) in the figure, which are approximately parallel to the boundaries of the cusps. In the cusps of the super track, attractive charged walls (shown in the figure as plus signs) are formed and in the cusps of good tracks, neutral walls are formed as indicated in the figure. The magnetizations tend to align with the boundary of the patterns due to magnetostrictive anisotropy and to reduce the boundary surface charge accumulation, i.e., to reduce the demagnetizing energy. The magnetizations also like to align with one of the three easy magnetization directions to minimize the magnetocrystalline energy. The combination of these reasons results in the aforementioned domain wall formations in the cusps.

When the in-plane field is directed into the cusps in conventional films [Fig. 5-5 (b)], attractive charged walls are formed in the cusps of good tracks because the magnetization 3 has lower energy than the magnetization 2 in the presence of the in-plane field. However these attractive charged walls are not as strong as the ones in the cusps of the super tracks because the magnetization 3 is not nearly parallel to the cusp boundary. The magnetization should deviate from the easy direction to get closer to the direction of the boundary which reduces the charged wall strength. Also negative surface charges are accumulated on the boundary since the magnetization direction is not parallel to the boundary as shown in the figure. All these lead to the shallower potential well in the cusps of good tracks than the super track. In the bad track, very weak attractive charged walls are created by the magnetizations 1 and 3. Therefore the potential well in the cusps of bad tracks is very shallow as shown in Fig. 4-22 (a).

In nearly isotropic films, attractive charged walls are formed in the cusps of bad tracks as shown in Fig. 5-5 (c). If there were no three-fold anisotropy, the magnetization would perfectly align with the boundary of the cusps in the direction of the in-plane field. The strength of the attractive charged walls would be the same for all three cusps. The potential well in the nearly isotropic film is much lower than that of the conventional film as shown in Fig. 5-5 (b). This is the reason that the collapse fields of bad tracks in nearly isotropic films are substantially higher than those in conventional films. Two peaks of the potential well of the bad track around 130° and 240° correspond to the strong repulsive charged walls encountered by the bubbles in the cusps as explained in Subsection 5.2.1 (Fig. 5-1).

By looking at the potential well curves, one can predict when the bubbles will collapse. Bubbles collapse at the in-plane field direction where the potential well is the shallowest.

5.5.2. Variation of Magnetostriction Coefficients - Nearly Isotropic Films

The reason that the minimum drive fields for circulation around isolated 2 μm disks (Fig. 4-23) do not vary much as Δ varies can be explained with the same reasoning as was used earlier. For the smaller disks, the bubble size is relatively large compared to the disks, so that the bubble has to move only a small distance as the in-plane field changes direction. The distance that the bubble has to travel during the charged wall flip motion is therefore small and easily followed by the bubble. The effect of the three-fold anisotropy is thus less pronounced for the small disks than for the large disks. The decrease of the minimum drive with the decrease of the magnetostrictive anisotropy (Δ) confirms the theory presented in Chapter 2 that the three-fold magnetostrictive anisotropy strongly affects the anisotropic bubble motion. It is to be noted that the three-fold crystalline anisotropy constants for the three films are almost the same. Therefore, the contributions to the minimum drive fields from the crystalline anisotropy remained essentially unchanged as the magnetostrictive anisotropy changed.

The fact that the bias margins for the two wafers (with Δ values 0.29 and 0.11) exhibit almost isotropic propagation suggests that one may be getting diminishing returns by decreasing Δ to obtain more isotropic films once Δ reaches about 0.3. By adding more Dy to reduce Δ further, one increases the damping of the material because the damping constant of Dy is quite large. This in turn reduces the mobility of the charged wall, which limits the maximum operating frequency of the device. Therefore, it seems that there is no need to reduce Δ more than the value 0.3 for these films. However, it should be remembered that the Δ value for optimum device operation may vary somewhat depending on garnet film characteristics, propagation track shapes and ion implantation conditions. The margin widths (about 12% of mid-bias value) of AKb1 and AKa8 are somewhat smaller than that of AK92 (about 14%) because the bubble sizes of the wafers AKb1 and AKa8 (0.67 μm and 0.62 μm) are larger than that of AK92 (0.5 μm).

5.6. Variation of Ambient Temperature

The temperature dependence of bubble propagation is of considerable practical interest because it greatly influences the operating temperature range of the bubble memory device. It has been reported that the operating temperature range of ion implanted devices depends on the garnet film characteristics and the ion implantation conditions. Mizuno and Urai demonstrated that hydrogen implantation allows much higher operating temperature limits than the helium implantation for the same garnet films[56]. Fratello et al.[57] and Arbaugh and Fairholme[58] showed that bismuth substituted garnet films gave a wide operating temperature range.

The wafer tested (CA 72) was implanted with deuterium and the garnet film was Bi substituted. Therefore, wide operating temperature range was expected from the sample. Indeed, good overlapping bias margins of good and bad tracks (at least 13% of mid-bias value) up to 120 °C were obtained[59]. Margin degradation at high temperature was due to a decrease of the collapse field at high drive field. Since the nearly isotropic propagation is maintained throughout the temperature range tested, the degree of isotropy $\Delta[(\lambda_{111} - \lambda_{100})/\lambda_{111}]$ is believed to remain constant in the temperature range, which suggests that the ratio of magnetostriction coefficients λ_{111} and λ_{100} does not vary with the temperature change. The decrease of the minimum drive is attributed to the decrease of both the three fold magnetocrystalline anisotropy[56] and the magnetostrictive three fold anisotropy[59] with the increase of the temperature.

Chapter 6
Conclusions

6.1. Summary of Contributions

The objectives of the research were two-fold: firstly, fabrication of contiguous disk ion implanted bubble propagation devices for 0.5 μm bubbles which would lead to bubble memory chips with a storage density of 16 to 64 Mb/cm^2 and understanding of bubble propagation phenomena in the devices, and, secondly, realization of isotropic propagation devices which would greatly simplify the chip design.

The propagation device structure used as a mask for ion implantation requires 0.5 to 0.7 μm minimum lithographic features. Using mid-U.V. exposure and AZ 4070 photoresist together with electroplating, excellent gold masks for ion implantation with little undercutting were fabricated.

Ion implantation conditions for the devices were studied. The difference of bubble propagation behavior in good and bad tracks depending on ion implantation conditions were understood. Double deuterium implantation with implantation depth of about 2300 Å and implantation dose of about 7.5 $\times$ 10^{15}/cm^2 gave good propagation margins for 2.5 μm period devices employing 0.5 μm diameter bubbles. Annealing of these devices showed good bubble propagation until 200 °C. The bias margin deteriorated somewhat after a 250 °C anneal and became negligible after a 300 °C anneal.

The lack of visibility of the small submicron bubbles caused a major problem early on for device testing. To improve the visibility, a MTI 66 silicon intensified T.V. camera, Leitz 250 W lamp housing and an extender between the microscope and the T.V. camera were used. The total magnification achieved was 3500. Eventually, new garnet films incorporated with Bi were used, which gave excellent visibility up to bubble collapse.

Using the devices thus fabricated and the improved testing facility, bubble propagation failure modes on the propagation tracks were studied. Bubble collapse at cusps (especially at bad track

cusps), bubble skidding along the track, bubble stripeout across and along the tracks and bubble position skip at the end of the tracks were observed and understood in terms of the three-fold magnetocrystalline and magnetostrictive anisotropies of the garnets.

Propagation track shapes and sizes were varied to understand bubble propagation in various shaped devices. Minimum drive field and collapse field variation of isolated elements and propagation tracks with respect to shape and size variation were analyzed and understood. The diamond patterns exhibited best overall performance. The snake patterns showed the lowest minimum drive field and the best bias margins if only good tracks were considered. A very good bias margin (13% of mid-bias value and 35 Oe minimum drive field) was obtained for 1.75 μm period good snake patterns using 0.5 μm diameter bubbles.

The temperature dependence of bias margins was studied from 0 °C to 130 °C. Good overlapping margins (at least 13%) of good and bad tracks were obtained throughout the temperature range for garnets with nearly isotropic magnetostriction. Since the nearly isotropic propagation is maintained throughout the temperature range tested, the degree of isotropy $\Delta[(\lambda_{111} - \lambda_{100})/\lambda_{111}]$ is believed to remain constant in the temperature range, which suggests that the ratio of magnetostriction coefficients λ_{111} and λ_{100} does not vary with the temperature change. The minimum drive field decreased with the increase of the temperature, which is attributed to the decrease of both the three fold magnetocrystalline anisotropy[56] and the magnetostrictive three fold anisotropy[59] with the increase of the temperature.

Lastly, the effects of varying the magnetostriction coefficients was studied. Bubble collapse field increase in bad tracks fabricated with nearly isotropic films compared with conventional films was analyzed and understood. Nearly isotropic propagation was achieved for most of the 2.5 μm period propagation tracks tested, when Δ $[=(\lambda_{111}-\lambda_{100})/\ \lambda_{111}]$ was less than about 0.5, given proper ion implantation. Reduction of Δ below 0.3 may not be desirable due to increased damping caused by the increased Dy content. This experimental study thus corroborates suggestions of Hubert[14] and of Kryder and Saunders[15] who suggested that nearly isotropic propagation can be achieved by properly choosing the magnetostriction coefficients λ_{111} and λ_{100}.

6.2. Suggestions for Future Research

The ferrofluid observation of charged walls at the cusps of tracks fabricated with a highly anisotropic film and an isotropic film is desired. The ferrofluid patterns of charged walls at the cusps are expected to determine conclusively whether the explanation of the collapse field difference between the anisotropic film and the isotropic film given in subsection 5.5.1.4. is proper. It will be easier to see the Bitter patterns if larger propagation patterns are used.

As was mentioned in Section 4.3, lower lattice strain than expected was observed for nearly isotropic Bi incorporated films. By implanting both Bi and non-Bi incorporated films at the same time with the same dose and energy, it will be made certain whether the Bi incorporated film indeed exhibits less strain than the non-Bi incorporated film. If that is indeed the case, it would be a worthwhile effort to investigate the reason.

It is necessary to accurately determine magnetization and magnetostriction coefficients in ion implanted layers. By typical FMR measurements, only λ/M_s is determined. The measurement of the temperature variation of λ and M_s will help explain the dependence of bubble propagation margins on temperature more fully.

The study of bubble propagation at high frequency of in-plane field is another area of interest. At high drive field frequency, the minimum drive field may vary more with the change of the magnetostriction coefficients.

Finally, it would be a tremendous contribution to the development of ion implanted bubble devices if one could develop a computer simulation program which could accurately predict the bias margin, given bubble film characteristics and the device layout within reasonable computing time, using the theory and the experimental results presented in this thesis and additional future improvement of understanding of the bubble propagation process.

Appendix A
Ion Implantation Range Statistics for Deuterium

Lindhard, Scharff and Schiott range statistics[60] for deuterium atoms in Au, SiO_2 and garnet are listed here. Since singly ionized deuterium molecules (D^+_2) are actually used for ion implantation, the energy listed has to be doubled to obtain the desired projected range. These statistics were provided by IBM Corporation.

Deuterium atom in gold

ENERGY (KEV)	PROJECTED RANGE (MICRONS)	PROJECTED STANDARD DEVIATION (MICRONS)	RANGE (MICRONS)	STANDARD DEVIATION (MICRONS)	NUCLEAR ENERGY LOSS (KEV/MICRON)	ELECTRONIC ENERGY LOSS (KEV/MICRON)
1	0.0063	0.01994	0.0955	0.0031	0.3328E+01	0.1472E+02
2	0.0108	0.02546	0.1425	0.0042	0.3636E+01	0.2082E+02
4	0.0194	0.03429	0.2118	0.0055	0.3680E+01	0.2945E+02
6	0.0282	0.04262	0.2667	0.0063	0.3634E+01	0.3606E+02
8	0.0373	0.05033	0.3138	0.0069	0.3517E+01	0.4164E+02
10	0.0468	0.05747	0.3559	0.0074	0.3329E+01	0.4656E+02
20	0.0981	0.08776	0.5247	0.0089	0.2719E+01	0.6584E+02
30	0.1508	0.11123	0.6567	0.0097	0.2295E+01	0.8064E+02
40	0.2041	0.13027	0.7690	0.0102	0.2007E+01	0.9312E+02
50	0.2568	0.14625	0.8685	0.0105	0.1769E+01	0.1041E+03
60	0.3098	0.15954	0.9588	0.0108	0.1552E+01	0.1140E+03
70	0.3625	0.17070	1.0421	0.0110	0.1381E+01	0.1232E+03
80	0.4145	0.18026	1.1197	0.0112	0.1258E+01	0.1317E+03
90	0.4653	0.18870	1.1928	0.0114	0.1181E+01	0.1397E+03
100	0.5143	0.19642	1.2619	0.0115	0.1152E+01	0.1472E+03
110	0.5612	0.20376	1.3277	0.0116	0.1145E+01	0.1544E+03
120	0.6070	0.21053	1.3906	0.0117	0.1062E+01	0.1613E+03
130	0.6522	0.21660	1.4510	0.0118	0.9876E+00	0.1679E+03
140	0.6969	0.22206	1.5092	0.0119	0.9229E+00	0.1742E+03
150	0.7409	0.22698	1.5653	0.0120	0.8676E+00	0.1803E+03
160	0.7843	0.23146	1.6196	0.0120	0.8217E+00	0.1862E+03
170	0.8269	0.23557	1.6723	0.0121	0.7851E+00	0.1920E+03
180	0.8688	0.23938	1.7234	0.0121	0.7580E+00	0.1975E+03
190	0.9098	0.24295	1.7732	0.0122	0.7403E+00	0.2029E+03
200	0.9501	0.24634	1.8216	0.0122	0.7319E+00	0.2082E+03
300	1.3183	0.27200	2.2522	0.0125	0.5373E+00	0.2550E+03
400	1.6456	0.28682	2.6155	0.0127	0.4439E+00	0.2945E+03
500	1.9390	0.29768	2.9357	0.0129	0.4016E+00	0.3292E+03

Deuterium atom in SiO_2

ENERGY (KEV)	PROJECTED RANGE (MICRONS)	PROJECTED STANDARD DEVIATION (MICRONS)	RANGE (MICRONS)	STANDARD DEVIATION (MICRONS)	NUCLEAR ENERGY LOSS (KEV/MICRON)	ELECTRONIC ENERGY LOSS (KEV/MICRON)
1	0.0188	0.01599	0.0623	0.0087	0.7151E+01	0.1319E+02
2	0.0388	0.02463	0.1071	0.0123	0.5594E+01	0.1865E+02
4	0.0800	0.03748	0.1804	0.0160	0.3864E+01	0.2637E+02
6	0.1206	0.04669	0.2414	0.0180	0.3136E+01	0.3230E+02
8	0.1583	0.05378	0.2944	0.0193	0.2663E+01	0.3730E+02
10	0.1945	0.05938	0.3421	0.0202	0.2258E+01	0.4170E+02
20	0.3533	0.07587	0.5337	0.0225	0.1410E+01	0.5897E+02
30	0.4868	0.08423	0.6832	0.0235	0.1078E+01	0.7223E+02
40	0.6043	0.08930	0.8102	0.0242	0.8524E+00	0.8340E+02
50	0.7098	0.09279	0.9224	0.0246	0.7506E+00	0.9324E+02
60	0.8064	0.09541	1.0240	0.0249	0.6518E+00	0.1021E+03
70	0.8961	0.09743	1.1176	0.0251	0.5777E+00	0.1103E+03
80	0.9803	0.09903	1.2048	0.0253	0.5200E+00	0.1179E+03
90	1.0597	0.10035	1.2868	0.0255	0.4735E+00	0.1251E+03
100	1.1351	0.10144	1.3643	0.0256	0.4353E+00	0.1319E+03
110	1.2072	0.10238	1.4381	0.0257	0.4032E+00	0.1383E+03
120	1.2762	0.10317	1.5087	0.0258	0.3759E+00	0.1445E+03
130	1.3425	0.10386	1.5764	0.0259	0.3523E+00	0.1503E+03
140	1.4065	0.10448	1.6415	0.0260	0.3317E+00	0.1560E+03
150	1.4683	0.10502	1.7043	0.0260	0.3136E+00	0.1615E+03
160	1.5282	0.10551	1.7652	0.0261	0.2974E+00	0.1668E+03
170	1.5863	0.10595	1.8241	0.0261	0.2830E+00	0.1719E+03
180	1.6428	0.10634	1.8813	0.0262	0.2701E+00	0.1769E+03
190	1.6977	0.10670	1.9370	0.0262	0.2583E+00	0.1818E+03
200	1.7513	0.10704	1.9913	0.0263	0.2476E+00	0.1865E+03
210	1.8037	0.10735	2.0442	0.0263	0.2378E+00	0.1911E+03
220	1.8548	0.10763	2.0958	0.0264	0.2288E+00	0.1956E+03
230	1.9048	0.10787	2.1463	0.0264	0.2206E+00	0.2000E+03
240	1.9538	0.10812	2.1957	0.0264	0.2129E+00	0.2043E+03
250	2.0017	0.10835	2.2441	0.0265	0.2058E+00	0.2085E+03
260	2.0488	0.10856	2.2916	0.0265	0.1992E+00	0.2126E+03
270	2.0950	0.10876	2.3381	0.0265	0.1930E+00	0.2167E+03
280	2.1403	0.10895	2.3838	0.0265	0.1873E+00	0.2207E+03
290	2.1849	0.10912	2.4287	0.0266	0.1818E+00	0.2246E+03
300	2.2287	0.10928	2.4728	0.0266	0.1768E+00	0.2284E+03
400	2.6325	0.11034	2.8790	0.0268	0.1388E+00	0.2637E+03
500	2.9889	0.11106	3.2369	0.0269	0.1149E+00	0.2949E+03

Deuterium atom in garnet

ENERGY (KEV)	PROJECTED RANGE (MICRONS)	PROJECTED STANDARD DEVIATION (MICRONS)	RANGE (MICRONS)	STANDARD DEVIATION (MICRONS)	NUCLEAR ENERGY LOSS (KEV/MICRON)	ELECTRONIC ENERGY LOSS (KEV/MICRON)
1	0.0097	0.01237	0.0506	0.0063	0.8430E+01	0.1771E+02
2	0.0195	0.01875	0.0849	0.0086	0.6883E+01	0.2504E+02
4	0.0405	0.02909	0.1402	0.0111	0.5029E+01	0.3541E+02
6	0.0606	0.03785	0.1856	0.0125	0.4382E+01	0.4337E+02
8	0.0821	0.04469	0.2252	0.0133	0.3541E+01	0.5008E+02
10	0.1025	0.05044	0.2606	0.0140	0.3164E+01	0.5599E+02
12	0.1218	0.05559	0.2930	0.0144	0.3006E+01	0.6133E+02
14	0.1424	0.05970	0.3231	0.0148	0.2451E+01	0.6625E+02
16	0.1625	0.06317	0.3513	0.0151	0.2266E+01	0.7082E+02
18	0.1817	0.06630	0.3780	0.0153	0.2119E+01	0.7512E+02
20	0.2002	0.06917	0.4032	0.0156	0.2008E+01	0.7918E+02
22	0.2180	0.07183	0.4273	0.0157	0.1935E+01	0.8305E+02
24	0.2353	0.07432	0.4503	0.0159	0.1900E+01	0.8674E+02
26	0.2520	0.07666	0.4724	0.0160	0.1849E+01	0.9028E+02
28	0.2683	0.07887	0.4938	0.0162	0.1778E+01	0.9369E+02
30	0.2842	0.08094	0.5144	0.0163	0.1713E+01	0.9698E+02
32	0.2998	0.08289	0.5343	0.0164	0.1652E+01	0.1002E+03
34	0.3151	0.08472	0.5537	0.0165	0.1596E+01	0.1032E+03
36	0.3300	0.08646	0.5725	0.0166	0.1543E+01	0.1062E+03
38	0.3447	0.08811	0.5908	0.0166	0.1493E+01	0.1091E+03
40	0.3591	0.08967	0.6087	0.0167	0.1447E+01	0.1120E+03
42	0.3733	0.09114	0.6261	0.0168	0.1403E+01	0.1147E+03
44	0.3873	0.09255	0.6431	0.0168	0.1361E+01	0.1174E+03
46	0.4010	0.09388	0.6597	0.0169	0.1321E+01	0.1201E+03
48	0.4146	0.09515	0.6761	0.0169	0.1284E+01	0.1227E+03
50	0.4279	0.09636	0.6920	0.0170	0.1248E+01	0.1252E+03
52	0.4411	0.09751	0.7077	0.0170	0.1214E+01	0.1277E+03
54	0.4541	0.09861	0.7231	0.0171	0.1182E+01	0.1301E+03
56	0.4669	0.09967	0.7382	0.0171	0.1151E+01	0.1325E+03
58	0.4796	0.10067	0.7530	0.0172	0.1122E+01	0.1348E+03
60	0.4921	0.10163	0.7676	0.0172	0.1094E+01	0.1371E+03
62	0.5045	0.10256	0.7819	0.0173	0.1068E+01	0.1394E+03
64	0.5167	0.10344	0.7961	0.0173	0.1042E+01	0.1416E+03
66	0.5288	0.10429	0.8100	0.0173	0.1018E+01	0.1438E+03
68	0.5407	0.10510	0.8237	0.0174	0.9953E+00	0.1460E+03
70	0.5526	0.10588	0.8372	0.0174	0.9735E+00	0.1481E+03
72	0.5643	0.10664	0.8505	0.0174	0.9528E+00	0.1502E+03
74	0.5758	0.10736	0.8636	0.0174	0.9332E+00	0.1523E+03
76	0.5873	0.10806	0.8766	0.0175	0.9146E+00	0.1544E+03
78	0.5987	0.10873	0.8894	0.0175	0.8970E+00	0.1564E+03
80	0.6099	0.10938	0.9020	0.0175	0.8804E+00	0.1584E+03
82	0.6210	0.11001	0.9145	0.0175	0.8647E+00	0.1603E+03
84	0.6321	0.11062	0.9269	0.0176	0.8500E+00	0.1623E+03
86	0.6430	0.11120	0.9391	0.0176	0.8362E+00	0.1642E+03
88	0.6538	0.11177	0.9511	0.0176	0.8234E+00	0.1661E+03
90	0.6645	0.11232	0.9630	0.0176	0.8114E+00	0.1680E+03
92	0.6752	0.11286	0.9748	0.0176	0.8003E+00	0.1698E+03
94	0.6857	0.11338	0.9865	0.0177	0.7901E+00	0.1717E+03
96	0.6961	0.11388	0.9980	0.0177	0.7807E+00	0.1735E+03
98	0.7065	0.11437	1.0094	0.0177	0.7722E+00	0.1753E+03
100	0.7168	0.11485	1.0207	0.0177	0.7646E+00	0.1771E+03

Appendix B
Garnet Film Characteristics

Composition : $\{BiDySmLuY\}_3[FeGa]_5O_{12}$

CA 71		
Thickness	t	0.65 μm
Collapse Field	H_c	580 Oe
Material Length	l	0.054 μm
Magnetization	$4\pi M$	960 G
Uniaxial Anisotropy	H_k	1850 Oe
Quality Factor	Q	1.9
Bubble Diameter	d	0.49 μm
Magnetostriction Coeff.	λ_{111}	-3.1×10^{-6}
	λ_{100}	-2.1×10^{-6}

CA72		
Thickness	t	0.67 μm
Collapse Field	H_c	550 Oe
Material Length	l	0.052 μm
Magnetization	$4\pi M$	910 G
Uniaxial Anisotropy	H_k	2050 Oe
Quality Factor	Q	2.3

Bubble Diameter	d	047 μm
Magnetostriction Coeff.	λ_{111}	-2.9×10^{-6}
	λ_{100}	-2.0×10^{-6}

CA 77

Thickness	t	0.71 μm
Collapse Field	H_c	635 Oe
Material Length	l	0.054 μm
Magnetization	$4\pi M$	1070 G
Uniaxial Anisotropy	H_k	1850 Oe
Quality Factor	Q	1.7
Bubble Diameter	d	0.49 μm
Magnetostriction Coeff.	λ_{111}	-2.9×10^{-6}
	λ_{100}	-2.0×10^{-6}

AK 92

Thickness	t	0.64 μm
Collapse Field	H_c	570 Oe
Material Length	l	0.056 μm
Magnetization	$4\pi M$	990 G
Uniaxial Anisotropy	H_k	2160 Oe
Quality Factor	Q	2.2
Bubble Diameter	d	0.50 μm
Magnetostriction Coeff.	λ_{111}	-3.1×10^{-6}
	λ_{100}	-1.5×10^{-6}

AK a8

Thickness	t	0.81 μm
Collapse Field	H_c	590 Oe
Material Length	l	0.069 μm
Magnetization	$4\pi M$	970 G
Uniaxial Anisotropy	H_k	1970 Oe
Quality Factor	Q	2.0
Bubble Diameter	d	0.62 μm
Magnetostriction Coeff.	λ_{111}	-3.5×10^{-6}
	λ_{100}	-2.5×10^{-6}

AK b1

Thickness	t	0.70 μm
Collapse Field	H_c	460 Oe
Material Length	l	0.074 μm
Magnetization	$4\pi M$	830 G
Uniaxial Anisotropy	H_k	2150 Oe
Quality Factor	Q	2.6
Bubble Diameter	d	0.67 μm
Magnetostriction Coeff.	λ_{111}	-3.8×10^{-6}
	λ_{100}	-3.4×10^{-6}

AH 27

Thickness	t	1.28 μm
Collapse Field	H_c	314 Oe
Material Length	l	0.113 μm
Magnetization	$4\pi M$	555 G
Uniaxial Anisotropy	H_k	1940 Oe
Quality Factor	Q	3.5
Bubble Diameter	d	1.02 μm
Magnetostriction Coeff.	λ_{111}	-3.7×10^{-6}
	λ_{100}	-2.5×10^{-6}

S 74

Composition : $\{SmGdTmY\}_3[FeGaAl]_5O_{12}$

Thickness	t	1.15 μm
Collapse Field	H_c	303 Oe
Material Length	l	0.137 μm
Magnetization	$4\pi M$	598 G
Uniaxial Anisotropy	H_k	1780 Oe
Quality Factor	Q	3.01
Bubble Diameter	d	1.23 μm
Magnetostriction Coeff.	λ_{111}	-2.5×10^{-6}
	λ_{100}	$+1\times10^{-6}$ (estimated)

Appendix C
Ion Implantation Conditions

Wafer ID	Region	First Implant		Second Implant	
		Energy (KeV)	Dose(10^{15}/cm^2)	Energy (Kev)\	Dose(10^{15}/cm^2)
CA71 and 72	1	40	12	16	8
	2	40	8.5	16	5.7
	3	32	11.3	12	7.5
	4	32	7.5	12	5
CA73	1	40	13.5	16	9
	2	40	10	16	6.7
	3	32	12.2	12	8.1
	4	32	9	12	6
CA77	1	40	11	16	7.3
	2	40	7.2	16	4.8
	3	32	10	12	6.7
	4	32	6	12	4
AK91	1	40	12.3	16	8.2
AK92	1	40	12.3	16	8.2
	2	40	9.3	16	6.2
	3	32	11.5	12	7.7
	4	32	8.5	12	5.7
AKa8 and b1	1	40	9.3	16	6.2
	2	40	6.8	16	4.5
	3	32	8.5	12	5.7
	4	32	5.7	12	3.8
S74 and 59	1	68	10	32	6.7
	2	68	8	32	5.3
AH27	1	68	17.5	32	12

References

1. A. J. Perneski, "Propagation Of Cylindrical Magnetic Domains In Orthoferrites", *IEEE Trans. Magn.*, **Mag-5**, pp. 554(1969).

2. I. S. Gergis, P. K. George And T. Kobayashi, "Gap Tolerant Bubble Propagation Circuit", *IEEE Trans. Magn.*, **Mag-12**, pp. 651(1976).

3. P. I. Bonyhard And J. L. Smith, "68 Kbit Capacity 16 μm Period Magnetic Bubble Memory Design With 2 μm Minimum Feature", *IEEE Trans. Magn.*, **Mag-12**, pp. 614(1976).

4. A. H. Bobeck And I. Danylchuk, "Characterization And Test Results For A 272 K Bubble Memory", *IEEE Trans. Magn.*, **Mag-13**, pp. 1370(1977).

5. K. Yamagish, T. Satoh, T. Miyashita, M. Ohashi, K. Betsui, K. Matsuda, And K. Komenou, "Design And Characterization For A 4 μm Period Permalloy Bubble Devices", *IEEE Trans. Magn.*, **Mag-19**, pp. 1853(1983).

6. Y.S. Lin, G.S. Almasi, And G.E. Keefe, "Contiguous-Disk Bubble Devices", *IEEE Trans. Magn.*, **Mag-13**, pp. 1744-1764(1977).

7. R.Wolfe Et Al., "Ion Implanted Patterns For Magnetic Bubble Propagation ", *AIP Conf. Proc.*, **10**, pp. 339-343(1972).

8. T. J. Walsh And S. H. Charap, "Novel Bubble Drive", *AIP Conf. Proc.*, **24**, pp. 550(1974).

9. A. H. Bobeck, S. L. Blank, A. D. Butherus, F. J. Ciak And W. Strauss, "Current-Access Magnetic Bubble Circuits", *Bell Syst. Tech. J.*, **58**, pp. 1453(1979).

10. M. H. Kryder, "Magnetic Bubble Scaling And Density Limits", *IEEE Trans. Magn.*, **Mag-15**, pp. 1009(1979).

11. Y.S. Lin, G.S. Almasi, D.B. Dove, G.E. Keefe, And C.C. Shir, "Orientation Dependence Of Propagation Margin Of 1 μm Bubble Contiguous-Disk Devices--Clues And Cures", *J. Appl. Phys.*, **50**, pp. 2258(1979).

12. R. Wolfe, T.J. Nelson, "Crystal Symmetry Effects In Ion-Implanted Propagation Patterns For Magnetic Bubbles: 'Roof-Top' Design", *IEEE Trans. Magn.*, **Mag-15**, pp. , September (1979).

13. T. J. Nelson, V. J. Fratello, D. J. Muehlner, B. J. Roman, And E. G. Slusky, "Four-Micron Period Ion-Implanted Bubble Test Circuits", *IEEE Trans. Magn.*, **Mag-22**, pp. 93(1986).

14. A. Hubert, "Domain Wall Phenomenon In Bubble Propagation Layers", *J. Of Magnetism And Magnetic Materials*, pp. 249(1983).

15. M. H. Kryder, D. Saunders, "The Effects Of Stress Relaxation And Anisotropic Magnetostriction On Charged Walls In Ion-Implanted Garnets", *IEEE Trans. Magn.*, No. Mag-19, pp. 1817(1983).

16. S. Chikazumi And S. Charap, *Physics Of Magnetism*, Krieger Publishing Company, 1964

17. A.H. Eschenfelder, *Magnetic Bubble Technology*, Springer-Verlag, New York, 1980.

18. A. A. Thiele, "Device Implications Of The Theory Of Cylindrical Magnetic Domains", *Bell Syst. Tech. J.*, **50**, pp. 725(1971).

19. J. Wu, *Solid State Magnetic Devices : Magnetic Bubble Logic Devices And Vertical Block Line Memory*, PhD dissertation, Carnegie Mellon University, 1986.

20. V. J. Fratello, R. D. Pierce, And C. D. Brandle, "Variation Of The Temperature Coefficient Of Collapse Field In Bismuth-Based Bubble Garnets", *J. Appl. Phys.*, **57**, pp. 4043(1985).

21. C. Krafft, *Deuterium Implantation In Magnetic Garnets*, PhD dissertation, Carnegie-Mellon University, 1984.

22. G. Suran, "Magnetic And Some Crystalline Properties Of H^+ Ion-Implanted Garnet Layers : A Study As A Function Of Annealing Treatment", *J. Appl. Phys.*, **54**, pp. 2006(1983).

23. R. Hirko And K. Ju, "Ion-Implantation Conditions And Annealing Effects For Contiguous Disk Bubble Devices", *IEEE Trans. Magn.*, **Mag-16**, pp. 958(1980).

24. Y. Satoh, M. Ohashi, T. Miyashita, And K. Komenou, "Magnetization, Strain, And Anisotropy Field Of Ne^+ And H^+ Ion-Implanted Layers In Bubble Garnet Films", *J. Appl. Phys.*, **53**, pp. 3740(1982).

25. T. Ikeda, T. Takeuchi, R. Imura, T. Sato, R. Suzuki, and Y. Sugita, "Optimization Of Ion Implantation Conditions For 4 μm Period Ion Implanted Bubble Devices", *Presented At The 1983 Intermag Conference*(1983).

26. K. Y. Ahn, D. E. Cox, A. G. Gangulee, S. M. Kane, R. J. Kobliska, R. P. McGouey, And A. M. Tuxford, "Fabricaton Of Contiguous-Disk Magnetic Bubble Devices", *IEEE Trans. Magn.*, **Mag-16**, pp. 93(1980).

27. D. A. Saunders And M. H. Kryder, "Stresses And Magnetoelastic Anisotropies At Implantation Edges In Ion Implanted Garnet Films", *J. Appl. Phys.*, **57**, pp. 4061(1985).

28. H. Makino, Y. Hidaka, And H. Matsutera, "Large Magnetic Anisotropy Change Induced By Hydrogen Ion Implantation In Europium Iron Garnet LPE Films", *J. of Magnetism and Magnetic Materials*, **35**, pp. 311(1983).

29. G. S. Almasi, E. A. Geiss, R. J. Hendel, G.E. Keefe, Y. S. Lin And M. Slusarczuk, "Bubble Domain Propagation Mechanisms In Ion-Implanted Structures", *AIP Conf. Proc.*, pp. 630(1974).

30. Y. Hidaka And H. Matsutera, "Charged Wall Formation Mechanism In Ion-Implanted Contiguous Disk Bubble Devices", *Appl. Phy. Let.*, **39**, pp. 116(1982).

31. S.C.M. Backerra, W.H. De Roode And U. Enz, "The Influence Of Implantation-Induced Stress Gardients In Magnetic Bubble Layers", *Phillips J. Res.*, **36**, pp. 112(1980).

32. D. A. Saunders And M. H. Kryder, "Charged Walls In A Fourfold Symmetric (100) Garnet Film", *IEEE Trans. Magn.*, **Mag-16**, pp. 955(1980).

33. D. A. Saunders, , PhD dissertation, Carnegie Mellon University, 1987.

34. C.C. Shir And Y.S. Lin, "Critical Curves For Determining Magnetization Directions In Implanted Garnet Films", *J. Appl. Phys.*, **50**, pp. 4246-4258(1979).

35. E. C. Stoner And E. P. Wolhfarth, "", *Phil. Trans. Roy. Soc.*, **A240**, pp. 74(1948).

36. Y. Sugita, R. Suzuki, T. Ikeda, T. Takeuchi, N. Kodama, M. Takeshita, R. Imura, T. Satoh, H. Umezaki, And N. Koyama, "Ion-Implanted And Permalloy Hybrid Magnetic Bubble Memory Devices", *IEEE Trans. Magn.*, **Mag-22**, pp. 239(1986).

37. H. Makino, O. Okada, Y. Hidaka, "Dysprosium Containing Bubble Garnet Composition For Ion-Implanted Contiguous Disk Devices", *J. Appl. Phys.*, pp. 2551(1984).

38. V. J. Fratello, R. Wolfe, S. L. Blank And T. J. Nelson, "High Curie Temperature Drive Layer Materials For Ion-Implanted Magnetic Bubble Devices", *J. Appl. Phys.*, **55**, pp. 2554(1984).

39. S. Jo And M. H. Kryder, "Nearly Isotropic Propagation Of 0.5 Micrometer Bubbles In Contiguous Disk Devices", *IEEE Trans. Magn.*, **Mag-22**, pp. 1278(1986).

40. J.S. Best, "Critical Curves For Implanted Garnet Films In The Presence Of A Demagnetizing Field", *J. Appl. Phys.*, **52**, pp. 2367-2369(1981).

41. B.A. Calhoun And I.L. Sanders, "Minimum Drive Fields In Contiguous-Disk Bubble Devices", *J. Appl. Phys.*, **52**, pp. 2386-2387(1981).

42. C. C. Shir, I. L. Sanders And Y. S. Lin, "The Role Of Charged Walls In Contiguous-Disk Bubble Devices-A Review", *IEEE Trans. Magn.*, **Mag-18**, pp. 217(1981).

43. H. Fukushima And N. Hayashi, "Computer Simulation Of Magnetization Distributions In Contiguous-Disk Bubble Devices", *Presented At The 1987 Intermag Conference* .

44. M.H. Kryder, "Ion Implanted Contiguous Disk Devices: Projections Of Performance", *IEEE Trans. Magn.*, **Mag-17**, pp. 2385(1981).

45. R. Campbell, "Magnetic Bubble Materials With Isotropic Magnetostriction", Master's thesis, Carnegie Mellon University, 1985.

46. Fowlis, And Copeland, *Amer. Inst. Phys. Conf. Proc.*, pp. 240(1972).

47. L. C. Hsia, P. E. Wigen, R. L. Bergner, And R. D. Henry, *IEEE Trans. Magn.*, **Mag-17**, pp. 2559(1981).

48. X. Wang, C.S. Krafft, M.H. Kryder, "Measurement Of Magnetocrystalline Anisotropy Field And Magnetostriction Coefficient In Garnet Films", *IEEE Trans. Magn.*, **Mag-18**, pp. 1295, November (1982).

49. Hewlett-Packard Company, "Piglet 2 Command Reference Guide".

50. C. Krafft. Private Communication

51. J. R. Wullert II, "Analysis And Design Of Ion-Implanted Contiguous Disk Bubble Memory Devices", Master's thesis, Carnegie Mellon University, 1986.

52. Y. Hidaka And H. Matsutera, "Influences Of Ion Implantation On Charged Wall Properties In Magnetic Bubble Devices", *J. of Magnetism and Magnetic Materials*, **35**, pp. 315-318(1983).

53. C.C. Shir, "Triangular Propagation Patterns For Contiguous-Disk Magnetic Bubble Devices", *J. Appl. Phys.*, **52**, pp. 2388-2390(1981).

54. Michael Alex. Private Communication

55. T. Omi, C. L. Bauer, And M. H. Kryder, "Strain Profiles In Ion-Implanted Bubble Devices Investigated By Transmission Electron Diffraction", *J. Appl. Phys.*, **53**, pp. 2528(1982).

56. K. Mizuno And H. Urai, "Operation Temperature Ranges For Ion-Implanted Bubble Devices With 1 μm Bubbles", *IEEE Trans. Magn.*, **Mag-21**, pp. 1706-1708(1985).

57. V. J. Fratello, R. D. Pierce And C. D. Brandle, "High Curie Temperature Drive Layer Materials For Ion-Implanted Magnetic Bubble Devices", *J. Appl. Phys.*, **55**, pp. 2554(1984).

58. L. G. Arbaugh Jr. And R. J. Fairholme, "Characterization Of A Full Military Temperature Range One Mbit Bubble Memory Device", *IEEE Trans. Magn.*, **Mag-22**, pp. 1287(1986).

59. S. Jo And M. H. Kryder, "Temperature Dependence Of Submicron Ion Implanted Devices", *J. Appl. Phys.*, **61**, pp. 3488(1987).

60. J. Linhard, M, Scharff, And H. E. Schiott, "", *Mat. Fys. Medd. Dan. Vid. Selsk.*, **33, No. 14**, pp. (1963).

END
DATE
FILMED
4-88
DTIC